UCLA

UCLA Electronic Theses and Dissertations

Title

Development of Nanostructured Nickel-Rich Cathode Materials for Fast-Charging Lithium-Ion Batteries and of High-Conductivity Doped Semiconducting Polymers for Energy Applications

Permalink

https://escholarship.org/uc/item/0jr223vd

Author

Basile, Victoria Mignon

Publication Date

2021

Peer reviewed|Thesis/dissertation

eScholarship.org Powered by the California Digital Library
University of California

UNIVERSITY OF CALIFORNIA

Los Angeles

Development of Nanostructured Nickel-Rich Cathode Materials for Fast-Charging Lithium-Ion Batteries and of High-Conductivity Doped Semiconducting Polymers for Energy Applications

A dissertation submitted in partial satisfaction of the requirements for the degree Doctor of Philosophy in Chemistry

by

Victoria Mignon Basile

2021

© Copyright by

Victoria Mignon Basile

2021

ABSTRACT OF THE DISSERTATION

Development of Nanostructured Nickel-Rich Cathode Materials for Fast-Charging Lithium-Ion Batteries and of High-Conductivity Doped Semiconducting Polymers for Energy Applications

by

Victoria Mignon Basile
Doctor of Philosophy in Chemistry
University of California, Los Angeles, 2021
Professor Sarah H. Tolbert, Chair

The development of new materials for energy applications is necessary to create new solutions to minimize our use of fossil fuels. This dissertation is composed of two separate projects that use different materials to address energy challenges. The first part focuses on nanostructured nickel-rich cathode materials for use in fast-charging lithium-ion batteries. Fast-charging batteries are desired for use in electric vehicles to shorten charging times from hours to minutes, which could help with their larger scale implementation and reduction of fossil fuel use. Fast-charging can be achieved by nanostructuring certain battery materials, which decreases lithium-ion diffusion lengths and can help suppress slow discontinuous, first-order phase transitions, while retaining high capacity. This behavior has been termed pseudocapacitance. While a number of

pseudocapacitive anodes have been produced, there are few examples of high-capacity pseudocapacitive cathodes. Here, we studied the nickel-rich cathode materials $LiNi_{0.80}Co_{0.15}Al_{0.05}O_2$ (NCA) and $LiNi_{0.x}Mn_{0.y}Co_{0.z}O_2$ (NMCxyz), both of which are high-capacity materials that show suppressed discontinuous phase transitions. Because of this favorable continuous phase transition behavior, we hypothesized that only modest decreases in particle sizes would be needed to develop pseudocapacitive behavior. We used polymer templating with a sol-gel synthesis to synthesize nanoporous NCA and NMC materials with decreased particle sizes. We then studied the effect of the particle size on the electrochemical kinetic properties of the material and cycling behavior at fast-charging rates. The results showed improved (dis)charge kinetics compared to the bulk and identified characteristics of pseudocapacitance. Nanostructured NCA cathodes were also paired with a fast-charging pseudocapacitive anode to demonstrate their potential for commercial full-cell fast-charging devices.

The second part of this dissertation studies semiconducting polymers, which have potential applications in organic electronics, such as solar cells and thermoelectrics. These materials are interesting for energy applications because they are flexible, low-cost, and solution-processable. While semiconducting polymers show low conductivity, molecular doping can improve conductivity by adding mobile charge carriers. Here a novel redox-tunable dodecaborane-based dopant was introduced into a semiconducting polymer network and the resulting electronic, structural, and optical properties were studied. Large and strongly-oxidizing dopants were found to dramatically increase conductivity by producing more and higher-mobility charge carriers.

The dissertation of Victoria Mignon Basile is approved.

Bruce S. Dunn

Xiangfeng Duan

Chong Liu

Sarah H. Tolbert, Committee Chair

University of California, Los Angeles

2021

TABLE OF CONTENTS

LIST OF FIGURES

Chapter 2. Nanostructured $LiNi_{0.80}Co_{0.15}Al_{0.05}O_2$ (NCA) for Fast-Charging, High Capacity Cathodes

Chapter 3. Scalable Synthesis of Templated Nanoporous $LiNi_{0.80}Co_{0.15}Al_{0.05}O_2$ (NCA) for Fast-Charging Lithium-Ion Batteries

Chapter 4. Nanostructured $LiNi_{0.6}Mn_{0.2}Co_{0.2}O_2$ (NMC622) for Fast-Charging Lithium-Ion Batteries

Chapter 5. Dodecaborane-Based Dopants Designed to Shield Anion Electrostatics Lead to Increased Carrier Mobility in a Doped Conjugated Polymer

APPENDIX A. Detailed Procedure for X-Ray Diffraction of Nickel-Rich Layered Transition Metal Oxides

LIST OF TABLES

Chapter 2. Nanostructured $LiNi_{0.80}Co_{0.15}Al_{0.05}O_2$ (NCA) for Fast-Charging, High-Capacity Cathodes

Chapter 3. Scalable Synthesis of Templated Nanoporous $LiNi_{0.80}Co_{0.15}Al_{0.05}O_2$ (NCA) for Fast-Charging Lithium-Ion Batteries

Chapter 4. Nanostructured $LiNi_{0.6}Mn_{0.2}Co_{0.2}O_2$ (NMC622) for Fast-Charging Lithium-Ion Batteries

Chapter 5. Dodecaborane-Based Dopants Designed to Shield Anion Electrostatics Lead to Increased Carrier Mobility in a Doped Conjugated Polymer

ACKNOWLEDGEMENTS

There are a number of people I would like to thank for their support during my graduate career. First of all, I would like to thank my parents and sisters for always believing in me and always being there when I need them. I would also like the thank my husband and best friend, Bruce Ortiz, for going on this journey with me and supporting me every step of the way. I appreciate his sacrifice to move half-way across the country to Los Angeles and have loved getting to explore this city with him.

I would like to thank Professor Sarah Tolbert for being my advisor and all of her guidance and support throughout my graduate career. I am grateful for all of her advice on topics of science and on life. I am also appreciative for her encouragement to be involved in many outreach activities outside of lab work and for providing outreach opportunities through her Nanoscience Outreach Program. I feel lucky to have had such a strong female professional role model. I would also like to thank my committee members, Professor Bruce Dunn, Professor Xiangfeng Duan, and Professor Chong Liu for their guidance.

I would like to acknowledge and thank Battery Streak Inc. for giving me the opportunity to continue researching fast cathodes and for everything it taught me about commercial batteries. More specifically I would like to thank David Grant and Dr. Chun-Han Lai of Battery Streak Inc. I would also like to thank my collaborators within Battery Streak projects including, Professor Sarah Tolbert, Professor Bruce Dunn, Dr. Terri Lin, Dr. Jon Lau, Dr. Benjamin Lesel, Dr. Christopher Choi, Danielle Butts, Maggie Fox, and Yiyi Yao.

When I started graduate school, Dr. Benjamin Lesel was my mentor for my graduate research project and I would like to thank him for his mentorship, for his continued optimism, and

his love of science. I would like to thank Dr. Ignacio Martinez, Dr. John Cook, and Dr. Yan Yan for all of their help with XPS. From my TA positions at UCLA, I would like to specifically thank Professor Johnny Pang, who is always very enthusiastic about teaching and has made my many teaching experiences enjoyable.

The Tolbert lab has been a fun group of scientist to work with and I would like to thank both past and present members of the Tolbert lab. Specifically, I would like to acknowledge Dr. K.J. Winchell who started in the Tolbert lab at the same time as me and made my time in graduate school more enjoyable. I would like to acknowledge Sophia King for all of her advice and her honest opinions on my figures. Lastly, I would also like to specifically thank my mentee Casey Cornwell, who has been an incredible help and I could not have done this without him.

Previous Publications and Contributions of Co-Authors

Chapter 2 is a version of Victoria M. Basile, Chun-Han Lai, Christopher S. Choi, Danielle M. Butts, Sophia C. King, Bruce S. Dunn, and Sarah H. Tolbert, "Nanostructured $LiNi_{0.80}Co_{0.15}Al_{0.05}O_2$ (NCA) for Fast-Charging, High-Capacity Cathodes". I synthesized samples, assembled coin-cells, and performed electrochemical rate and kinetics testing. Chun-Han Lai did many background studies to determine the ideal electrode and electrolyte compositions, he also assembled and performed electrochemical tests on the full-cells. Christopher S. Choi performed and analyzed the data for the electrochemical galvanostatic intermittent titration technique (GITT) measurements and electrochemical impedance measurements (EIS). During Phase II of Research reopening during the COVID-19 pandemic, Christopher also assembled many coin-cells, which is greatly appreciated. Danielle M. Butts helped with preliminary GITT measurements and characterized samples using nitrogen porosimetry. Sophia C. King imaged and analyzed samples by transmission electron microscopy (TEM). I wrote the manuscript and Professor Bruce S. Dunn and Professor Sarah H. Tolbert helped edit the manuscript. This manuscript will be submitted for publication shortly after this dissertation is filed.

Chapter 3 is a version of Victoria M. Basile, Chun-Han Lai, Christopher S. Choi, Sophia C. King, Danielle M. Butts, Bruce S. Dunn, and Sarah H. Tolbert, "Scalable Synthesis of Templated Nanoporous $LiNi_{0.80}Co_{0.15}Al_{0.05}O_2$ (NCA) for Fast-Charging Lithium-Ion Batteries". I synthesized samples, assembled coin-cells, and performed electrochemical rate and kinetics testing. Chun-Han Lai did many background studies to determine the ideal electrode and electrolyte compositions. He also assembled and performed electrochemical tests on thick half-cells and full-cells, after numerous rounds of study and optimization. Chris S. Choi, performed and analyzed EIS measurements, he also assembled many coin-cells during Phase II of the Research reopening during the COVID-19 pandemic. Sophia C. King imaged and analyzed samples by TEM. Danielle M. Butts characterized samples using nitrogen porosimetry. I wrote the manuscript and Professor Bruce S. Dunn and Professor Sarah H. Tolbert helped edit the manuscript. This manuscript is written and is currently being edited by the co-authors.

Chapter 4 is a version of Victoria M. Basile, Casey Cornwell, and Sarah H. Tolbert, "Nanostructured $LiNi_{0.6}Mn_{0.2}Co_{0.2}O_2$ (NMC622) for Fast-Charging Lithium-Ion Batteries". Casey Cornwell and I both synthesized samples, characterized samples, assembled coin-cells, and performed electrochemical rate and kinetics testing. I wrote the manuscript and Casey Cornwell and Professor Sarah H. Tolbert helped edit the manuscript. This manuscript is written with the final pieces of data being collected by Casey Cornwell, the manuscript will then be edited by the co-authors.

Chapter 5 is a version of Taylor J. Aubry, Jonathan C. Axtell, Victoria M. Basile, K. J. Winchell, Jeffrey R. Lindemuth, Tyler M. Porter, Ji-Yuan Liu, Anastassia N. Alexandrova, Clifford P. Kubiak, Sarah H. Tolbert, Alexander M. Spokoyny, and Benjamin J. Schwartz. "Dodecaborane-Based Dopants Designed to Shield Anion Electrostatics Lead to Increased Carrier Mobility in a Doped Conjugated Polymer" *Advanced Materials,* 2019, 31 (11), 1805647. Taylor J. Aubry wrote the manuscript and collected and analyzed the spectroscopy and conductivity data. Jonathan C. Axtell synthesized the dopant. I collected and analyzed the XPS data. K.J. Winchell collected and analyzed the GIWAXS data and helped write the manuscript. Jeffrey R. Lindemuth collected AC-Hall Effect Data. Tyler M. Porter performed NMR self-exchange experiments. Ji-Yuan Liu performed DFT calculations. The PIs and/or project directors were Cliff Kubiak, Anastasia Alexandrova, Sarah Tolbert, Alexander Spokoyny and Benjamin Schwartz.

Professor Sarah H. Tolbert directed the research presented and the work was supported by: Department of Energy (DOE), Battery Streak Inc., California NanoSystems Institute (CNSI), and the University of California, Los Angles Graduate Division. Diffraction data in Chapter 5 was collected at the Stanford Synchrotron Radiation Lightsource, a national user facility operated by Stanford University on behalf of the U.S. Department of Energy, Office of Basic Science. TEM images were collected using instruments at the Electron Imaging Center for NanoMachines supported by NIH (1S10RR23057) and CNSI at UCLA.

VITA

2015 B.S. in Biochemistry, The University of Texas at Austin

2017 M.S. in Chemistry, University of California, Los Angeles

Publications

1. Jintao Fu, John S. Corsi, Samuel S. Welborn, **Victoria Basile**, Lin Wang, Alexander K. Ng, and Eric Detsi. "Eco-Friendly Synthesis of Nanoporous Magnesium by Air-Free Electrolytic Dealloying with Recovery of Sacrificial Elements for Energy Conversion and Storage Applications" *ACS Sustainable Chem. Eng.*, **2021**, *9* (7), 2762-2769.

2. Sophia C. King, Man Li, Tiphaine Galy, Yan Yan, Joon Sang Kang, **Victoria M. Basile**, Yolanda L. Li, Michal Marszewski, Laurent Pilon, Yongjie Hu, and Sarah H. Tolbert. "Examining the Role of Atomic Scale Heterogeneity on the Thermal Conductivity of Transparent, Thermally Insulating, Mesoporous Silica-Titania Thin Films" *J. Phys. Chem. C*, **2020**, *124* (50), 27442-27452.

3. Yolanda L. Li, Chih-Te Zee, Janice B. Lin, **Victoria M. Basile**, Mit Muni, Maria D. Flores, Julen Munarriz, Richard B. Kaner, Anastassia N. Alexandrova, K. N. Houk, Sarah H. Tolbert, and Yves Rubin. "Fjord-edge Graphene Nanoribbons with Site-Specific Nitrogen Substitution" *J. Am. Chem. Soc.*, **2020**, *142* (42), 18093-18102.

4. Taylor J. Aubry, K.J. Winchell, Charlene Z. Salamat, **Victoria M. Basile**, Jeffrey R. Lindemuth, Julia M. Stauber, Jonathan C. Axtell, Rebecca M. Kubena, Minh D. Phan, Matthew J. Bird, Alexander M. Spokoyny, Sarah H. Tolbert, and Benjamin J. Schwartz. "Tunable Dopants with Intrinsic Counterion Separation Reveal the Effects of Electron Affinity on Dopant Intercalation and Free Carrier Production in Sequentially Doped Conjugated Polymer Films" *Advanced Functional Materials*, **2020**, *30* (28), 2001800.

5. Timothy Lee, Jintao Fu, **Victoria Basile**, John Corsi, Zeyu Wang, and Eric Detsi. "Activated Alumina as Value-Added Byproduct from the Hydrolysis of Hierarchical Nanoporous Aluminum with Pure Water to Generate Hydrogen Fuel" *Renewable Energy*, **2020**, *155*, 189-196.

6. Taylor J. Aubry, Jonathan C. Axtell, **Victoria M. Basile**, K. J. Winchell, Jeffrey R. Lindemuth, Tyler M. Porter, Ji-Yuan Liu, Anastassia N. Alexandrova, Clifford P. Kubiak, Sarah H. Tolbert, Alexander M. Spokoyny, Benjamin J. Schwartz. "Dodecaborane-Based Dopants Designed to Shield Anion Electrostatics Lead to Increased Carrier Mobility in Doped Conjugated Polymers" *Advanced Materials*, **2019**, *31* (11), 1805647.

7. Feng Li,* **Victoria M. Basile**,* Michael J. Rose. "Electron Transfer through Surface-Grown, Ferrocene-Capped Oligophenylene Molecular Wires (5-50 Å) on *n*-Si(111) Photoelectrodes" *Langmuir*, **2015**, *31* (28), 7712-7716. (*authors contributed equally)

8. Feng Li, **Victoria M. Basile**, Ryan T. Pekarek, Michael J. Rose. "Steric Spacing of Molecular Linkers on Passivated Si(111) Photoelectrodes" *ACS Applied Materials and Interfaces*, **2014**, *6* (22), 20557-20568.

Presentations

1. American Chemical Society National Meeting, Oral Presentation (Virtual Conference), "NCA with decreased particle sizes as fast-charging cathode materials for lithium-ion batteries." **Victoria M. Basile**, Chun-Han Lai, Christopher S. Choi, Danielle M. Butts, Bruce S. Dunn, and Sarah H. Tolbert, August 2020.

2. 237th Electrochemical Society Meeting (Talk, Conference Canceled), "Nanostructured NCA as a Fast Charging High Rate Cathode Material for Lithium-Ion Batteries" **Victoria M. Basile**, Chun-Han Lai, Danielle M. Butts, Bruce S. Dunn, Sarah H. Tolbert. Montreal, Canada, May 2020.

3. 2019 Seaborg Symposium. "Nanostructured NCA ($LiNi_{0.80}Co_{0.15}Al_{0.05}O_2$) as a Fast Charging Pseudocapacitive Cathode Material for Lithium-Ion Batteries" **Victoria M. Basile**, Chun-Han Lai, Danielle M. Butts, Bruce S. Dunn, Sarah H. Tolbert. Los Angeles CA, November 2019.

4. American Chemical Society National Meeting (UCLA Showcase, Poster), "Studying the Surface Effects of PEDOT:PSS on Nanoporous $LiMn_2O_4$" **Victoria M. Basile**, Benjamin K. Lesel, Sarah H. Tolbert. San Francisco CA, April 2017.

5. American Chemical Society National Meeting (Poster), "Studying the Surface Effects of PEDOT:PSS on Nanoporous $LiMn_2O_4$" **Victoria M. Basile**, Benjamin K. Lesel, Sarah H. Tolbert. San Francisco CA, April 2017.

6. 7th Center for Electrochemistry Annual Workshop on Electrochemistry (Poster), "Synthesis and Effects of Modifying Extended Phenylene Wire Lengths on a Silicon(111) Surface" **Victoria M. Basile**, Feng Li, Michael J. Rose. Austin TX, February 2015.

7. American Chemical Society Southwest Regional Meeting (Poster), "Synthesis and Effects of Modifying Extended Phenylene Wire Lengths on a Silicon(111) Surface" **Victoria M. Basile**, Feng Li, Michael J. Rose. Fort Worth TX, November 2014.

CHAPTER 1

Introduction

As the need for reducing fossil fuel consumption increases, so does the demand to produce and store energy cleanly and renewably.[1] Solar cells and other renewable energy sources produce clean energy that can then be stored with lithium-ion batteries. Lithium-ion batteries are used heavily for personal electronics, electric vehicles (EVs), and solar power storage/back-up energy storage. For some devices, such as EVs and personal electronics, a fast-charging lithium-ion battery would greatly improve the way these devices are used. Currently, internal combustion engine (ICE) vehicles take only about 5 minutes to refuel, while EVs take anywhere from 4 to 12 hours to fully charge. If an EV lithium-ion battery was able to be fully charged in 5-10 minutes (comparable to refueling with gas), this could help lead to the usage of EVs over traditional ICE vehicles, which is important because transportation accounts for one of the major uses of fossil fuels.[1]

The first part of this dissertation (Chapters 2-4), focuses on fast-charging lithium-ion batteries, which have potential for use in EVs. While traditional lithium-ion batteries are able to store a high amount of charge through reversible faradaic redox reactions that results in high energy density, they charge slowly as a result of their low power density.[2] These traditional batteries have low power densities because the diffusion of lithium ions through the bulk of their material, which is generally accompanied by slow discontinuous, first-order phase transitions, limits their rate of charging and discharging.[3,4] Conversely, electric double layer capacitors (EDLCs) can be charged quickly because they store charge through non-faradaic surface adsorption/desorption of ions. However, EDLCs ultimately have low energy density due to ion repulsion that limits the amount of ions that can be adsorbed to the surface.[2] This restricts the practicality of EDLCs for use as a long range EV power source. Ideally for EVs, a material would have both high power density and high energy density, for fast-charging and long driving range, respectively. Intercalation pseudocapacitive materials store charge through reversible redox reactions accompanied by the intercalation of an ion for charge balance. These materials also lack slow, discontinuous phase transitions and have short, near-surface lithium-ion diffusion distances.[5–9] Therefore, pseudocapacitive materials can be charged and discharged quickly, while retaining high energy density, which makes them ideal for usage in EVs.

Intercalation pseudocapacitance can be intrinsic to the material, where fast charging capability without a phase transition is observed at all particle sizes.[10] Examples of heavily studied intrinsic pseudocapacitive materials include $RuO_2{:}xH_2O$[11–14] and T-Nb_2O_5.[9,10,15,16] For some battery materials that clearly undergo a first-order phase transition in the bulk, there can be a transition from battery-like to pseudocapacitive behavior at smaller particle sizes, marked by a suppression of their phase transition.[10] These are called extrinsic pseudocapacitive materials and exhibit fast-charging at small particle sizes, examples include: MoO_2,[17–19] MoS_2,[20–24] V_2O_5,[25,26] $LiCoO_2$,[27] and $LiMn_2O_4$.[28–31] Most of these pseudocapacitive materials operate in low to medium voltage ranges with high capacities (< 2.5 V vs. Li/Li^+ and > 200 mAh/g) and are generally used as anodes. Alternatively, there are fewer pseudocapacitive materials that operate at high voltages (> 3 V vs. Li/Li^+), which are generally used as cathodes. The pseudocapacitive materials that do operate at these high voltage ranges, $LiCoO_2$ and $LiMn_2O_4$, are limited by capacity that decreases with decreasing particle size.[27,29] Because a full-cell device is composed of both an anode and a cathode and most are limited by the lower capacities of cathodes, a high-capacity, fast-charging cathode is desired.

In Chapters 2 and 3 we studied the effects of nanostructuring the cathode material $LiNi_{0.80}Co_{0.15}Al_{0.05}O_2$ (NCA), which is a layered transition metal oxide. NCA is an interesting cathode material to study because it has high capacity and suppressed discontinuous, first-order phase transitions in the bulk.[32,33] The un-doped parent structure of NCA, $LiNiO_2$, undergoes three first-order phase transitions during cycling between 3.4 and 4.25 V vs. Li/Li^+.[34] Whereas for NCA, the small amount of cobalt and aluminum dopants act to suppress these phase transitions by stabilizing the layered structure.[32,33,35] Therefore, nanostructuring NCA would only be needed to decrease lithium-ion diffusion lengths and not to suppress phase transitions, meaning it could be possible to obtain fast-charging at moderately small particle sizes.

While NCA shows promise for a nanostructured fast-charging cathode material, this material has two major problems, cation mixing and air-sensitivity. The first problem, cation mixing, occurs when Ni^{2+} (from the starting materials) is present in the structure instead of the desired form of Ni^{3+}. The Ni^{2+} can migrate to the Li^+ layer because of their similar ionic radii (Ni^{2+} = 0.68 Å and Li^+ = 0.74 Å).[36] This is an issue for fast-charging applications because upon charging the nickel is oxidized to Ni^{3+} (0.56 Å),[36] which leads to local collapse of the lithium layers and impedes lithium diffusion.[37] The second problem is that NCA is sensitive to carbon dioxide and water in the air, which react with excess lithium on the surface of NCA to form insulating layers of Li_2CO_3.[38,39] This is a major issue because when NCA is nanostructured, the amount of available surface increases, resulting in a higher amount of insulating surface layers. Additionally, it has been proposed that Ni^{3+} near the surface of NCA can be reduced with air exposure, due to the instability of Ni^{3+}, which leads to the formation of a NiO-like structure.[40,41] NiO does not have a lithium-ion diffusion pathway and is made up of Ni^{2+}, which is electrochemically inactive, both of which result in poor electrochemical performance.[42] Another result of the formed NiO layer is the release of near surface lithium, which can then further react with the air to form a thicker Li_2CO_3 layer on the surface.[41] By keeping the nanostructured NCA air-free as much as possible, we aim to avoid the formation of any NiO or thick Li_2CO_3 layers.

In Chapter 2 we explored the use of the colloidal polymer template poly(methyl methacrylate) (PMMA) to synthesize nanostructured NCA. PMMA can be synthesized in a variety of colloid sizes,[43,44] which allows for flexible size control, and can easily be incorporated into the sol-gel synthesis of NCA.[45] The high temperatures required to anneal NCA with good cation ordering (> 700 °C) lead to particle size growth so two different annealing methods were used to control the NCA particle sizes. A conventional annealing method, with an hour long heating ramp and two-hour soak time at 800 °C, was used to obtain medium sized (~ 300 nm) particles of NCA. While a method analogous to rapid thermal annealing (RTA), with a 5-minute anneal at 850 °C, gave small particle sized (~ 150 nm) NCA. These two nanostructured NCAs were compared to bulk NCA, which has a large primary particle sizes (~ 425 nm) that make up the dense microsphere (~ 5 μm in diameter) structure of bulk NCA. The use of the PMMA templates allowed for greater nanoscale porosity in the nanostructured samples over that of bulk NCA. The electrochemical performance of the two nanostructured materials was then studied to assess the benefits of decreased particle sizes and increased nanoscale porosity. Interestingly, the medium sized NCA had the highest capacity retention at fast-rates, followed by the small particle size, and then bulk NCA. The rapid heating in the RTA synthesis led to fast combustion of the PMMA template, which created a reducing atmosphere and a reduced nickel surface on the small NCA particles.[46] Thus fast lithium-ion diffusion through the small NCA particle sizes was hindered by surface NiO layers. However, both nanostructured materials showed properties of pseudocapacitance and had highly capacitive contributions.

In Chapter 3, nanostructured NCA was synthesized with a block copolymer Pluronic template (F127 or F108). While there is less size control over the block copolymer templates, they are oxygen rich templates that should not reduce the NCA surface and are both readily commercially available and cheap. This second point is important because battery materials need to be scaled-up many times for the manufacturing of commercial battery devices.[47] Using the conventional annealing and RTA methods we were able to synthesize similarly sized medium (~ 275 nm) and small (~ 125 nm) particles of NCA with nanoscale porosity. These nanostructured NCA materials were analyzed electrochemically and both samples showed properties of pseudocapacitive charge storage. Again, the medium sized particles had the highest capacity retention. Although the surface of particles synthesized by RTA were not reduced, the rapid heating led to partial combustion of the Pluronic template, which reacted with the NCA surface to form insulating lithium carbonate layers that impeded lithium-ion diffusion at fast-rates. Both of the medium sized NCA materials from Chapter 2 and 3 were paired with a pseudocapacitive Nb_2O_5 anode for a full-cell device to show their viability for commercialization.

In Chapter 4 we turned our attention to another nickel-rich layered oxide cathode material, $LiNi_xMn_yCo_zO_2$ (NMCxyz). Unlike NCA, which has been found to have optimal electrochemical properties at one stoichiometry ($LiNi_{0.80}Co_{0.15}Al_{0.05}O_2$), NMC is studied over a range of stoichiometries.[48,49] Some of the most commonly studied within this range are $LiNi_{1/3}Mn_{1/3}Co_{1/3}O_2$ (NMC111), $LiNi_{0.6}Mn_{0.2}Co_{0.2}O_2$ (NMC622), and $LiNi_{0.8}Mn_{0.1}Co_{0.1}O_2$ (NMC811). There are advantages and disadvantages to varying the amounts of transition metals; high nickel content NMCs have greater specific capacity and rate capability but lower structural stability, while the opposite trend is seen at low nickel contents.[49,50] Adding Mn^{4+} and Co^{3+} as dopants adds structural stability to the NMC structure.[48,51,52] However, as the amount of Mn^{4+} in NMC is increased, so is the amount of Ni^{2+} for charge balance, which leads to a loss of some capacity and greater cation mixing.[48,53,54] Fortunately as is the case for NCA, discontinuous, first-order phase transitions are suppressed in bulk NMC materials.[55,56] Therefore we can also study the effect of nanostructuring using polymer template materials on the electrochemical properties of NMC cathode materials. Because the stoichiometry of NMC can be varied, a NMC material that balances high capacity and stability as the material is nanostructured was desired. Here we choose to study NMC622, which still has relatively high specific capacity (~170 mAh/g when cycled to 4.2 V vs. Li/Li^+) as well as good stability.[48] Nanostructured NMC622 was synthesized using Pluronic templates and a conventional annealing method, which resulted in particle sizes around 100-200 nm. The NMC622 cathode material was analyzed electrochemically and displayed fast charging capabilities and characteristics of pseudocapacitance.

In Chapter 5, we shift gears significantly, to study dodecaborane-based doped semiconducting polymers. As mentioned previously, while lithium-ion batteries allow for the storage of energy, green sources of energy, such as solar, are required to reduce the use of fossil fuels. Semiconducting polymers are of interest for use in energy applications because they are cheap, solution processable, and their properties can be easily tuned.[57,58] These materials can be used for solar cell applications, with poly(3-hexylthiophene-2,5-diyl) (P3HT) being one of the most commonly used polymers.[59,60] However, semiconducting polymers have low electrical conductivity, so they are often doped to create additional charge carriers, either electrochemically or through molecular doping to increase conductivity.[61,62] Here, a dodecaborane-based (DDB) dopant (a 12-boron core functionalized with a 3,5-bis(trifluoromethyl)benzyloxy substituent) was used to dope the semiconducting polymer P3HT. The DDB dopant has a high redox potential, 0.67 V vs. F_c/F_c^+, which is 500 mV higher than the traditional dopant 2,3,5,6-tetrafluoro-7,7,8,8-

tetracyanoquinodimethane (F_4TCQ), giving it a large energetic force for doping. However, with molecular doping, full film penetration and distribution can be an issue, and here this is exasperated by the large DDB dopant, which is about 2 nm in diameter.[63] Fortunately, a method developed by the Schwartz lab at UCLA called sequential processing, swells the polymer film to allow the molecular dopants to infiltrate the entire film.[64,65] X-ray photoelectron spectroscopy (XPS) was used to confirm full penetration of the DDB dopant into the P3HT polymer film. The large size of the DDB dopant allows for spatial separation of the dopant counteranion and conjugated polymer polaron creating mobile charge carriers. This results in doped P3HT films with high conductivity and high carrier mobility. Additionally, the substituent groups on the DDB dopant can be modified, which allows for easy tunability of the redox potential and electrical conductivity of semiconducting polymer films.

1.1 References

(1) Dell, R. M.; Rand, D. A. J. Energy Storage - A Key Technology for Global Energy Sustainability. *J. Power Sources* **2001**, *100* (1–2), 2–17. https://doi.org/10.1016/S0378-7753(01)00894-1.

(2) Winter, M.; Brodd, R. J. What Are Batteries, Fuel Cells, and Supercapacitors? *Chem. Rev.* **2004**, *104* (10), 4245–4269.

(3) Van Der Ven, A.; Bhattacharya, J.; Belak, A. A. Understanding Li Diffusion in Li-Intercalation Compounds. *Acc. Chem. Res.* **2013**, *46* (5), 1216–1225. https://doi.org/10.1021/ar200329r.

(4) Li, D.; Zhou, H. Two-Phase Transition of Li-Intercalation Compounds in Li-Ion Batteries. *Mater. Today* **2014**, *17* (9), 451–463. https://doi.org/10.1016/j.mattod.2014.06.002.

(5) Conway, B. E. Two-Dimensional and Quasi-Two-Dimensional Isotherms for Li Intercalation and UPD Processes at Surfaces. *Electrochim. Acta* **1993**, *38* (9), 1249–1258. https://doi.org/10.1016/0013-4686(93)80055-5.

(6) Augustyn, V.; Simon, P.; Dunn, B. Pseudocapacitive Oxide Materials for High-Rate Electrochemical Energy Storage. *Energy Environ. Sci.* **2014**, *7* (5), 1597–1614. https://doi.org/10.1039/c3ee44164d.

(7) Choi, C.; Ashby, D. S.; Butts, D. M.; DeBlock, R. H.; Wei, Q.; Lau, J.; Dunn, B. Achieving High Energy Density and High Power Density with Pseudocapacitive Materials. *Nat. Rev. Mater.* **2020**, *5*, 5–19. https://doi.org/10.1038/s41578-019-0142-z.

(8) Fleischmann, S.; Mitchell, J. B.; Wang, R.; Zhan, C.; Jiang, D. E.; Presser, V.; Augustyn, V. Pseudocapacitance: From Fundamental Understanding to High Power Energy Storage Materials. *Chem. Rev.* **2020**, *120* (14), 6738–6782. https://doi.org/10.1021/acs.chemrev.0c00170.

(9) Augustyn, V.; Come, J.; Lowe, M. A.; Kim, J. W.; Taberna, P.-L.; Tolbert, S. H.; Abruña, H. D.; Simon, P.; Dunn, B. High-Rate Electrochemical Energy Storage through Li^+ Intercalation Pseudocapacitance. *Nat. Mater.* **2013**, *12*, 518–522. https://doi.org/10.1038/nmat3601.

(10) Come, J.; Augustyn, V.; Kim, J. W.; Rozier, P.; Taberna, P.-L.; Gogotsi, P.; Long, J. W.; Dunn, B.; Simon, P. Electrochemical Kinetics of Nanostructured Nb_2O_5 Electrodes. *J. Electrochem. Soc.* **2014**, *161* (5), A718–A725. https://doi.org/10.1149/2.040405jes.

(11) Galizzioli, D.; Tantardini, F.; Trasatti, S. Ruthenium Dioxide: A New Electrode Material.

I. Behaviour in Acid Solutions of Inert Electrolytes. *J. Appl. Electrochem.* **1974**, *4*, 57–67. https://doi.org/10.1007/BF00615906.

(12) Zheng, J. P.; Cygan, P. J.; Jow, T. R. Hydrous Ruthenium Oxide as an Electrode Material for Electrochemical Capacitors. *J. Electrochem.* **1995**, *142* (8), 2699–2703. https://doi.org/10.1149/1.2050077.

(13) Dmowski, W.; Egami, T.; Swider-Lyons, K. E.; Love, C. T.; Rolison, D. R. Local Atomic Structure and Conduction Mechanism of Nanocrystalline Hydrous RuO_2 from X-Ray Scattering. *J. Phys. Chem. B* **2002**, *106* (49), 12677–12683. https://doi.org/10.1021/jp026228l.

(14) Hu, C. C.; Chang, K. H.; Lin, M. C.; Wu, Y. T. Design and Tailoring of the Nanotubular Arrayed Architecture of Hydrous RuO_2 for next Generation Supercapacitors. *Nano Lett.* **2006**, *6* (12), 2690–2695. https://doi.org/10.1021/nl061576a.

(15) Kodama, R.; Terada, Y.; Nakai, I.; Komaba, S.; Kumagai, N. Electrochemical and In Situ XAFS-XRD Investigation of Nb_2O_5 for Rechargeable Lithium Batteries. *J. Electrochem. Soc.* **2006**, *153* (3), A583–A588. https://doi.org/10.1149/1.2163788.

(16) Kong, L.; Liu, X.; Wei, J.; Wang, S.; Xu, B. B.; Long, D.; Chen, F. T-Nb_2O_5 Nanoparticle Enabled Pseudocapacitance with Fast Li-Ion Intercalation. *Nanoscale* **2018**, *10* (29), 14165–14170. https://doi.org/10.1039/c8nr03495h.

(17) Kim, H.-S.; Cook, J. B.; Tolbert, S. H.; Dunn, B. The Development of Pseudocapacitive Properties in Nanosized-MoO_2. *J. Electrochem. Soc.* **2015**, *162* (5), A5083–A5090. https://doi.org/10.1149/2.0141505jes.

(18) Zhu, Y.; Ji, X.; Cheng, S.; Chern, Z. Y.; Jia, J.; Yang, L.; Luo, H.; Yu, J.; Peng, X.; Wang, J.; Zhou, W.; Liu, M. Fast Energy Storage in Two-Dimensional MoO_2 Enabled by Uniform Oriented Tunnels. *ACS Nano* **2019**, *13* (8), 9091–9099. https://doi.org/10.1021/acsnano.9b03324.

(19) Yang, L. C.; Sun, W.; Zhong, Z. W.; Liu, J. W.; Gao, Q. S.; Hu, R. Z.; Zhu, M. Hierarchical MoO_2/N-Doped Carbon Heteronanowires with High Rate and Improved Long-Term Performance for Lithium-Ion Batteries. *J. Power Sources* **2016**, *306*, 78–84. https://doi.org/10.1016/j.jpowsour.2015.11.073.

(20) Cook, J. B.; Kim, H. S.; Yan, Y.; Ko, J. S.; Robbennolt, S.; Dunn, B.; Tolbert, S. H. Mesoporous MoS_2 as a Transition Metal Dichalcogenide Exhibiting Pseudocapacitive Li and Na-Ion Charge Storage. *Adv. Energy Mater.* **2016**, *6* (9), 1–12. https://doi.org/10.1002/aenm.201501937.

(21) Cook, J. B.; Lin, T. C.; Kim, H. S.; Siordia, A.; Dunn, B. S.; Tolbert, S. H. Suppression of Electrochemically Driven Phase Transitions in Nanostructured MoS_2 Pseudocapacitors Probed Using Operando X-Ray Diffraction. *ACS Nano* **2019**, *13* (2), 1223–1231. https://doi.org/10.1021/acsnano.8b06381.

(22) Cook, J. B.; Kim, H.-S.; Lin, T. C.; Lai, C.-H.; Dunn, B.; Tolbert, S. H. Pseudocapacitive Charge Storage in Thick Composite MoS_2 Nanocrystal-Based Electrodes. *Adv. Energy Mater.* **2017**, *7* (2), 1–12. https://doi.org/10.1002/aenm.201601283.

(23) Mahmood, Q.; Park, S. K.; Kwon, K. D.; Chang, S. J.; Hong, J. Y.; Shen, G.; Jung, Y. M.; Park, T. J.; Khang, S. W.; Kim, W. S.; Kong, J.; Park, H. S. Transition from Diffusion-Controlled Intercalation into Extrinsically Pseudocapacitive Charge Storage of MoS_2 by

Nanoscale Heterostructuring. *Adv. Energy Mater.* **2016**, *6* (1), 1501115. https://doi.org/10.1002/aenm.201501115.

(24) Yoo, H. D.; Li, Y.; Liang, Y.; Lan, Y.; Wang, F.; Yao, Y. Intercalation Pseudocapacitance of Exfoliated Molybdenum Disulfide for Ultrafast Energy Storage. *ChemNanoMat* **2016**, *2* (7), 688–691. https://doi.org/10.1002/cnma.201600117.

(25) Rauda, I. E.; Augustyn, V.; Saldarriaga-Lopez, L. C.; Chen, X.; Schelhas, L. T.; Rubloff, G. W.; Dunn, B.; Tolbert, S. H. Nanostructured Pseudocapacitors Based on Atomic Layer Deposition of V2O5 onto Conductive Nanocrystal-Based Mesoporous ITO Scaffolds. *Adv. Funct. Mater.* **2014**, *24* (42), 6717–6728. https://doi.org/10.1002/adfm.201401284.

(26) Sathiya, M.; Prakash, A. S.; Ramesha, K.; Tarascon, J. M.; Shukla, A. K. V_2O_5-Anchored Carbon Nanotubes for Enhanced Electrochemical Energy Storage. *J. Am. Chem. Soc.* **2011**, *133* (40), 16291–16299. https://doi.org/10.1021/ja207285b.

(27) Okubo, M.; Hosono, E.; Kim, J.; Enomoto, M.; Kojima, N.; Kudo, T.; Zhou, H.; Honma, I. Nanosize Effect on High-Rate Li-Ion Intercalation in $LiCoO_2$ Electrode. *J. Am. Chem. Soc.* **2007**, *129* (23), 7444–7452. https://doi.org/10.1021/ja0681927.

(28) Lesel, B. K.; Ko, J. S.; Dunn, B.; Tolbert, S. H. Mesoporous $Li_xMn_2O_4$ Thin Film Cathodes for Lithium-Ion Pseudocapacitors. *ACS Nano* **2016**, *10* (8), 7572–7581. https://doi.org/10.1021/acsnano.6b02608.

(29) Lesel, B. K.; Cook, J. B.; Yan, Y.; Lin, T. C.; Tolbert, S. H. Using Nanoscale Domain Size to Control Charge Storage Kinetics in Pseudocapacitive Nanoporous $LiMn_2O_4$ Powders. *ACS Energy Lett.* **2017**, *2* (10), 2293–2298. https://doi.org/10.1021/acsenergylett.7b00634.

(30) Okubo, M.; Mizuno, Y.; Yamada, H.; Kim, J.; Hosono, E.; Zhou, H.; Kudo, T.; Honma, I. Fast Li-Ion Insertion into Nanosized $LiMn_2O_4$ without Domain Boundaries. *ACS Nano* **2010**, *4* (2), 741–752. https://doi.org/10.1021/nn9012065.

(31) Xia, H.; Luo, Z.; Xie, J. Nanostructured $LiMn_2O_4$ and Their Composites as High-Performance Cathodes for Lithium-Ion Batteries. *Prog. Nat. Sci. Mater. Int.* **2012**, *22* (6), 572–584. https://doi.org/10.1016/j.pnsc.2012.11.014.

(32) Zhu, X.-J.; Liu, H.-X.; Gan, X.-Y.; Cao, M.-H.; Zhou, J.; Chen, W.; Xu, Q.; Ouyang, S.-X. Preparation and Characterization of $LiNi_{0.80}Co_{0.20-x}Al_xO_2$ as Cathode Materials for Lithium Ion Batteries. *J. Electroceramics* **2006**, *17* (2–4), 645–649. https://doi.org/10.1007/s10832-006-6705-6.

(33) Zhu, X.; Zhan, H.; Liu, H.; Zhou, Y. Synthesis and Characterization of $LiNi_{0.95-x}Co_xAl_{0.05}O_2$ for Lithium-Ion Batteries. *Rare Met.* **2006**, *25* (4), 303–308. https://doi.org/10.1016/S1001-0521(06)60058-2.

(34) Li, W.; Reimers, J. N.; Dahn, J. R. In Situ X-Ray Diffraction and Electrochemical Studies of $Li_{1-x}NiO_2$. *Solid State Ionics* **1993**, *67* (1–2), 123–130. https://doi.org/10.1016/0167-2738(93)90317-V.

(35) Faenza, N. V.; Pereira, N.; Halat, D. M.; Vinckeviciute, J.; Bruce, L.; Radin, M. D.; Mukherjee, P.; Badway, F.; Halajko, A.; Cosandey, F.; Grey, C. P.; Van Der Ven, A.; Amatucci, G. G. Phase Evolution and Degradation Modes of R3m $Li_xNi_{1-y-z}Co_yAl_zO_2$ Electrodes Cycled Near Complete Delithiation. *Chem. Mater.* **2018**, *30* (21), 7545–7574. https://doi.org/10.1021/acs.chemmater.8b02720.

(36) Kalyani, P.; Kalaiselvi, N. Various Aspects of $LiNiO_2$ Chemistry: A Review. *Sci. Technol. Adv. Mater.* **2005**, *6* (6), 689–703. https://doi.org/10.1016/j.stam.2005.06.001.

(37) Delmas, C.; Pérès, J. P.; Rougier, A.; Demourgues, A.; Weill, F.; Chadwick, A. V.; Broussely, M.; Perton, F.; Biensan, P.; Willmann, P. On the Behavior of the Li_xNiO_2 System: An Electrochemical and Structural Overview. *J. Power Sources* **1997**, *68* (1), 120–125. https://doi.org/10.1016/S0378-7753(97)02664-5.

(38) Cho, D.-H.; Jo, C.-H.; Cho, W.; Kim, Y.-J.; Yashiro, H.; Sun, Y.-K.; Myung, S.-T. Effect of Residual Lithium Compounds on Layer Ni-Rich $Li[Ni_{0.7}Mn_{0.3}]O_2$. *J. Electrochem. Soc.* **2014**, *161* (6), A920–A926. https://doi.org/10.1149/2.042406jes.

(39) Zhuang, G. V.; Chen, G.; Shim, J.; Song, X.; Ross, P. N.; Richardson, T. J. Li_2CO_3 in $LiNi_{0.8}Co_{0.15}Al_{0.05}O_2$ Cathodes and Its Effects on Capacity and Power. *J. Power Sources* **2004**, *134* (2), 293–297. https://doi.org/10.1016/j.jpowsour.2004.02.030.

(40) Liu, H.; Yang, Y.; Zhang, J. Investigation and Improvement on the Storage Property of $LiNi_{0.8}Co_{0.2}O_2$ as a Cathode Material for Lithium-Ion Batteries. *J. Power Sources* **2006**, *162* (1), 644–650. https://doi.org/10.1016/j.jpowsour.2006.07.028.

(41) Liu, H. S.; Zhang, Z. R.; Gong, Z. L.; Yang, Y. Origin of Deterioration for $LiNiO_2$ Cathode Material during Storage in Air. *Electrochem. Solid-State Lett.* **2004**, *7* (7), A190–A193. https://doi.org/10.1149/1.1738471.

(42) Zhang, H.; May, B. M.; Serrano-Sevillano, J.; Casas-Cabanas, M.; Cabana, J.; Wang, C.; Zhou, G. Facet-Dependent Rock-Salt Reconstruction on the Surface of Layered Oxide Cathodes. *Chem. Mater.* **2018**, *30* (3), 692–699.

https://doi.org/10.1021/acs.chemmater.7b03901.

(43) He, G.; Pan, Q.; Rempel, G. L. Synthesis of Poly(Methyl Methacrylate) Nanosize Particles by Differential Microemulsion Polymerization. *Macromol. Rapid Commun.* **2003**, *24* (9), 585–588. https://doi.org/10.1002/marc.200390089.

(44) Zou, D.; Ma, S.; Guan, R.; Park, M.; Sun, L.; Aklonis, J. J.; Salovey, R. Model Filled Polymers. V. Synthesis of Crosslinked Monodisperse Polymethacrylate Beads. *J. Polym. Sci. Part A Polym. Chem.* **1992**, *30* (1), 137–144. https://doi.org/10.1002/pola.1992.080300118.

(45) Sasahara, K.; Hyodo, T.; Shimizu, Y.; Egashira, M. Macroporous and Nanosized Ceramic Films Prepared by Modified Sol-Gel Method with PMMA Microsphere Templates. *J. Eur. Ceram. Soc.* **2004**, *24* (6), 1961–1967. https://doi.org/10.1016/S0955-2219(03)00518-1.

(46) Zeng, W. R.; Li, S. F.; Chow, W. K. Review on Chemical Reactions of Burning Poly(Methyl Methacrylate) PMMA. *J. Fire Sci.* **2002**, *20* (5), 401–433. https://doi.org/10.1106/073490402031482.

(47) Kwade, A.; Haselrieder, W.; Leithoff, R.; Modlinger, A.; Dietrich, F.; Droeder, K. Current Status and Challenges for Automotive Battery Production Technologies. *Nat. Energy* **2018**, *3*, 290–300. https://doi.org/10.1038/s41560-018-0130-3.

(48) Kasnatscheew, J.; Evertz, M.; Kloepsch, R.; Streipert, B.; Wagner, R.; Cekic Laskovic, I.; Winter, M. Learning from Electrochemical Data: Simple Evaluation and Classification of $LiMO_2$-Type-Based Positive Electrodes for Li-Ion Batteries. *Energy Technol.* **2017**, *5* (9), 1670–1679. https://doi.org/10.1002/ente.201700068.

(49) Noh, H. J.; Youn, S.; Yoon, C. S.; Sun, Y. K. Comparison of the Structural and Electrochemical Properties of Layered Li[$Ni_xCo_yMn_z$]O_2 (x = 1/3, 0.5, 0.6, 0.7, 0.8 and 0.85) Cathode Material for Lithium-Ion Batteries. *J. Power Sources* **2013**, *233*, 121–130. https://doi.org/10.1016/j.jpowsour.2013.01.063.

(50) Wang, S.; Yan, M.; Li, Y.; Vinado, C.; Yang, J. Separating Electronic and Ionic Conductivity in Mix-Conducting Layered Lithium Transition-Metal Oxides. *J. Power Sources* **2018**, *393*, 75–82. https://doi.org/10.1016/j.jpowsour.2018.05.005.

(51) Schipper, F.; Erickson, E. M.; Erk, C.; Shin, J.-Y.; Chesneau, F. F.; Aurbach, D. Review—Recent Advances and Remaining Challenges for Lithium Ion Battery Cathodes. *J. Electrochem. Soc.* **2017**, *164* (1), A6220–A6228. https://doi.org/10.1149/2.0351701jes.

(52) Kim, J. M.; Chung, H. T. Role of Transition Metals in Layered Li[Ni,Co,Mn]O_2 under Electrochemical Operation. *Electrochim. Acta* **2004**, *49* (21), 3573–3580. https://doi.org/10.1016/j.electacta.2004.03.025.

(53) Sun, H.; Zhao, K. Electronic Structure and Comparative Properties of $LiNi_xMn_yCo_zO_2$ Cathode Materials. *J. Phys. Chem. C* **2017**, *121* (11), 6002–6010. https://doi.org/10.1021/acs.jpcc.7b00810.

(54) Wang, D.; Xin, C.; Zhang, M.; Bai, J.; Zheng, J.; Kou, R.; Peter Ko, J. Y.; Huq, A.; Zhong, G.; Sun, C. J.; Yang, Y.; Chen, Z.; Xiao, Y.; Amine, K.; Pan, F.; Wang, F. Intrinsic Role of Cationic Substitution in Tuning Li/Ni Mixing in High-Ni Layered Oxides. *Chem. Mater.* **2019**, *31* (8), 2731–2740. https://doi.org/10.1021/acs.chemmater.8b04673.

(55) Märker, K.; Reeves, P. J.; Xu, C.; Griffith, K. J.; Grey, C. P. Evolution of Structure and

Lithium Dynamics in $LiNi_{0.8}Mn_{0.1}Co_{0.1}O_2$ (NMC811) Cathodes during Electrochemical Cycling. *Chem. Mater.* **2019**, *31* (7), 2545–2554. https://doi.org/10.1021/acs.chemmater.9b00140.

(56) Xu, C.; Reeves, P. J.; Jacquet, Q.; Grey, C. P. Phase Behavior during Electrochemical Cycling of Ni-Rich Cathode Materials for Li-Ion Batteries. *Adv. Energy Mater.* **2020**, 2003404. https://doi.org/10.1002/aenm.202003404.

(57) Kovacik, P.; Del Hierro, G.; Livernois, W.; Gleason, K. K. Scale-up of OCVD: Large-Area Conductive Polymer Thin Films for next-Generation Electronics. *Mater. Horizons* **2015**, *2* (2), 221–227. https://doi.org/10.1039/c4mh00222a.

(58) Mei, J.; Bao, Z. Side Chain Engineering in Solution-Processable Conjugated Polymers. *Chem. Mater.* **2014**, *26* (1), 604–615. https://doi.org/10.1021/cm4020805.

(59) Berger, P. R.; Kim, M. Polymer Solar Cells: P3HT:PCBM and Beyond. *J. Renew. Sustain. Energy* **2018**, *10* (1), 013508. https://doi.org/10.1063/1.5012992.

(60) Dang, M. T.; Hirsch, L.; Wantz, G. P3HT:PCBM, Best Seller in Polymer Photovoltaic Research. *Adv. Mater.* **2011**, *23* (31), 3597–3602. https://doi.org/10.1002/adma.201100792.

(61) Yuen, J. D.; Dhoot, A. S.; Namdas, E. B.; Coates, N. E.; Heeney, M.; McCulloch, I.; Moses, D.; Heeger, A. J. Electrochemical Doping in Electrolyte-Gated Polymer Transistors. *J. Am. Chem. Soc.* **2007**, *129* (46), 14367–14371. https://doi.org/10.1021/ja0749845.

(62) Salzmann, I.; Heimel, G. Toward a Comprehensive Understanding of Molecular Doping Organic Semiconductors (Review). *J. Electron Spectros. Relat. Phenomena* **2015**, *204* (Part A), 208–222. https://doi.org/10.1016/j.elspec.2015.05.001.

(63) Kolesov, V. A.; Fuentes-Hernandez, C.; Chou, W. F.; Aizawa, N.; Larrain, F. A.; Wang, M.; Perrotta, A.; Choi, S.; Graham, S.; Bazan, G. C.; Nguyen, T. Q.; Marder, S. R.; Kippelen, B. Solution-Based Electrical Doping of Semiconducting Polymer Films over a Limited Depth. *Nat. Mater.* **2017**, *16* (4), 474–481. https://doi.org/10.1038/NMAT4818.

(64) Scholes, D. T.; Hawks, S. A.; Yee, P. Y.; Wu, H.; Lindemuth, J. R.; Tolbert, S. H.; Schwartz, B. J. Overcoming Film Quality Issues for Conjugated Polymers Doped with F_4TCNQ by Solution Sequential Processing: Hall Effect, Structural, and Optical Measurements. *J. Phys. Chem. Lett.* **2015**, *6* (23), 4786–4793. https://doi.org/10.1021/acs.jpclett.5b02332.

(65) Hawks, S. A.; Aguirre, J. C.; Schelhas, L. T.; Thompson, R. J.; Huber, R. C.; Ferreira, A. S.; Zhang, G.; Herzing, A. A.; Tolbert, S. H.; Schwartz, B. J. Comparing Matched Polymer:Fullerene Solar Cells Made by Solution-Sequential Processing and Traditional Blend Casting: Nanoscale Structure and Device Performance. *J. Phys. Chem. C* **2014**, *118* (31), 17413–17425. https://doi.org/10.1021/jp504560r.

CHAPTER 2

Nanostructured $LiNi_{0.80}Co_{0.15}Al_{0.05}O_2$ (NCA) for Fast-Charging, High-Capacity Cathodes

2.1 Introduction

As the popularity of electric vehicles (EVs) rises, fast-charging lithium-ion batteries are key for large-scale implementation.[1,2] Charging times on the order of minutes, instead of hours, are required to be comparable to internal combustion engine fueling times. Short charging times can be accomplished with supercapacitors,[3] however the range of supercapacitor EVs is limited to less than 20 miles.[4,5] One solution for fast-charging, while still retaining a high driving range, is the use of lithium-ion batteries with shortened lithium-ion diffusion lengths through nanostructuring.

Materials can be nanostructured using many techniques such as nanoparticle synthesis/assembly, hydrothermal synthesis, or electrodeposition.[6] One relatively simple technique, which results in high surface area as well as homogeneous nanoscale porosity, is sol-gel synthesis combined with colloidal polymer templates such as poly(methyl methacrylate) (PMMA).[7] Although the colloidal template is easily removed by moderate heating to leave a nanoporous structure, high crystallization temperatures (>700 °C) are required for many battery materials, which can diminish the desired nanostructure. Generally, conventional slow heating promotes grain growth, while rapid thermal annealing (RTA) can support smaller particle sizes.[8]

Nanostructured battery materials allow for the reduction of lithium-ion diffusion lengths so that slow solid-state diffusion is no longer rate limiting and fast-charging can be achieved. This process, where pseudocapacitive characteristics emerge as a result of nanostructuring, has been termed ‘extrinsic pseudocapacitance’. One of the best examples of this phenomenon is with the well-known cathode material, $LiCoO_2$.[9] Even though the material in bulk form does not exhibit pseudocapacitive properties, when reduced to dimensions ~6nm, galvanostatic experiments lead to a linear dQ/dV, indicative of a capacitive response. Similar examples of extrinsic pseudocapacitance have been seen in many nanostructured materials with medium voltage ranges, such as MoO_2,[10–12] MoS_2,[13–15] and TiO_2.[16–18] In some of these materials, the key to the development of pseudocapacitive properties is suppression of bulk intercalation induced phase transitions at small size.[10,11,16,19] Pseudocapacitive behavior has generated considerable interest, especially for EVs, because it allows for the desirable combination of fast-charging and reasonable driving range. A variety of electrochemical measurement methods have been developed to identify signatures of pseudocapacitive charge storage.[18,20–24]

While there are several examples of pseudocapacitive materials that operate in a ‘medium’ potential range below 2.5 V vs. Li/Li^+, there are fewer examples of pseudocapacitive materials operating at high-voltage. One known pseudocapacitive material operating in the 3.4-4.5 voltage range (vs. Li/Li^+) is nanostructured $LiMn_2O_4$, but it suffers from low capacity that is further reduced by an inactive surface in nanostructured form.[25–27] For practical fast-charging energy storage devices, pseudocapacitive cathodes with higher capacity are needed. One cathode material for lithium-ion batteries that has generated considerable interest because of its high specific capacity is $LiNi_{0.80}Co_{0.15}Al_{0.05}O_2$ (NCA), a layered transition metal oxide. In the bulk, NCA already shows fast charging due to the stabilizing effects of cobalt and aluminum dopants that suppress phase transitions.[28–30] Therefore, NCA is an interesting candidate to explore in nanostructured form to produce a high-rate cathode material through extrinsic pseudocapacitance. Importantly, since nanostructuring in NCA is only necessary to decrease diffusion lengths and not to suppress phase transitions, pseudocapacitive behavior may begin to develop at larger sizes.

Despite its promise, NCA also has a number of drawbacks. NCA of all sizes suffers from cation mixing, which occurs when partly-reduced Ni^{2+} present in the transition-metal-oxide layers migrates to the Li^+ layer due to their similar ionic sizes.[31] This leads to local shrinkage of the lithium diffusion pathways during cycling and decreased electrochemical performance.[32] In order to mitigate the effect of cation mixing, high calcination temperatures (which are not ideal for maintaining nanoscale structure) under oxygen flow are required to promote the oxidation of Ni^{2+} to Ni^{3+}.[33] The degree of cation mixing is easily determined using X-ray diffraction (XRD) by examining the integrated intensity ratio of the (003) to (104) diffraction peaks. Previous studies have determined that a $I(003)/I(104)$ ratio above 1.2 is necessary for optimal electrochemical performance.[34]

It is also well known that NCA is sensitive to CO_2 and water in the air, which react with excess lithium on the surface and near-surface lithium to form an insulating Li_2CO_3 layer.[35] The removal of lattice-lithium near the surface, combined with reduction of near-surface nickel, can further result in the formation of an electrochemically inactive rock-salt (NiO-like) layer beneath the Li_2CO_3.[36,37] Both the Li_2CO_3 and NiO-like layers can hinder lithium-ion diffusion, especially at high rates.[35] Unfortunately, nanostructured NCA, with decreased particle sizes, should have increased sensitivity to air. As a result, all nanostructured NCA in this work was kept air-free.

Another component for our fast-charging cathode is an optimized binder. Recently, conductive polymers, such as poly(3-hexylthiophene-2,5-diyl) (P3HT),[38] poly(3,4-ethylenedioxythiophene):poly(styrenesulfonate) (PEDOT:PSS),[39] and polypyrrole (PPy),[40] have been used as conductive binders for battery electrodes due to their high electronic and ionic conductivity compared to traditional insulating binders, such as polyvinylidene fluoride (PVDF). P3HT, in particular, has shown promise as a conductive binder for NCA cathodes that helped suppress electrolyte breakdown at the NCA surface.[38] P3HT, which has been widely studied for use in organic photovoltaics,[41] is electrochemically doped in the operational voltage window of NCA (2.7-4.2 V), facilitating electronic/ionic conductivity and thus high-rate charge storage.[38] Thus, P3HT was used as the binder in our system to facilitate high-rate charging and discharging.

While the prospects for adopting nanostructured NCA are excellent, there are only a few examples of such materials in the literature, and many show rather ordinary rate capabilities. This includes nanoporous microspheres (151 mAh/g capacity at 2C),[42] nanocrystals (82 mAh/g capacity at 3C),[43] nanoplates (139 mAh/g capacity at 10C),[44,45] and holey 2D nanosheets (which show the most impressive rate behavior with 153 mAh/g capacity at 10C).[46] Unfortunately, none of these materials were cycled faster than 10C and no kinetic analyses were performed to identify their characteristic behavior. In this letter, we thus present methods to synthesize porous nanostructured NCA with two different particle sizes. Electrochemical kinetics are used to examine high-rate performance and understand charge storage processes. We then paired the nanostructured NCA with a pseudocapacitive anode to test the high-rate performance and long-term cyclability in a full-cell as validation of practicability.

2.2 Results and Discussion

Nanostructured NCA was synthesized using nitrate salts and PMMA colloidal templates (250 nm diameter)[47] that were stabilized in solution using the triblock copolymer, Pluronic F127. The homogeneous salt and polymer solution was dried and then heated using a two-step process. First, the powder was heated to 450 °C under oxygen to remove the polymer template, leaving a nanoporous NCA precursor with a surface area of 23 ± 2 m^2/g and $28\pm5\%$ porosity (Fig. S2.1). Next, the precursor was calcined at higher temperatures under oxygen to obtain the desired NCA crystal structure. Additional synthetic details can be found in the SI.

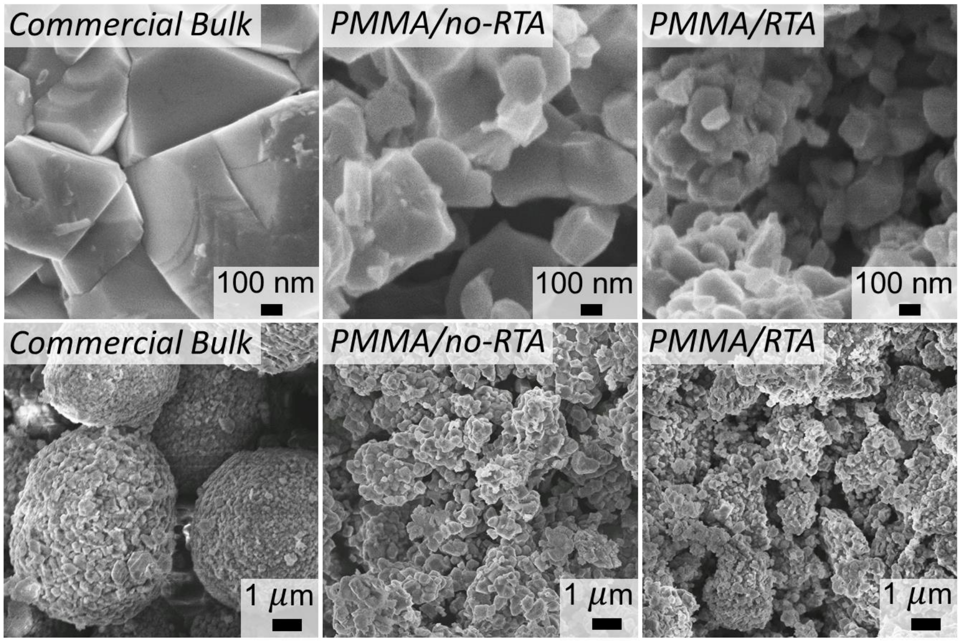

Figure 2.1. High- (top) and low- (bottom) magnification SEM images of commercial bulk, PMMA/no-RTA, and PMMA/RTA NCA samples (from left to right).

The particle size of nanostructured NCA was controlled by modifying the calcination method. A conventional heat treatment (2 hours at 800 °C under oxygen) resulted in medium sized particles (~300 nm); referred to as PMMA/no-RTA (Figs. 2.1, S2.2; Tbl. 2.1). In contrast, rapid thermal annealing (RTA), where the sample is placed into a hot furnace (850 °C) for only 5 minutes, resulted in small sized particles (~150 nm) (Fig. S2.3a). With this short heating, considerable cation mixing remained, as evidenced by the low $I(003)/I(104)$ ratio (Fig. S2.3c). To produce more crystalline materials, an additional 12 hour hold at 700 °C was applied, and this two-step heating is referred to as PMMA/RTA (Figs. 2.1, S2.2; Tbl. 2.1). The additional hold allowed for short-range ordering of the cations and decreased cation mixing without significant particle size growth (Fig. S2.3a-c). However, heating at these high temperatures in both PMMA/no-RTA and PMMA/RTA led to a decrease in surface area, near the lower detection limit of nitrogen porosimetry (Fig. S2.4). The data also indicates that the pore sizes for all samples were large and dominantly outside the range that can be effectively measured using nitrogen porosimetry. However, for the nanostructured samples, we observed a much looser packing of the primary particles compared to the dense microsphere secondary particle structure seen in bulk materials; this should allow for greater electrolyte penetration (Fig. 2.1).

Table 2.1. *I*(003)/*I*(104) ratios calculated from XRD, primary and secondary particle sizes measured from 150 particles in SEM, and air-free surface-Ni^{2+} fractions measured by XPS for NCA materials examined here.

Sample	*I*(003)/ *I*(104)	Primary particle size measured by SEM	Secondary particle size measured by SEM	Surface-Ni^{2+} %
PMMA/ RTA	1.23	~150 nm	-	68%
PMMA/no-RTA	1.25	~300 nm	-	39%
Commercial Bulk	1.34	~425 nm	~5 μm	51%

XRD was used to confirm synthesis of the desired NCA crystal structure using the *I*(003)/*I*(104) ratio. Both nanostructured NCAs were above the 1.2 ratio required for good electrochemical performance (Tbl. 2.1, Fig. S2.5). The structure was further investigated by Rietveld refinement of the XRD pattern (Fig. S2.5), the results are shown in table S2.1 and additional details can be found in the SI.[48] The refined lattice parameters can be used to calculate the slab thickness (*S*, TMO_6), and the interslab thickness (*I*, LiO_6), which is the lithium-diffusion layer thickness.[49] PMMA/no-RTA has a slightly larger interslab value (Tbl. S2.1), which enables faster lithium-ion diffusion and can be a result of a lesser degree of cation mixing.[50] Cation mixing is low for all samples; and while more reliable cation mixing values can be obtained by combined refinement of X-ray and neutron diffraction, that is outside the scope of this letter.[48] The crystallite sizes determined by the refinement are smaller than what is visually observed by SEM, and this is likely due to some crystallographic disorder that further broadens the peaks.

X-ray photoelectron spectroscopy (XPS) was used to establish the oxidation state of the nickel at the surface of the NCA samples. Because of the increased sensitivity to CO_2 and water for small NCA particles, the samples were kept in a glovebox and transferred air-free for XPS analysis. Ni 2p XPS spectra showed that PMMA/RTA samples had the highest fraction of Ni^{2+} on its surface (Tbl. 2.1, Fig. S2.6).[51] We attribute this to the fact that a reducing atmosphere is formed upon thermal decomposition of PMMA.[52,53] Since PMMA/RTA was only oxidized at high temperatures for 5 minutes, this could lead to incomplete nickel oxidation. In contrast, PMMA/no-RTA samples had the lowest Ni^{2+} fraction, which should be favorable for fast surface charge-transfer processes. While the fractions of Ni^{2+} measured by XPS are high, no impurities are seen by XRD because XPS is a surface sensitive measurement, probing only the first couple nanometers of the sample's surface.

We used XPS combined with argon-ion etching to determine the relative thickness of the Li_2CO_3 layer formed on the surface of nanostructured samples kept air-free and those exposed to ambient air for 1 week (Figs. 2.2a, S2.7). O 1s spectra were used to compare relative amounts of NCA to Li_2CO_3.[51,54] All unetched samples were covered with Li_2CO_3 (80-90%). After just 30 seconds of etching, the fraction of Li_2CO_3 decreased to ~40% for air-free samples, but only to ~70% for air-exposed samples. The etch rate can be roughly estimated to be 3-8 nm/min based on SiO_2.[55] However, because the Ar plasma often cannot reach the inner surfaces of porous materials,

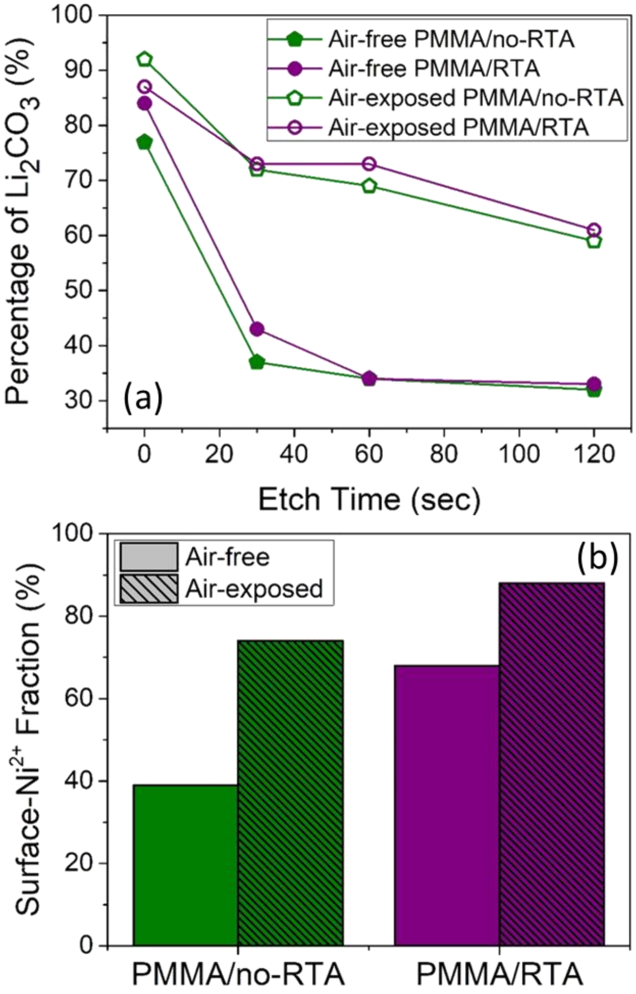

Figure 2.2. (a) O 1s XPS spectra were used to determine the percentage of Li_2CO_3 (with respect to NCA) on the surface of PMMA/no-RTA (green) and PMMA/RTA (purple) samples that were either kept in a glovebox and transferred air-free for analysis (air-free, solid symbol) or exposed to air for 1 week prior to analysis (air-exposed, open symbol). The samples were etched using an argon plasma for 30-120 seconds. (b) Bar graph of the fraction of Ni^{2+} (relative to Ni^{3+}) on the surface of air-free samples (solid) compared to those that were air-exposed (diagonally lined) for PMMA/no-RTA and PMMA/RTA. The fraction of Ni^{2+} was obtained using the Ni 2p XPS spectra.

we find that some residual Li_2CO_3 always remains. The surface of the pristine PMMA/no-RTA material was then studied by transmission electron microscopy (TEM) (Fig. S2.8a). The pristine particle shows a smooth surface with little to no Li_2CO_3, which agrees with the XPS results.

Additionally, upon air exposure the fraction of Ni^{2+} increased (Fig. 2.2b). From these data, we conclude that air-free samples have thinner Li_2CO_3 layers and less electrochemically inactive surface Ni^{2+}, both of which should result in enhanced cycling performance.

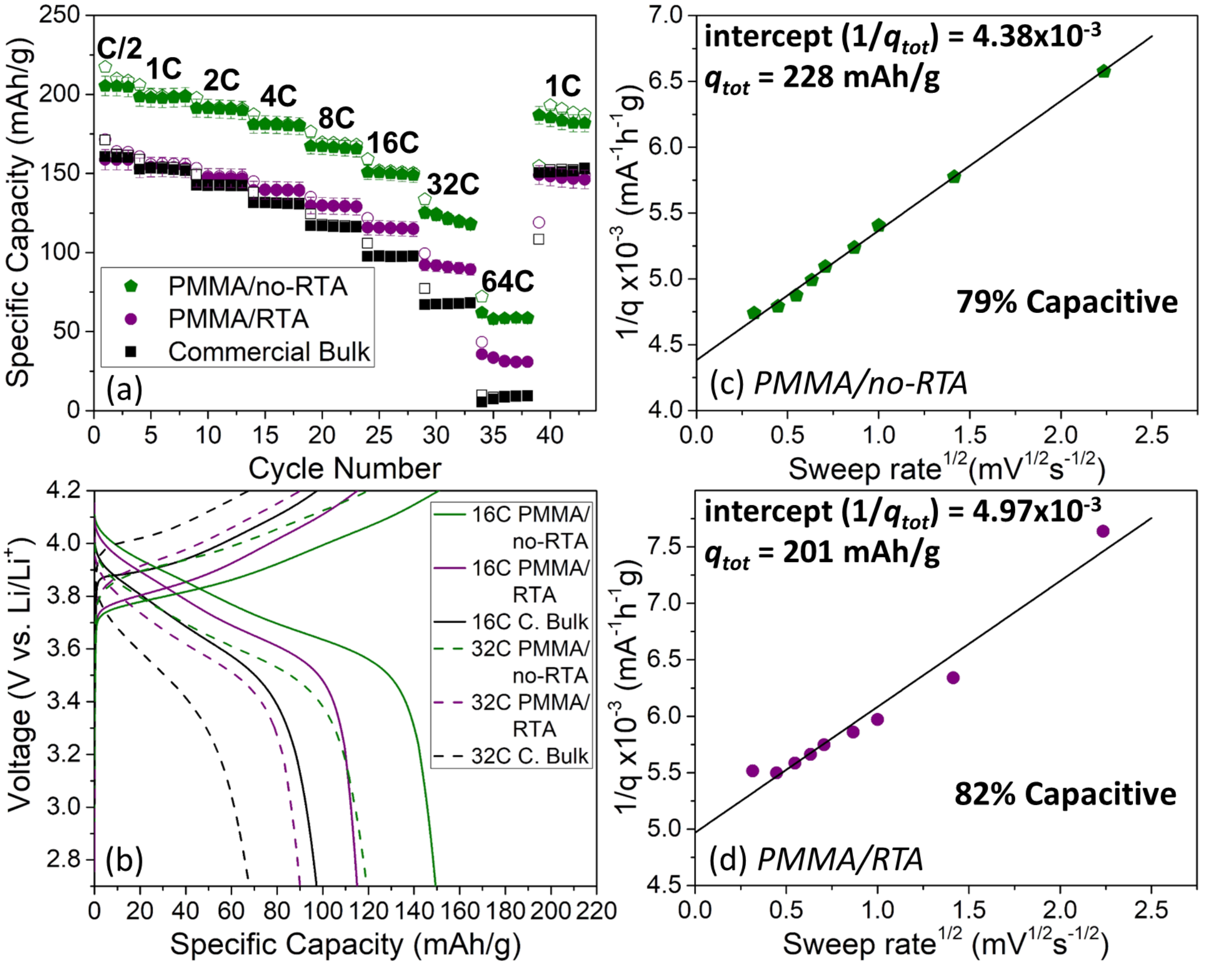

Figure 2.3. (a) Specific charge (open symbols) and discharge (filled symbols) capacity from galvanostatic cycling from 2.7-4.2 V at rates from C/2 to 64C for PMMA/no-RTA (green pentagon), PMMA/RTA (purple circle), and commercial bulk NCA (black square). (b) Galvanostatic cycling of PMMA/no-RTA, PMMA/RTA, and commercial bulk NCA at 16C (solid line) and 32C (dashed line). (c-d) Trasatti analysis for determination of the total charge storage (q_{tot}, extrapolation of the y-intercept as $v \rightarrow 0$ gives $1/q_{tot}$) for PMMA/no-RTA (c) and PMMA/RTA (d), the calculated capacitive contribution is displayed on the graph.

The air-free nanostructured NCA samples were cycled galvanostatically between 2.7 and

4.2 V vs. Li/Li$^+$ and compared to commercial bulk NCA at various rates from C/2 to 64C, after 3 activation cycles at C/5 (Figs. 2.3a, S2.9). Both NCA and P3HT have been shown to undergo degradation when cycled above 4.2 V vs. Li/Li$^+$, so to ensure stable and reversible performance, cathodes were kept below 4.2 V.[56,57] TEM was used to study the PMMA/no-RTA particle after cycling (cycled galvanostatically, following the voltage range and rates above) in figure S2.8b. After cycling we see the presence of Li_2CO_3 and NiO surface layers using fast Fourier transform, which is expected for uncoated cycled NCA.[36,58] PMMA/no-RTA samples had the highest overall specific capacity, retaining 150 mAh/g at 16C and 121 mAh/g at 32C (Fig. 2.3b). PMMA/RTA, which had similar capacities to bulk NCA at slow rates, had specific capacities between that of PMMA/no-RTA and bulk NCA at 64C. The fact that both nanostructured NCAs have greater capacity than bulk at high rates indicates that the decreased lithium-ion diffusion lengths allow for faster charge/discharge kinetics. However, the smaller-size PMMA/RTA, which should have shorter lithium-ion diffusion distances, had lower overall capacity than PMMA/no-RTA. We attribute this to the higher amount of electrochemically inactive Ni^{2+} on the surface of the PMMA/RTA sample. Looking at the discharge capacity retention (Fig. S2.10) at 64C, bulk retains 5% of its original capacity, PMMA/RTA retains 20%, and PMMA/no-RTA retains 29%. Both nanostructured NCAs had high capacity retention of about 58% at 32C. Figure 2.2b shows that the voltage varies linearly with capacity, consistent with both solid-solution intercalation and pseudocapacitive behavior.

For these nanoscale materials, parasitic reactions with CO_2 and water are clearly an issue. Figure S2.11 shows the rate performance of electrodes prepared air-free and exposed to air. Air-exposed samples for both PMMA/no-RTA and PMMA/RTA showed lower overall capacity and poorer rate capability. Additionally, nanostructured NCA electrodes were made with a traditional

PVDF binder for comparison (Fig. S2.11) and showed lower capacity at all rates. These data confirm that additional insulating surface layers of Li_2CO_3, NiO, or PVDF are detrimental to the performance of nanostructured NCA.

The charge storage properties of the nanostructured NCA were studied using various kinetic analyses. First, an approach developed by Trasatti was used to quantify capacitive and diffusion-controlled charge storage.[13,23] Capacitive charge storage (q_{cap}) can be extrapolated from a plot of q (voltammetric charges) versus $v^{-1/2}$ as $v \to \infty$, because at infinitely fast rates, diffusion-limited redox sites are excluded (Fig. S2.12). Then, the total charge storage (q_{tot}) can be extrapolated from a plot of $1/q$ versus $v^{1/2}$ as $v \to 0$ (long time-scale). Using these extrapolated values, the capacitive contribution to charge storage can be calculated; by this analysis PMMA/no-RTA and PMMA/RTA materials were 79% and 82% capacitive, respectively (Fig. 2.3c-d).

The next analysis builds the relationship between peak current (i) and sweep rate (v) by the following power-law equation,

$$i = av^b \tag{1}$$

where a is a constant and b can vary between 0.5 and 1, depending on whether there is a semi-infinite diffusion-controlled redox process (typical of battery materials) or a capacitive charge storage process, respectively.[18,59] The anodic and cathodic redox peaks from cyclic voltammograms (CVs) are used to derive the b-values (Fig. 2.4a-b). The average b-values for PMMA/no-RTA and PMMA/RTA were 0.94 and 0.92, respectively, indicating the materials are dominated by capacitor-like responses. Previously, b-values near 0.9 have been reported for commercial NCA using a P3HT binder.[38]

The previous expression can also be separated into capacitor-like (k_1) and diffusion-limited (k_2) contributions to the current, each with appropriate limiting exponents.[22]

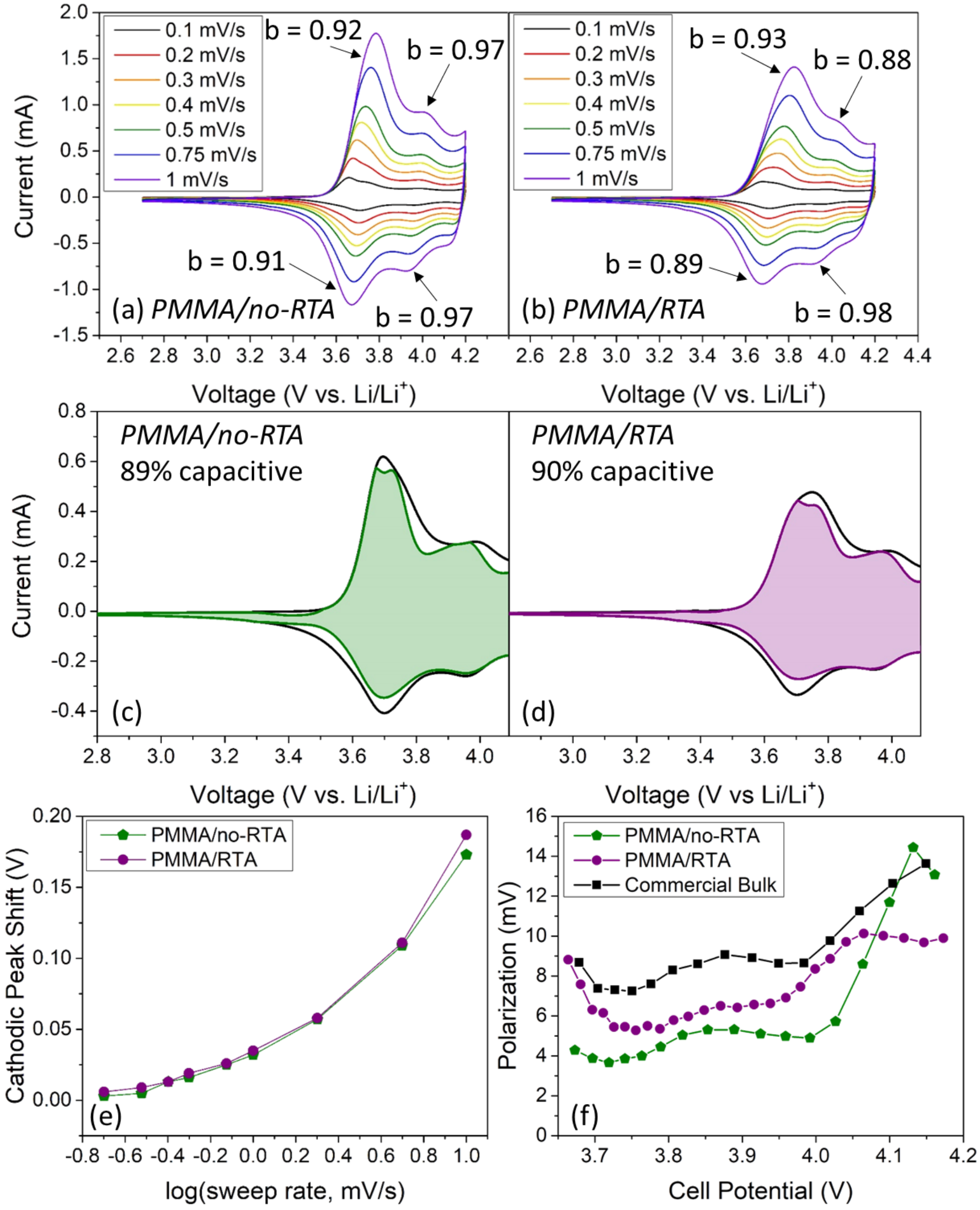

Figure 2.4. CV curves for PMMA/no-RTA (a) and PMMA/RTA (b). Anodic and cathodic peaks were used to derive *b*-values, which are displayed on graph. CV curves at 0.3 mV/s for PMMA/no-RTA (c, green) and PMMA/RTA (d, purple), showing capacitive contribution as a shaded region, with the total percent capacitive contribution displayed on the graph. (e) Cathodic peak shift for PMMA/no-RTA (green pentagon) and PMMA/RTA (purple circle). (f) Polarization versus cell potential obtained from GITT experiment for PMMA/no-RTA, PMMA/RTA, and commercial bulk (black square).

$$i = k_1 v + k_2 v^{1/2} \tag{2}$$

Equation 2 allows for qualitatively resolving the capacitive contribution to charge storage over the full voltage range, which will be referred to here as k_1/k_2 analysis.[20,25] CV curves at slow sweep rates were used to determine the capacitor-like charge storage fraction, to ensure sufficient time for any slower, diffusion-controlled processes to occur. The data shows that the capacitive fraction for both PMMA/no-RTA and PMMA/RTA was in the range of 90% (Fig. 2.4c-d). These values are in reasonable agreement with those determined by the Trasatti analysis for total charge, and indicate that the kinetics are indeed capacitor-like. Additionally, the peak voltage differences for both nanostructured samples is small and remains so (< 0.20 V) at sweep rates up to 10 mV/s (Fig. 2.4e).[59] Both the kinetic analysis and the small difference in peak voltage are pseudocapacitive signatures.

These kinetic analyses were also performed on nanostructured NCA electrodes that were exposed to air before being assembled into a coin-cell, the results of which are summarized in Table 2.2. The air-exposed samples had lower average *b*-values (Figs. S2.13a, S2.14a), meaning they are less capacitor-like than the air-free nanostructured NCAs. While the charge storage values determined by k_1/k_2 analysis are only slightly lower than what was seen for the air-free samples (Figs. S2.13b, S2.2.14b), the air-exposed samples have less capacitive contribution around the redox peaks. This indicates that the non-surface redox processes are slower in these samples,[25] which is a result of the higher fractions of insulating Li_2CO_3 and NiO on their surface (Fig. 2.2). Lastly, the Trasatti analysis indicated that the air-exposed materials had low capacitive contributions, 51% and 55% for air-exposed PMMA/no-RTA and PMMA/RTA, respectively (Figs. S2.13c-d, S2.14c-d).

Additionally, nanostructured NCA electrodes with PVDF as the binder were analyzed using these kinetic methods (electrodes were kept air-free). The PVDF-binder electrodes showed similar results, in that the *b*-values and capacitive contributions from k_1/k_2 and Trasatti analyses were lower than the nanostructured NCA electrodes made air-free and with P3HT as the binder (Figs. S2.15, S2.16, Tbl. 2.2). These results are as expected since PVDF is insulating and can impede lithium-ion diffusion at fast rates. For both the air-exposed and air-free PVDF-binder electrodes, the separation between the first anodic and cathodic peak was greater than that for air-free electrodes made with P3HT (Tbl. 2.2). This also suggests lithium-ion diffusion is hindered in these electrodes.[59]

Table 2.2. Summary of kinetic analyses and separation in first anodic and cathodic peaks for the different nanostructured NCA samples (unless otherwise stated P3HT was used as the binder, samples made with a PVDF binder were kept air-free).

Sample	Capacitive % - Trasatti analysis	Average *b*-values	Capacitive % - k_1/k_2 analysis	Peak separation at 0.5 mV/s (mV)
PMMA/no-RTA (air-free)	79%	0.94	89%	46
PMMA/no-RTA (air-exposed)	51%	0.82	82%	164
PMMA/no-RTA (PVDF binder)	67%	0.83	84%	153
PMMA/RTA (air-free)	82%	0.92	90%	85
PMMA/RTA (air-exposed)	55%	0.77	86%	216
PMMA/RTA (PVDF binder)	58%	0.83	88%	183

Next, galvanostatic intermittent titration technique (GITT) was performed in order to observe how the polarization behavior of the NCA electrodes varies with decrease in NCA particle sizes. Here, polarization is defined as the voltage change during relaxation of each GITT pulse

(Fig. S2.17), and has contributions from ohmic, charge-transfer, and concentration polarization.[60] Polarization is then plotted versus cell voltage for each sample in figure 2.4f. The data indicates that PMMA/no-RTA materials had the lowest polarization, followed by PMMA/RTA, and then bulk NCA. It has been shown that an increase in NiO-like structure leads to increased polarization in NCA.[61] Although PMMA/RTA is expected to have the shortest lithium-ion diffusion lengths and thus the lowest concentration polarization, it also had the highest fraction of surface Ni^{2+}, which should increase polarization related to charge-transfer. The relative ordering of polarization across the three samples is in excellent agreement with the galvanostatic rate behavior, which shows the best rate capabilities in PMMA/no-RTA samples and the worst in the bulk NCA. These data demonstrate how fast cycling behavior in nanostructured materials with reactive surfaces is a balance between reducing lithium-ion diffusion distances without decreasing charge-transfer rates.

The nanostructured NCA electrodes were also investigated using electrochemical impedance spectroscopy (EIS) with cycling up to 500 cycles. Nyquist plots for PMMA/no-RTA and PMMA/RTA after 100 cycles are shown in figure S2.18a. Both nanostructured samples display two semicircles, which have been ascribed to the resistance of lithium-ion diffusion through the solid electrolyte interphase (SEI) surface film (R_f) and charge-transfer resistance at the interface of the NCA particle (R_{ct}), for the first and second semicircle, respectively.[42,56,62] Both samples show similar increases in R_{ct} as the number of cycles increase (Fig. S2.18b), which agrees with previous literature.[42,56] The PMMA/no-RTA sample has slightly lower R_{ct}, which is expected because of the lower fraction of Ni^{2+} on the surface. While, the PMMA/RTA sample has a slightly lower R_f, but it has been shown that smaller particle sizes/higher surface areas lead to smaller R_f values.[63] Additionally, the R_f for both samples remains relatively steady as cycles increase, suggesting the presence of a stable surface layer.[62]

To determine the viability of a fast-charging full-cell made from these materials, we paired the nanostructured PMMA/no-RTA cathode with a pseudocapacitive Nb_2O_5-rGO (reduced

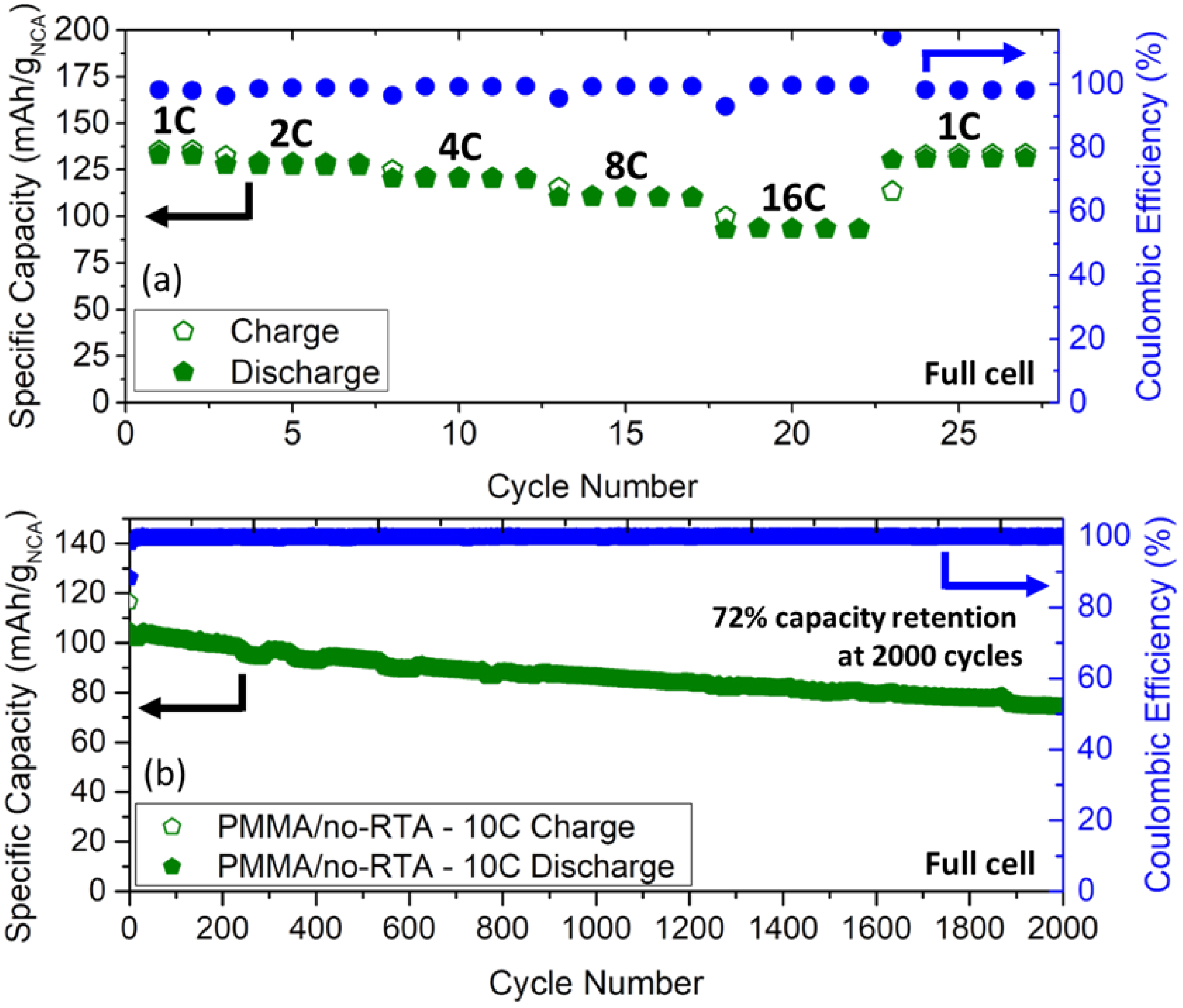

Figure 2.5. Full-cell device made with a PMMA/no-RTA NCA cathode and a Nb_2O_5-rGO anode cycled galvanostatically at various C-rates (a) and long-term cycling at 10C from 1.0-2.8 V (b). We observe 72% capacity retention after 2000 cycles. Specific capacity for charge is shown with open symbols, discharge with closed symbols, and the columbic efficiency is shown in blue.

graphene oxide) anode at higher mass loadings (5-6 mg/cm^2).[64] Orthorhombic Nb_2O_5 is an excellent pseudocapacitive anode, which is often integrated with conductive carbon, such as rGO, to increase electronic conductivity.[59,65,66] The full-cell was cycled from 1.0-2.8 V at various C-rates and at 16C the full-cell retains 70% of its 1C capacity (Fig. 2.5a). Compared to a PMMA/RTA full-cell, the PMMA/no-RTA cell has higher capacity at all rates (Fig. S2.19). The PMMA/no-RTA full-cell was then cycled at 10C for 2000 cycles (Fig. 2.5b). The initial specific discharge capacity was 103 mAh/g normalized by the NCA active mass. If we consider the combination of both anode and cathode masses, the resulting NCA/Nb_2O_5 cell corresponds to an energy density of 95 Wh/kg at a current density of 1260 W/kg. After 2000 cycles, the discharge capacity was 74 mAh/g, a capacity retention of 72%. The PMMA/no-RTA full-cell shows similar/slightly better capacity retention after 2000 cycles at 10C compared to a bulk NCA full-cell cycled at a slower rate of 8C (Fig. S2.20a). While the PMMA/RTA full-cell shows lower overall capacity and a capacity retention of only 64% after 2000 cycles at 10C (Fig. S2.20b). The ability of the PMMA/no-RTA full-cell to charge quickly over many cycles, without excessive capacity fade and similar capacity retention to a commercial bulk NCA, indicates the promise of this nanostructured material for commercialization.

2.3 Conclusions

In summary, nanostructured NCAs with decreased particle sizes and thus shortened lithium-ion diffusion lengths were synthesized. The nanostructured NCA materials showed pseudocapacitive signatures in both size ranges. However, because NCA has a reactive surface, the smallest sized NCA forms more insulating surface layers, which cause a decrease in fast-charging performance. The PMMA/no-RTA NCA with medium sized particles and low amounts of Li_2CO_3/NiO achieved the highest capacity at fast rates, 150 mAh/g at 16C and 59 mAh/g at 64C. Because bulk NCA already has suppressed phase transitions, particle sizes do not need to be heavily decreased in order for the material to exhibit extrinsic pseudocapacitance characteristics.

Interestingly, the best balance between diffusion limitations and charge-transfer resistance appears to not be at the absolute smallest sized grains. We note that if smaller NCA particle sizes with ideal crystal structures and stable surfaces could be produced, then more capacitive behavior would be expected. As demonstrated in full-cell tests, nanostructured NCA shows great promise for future fast-charging applications.

2.4 Supplementary Information

Materials

The following chemicals were purchased and used as received: lithium nitrate (98+%, MilliporeSigma), nickel nitrate hexahydrate (99.9985%, Alfa Aesar), cobalt nitrate hexahydrate (99+%, Acros Organics), aluminum nitrate nonahydrate (98%, Alfa Aesar), triblock copolymer Pluronic F127 ($EO_{100}PO_{65}EO_{100}$ M_W = 12600 Da, BASF), ammonium persulfate (98%, Alfa Aesar), ammonium lauryl sulfate (~30% in H_2O, Sigma Aldrich), methyl methacrylate (contains ≤30 ppm MEHQ as inhibitor, 99%, Sigma Aldrich), and hexanes (Fisher Chemical). Commercial bulk NCA was purchased from Quallion Corporation to use as a control. For electrode and coin cell assembly, the following chemicals were purchased and used as received: multi-walled carbon nanotubes (>95%, OD: 5-15 nm, US Research Nanomaterials, Inc.), carbon nanofibers (DxL 100 nm x 20-200 μm, Sigma-Aldrich), poly(3-hexylthiophene-2,5-diyl) (P3HT) (MW 15000-30000, PDI = 1.6-1.8, regioregularity = 89-94%, Rieke Metals), *o*-xylenes (99%, Extra Dry, ACROS Organics), carbon black, Super P (Alfa Aesar), styrene-butadiene rubber (SBR, MTI corp.), carboxymethyl cellulose (CMC, MTI corp.), polyvinylidene fluoride (PVDF, Kynar), and N-methyl-2-pyrrolidone (NMP, Alfa Aesar).

Characterization

X-ray diffraction (XRD) was collected using a Bruker D8 Discover Powder X-ray Diffractometer using a Bragg-Brentano geometry. Scanning electron microscopy (SEM) images were obtained with a JOEL JSM-6700F field emission scanning electron microscope with 5 kV accelerating voltage. To examine the structure of the particles before and after cycling by transmission electron microscopy (TEM), we used an FEI Technai G^2 TF20 High-Resolution EM, CryoEM and CryoET operating at an accelerating voltage of 200 kV with a TIETZ F415MP 16 megapixel 4k×4k CCD detector. The fast Fourier transform (FFT) of the image was used to analyze the lattice planes in the sample. For the pristine TEM sample, the powder was removed from the glovebox and immediately dispersed in ethanol by ultra-sonication to deposit onto a carbon coated copper TEM grid; the grid was then exposed to air for less than 10 minutes before analysis. For the cycled TEM sample, after cycling (described below) the powder was scrapped off of the electrode, dispersed in dry acetonitrile and sonicated under argon for 1 hour. The sample was then deposited onto a TEM grid inside a glovebox; the grid was exposed to air for less than 5 minutes before analysis. Nitrogen porosimetry measurements were performed using either a Micromeritics TriStar II 3020 porosimeter or a Micromeritics ASAP 2020 Plus porosimeter. The adsorption branch of the isotherm was used to determine the surface area using the Brunauer-Emmett-Teller (BET) model. Volume weighted pore size distribution was determined from the adsorption isotherm using the Barrett-Joyner-Halenda (BJH) model with the Halsey equation and Faas correction. Surface sensitive elemental analysis was performed using X-ray photoelectron spectroscopy (XPS) using a Kratos Axis Ultra DLD spectrometer with a monochromatic Al Kα radiation source and a charge neutralizer filament to control charging of the sample. All spectra were calibrated to the advantageous carbon 1s peak at 284.8 eV. The air-free samples were transferred from a glovebox to the XPS sample chamber using an air-free sample transfer holder. The air-exposed samples were taken out of the glovebox and exposed to ambient air for 1 week before analysis. Argon ion etching was performed on select samples in the XPS chamber with a raster size of 2 mm x 2 mm and an acceleration voltage of 4 kV for 30 seconds to 2 minutes.

Rietveld refinement using MAUD software

The XRD data was analyzed by Rietveld refinement using MAUD software. A $R\bar{3}m$ space group was used with Li^+/Ni^{2+} set at the 3b sites (0, 0, 0.5), $Li^+/Ni^{3+}/Co^{3+}/Al^{3+}$ at the 3a sites (0, 0, 0), and O at the 6c sites (0, 0, z_{ox}), where $z_{ox} \approx 0.250$ Å. The calculated pattern is evaluated with a weighted profile R factor (R_{wp}), where a R_{wp} less than 10% is considered a good fit. The refined c lattice parameter and value for z_{ox} were then used to calculate the slab (S) and interslab (I) thicknesses, where the interslab thickness is the thickness of the lithium-ion diffusion layer, using the following formulas:[49,50]

$$S = 2\left(\frac{1}{3} - z_{ox}\right)c$$

$$I = \frac{c}{3} - S$$

Synthesis of the colloidal poly(methyl methacrylate) (PMMA) templates

The synthesis of the colloidal PMMA template is based on previous literature.[47,67] Deionized water (165 mL) was added to a three-neck round-bottom flask in an oil bath with a magnetic stirrer and a reflux condenser. The methyl methacrylate monomer (12.56 mL) was added dropwise to the flask. The solution was then heated from room temperature to 73 °C over 10 minutes, once the reaction temperature exceeded 55 °C, the initiator, ammonium persulfate (0.08 g in 10 mL H_2O) was added dropwise. The reaction was then held at 73 °C for 3 hours. The resulting colloidal solution of PMMA was then extracted with hexanes in order to remove any unreacted monomer. SEM was used to determine the colloid size, which was 250 nm in diameter.

Synthesis of nanostructured $LiNi_{0.80}Co_{0.15}Al_{0.05}O_2$

Stoichiometric amounts of nickel nitrate hexahydrate, cobalt nitrate hexahydrate, and aluminum nitrate nonahydrate were dissolved in water, so that the total transition metal concentration (Ni+Co+Al) was 0.6 M. Lithium nitrate was also dissolved with 5% molar excess (Li:(Ni+Co+Al) = 1.05:1). Once completely dissolved, this solution was mixed with the colloidal 250 nm PMMA template (synthesis above) in a 1:1.5 vol ratio of the final NCA material to PMMA. This was followed by the addition of 3.8 wt% Pluronic F127 (with respect to colloidal PMMA) in order to stabilize the colloidal template in the salt solution. This solution was then stirred for 3 hours before it was poured into a petri dish and dried in an 80 °C oven overnight. The resulting powder was heated in a tube furnace under flowing oxygen, first at 180 °C to drive out any remaining water and then at 450 °C to remove the template, leaving a nanostructured NCA precursor. The NCA precursor was then ground with a mortar and pestle before further heat treatment. Either a rapid thermal annealing (RTA) or a conventional heat treatment was used to obtain "PMMA/RTA" or "PMMA/no-RTA" samples, respectively. For PMMA/no-RTA the following heat treatment program was followed, all under flowing oxygen: a 1 hour ramp from room temperature to 800 °C, followed by 2 hours at 800 °C, then the oven was let naturally cool to 350 °C before the sample was taken directly into a glovebox while hot, to decrease exposure to water in the air. For the PMMA/RTA sample: the furnace was preheated to 850 °C, the sample was then added to the hot furnace and the oxygen flow was turned on. The sample was kept at 850 °C for 5 minutes, the furnace was then opened to allow for immediate cooling to 700 °C. The sample was held at 700

°C for 12 hours under oxygen flow, then cooled naturally to 350 °C to be directly taken into a glovebox.

Electrochemical Analysis (Half-cells)

The synthesized nanostructured NCA powders were cast into slurries on a carbon coated aluminum current collector with the composition of: 90 wt% active material, 3 wt% multi-walled carbon nanotubes, 4 wt% carbon nanofibers, and 3 wt% P3HT as a binder in *o*-xylenes (15 wt% solution). The slurries for the nanostructured NCA were assembled in a glovebox to minimize exposure to CO_2 and water. After casting the slurries with a doctor blade, the slurries were heated on a hotplate for 5 hours before being placed under vacuum in the antechamber of the glovebox to dry further overnight. For slurries made with a PVDF binder, the same procedure was followed except 2.5 wt% of PVDF in NMP was used instead of P3HT in o-xylenes. Electrodes 0.7 cm^2 were punched out of the slurries in the glovebox. Electrodes surrounding the cycled electrodes, which were kept completely air-free, were taken out of the glovebox and weighed on a microbalance to give an average mass loading and to calculate error bars for the cycled electrodes. The commercial bulk NCA slurries were cast in ambient air using the same material compositions, the slurries were then dried in a vacuum oven at 120 °C overnight. Active material mass loadings ranged from 1.2 – 1.9 mg/cm^2 for all NCA half-cell electrodes. The half-cell electrodes were tested in CR2032 coin cells against a Li counter electrode, with a Celgard 2400 separator and 1 M $LiPF_6$ in 1:1:1 ethylene carbonate:dimethyl carbonate:diethyl carbonate (EC:DMC:DEC). The coin cells were cycled galvanostatically from 2.7-4.2 V (vs. Li/Li^+) at various C-rates on an Arbin Instruments BT2000 battery testing system (the cycled sample analyzed by TEM was also cycled following this galvanostatic program, ~50 cycles). Cyclic voltammetry was performed using a BioLogic VSP potentiostat/galvanostat from 2.7-4.2 V at different scan rates. Additionally, galvanostatic intermittent titration technique (GITT) measurements were performed using a Biologic VMP potentiostat/galvanostat. A minimum of 10 charge-discharge cycles were performed at various C-rates prior to the pulse-rest GITT protocol. During the GITT experiment, a C/10 constant-current pulse was applied for 30 minutes with a 30 min rest period between pulses. The sequence was repeated for both charge and discharge cycles and for varying composition x in $Li_{1-x}Ni_{0.80}Co_{0.15}Al_{0.05}O_2$ until the full voltage range (2.7–4.2 V) was covered. Electrochemical impedance spectroscopy (EIS) was performed on the nanostructured NCA electrodes in half-cells at open circuit voltage (OCV) using a BioLogic VSP potentiostat/galvanostat. Measurements were taken after various numbers of cycles at 10C between 2.7-4.2 V, with a frequency range of 100 mHz - 300 kHz and a potential amplitude of 10 mV.

Electrochemical Analysis (Full-cells)

NCA slurries for full cells were cast air-free using the same methods as the previous section but with higher mass loadings (5-7 mg/cm^2). The NCA cathode electrode was paired with a Nb_2O_5-rGO anode electrode (5-7 mg/cm^2) to construct a full cell. To prepare the Nb_2O_5 electrode, 90 wt% of Nb_2O_5-rGO (Battery Streak Inc., Newbury Park, CA) was mixed with 10 wt% aqueous conductive binder to form a uniform slurry. The binder was composed of a 1:1:1:1 weight ratio of carbon nanofibers:Super P:SBR:CMC. The slurry was then cast on copper foil using a doctor blade, followed by vacuum drying for 12 hours. The resulting electrode tape was punched into 0.7 cm^2 electrodes. The NCA/Nb_2O_5-rGO full cells were assembled in a CR2032 coin cell using a glass fiber separator with 1 M $LiPF_6$ in 1:1:1 EC:DMC:DEC electrolyte. The cells were cycled galvanostatically from 1.0-2.8 V at various C-rates and at 10C for 2000 cycles on a BioLogic VMP potentiostat/galvanostat.

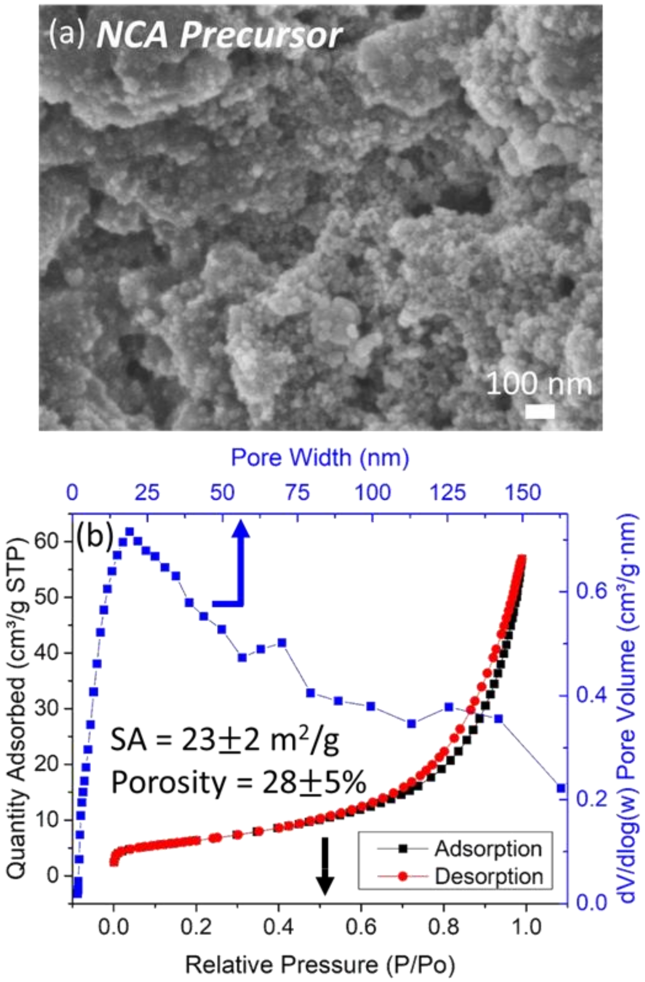

Figure S2.1. (a) SEM image of the nanostructured NCA precursor after being heated at 450 °C to remove the colloidal PMMA template, but before crystallization of the final NCA material. (b) Nitrogen porosimetry adsorption-desorption isotherms (black and red, respectively) of the NCA precursor, and the BJH adsorption volume-weighted pore size distribution (blue). The surface area of the precursor was 23±2 m^2/g with a porosity of 28±5%. The isotherm shape fits a Type II isotherm, which describes macroporous materials; the isotherm hysteresis fits a H3 hysteresis, which also describes macropores.[68] The pore size distribution indicates a peak in pore sizes around 20 nm, but also contains a large fraction of pores of larger sizes.

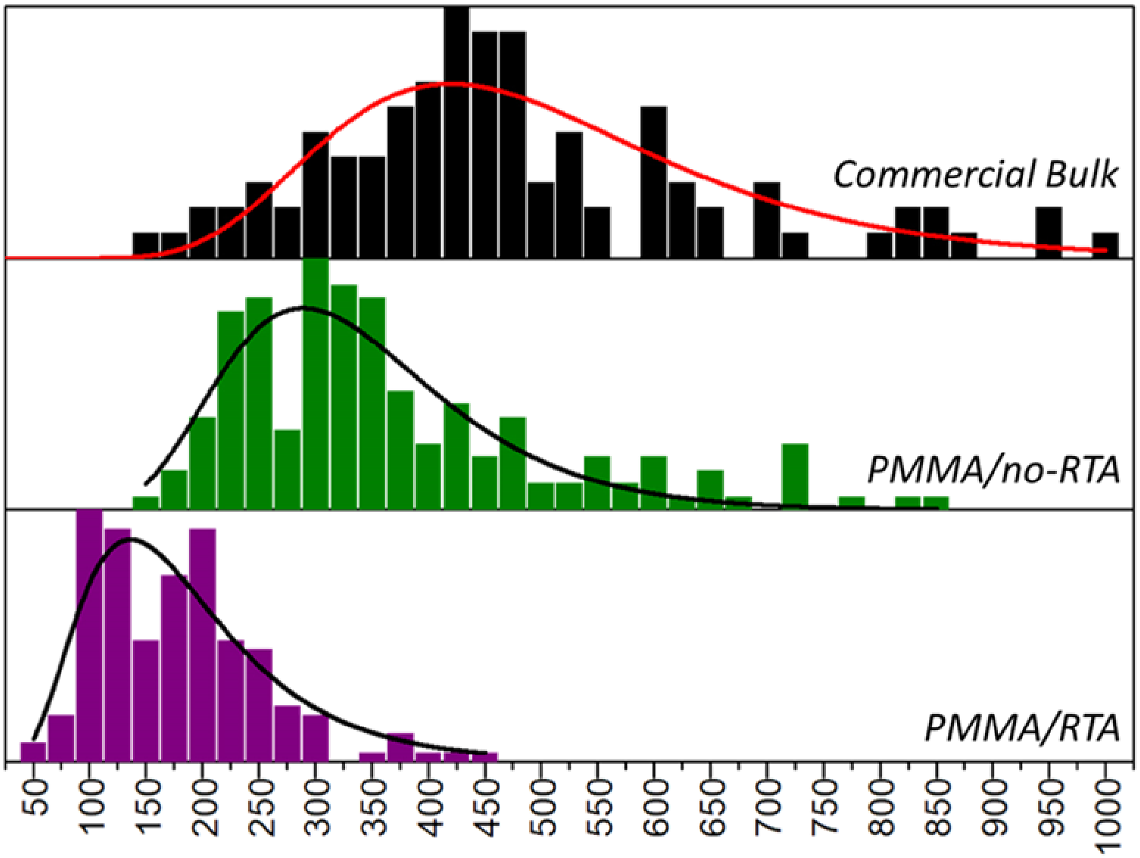

Figure S2.2. Histograms of NCA particle size distributions generated by measuring 150 particles in SEM of commercial bulk (black, top), PMMA/no-RTA (green, middle), and PMMA/RTA NCA (purple, bottom), binned in 25 nm increments. Note that for the bulk NCA, sizes correspond to primary particles, and those primary particles are agglomerated into non-porous secondary particles with micron scale dimensions. The histograms were fit using a log-normal distribution (shown in red for commercial bulk and black for the PMMA template materials). The maximum of the fit was used as the average particle size for each sample listed in **Table 2.1** in the main text.

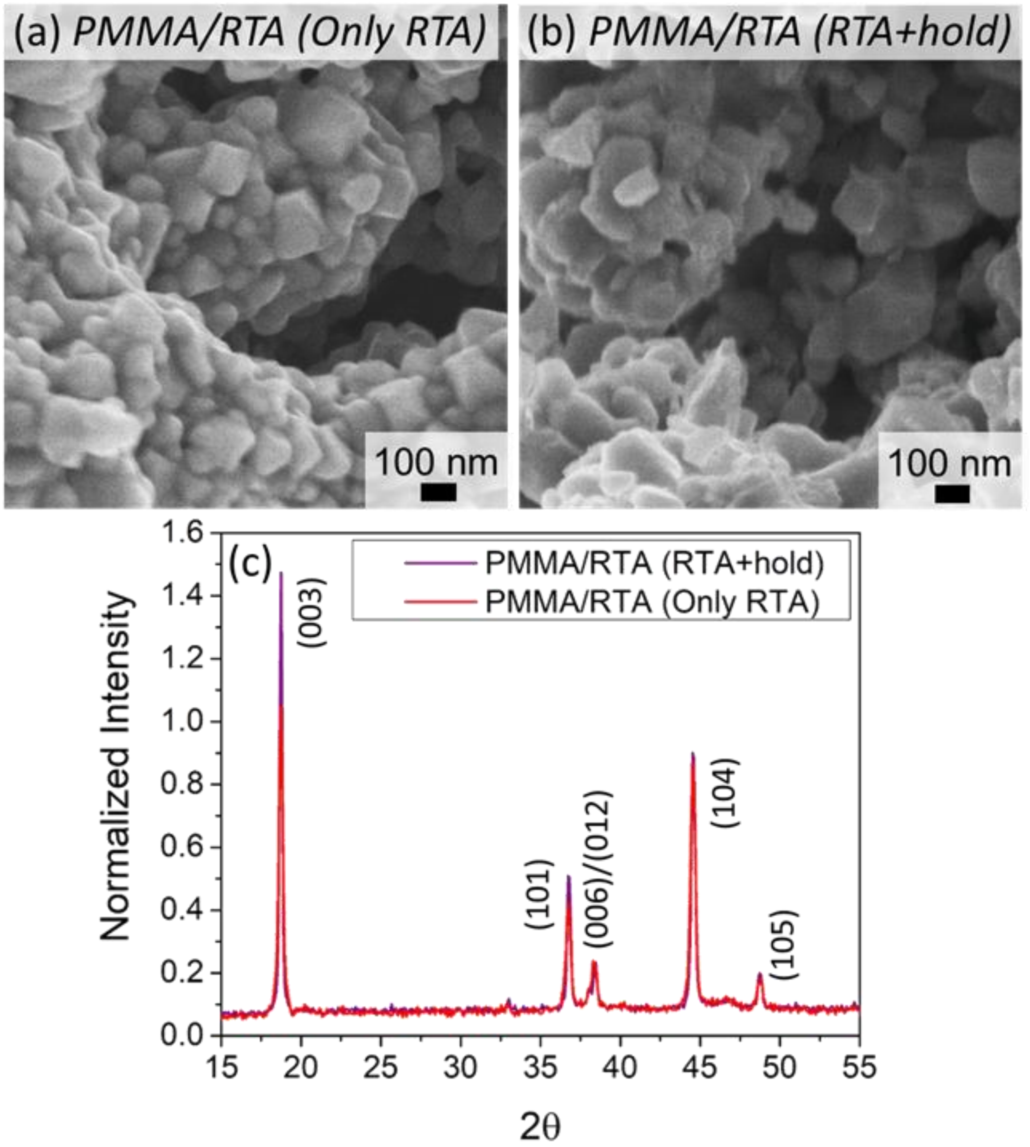

Figure S2.3. (a) SEM image of nanostructured NCA synthesized by heating at 850 °C for only 5 minutes under oxygen (only RTA), this resulted in small particle sizes. (b) SEM image of NCA synthesized with RTA method, 850 °C for 5 minutes, followed by holding at 700 °C for 12 hours under oxygen (this is the normal synthesis method used, referred as PMMA/RTA in the main text and supporting information). The two SEM images show that there is not significant growth of the particles after the hold step at 700 °C. (c) XRD patterns for NCA samples with (RTA+hold) and without (only RTA) the 700 °C hold step after heating to 850 °C, normalized to the (104) peak. The 700 °C hold step resulted in increased cation ordering, as indicated by an increase of the (003) diffraction peak, and an increase in the $I(003)/I(104)$ integrated intensity ratio from 1.13 to 1.23.

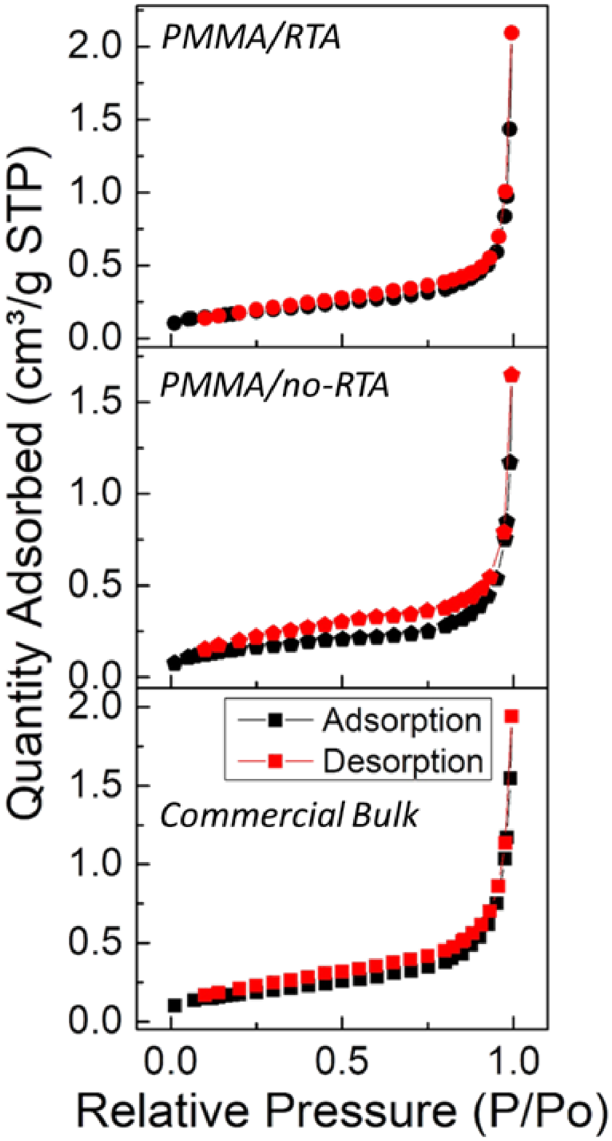

Figure S2.4. Nitrogen porosimetry adsorption-desorption isotherms (black and red, respectively) of PMMA/RTA (top, circle), PMMA/no-RTA (middle, pentagon), and commercial bulk (bottom, square).

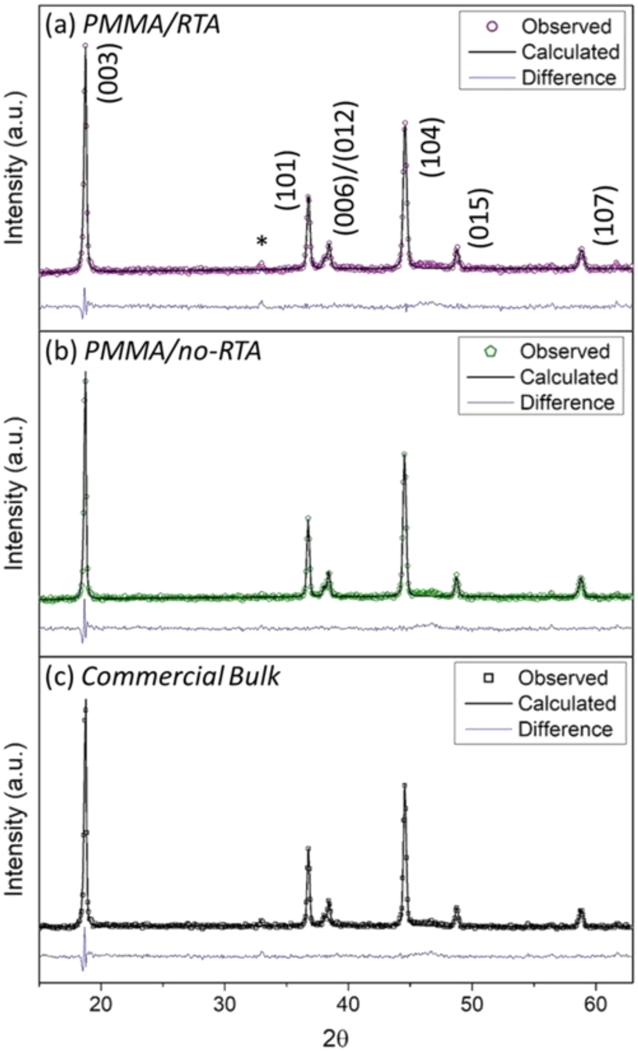

Figure S2.5. Rietveld refinement of XRD patterns for PMMA/RTA (a), PMMA/no-RTA (b), and commercial bulk NCA (c). The observed XRD pattern is shown with open symbols, the calculated pattern is shown in black, and the difference in the observed and calculated patterns is shown below the patterns in blue. The *I*(003)/*I*(104) ratios of each pattern are listed in **Table 2.1** in the main text. The peaks marked with * are the silicon (200) peak from the silicon sample holder.

Table S2.1. Refined lattice parameters, crystallite size, Ni^{2+} in Li sites, weighted profile R-factor (R_{wp}), z_{ox} of the 6c site, and calculated slab and interslab thicknesses from the structural analysis from Rietveld refinement of XRD patterns for PMMA/RTA, PMMA/no-RTA, and commercial bulk NCA

	a **(Å)**	***c*** **(Å)**	***c/a***	**Crystallite size (nm)**	**Ni^{2+} in Li sites**	**R_{wp} (%)**	**z_{ox} (Å)**	**S (Å)**	**I (Å)**
PMMA/ RTA	2.8633(3)	14.178(4)	4.95	100	0.024(9)	3.96%	0.259(9)	2.11	2.62
PMMA/ no-RTA	2.8653(3)	14.189(4)	4.95	170	0.031(9)	4.35%	0.260(7)	2.08	2.65
Comm. Bulk	2.8642(4)	14.183(3)	4.95	160	0.033(8)	4.34%	0.259(9)	2.11	2.62

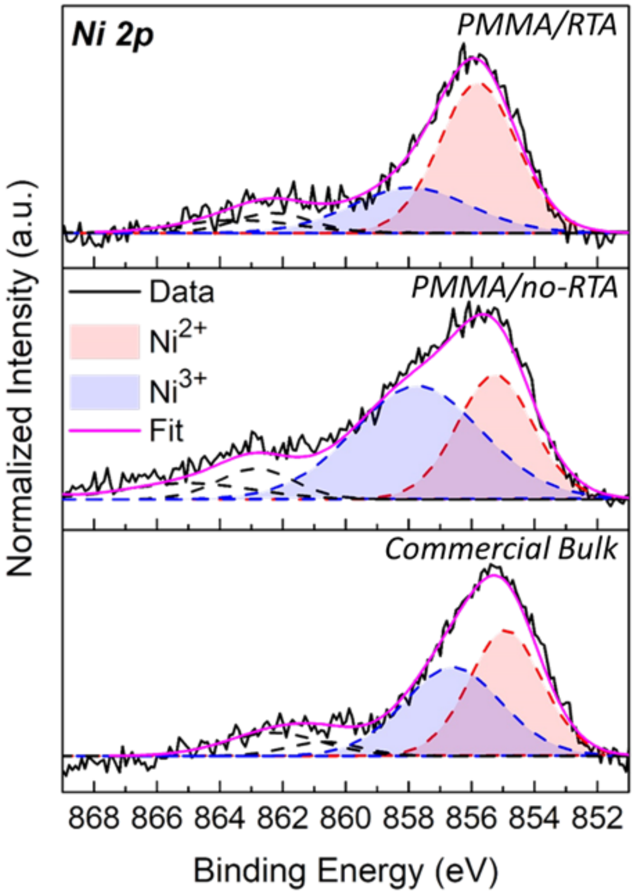

Figure S2.6. Ni 2p$_{3/2}$ XPS spectra for PMMA/RTA (top), PMMA/no-RTA (middle), and commercial bulk (bottom). The experimental data is shown in black and the overall fit is shown in pink. For ease of comparison of the relative amount of Ni^{2+} and Ni^{3+} present in each sample, the Ni^{2+} peak (~855 eV) is shaded in red and the Ni^{3+} peak (~857 eV) is shaded in blue; quantification of the fraction of Ni^{2+} to Ni^{3+} is provided in **Table 2.1** in the main text. Ni 2p characteristic satellite peaks are shown with dotted black lines.

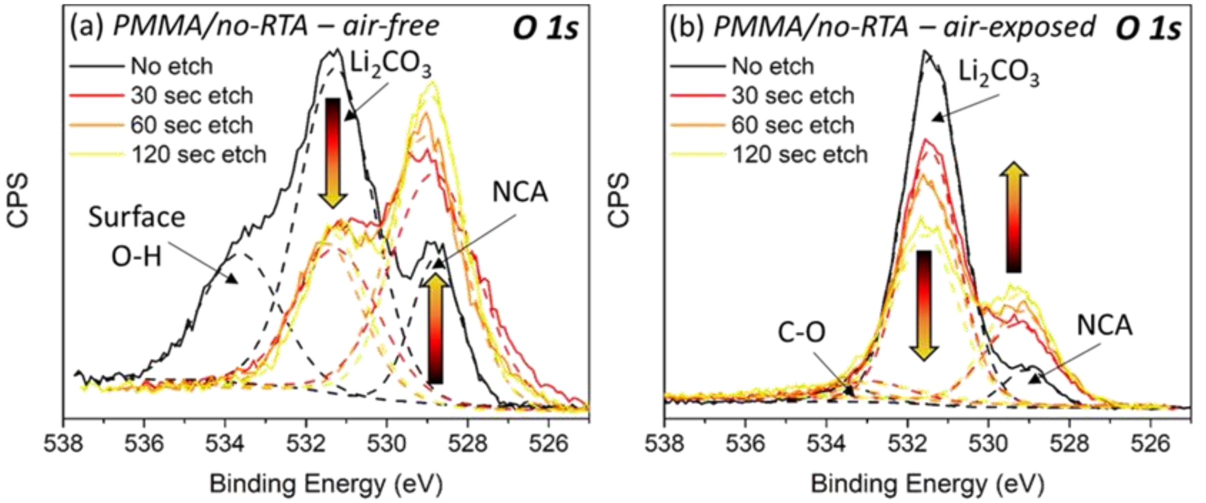

Figure S2.7. (a) Representative O 1s spectrum for the air-free samples used to make the graph in figure 2.2a of the main text, which shows the progression of the Li_2CO_3 (~531 eV) and NCA (529 eV) O 1s peaks as the samples were etched. The air-free samples contain a high binding energy surface O-H peak that has been observed by previous groups during air-free XPS analysis of NCA;[54,69] we observed that this peak disappears after the first argon ion etch. (b) Representative O 1s spectrum for the air-exposed samples used to make the graph in figure 2.2a of the main text. The air-exposed spectrum contains a strong C-O peak due to contact with CO_2 in the air.

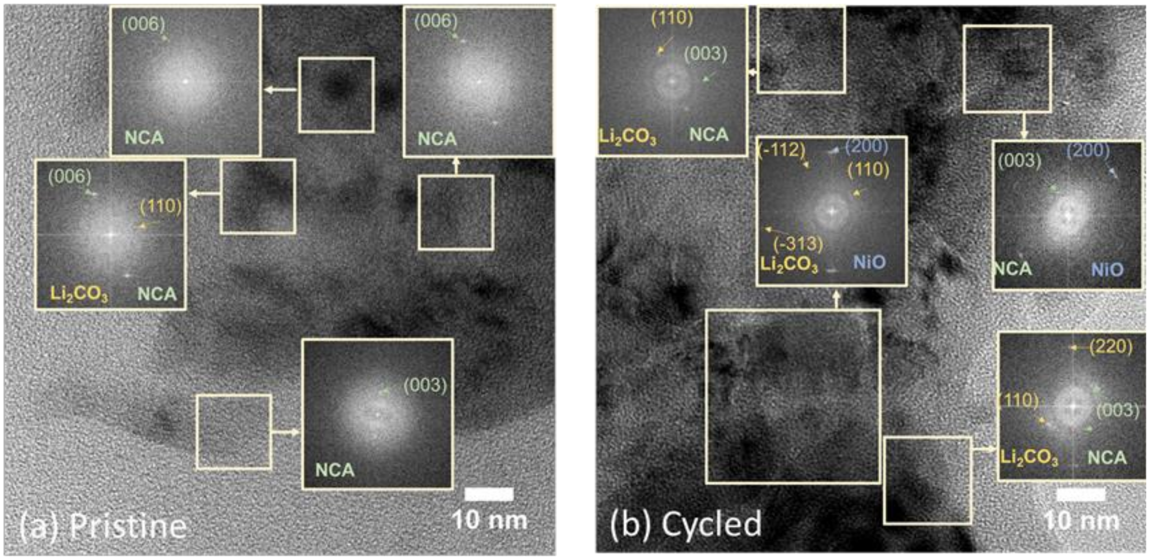

Figure S2.8. TEM images of (a) a pristine PMMA/no-RTA particle and (b) a PMMA/no-RTA particle after being cycling galvanostatically for ~50 cycles at various C-rates from 2.7-4.2 V vs. Li/Li^+. FFT was used to analyze lattice planes on the particles, after cycling the PMMA/no-RTA particle had an amorphous layer of 8-14 nm.

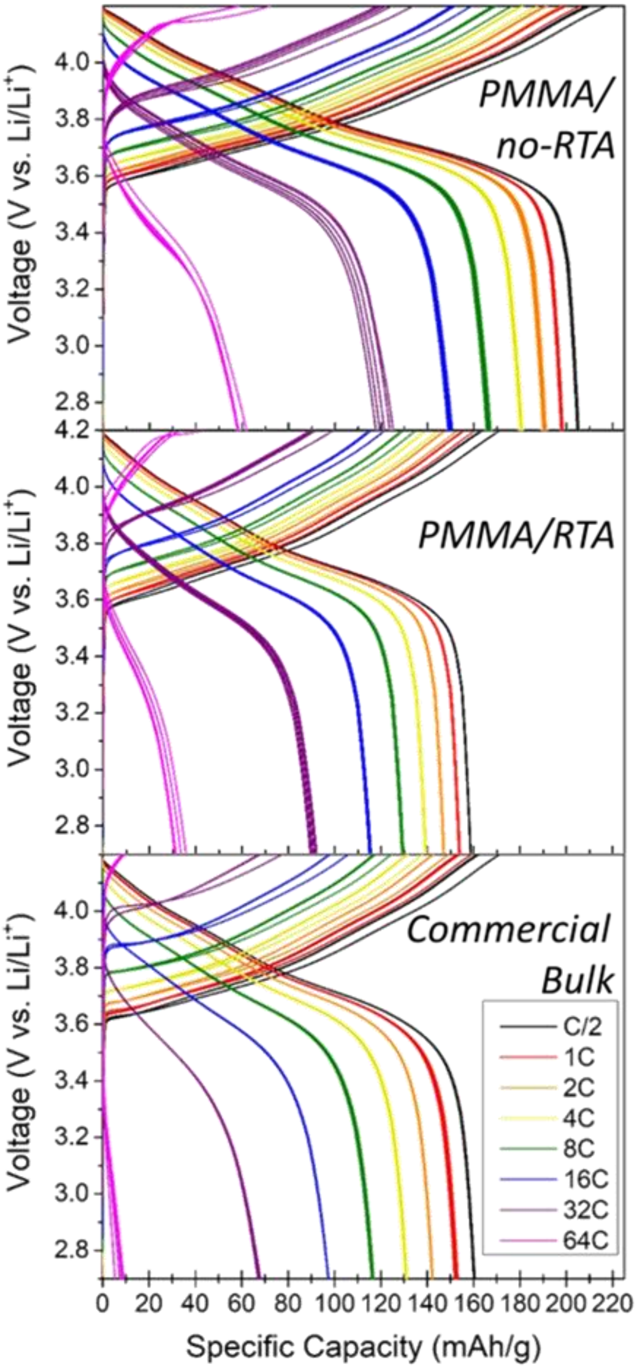

Figure S2.9. Galvanostatic cycling curves for PMMA/no-RTA (top), PMMA/RTA (middle), and commercial bulk (bottom) at various C-rates from C/2 to 64C after 3 activation cycles at C/5.

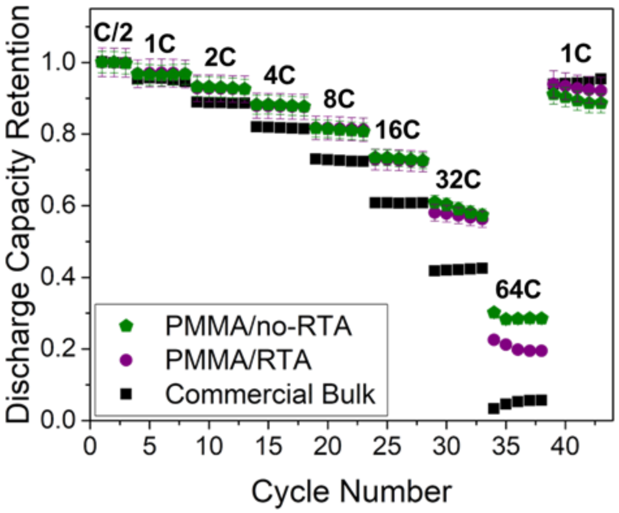

Figure S2.10. Discharge capacity retention relative to the capacity at C/2 for PMMA/no-RTA (green pentagon), PMMA/RTA (purple circle), and commercial bulk NCA (black square).

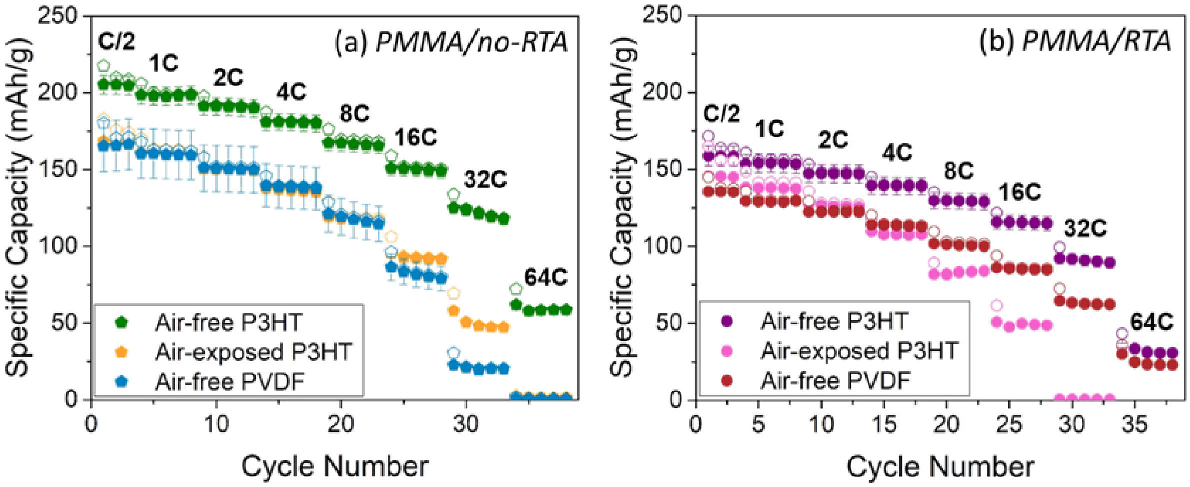

Figure S2.11. Galvanostatic charge (open symbols) and discharge (filled symbols) specific capacity at different rates (after 3 activation cycles at C/5) from 2.7-4.2 V for (a) PMMA/no-RTA samples where the electrodes were either kept air-free (green pentagon) or exposed to air (orange pentagon), or made with a PVDF binder and kept-air free (blue pentagon) and for (b) PMMA/RTA samples, again either kept air-free (purple circle) or exposed to air (pink circle) or made with a PVDF binder and kept air-free (red circle).

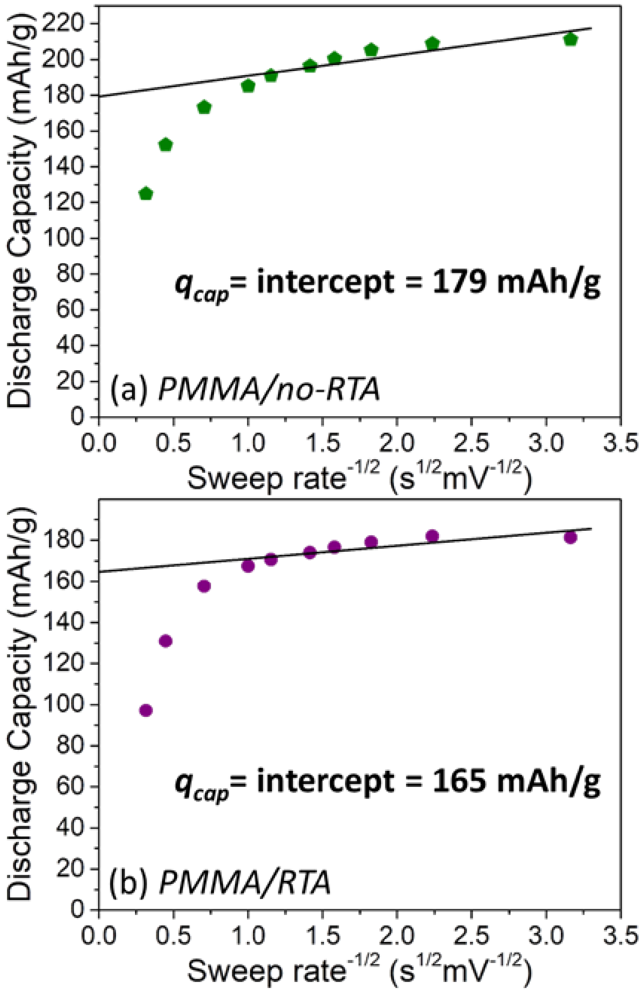

Figure S2.12. Trasatti analysis for determination of the capacitive charge storage (q_{cap}) as the extrapolated y-intercept as $v \to \infty$ for PMMA/no-RTA (a) and PMMA/RTA (b). The q_{cap} value is displayed on the graphs.

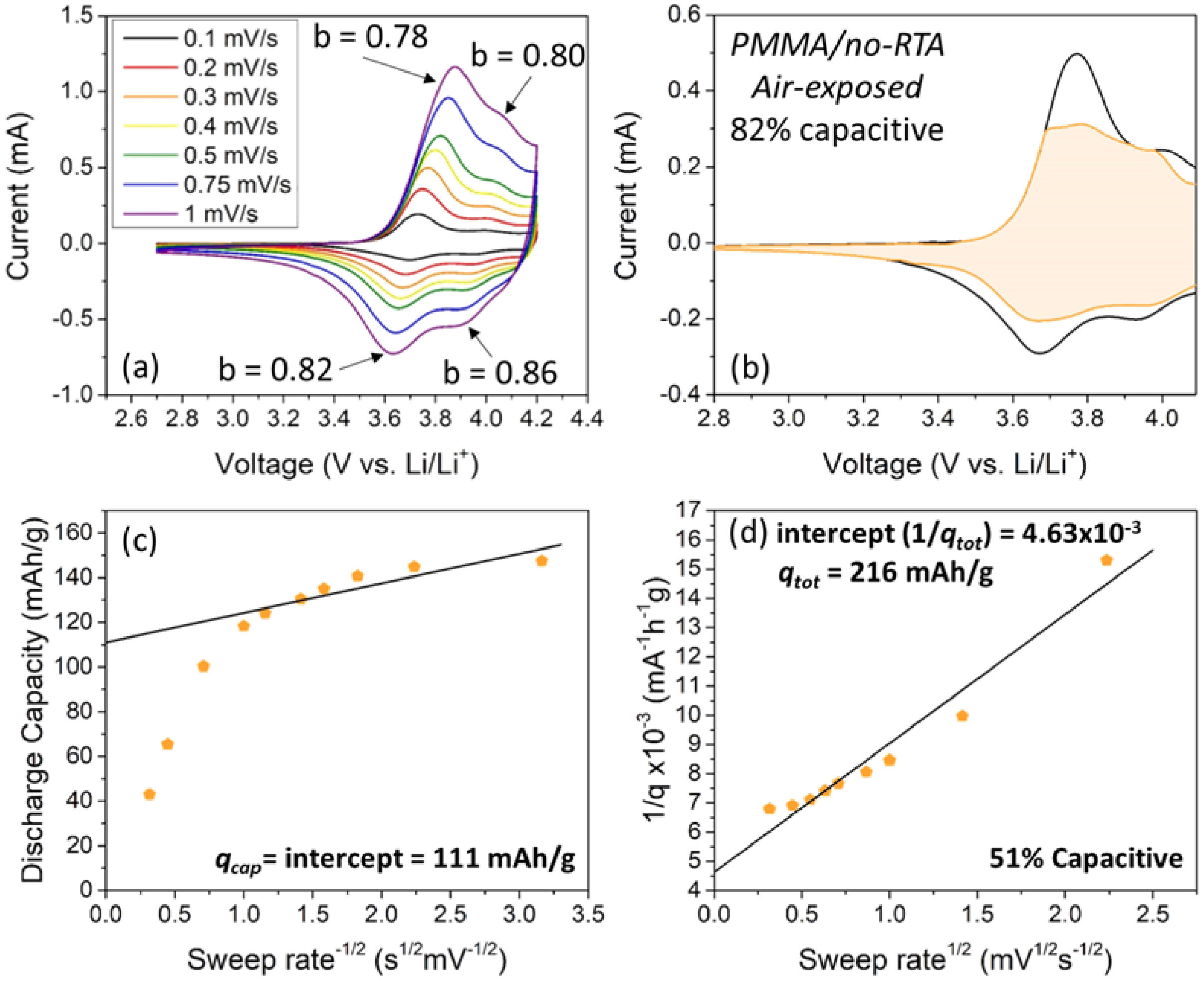

Figure S2.13. Kinetic analyses of air-exposed PMMA/no-RTA. (a) *b*-values derived from anodic and cathodic peaks from 0.1-1 mV/s sweep rates. (b) CV curve at 0.3 mV/s used to derive capacitive contribution (orange shaded region). (c) Trasatti analysis for determination of q_{cap} as the extrapolated y-intercept as $v \to \infty$. (d) Trasatti analysis for determination of q_{tot} with the extrapolated y-intercept as $v \to 0$.

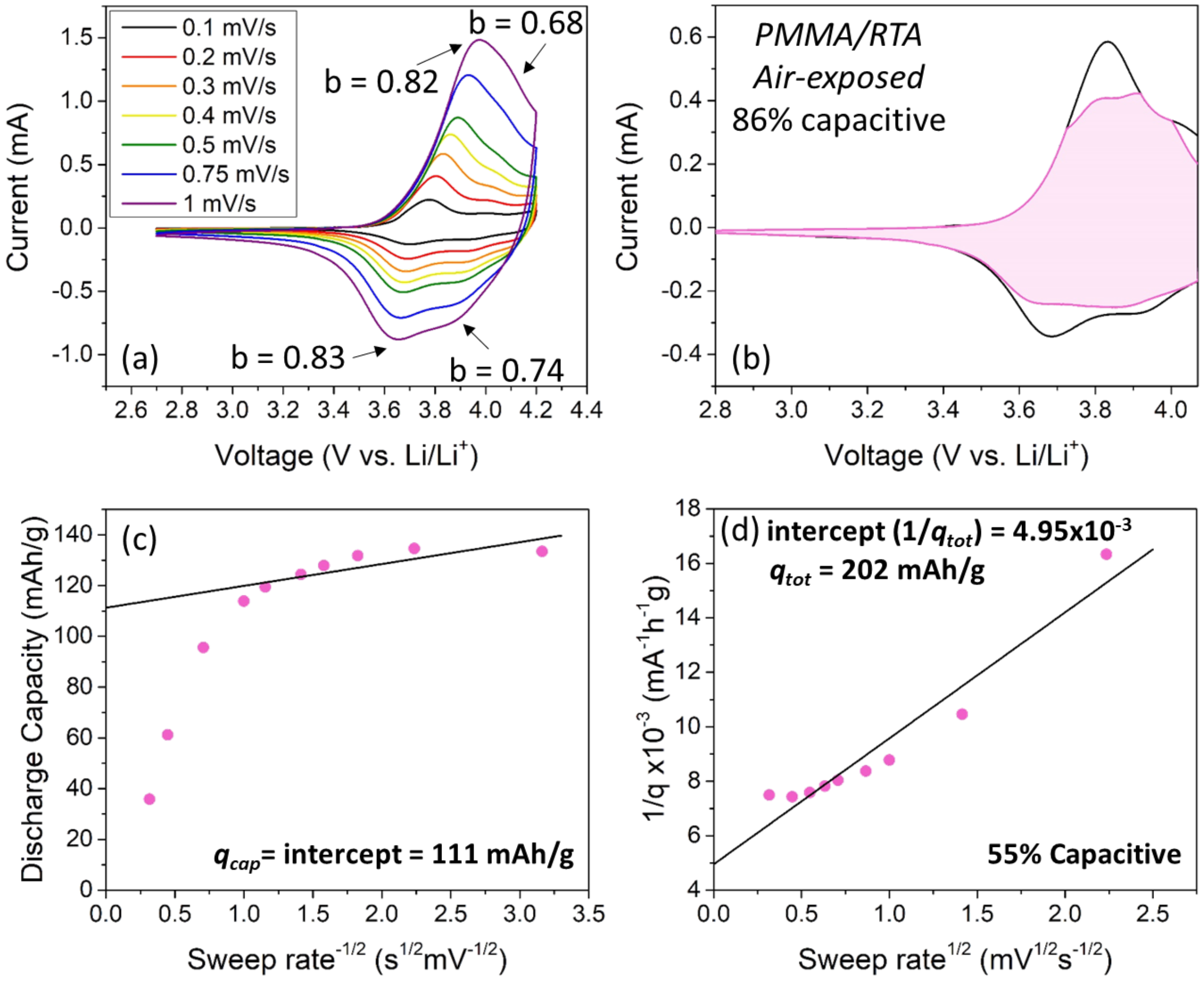

Figure S2.14. Kinetic analyses of air-exposed PMMA/RTA. (a) *b*-values derived from anodic and cathodic peaks from 0.1-1 mV/s sweep rates. (b) CV curve at 0.3 mV/s used to derive capacitive contribution (pink shaded region). (c) Trasatti analysis for determination of q_{cap} as the extrapolated y-intercept as $v \rightarrow \infty$. (d) Trasatti analysis for determination of q_{tot} with the extrapolated y-intercept as $v \rightarrow 0$.

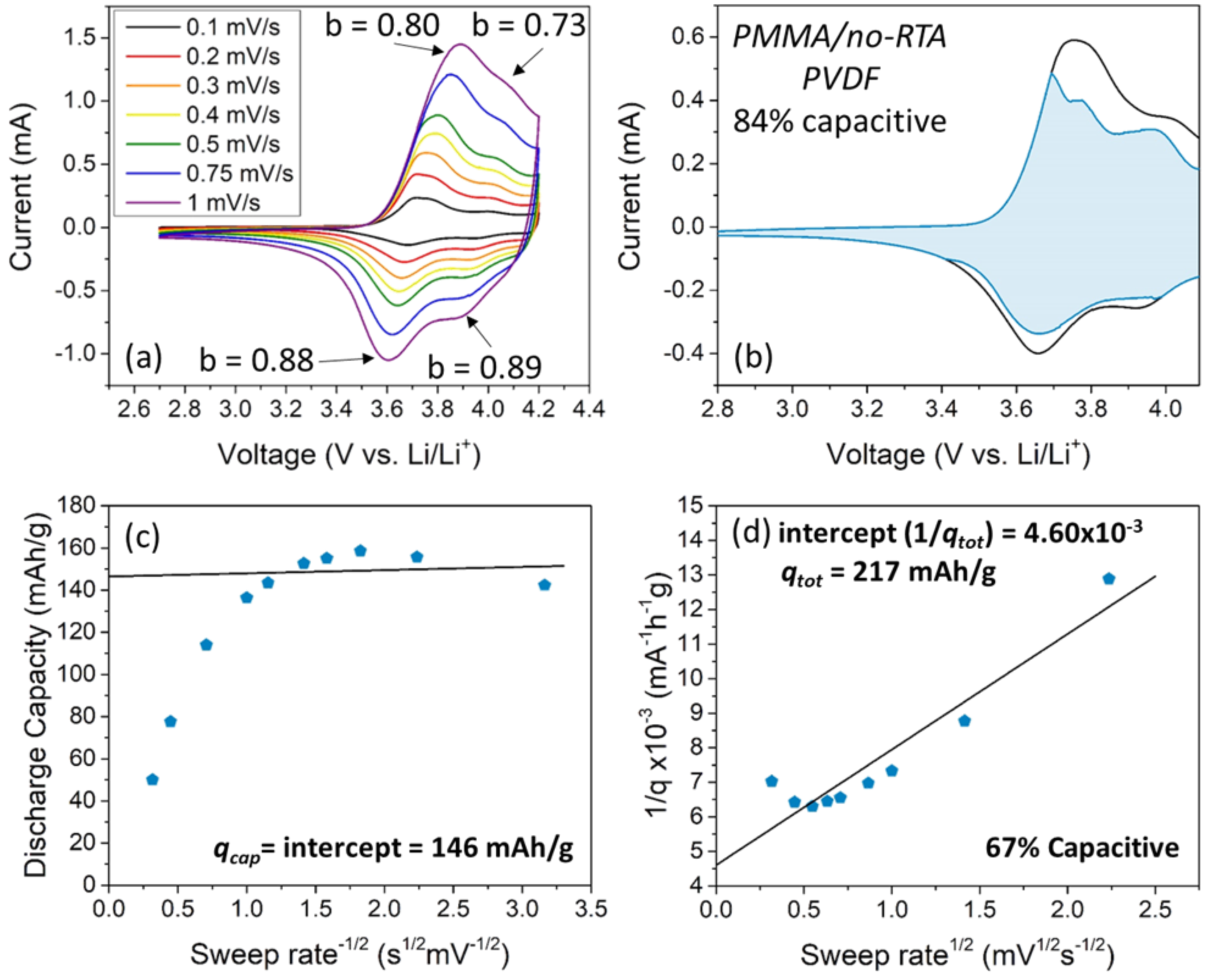

Figure S2.15. Kinetic analyses of PMMA/no-RTA made with PVDF as the binder. (a) *b*-values derived from anodic and cathodic peaks from 0.1-1 mV/s sweep rates. (b) CV curve at 0.3 mV/s used to derive capacitive contribution (blue shaded region). (c) Trasatti analysis for determination of q_{cap} as the extrapolated y-intercept as $v \rightarrow \infty$. (d) Trasatti analysis for determination of q_{tot} with the extrapolated y-intercept as $v \rightarrow 0$.

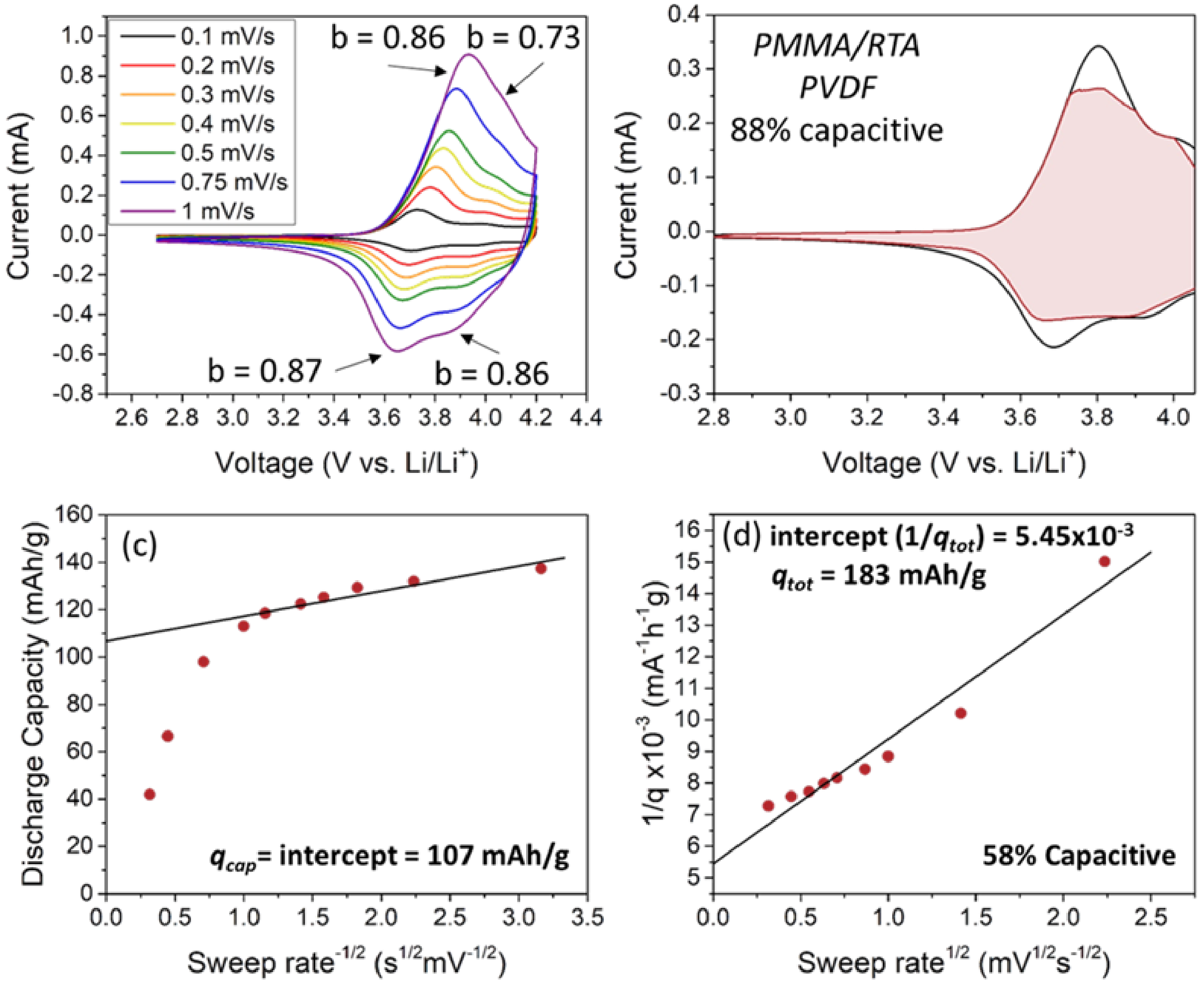

Figure S2.16. Kinetic analyses of PMMA/RTA made with PVDF as the binder. (a) *b*-values derived from anodic and cathodic peaks from 0.1-1 mV/s sweep rates. (b) CV curve at 0.3 mV/s used to derive capacitive contribution (red shaded region). (c) Trasatti analysis for determination of q_{cap} as the extrapolated y-intercept as $v \rightarrow \infty$. (d) Trasatti analysis for determination of q_{tot} with the extrapolated y-intercept as $v \rightarrow 0$.

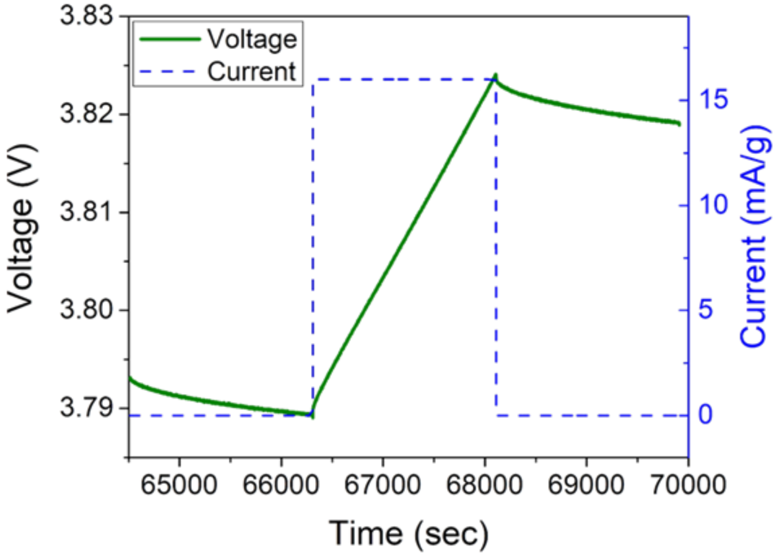

Figure S2.17. Representative GITT current charge pulse (blue dotted line) and resulting voltage profiles (green line) for PMMA/no-RTA, polarization is defined as the change in voltage from the end of the current pulse to the end of the relaxation period.

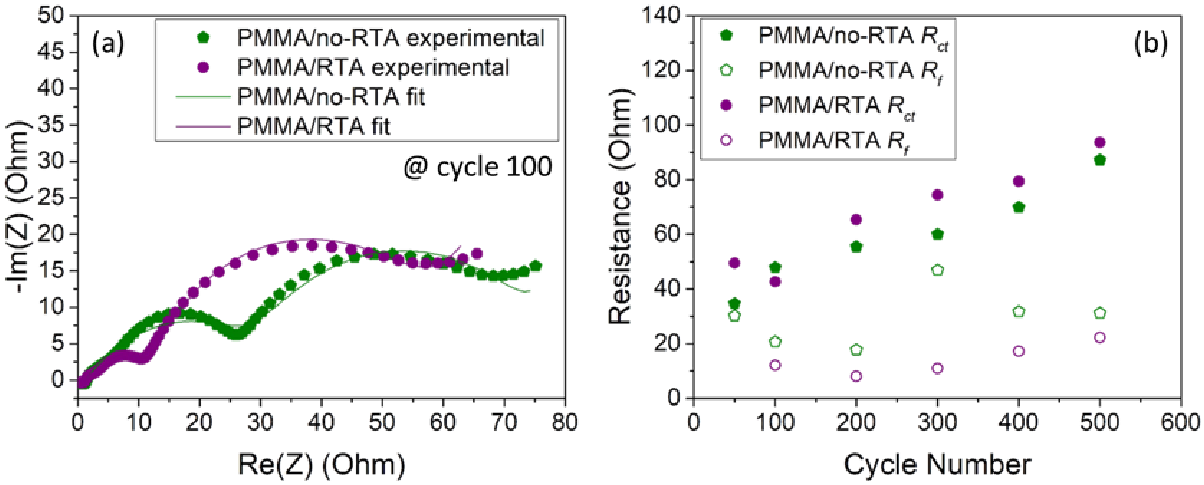

Figure S2.18. (a) Nyquist plots of PMMA/no-RTA (green hexagon) and PMMA/RTA (purple circle, experimental data is shown by the symbol and the fit is shown by the solid line. (b) Evolution of the charge transfer resistance (R_{ct}, filled symbol) and surface film resistance (R_f, open symbol) with cycling from 50-500 cycles.

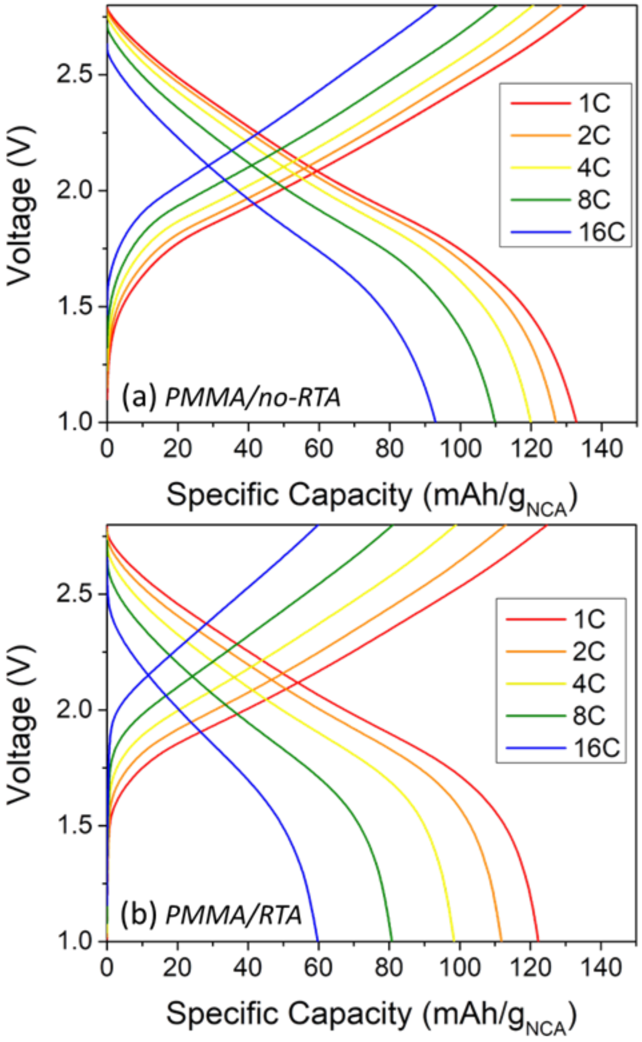

Figure S2.19. Galvanostatic charge-discharge curves for the full-cells of PMMA/no-RTA (a) and PMMA/RTA (b) with Nb_2O_5/rGO as the anode at various C-rates.

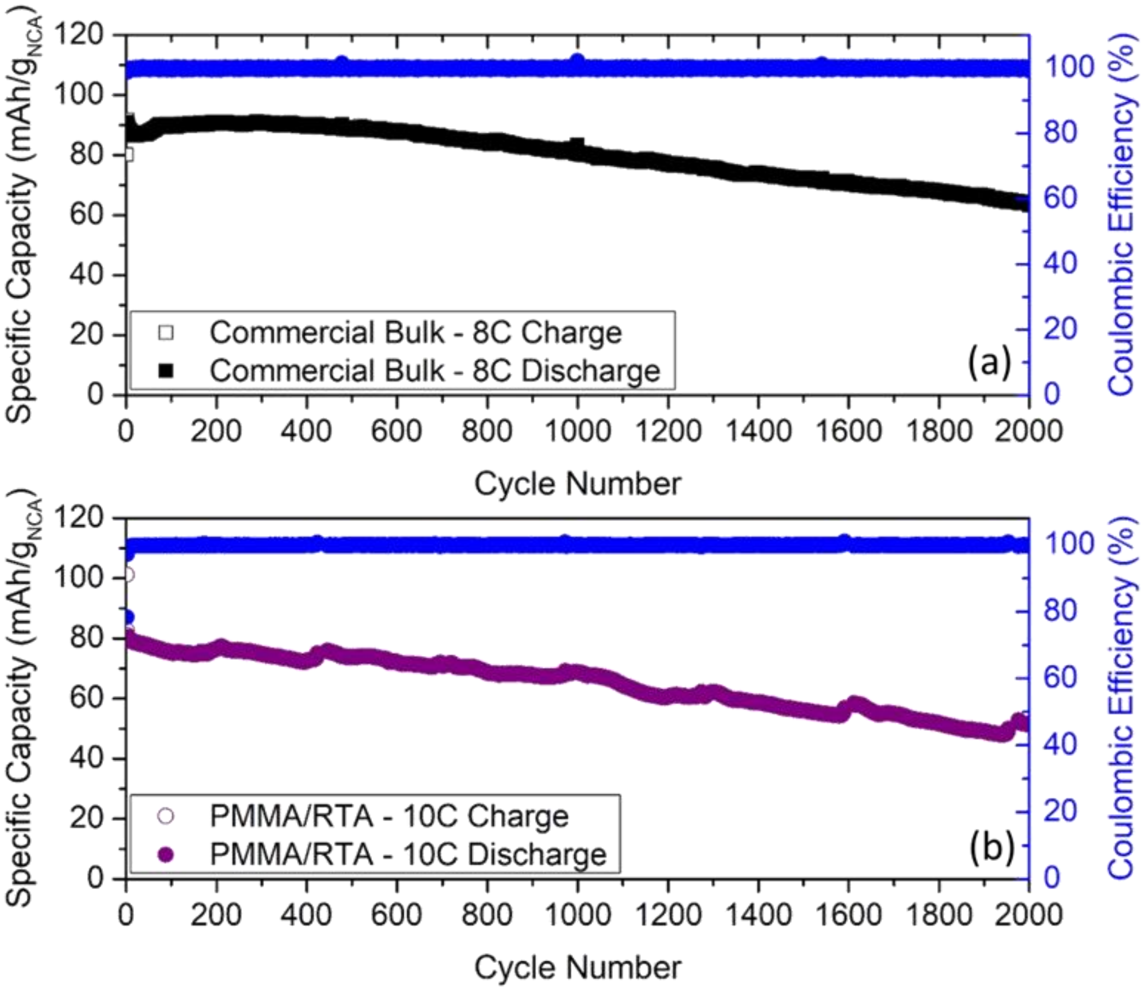

Figure S2.20. Long-term electrochemical cycle performance of full-cell commercial bulk NCA at 8C (a) and PMMA/RTA NCA at 10C (b) for 2000 cycles, cycled from 1.0-2.8 V. The specific capacity on charge is shown with open symbols (commercial bulk = black square, PMMA/RTA = purple circle), the specific capacity on discharge is shown with filled symbols, and the columbic efficiency is shown blue symbols in both cases, using the y-axis on the right.

2.5 References

(1) Neaimeh, M.; Salisbury, S. D.; Hill, G. A.; Blythe, P. T.; Scoffield, D. R.; Francfort, J. E. Analysing the Usage and Evidencing the Importance of Fast Chargers for the Adoption of Battery Electric Vehicles. *Energy Policy* **2017**, *108*, 474–486.

https://doi.org/10.1016/j.enpol.2017.06.033.

(2) Coffman, M.; Bernstein, P.; Wee, S. Electric Vehicles Revisited: A Review of Factors That Affect Adoption. *Transp. Rev.* **2017**, *37* (1), 79–93. https://doi.org/10.1080/01441647.2016.1217282.

(3) Zhang, L. L.; Zhao, X. S. Carbon-Based Materials as Supercapacitor Electrodes. *Chem. Soc. Rev.* **2009**, *38* (9), 2520–2531. https://doi.org/10.1039/b813846j.

(4) Horn, M.; MacLeod, J.; Liu, M.; Webb, J.; Motta, N. Supercapacitors: A New Source of Power for Electric Cars? *Econ. Anal. Policy* **2019**, *61*, 93–103. https://doi.org/10.1016/j.eap.2018.08.003.

(5) Zhu, C.; Lu, R.; Tian, L.; Wang, Q. The Development of an Electric Bus with Super-Capacitors as Unique Energy Storage. *2006 IEEE Veh. Power Propuls. Conf.* **2006**, 6–10.

(6) Khalaf, M. M.; Ibrahimov, H. G.; Ismailov, E. H.; Mai Mostafa Khalaf, H. G. I. and E. H. I. Nanostructured Materials: Importance, Synthesis and Characterization - A Review. *Chem. J.* **2012**, *2* (3), 118–125.

(7) Wang, T.; Sel, O.; Djerdj, I.; Smarsly, B. Preparation of a Large Mesoporous CeO_2 with Crystalline Walls Using PMMA Colloidal Crystal Templates. *Colloid Polym. Sci.* **2006**, *285*, 1–9. https://doi.org/10.1007/s00396-006-1526-3.

(8) Yano, K.; Nandwana, V.; Poudyal, N.; Rong, C. B.; Liu, J. P. Rapid Thermal Annealing of FePt Nanoparticles. *J. Appl. Phys.* **2008**, *104* (1), 013918-1-013918–4. https://doi.org/10.1063/1.2953078.

(9) Okubo, M.; Hosono, E.; Kim, J.; Enomoto, M.; Kojima, N.; Kudo, T.; Zhou, H.; Honma, I. Nanosize Effect on High-Rate Li-Ion Intercalation in $LiCoO_2$ Electrode. *J. Am. Chem. Soc.* **2007**, *129* (23), 7444–7452. https://doi.org/10.1021/ja0681927.

(10) Kim, H.-S.; Cook, J. B.; Tolbert, S. H.; Dunn, B. The Development of Pseudocapacitive Properties in Nanosized-MoO_2. *J. Electrochem. Soc.* **2015**, *162* (5), A5083–A5090. https://doi.org/10.1149/2.0141505jes.

(11) Zhu, Y.; Ji, X.; Cheng, S.; Chern, Z. Y.; Jia, J.; Yang, L.; Luo, H.; Yu, J.; Peng, X.; Wang, J.; Zhou, W.; Liu, M. Fast Energy Storage in Two-Dimensional MoO_2 Enabled by Uniform Oriented Tunnels. *ACS Nano* **2019**, *13* (8), 9091–9099. https://doi.org/10.1021/acsnano.9b03324.

(12) Yang, L. C.; Sun, W.; Zhong, Z. W.; Liu, J. W.; Gao, Q. S.; Hu, R. Z.; Zhu, M. Hierarchical MoO_2/N-Doped Carbon Heteronanowires with High Rate and Improved Long-Term Performance for Lithium-Ion Batteries. *J. Power Sources* **2016**, *306*, 78–84. https://doi.org/10.1016/j.jpowsour.2015.11.073.

(13) Cook, J. B.; Kim, H. S.; Yan, Y.; Ko, J. S.; Robbennolt, S.; Dunn, B.; Tolbert, S. H. Mesoporous MoS_2 as a Transition Metal Dichalcogenide Exhibiting Pseudocapacitive Li and Na-Ion Charge Storage. *Adv. Energy Mater.* **2016**, *6* (9), 1–12. https://doi.org/10.1002/aenm.201501937.

(14) Luo, S.; Xu, L.; Li, J.; Yang, W.; Liu, M.; Ma, L. Facile Synthesis of MoS_2 Hierarchical Nanostructures as Electrodes for Capacitor with Enhanced Pseudocapacitive Property. *Nano* **2020**, *15* (1), 2050011. https://doi.org/10.1142/S1793292020500113.

(15) Mahmood, Q.; Park, S. K.; Kwon, K. D.; Chang, S. J.; Hong, J. Y.; Shen, G.; Jung, Y. M.; Park, T. J.; Khang, S. W.; Kim, W. S.; Kong, J.; Park, H. S. Transition from Diffusion-Controlled Intercalation into Extrinsically Pseudocapacitive Charge Storage of MoS_2 by Nanoscale Heterostructuring. *Adv. Energy Mater.* **2016**, *6* (1), 1501115. https://doi.org/10.1002/aenm.201501115.

(16) Wang, J.; Polleux, J.; Lim, J.; Dunn, B. Pseudocapacitive Contributions to Electrochemical Energy Storage in TiO_2 (Anatase) Nanoparticles. *J. Phys. Chem. C* **2007**, *111* (40), 14925–14931. https://doi.org/10.1021/jp074464w.

(17) Luo, H.; Chen, Y.; Huang, J.; Chen, Z.; Xia, X.; Li, J.; Liu, H. 3.3 Nm-Sized TiO2/Carbon Hybrid Spheres Endowed with Pseudocapacitance-Dominated Superhigh-Rate Li-Ion and Na-Ion Storage. *Nanoscale* **2020**, *12* (13), 7366–7375. https://doi.org/10.1039/c9nr10750a.

(18) Lindström, H.; Södergren, S.; Solbrand, A.; Rensmo, H.; Hjelm, J.; Hagfeldt, A.; Lindquist, S.-E. Li^+ Ion Insertion in TiO_2 (Anatase). 2. Voltammetry on Nanoporous Films. *J. Phys. Chem. B* **1997**, *101* (39), 7717–7722. https://doi.org/10.1021/jp970490q.

(19) Cook, J. B.; Lin, T. C.; Kim, H. S.; Siordia, A.; Dunn, B. S.; Tolbert, S. H. Suppression of Electrochemically Driven Phase Transitions in Nanostructured MoS_2 Pseudocapacitors Probed Using Operando X-Ray Diffraction. *ACS Nano* **2019**, *13* (2), 1223–1231. https://doi.org/10.1021/acsnano.8b06381.

(20) Augustyn, V.; Simon, P.; Dunn, B. Pseudocapacitive Oxide Materials for High-Rate Electrochemical Energy Storage. *Energy Environ. Sci.* **2014**, *7* (5), 1597–1614. https://doi.org/10.1039/c3ee44164d.

(21) Choi, C.; Ashby, D. S.; Butts, D. M.; DeBlock, R. H.; Wei, Q.; Lau, J.; Dunn, B. Achieving High Energy Density and High Power Density with Pseudocapacitive Materials. *Nat. Rev. Mater.* **2020**, *5*, 5–19. https://doi.org/10.1038/s41578-019-0142-z.

(22) Liu, T.-C.; Pell, W. G.; Conway, B. E.; Roberson, S. L. Behavior of Molybdenum Nitrides as Materials for Electrochemical Capacitors. *J. Electrochem. Soc.* **1998**, *145* (6), 1882–188. https://doi.org/10.1149/1.1838571.

(23) Ardizzone, S.; Fregonara, G.; Trasatti, S. “Inner” and “Outer” Active Surface of RuO_2

Electrodes. *Electrochim. Acta* **1990**, *35* (1), 263–267. https://doi.org/10.1016/0013-4686(90)85068-X.

(24) Conway, B. E. Transition from "Supercapacitor" to "Battery" Behavior in Electrochemical Energy Storage. *J. Electrochem. Soc.* **1991**, *138* (6), 1539–1548. https://doi.org/10.1149/1.2085829.

(25) Lesel, B. K.; Cook, J. B.; Yan, Y.; Lin, T. C.; Tolbert, S. H. Using Nanoscale Domain Size to Control Charge Storage Kinetics in Pseudocapacitive Nanoporous $LiMn_2O_4$ Powders. *ACS Energy Lett.* **2017**, *2* (10), 2293–2298. https://doi.org/10.1021/acsenergylett.7b00634.

(26) Okubo, M.; Mizuno, Y.; Yamada, H.; Kim, J.; Hosono, E.; Zhou, H.; Kudo, T.; Honma, I. Fast Li-Ion Insertion into Nanosized $LiMn_2O_4$ without Domain Boundaries. *ACS Nano* **2010**, *4* (2), 741–752. https://doi.org/10.1021/nn9012065.

(27) Xia, H.; Luo, Z.; Xie, J. Nanostructured $LiMn_2O_4$ and Their Composites as High-Performance Cathodes for Lithium-Ion Batteries. *Prog. Nat. Sci. Mater. Int.* **2012**, *22* (6), 572–584. https://doi.org/10.1016/j.pnsc.2012.11.014.

(28) Zhu, X.; Zhan, H.; Liu, H.; Zhou, Y. Synthesis and Characterization of $LiNi_{0.95-x}Co_xAl_{0.05}O_2$ for Lithium-Ion Batteries. *Rare Met.* **2006**, *25* (4), 303–308. https://doi.org/10.1016/S1001-0521(06)60058-2.

(29) Wang, M.; Navrotsky, A. Enthalpy of Formation of $LiNiO_2$, $LiCoO_2$ and Their Solid Solution, $LiNi_{1-x}Co_xO_2$. *Solid State Ionics* **2004**, *166* (1–2), 167–173. https://doi.org/10.1016/j.ssi.2003.11.004.

(30) Trease, N. M.; Seymour, I. D.; Radin, M. D.; Liu, H.; Liu, H.; Hy, S.; Chernova, N.; Parikh, P.; Devaraj, A.; Wiaderek, K. M.; Chupas, P. J.; Chapman, K. W.; Whittingham, M. S.; Meng, Y. S.; Van Der Van, A.; Grey, C. P. Identifying the Distribution of Al^{3+} in

$LiNi_{0.8}Co_{0.15}Al_{0.05}O_2$. *Chem. Mater.* **2016**, *28* (22), 8170–8180. https://doi.org/10.1021/acs.chemmater.6b02797.

(31) Liu, W.; Oh, P.; Liu, X.; Lee, M. J.; Cho, W.; Chae, S.; Kim, Y.; Cho, J. Nickel-Rich Layered Lithium Transition-Metal Oxide for High-Energy Lithium-Ion Batteries. *Angew. Chemie - Int. Ed.* **2015**, *54* (15), 4440–4457. https://doi.org/10.1002/anie.201409262.

(32) Delmas, C.; Pérès, J. P.; Rougier, A.; Demourgues, A.; Weill, F.; Chadwick, A. V.; Broussely, M.; Perton, F.; Biensan, P.; Willmann, P. On the Behavior of the Li_xNiO_2 System: An Electrochemical and Structural Overview. *J. Power Sources* **1997**, *68* (1), 120–125. https://doi.org/10.1016/S0378-7753(97)02664-5.

(33) Ohzuku, T.; Ueda, A.; Nagayama, M. Electrochemistry and Structural Chemistry of $LiNiO_2$ (R3m) for 4 Volt Secondary Lithium Cells. *J. Electrochem. Soc.* **1993**, *140* (7), 1862–1870. https://doi.org/10.1149/1.2220730.

(34) Ohzuku, T.; Ueda, A.; Nagayama, M.; Iwakoshi, Y.; Komori, H. Comparative Study of $LiCoO_2$, $LiNi_{1/2}Co_{1/2}O_2$ and $LiNiO_2$ for 4 Volt Secondary Lithium Cells. *Electrochim. Acta* **1993**, *38* (9), 1159–1167. https://doi.org/10.1016/0013-4686(93)80046-3.

(35) Cho, D.-H.; Jo, C.-H.; Cho, W.; Kim, Y.-J.; Yashiro, H.; Sun, Y.-K.; Myung, S.-T. Effect of Residual Lithium Compounds on Layer Ni-Rich $Li[Ni_{0.7}Mn_{0.3}]O_2$. *J. Electrochem. Soc.* **2014**, *161* (6), A920–A926. https://doi.org/10.1149/2.042406jes.

(36) Zhang, H.; May, B. M.; Serrano-Sevillano, J.; Casas-Cabanas, M.; Cabana, J.; Wang, C.; Zhou, G. Facet-Dependent Rock-Salt Reconstruction on the Surface of Layered Oxide Cathodes. *Chem. Mater.* **2018**, *30* (3), 692–699. https://doi.org/10.1021/acs.chemmater.7b03901.

(37) Liu, H.; Yang, Y.; Zhang, J. Investigation and Improvement on the Storage Property of

$LiNi_{0.8}Co_{0.2}O_2$ as a Cathode Material for Lithium-Ion Batteries. *J. Power Sources* **2006**, *162* (1), 644–650. https://doi.org/10.1016/j.jpowsour.2006.07.028.

(38) Lai, C.-H.; Ashby, D. S.; Lin, T. C.; Lau, J.; Dawson, A.; Tolbert, S. H.; Dunn, B. S. Application of Poly(3-Hexylthiophene-2,5-Diyl) as a Protective Coating for High Rate Cathode Materials. *Chem. Mater.* **2018**, *30* (8), 2589–2599. https://doi.org/10.1021/acs.chemmater.7b05116.

(39) Kim, J. M.; Park, H. S.; Park, J. H.; Kim, T. H.; Song, H. K.; Lee, S. Y. Conducting Polymer-Skinned Electroactive Materials of Lithium-Ion Batteries: Ready for Monocomponent Electrodes without Additional Binders and Conductive Agents. *ACS Appl. Mater. Interfaces* **2014**, *6* (15), 12789–12797. https://doi.org/10.1021/am502736m.

(40) Huang, Y.; Goodenough, J. B. High-Rate $LiFePO_4$ Lithium Rechargeable Battery Promoted by Electrochemically Active Polymers. *Chem. Mater.* **2008**, *20* (23), 7237–7241. https://doi.org/10.1021/cm8012304.

(41) Berger, P. R.; Kim, M. Polymer Solar Cells: P3HT:PCBM and Beyond. *J. Renew. Sustain. Energy* **2018**, *10* (1), 013508. https://doi.org/10.1063/1.5012992.

(42) Chen, Y.; Li, P.; Zhao, S.; Zhuang, Y.; Zhao, S.; Zhou, Q.; Zheng, J. Influence of Integrated Microstructure on the Performance of $LiNi_{0.8}Co_{0.15}Al_{0.05}O_2$ as a Cathodic Material for Lithium Ion Batteries. *RSC Adv.* **2017**, *7* (46), 29233–29239. https://doi.org/10.1039/c7ra04206j.

(43) Asakura, R.; Novák, P.; Robert, R. Colloidal Synthesis and Electrochemistry of Surface Coated Nano-$LiNi_{0.80}Co_{0.15}Al_{0.05}O_2$. *J. Electrochem. Soc.* **2017**, *164* (12), A2617–A2624. https://doi.org/10.1149/2.1431712jes.

(44) Wang, Q.; Zhang, L.; Zhao, P.; Du, Z. Facile Synthesis of a High-Capacity

$LiNi_{0.8}Co_{0.15}Al_{0.05}O_2$ Nanoplate Cathode with a {010} Orientation for Lithium-Ion Batteries. *Int. J. Electrochem. Sci.* **2018**, *13* (11), 10382–10389. https://doi.org/10.20964/2018.11.15.

(45) Wang, Z.; Liu, H.; Wu, J.; Lau, W. M.; Mei, J.; Liu, H.; Liu, G. Hierarchical $LiNi_{0.8}Co_{0.15}Al_{0.05}O_2$ Plates with Exposed {010} Active Planes as a High Performance Cathode Material for Li-Ion Batteries. *RSC Adv.* **2016**, *6* (38), 32365–32369. https://doi.org/10.1039/c6ra02694j.

(46) Wu, Y.; Cao, T.; Wang, R.; Meng, F.; Zhang, J.; Cao, C. A General Strategy for the Synthesis of Two-Dimensional Holey Nanosheets as Cathodes for Superior Energy Storage. *J. Mater. Chem. A* **2018**, *6* (18), 8374–8381. https://doi.org/10.1039/c8ta02327a.

(47) Zou, D.; Ma, S.; Guan, R.; Park, M.; Sun, L.; Aklonis, J. J.; Salovey, R. Model Filled Polymers. V. Synthesis of Crosslinked Monodisperse Polymethacrylate Beads. *J. Polym. Sci. Part A Polym. Chem.* **1992**, *30* (1), 137–144. https://doi.org/10.1002/pola.1992.080300118.

(48) Liu, H.; Liu, H.; Lapidus, S. H.; Meng, Y. S.; Chupas, P. J.; Chapman, K. W. Sensitivity and Limitations of Structures from X-Ray and Neutron-Based Diffraction Analyses of Transition Metal Oxide Lithium-Battery Electrodes. *J. Electrochem. Soc.* **2017**, *164* (9), A1802–A1811. https://doi.org/10.1149/2.0271709jes.

(49) Sivaprakash, S.; Majumder, S. B.; Nieto, S.; Katiyar, R. S. Crystal Chemistry Modification of Lithium Nickel Cobalt Oxide Cathodes for Lithium Ion Rechargeable Batteries. *J. Power Sources* **2007**, *170* (2), 433–440. https://doi.org/10.1016/j.jpowsour.2007.04.029.

(50) Guilmard, M.; Pouillerie, C.; Croguennec, L.; Delmas, C. Structural and Electrochemical Properties of $LiNi_{0.70}Co_{0.15}Al_{0.15}O_2$. *Solid State Ionics* **2003**, *160* (1–2), 39–50.

https://doi.org/10.1016/S0167-2738(03)00106-1.

(51) Li, X.; Ge, W.; Wang, H.; Yan, X.; Deng, B.; Chen, T.; Qu, M. Enhancing Cycle Stability and Storage Property of $LiNi_{0.8}Co_{0.15}Al_{0.05}O_2$ by Using Fast Cooling Method. *Electrochim. Acta* **2017**, *227* (10), 225–234. https://doi.org/10.1016/j.electacta.2016.12.138.

(52) Zeng, W. R.; Li, S. F.; Chow, W. K. Review on Chemical Reactions of Burning Poly(Methyl Methacrylate) PMMA. *J. Fire Sci.* **2002**, *20* (5), 401–433. https://doi.org/10.1106/073490402031482.

(53) Odziomek, M.; Bahri, M.; Boissiere, C.; Sanchez, C.; Lassalle-Kaiser, B.; Zitolo, A.; Ersen, O.; Nowak, S.; Tard, C.; Giraud, M.; Faustini, M.; Peron, J. Aerosol Synthesis of Thermally Stable Porous Noble Metals and Alloys by Using Bi-Functional Templates. *Mater. Horizons* **2020**, *7* (2), 541–550. https://doi.org/10.1039/c9mh01408j.

(54) Grenier, A.; Liu, H.; Wiaderek, K. M.; Lebens-Higgins, Z. W.; Borkiewicz, O. J.; Piper, L. F. J.; Chupas, P. J.; Chapman, K. W. Reaction Heterogeneity in $LiNi_{0.8}Co_{0.15}Al_{0.05}O_2$ Induced by Surface Layer. *Chem. Mater.* **2017**, *29* (17), 7345–7352. https://doi.org/10.1021/acs.chemmater.7b02236.

(55) Lu, Y. C.; Mansour, A. N.; Yabuuchi, N.; Shao-Horn, Y. Probing the Origin of Enhanced Stability of "$AlPO_4$" Nanoparticle Coated $LiCoO_2$ during Cycling to High Voltages: Combined XRD and XPS Studies. *Chem. Mater.* **2009**, *21* (19), 4408–4424. https://doi.org/10.1021/cm900862v.

(56) Yang, X.; Chen, J.; Zheng, Q.; Tu, W.; Xing, L.; Liao, Y.; Xu, M.; Huang, Q.; Cao, G.; Li, W. Mechanism of Cycling Degradation and Strategy to Stabilize a Nickel-Rich Cathode. *J. Mater. Chem. A* **2018**, *6* (33), 16149–16163. https://doi.org/10.1039/c8ta03041c.

(57) Gonçalves, R.; Pereira, E. C.; Marchesi, L. F. The Overoxidation of Poly(3-

Hexylthiophene) (P3HT) Thin Film: CV and EIS Measurements. *Int. J. Electrochem. Sci.* **2017**, *12* (3), 1983–1991. https://doi.org/10.20964/2017.03.44.

(58) Zhou, H.; Yang, Z.; Xiao, D.; Xiao, K.; Li, J. An Electrolyte to Improve the Deep Charge–Discharge Performance of $LiNi_{0.8}Co_{0.15}Al_{0.05}O_2$ Cathode. *J. Mater. Sci. Mater. Electron.* **2018**, *29* (8), 6648–6659. https://doi.org/10.1007/s10854-018-8650-y.

(59) Augustyn, V.; Come, J.; Lowe, M. A.; Kim, J. W.; Taberna, P.-L.; Tolbert, S. H.; Abruña, H. D.; Simon, P.; Dunn, B. High-Rate Electrochemical Energy Storage through Li^+ Intercalation Pseudocapacitance. *Nat. Mater.* **2013**, *12*, 518–522. https://doi.org/10.1038/nmat3601.

(60) Ryu, J.-H. Polarization Behavior of $Li_4Ti_5O_{12}$ Negative Electrode for Lithium-Ion Batteries. *J. Electrochem. Sci. Technol.* **2011**, *2* (3), 136–142. https://doi.org/10.5229/jecst.2011.2.3.136.

(61) Makimura, Y.; Sasaki, T.; Nonaka, T.; Nishimura, Y. F.; Uyama, T.; Okuda, C.; Itou, Y.; Takeuchi, Y. Factors Affecting Cycling Life of $LiNi_{0.8}Co_{0.15}Al_{0.05}O_2$ for Lithium-Ion Batteries. *J. Mater. Chem. A* **2016**, *4* (21), 8350–8358. https://doi.org/10.1039/C6TA01251E.

(62) Park, B. C.; Kim, H. B.; Bang, H. J.; Prakash, J.; Sun, Y. K. Improvement of Electrochemical Performance of $Li[Ni_{0.8}Co_{0.15}Al_{0.05}]O_2$ Cathode Materials by AlF_3 Coating at Various Temperatures. *Ind. Eng. Chem. Res.* **2008**, *47* (11), 3876–3882. https://doi.org/10.1021/ie0715308.

(63) Chen, C. F.; Mukherjee, P. P. Probing the Morphological Influence on Solid Electrolyte Interphase and Impedance Response in Intercalation Electrodes. *Phys. Chem. Chem. Phys.* **2015**, *17* (15), 9812–9827. https://doi.org/10.1039/c4cp05758a.

(64) Lai, C. H.; Ashby, D.; Moz, M.; Gogotsi, Y.; Pilon, L.; Dunn, B. Designing Pseudocapacitance for Nb_2O_5/Carbide-Derived Carbon Electrodes and Hybrid Devices. *Langmuir* **2017**, *33* (37), 9407–9415. https://doi.org/10.1021/acs.langmuir.7b01110.

(65) Lubimtsev, A. A.; Kent, P. R. C.; Sumpter, B. G.; Ganesh, P. Understanding the Origin of High-Rate Intercalation Pseudocapacitance in Nb_2O_5 Crystals. *J. Mater. Chem. A* **2013**, *1* (47), 14951–14956. https://doi.org/10.1039/c3ta13316h.

(66) Jiang, S.; Dong, S.; Wu, L.; Chen, Z.; Shen, L.; Zhang, X. Pseudocapacitive T-Nb_2O_5/N-Doped Carbon Nanosheets Anode Enable High Performance Lithium-Ion Capacitors. *J. Electroanal. Chem.* **2019**, *842*, 82–88. https://doi.org/10.1016/j.jelechem.2019.04.042.

(67) He, G.; Pan, Q.; Rempel, G. L. Synthesis of Poly(Methyl Methacrylate) Nanosize Particles by Differential Microemulsion Polymerization. *Macromol. Rapid Commun.* **2003**, *24* (9), 585–588. https://doi.org/10.1002/marc.200390089.

(68) Thommes, M.; Kaneko, K.; Neimark, A. V.; Olivier, J. P.; Rodriguez-Reinoso, F.; Rouquerol, J.; Sing, K. S. W. Physisorption of Gases, with Special Reference to the Evaluation of Surface Area and Pore Size Distribution (IUPAC Technical Report). *Pure Appl. Chem.* **2015**, *87* (9–10), 1051–1069. https://doi.org/10.1515/pac-2014-1117.

(69) You, Y.; Celio, H.; Li, J.; Dolocan, A.; Manthiram, A. Modified High-Nickel Cathodes with Stable Surface Chemistry Against Ambient Air for Lithium-Ion Batteries. *Angew. Chemie - Int. Ed.* **2018**, *57* (22), 6480–6485. https://doi.org/10.1002/anie.201801533.

CHAPTER 3

Scalable Synthesis of Templated Nanoporous $LiNi_{0.80}Co_{0.15}Al_{0.05}O_2$ (NCA) for Fast-Charging Lithium-Ion Batteries

3.1 Introduction

High-capacity and fast charging/discharging batteries have many commercial applications, especially in personal electronics and electric vehicles. One way to achieve both high-capacity and fast charging is through pseudocapacitive charge storage.[1–3] Pseudocapacitive materials have been classified as intrinsically or extrinsically pseudocapacitive. Intrinsic pseudocapacitive materials, such as $RuO_2 \cdot xH_2O$[4–6] and T-Nb_2O_5,[7–9] lack first-order, discontinuous phase transitions and exhibit fast charging at all particle sizes. Extrinsic materials exhibit properties of traditional battery materials at larger particle sizes and pseudocapacitive properties at small particle sizes. This transition from battery-like to pseudocapacitive behavior occurs with the suppression of slow, discontinuous phase transitions and the shortening of lithium-ion diffusion lengths as particle sizes of these materials are decreased. One method to decrease the particle sizes of these materials is through nanostructuring. Some examples of extrinsic pseudocapacitive materials include MoO_2,[10–12] MoS_2,[13–16] and $LiMn_2O_4$.[17–20]

While both a fast-charging anode and cathode material are required for a fast-charging device, the two most well-known high-voltage (>3 V vs. Li/Li^+) extrinsic pseudocapacitive materials, $LiCoO_2$ and $LiMn_2O_4$, exhibit decreased capacity when nanostructured.[17,21] Because of this reduced capacity, they are not ideal for use in commercial fast-charging devices. $LiNi_{0.80}Co_{0.15}Al_{0.05}O_2$ (NCA), a high-voltage layered transition metal oxide, already satisfies one of the common requirements of pseudocapacitance in the bulk, which is suppression of discontinuous first-order phase transitions. The parent structure of NCA, $LiNiO_2$, undergoes three first-order phase transitions upon charge/discharge,[22] but when $LiNiO_2$ is doped with cobalt and aluminum to form NCA, these discontinuous phase transitions are suppressed and replaced by second-order or solid-solution phase behavior.[22,23] Thus, fast-charging behavior can potentially be induced in NCA by only moderately decreasing particle sizes. Indeed, we have previously observed increased charge/discharge kinetics in nanostructured NCA templated using preformed poly(methyl methacrylate) (PMMA) colloids.[24]

Cobalt and aluminum doping also help to decrease cation mixing, which reduces lithium diffusion kinetics in nickel-rich layered transition metal oxide materials. Cation mixing is the exchange of Ni^{2+} and Li^{+} ions within the layered structured, due to the similar ionic sizes of Ni^{2+} and Li^{+}. Because most low cost nickel starting reagents are in the 2+ oxidation state, and because of the increased stability of Ni^{2+} at high temperatures, it is difficult to fully oxide Ni^{2+} to Ni^{3+} during synthesis.[25] It has been proposed that upon charging, the Ni^{2+} ions in the lithium layer oxidize to Ni^{3+}, which leads to the local collapse of the lithium interlayer distance due to the smaller ionic size of Ni^{3+}, preventing the complete reintercalation of lithium-ions upon discharge.[26] The shrinkage of the interlayer spacing also hinders the diffusion of lithium during charge/discharge, which is detrimental to electrochemical performance, especially at fast rates.[27] Fortunately, the cobalt and aluminum dopants in NCA help stabilize the layered structure and lessen the degree of cation mixing by decreasing the Ni-Ni intralayer spacing, thereby increasing the difficulty of Ni migration,[28,29] but high temperatures are still needed during synthesis to produce materials with low levels of cation mixing.

Besides cation mixing, a problem for NCA production and storage is that exposure to carbon dioxide and water in the air is detrimental to electrochemical performance,[30–33] this is especially true for NCA with decreased particle sizes or nanoporous materials. Carbon dioxide and water react with excess lithium species on the surface of NCA particles to form an insulating layer of Li_2CO_3.[30] Additionally, it is proposed that the instability of Ni^{3+} near the surface of the particles results in reduction to Ni^{2+}, which leads to the formation of both NiO-like structures and Li_2CO_3 on the surface.[33] Previously we demonstrated that exposure to ambient conditions and the formation of these insulating Li_2CO_3 and NiO structures led to decreased capacity and rate capability at fast-rates for nanostructured NCA.[24] As a result, nanoporous NCA is best processed under inert conditions.

To enhance fast-charging, NCA must be nanostructured to decrease lithium-ion diffusion distances without increasing charge transfer resistance from insulating surface layers. There are many methods for nanostructuring materials such as hydrothermal synthesis, freeze-drying, or template-directed synthesis.[34] Template-directed sol-gel synthesis is a relatively simple method to obtain nanostructured and nanoporous materials.[35,36] Previously, we synthesized nanostructured NCA by combining a sol-gel synthesis and colloidal PMMA as a template.[24] Because NCA requires high temperatures for crystallization, which can coarsen nanoporous architectures, different heating methods were used to control particle sizes. A method analogous to rapid thermal annealing (RTA) resulted in small particle sizes and a conventional annealing (CA) method resulted in medium particle sizes, when compared to the primary particle sizes of bulk NCA. While RTA led to the smallest particle sizes, and therefore the shortest lithium-ion diffusion lengths, the short oxidation time at high temperatures produced a reduced nickel surface because of the fast combustion of the PMMA template, and resulted in poorer electrochemical performance.[24,37] The PMMA colloids were also produced in small batches using kinetically controlled methods.

Therefore, it is desirable to nanostructure NCA using a more scalable template that will not form a reducing atmosphere upon calcination. Here, Pluronic block-copolymers (F127 or F108) were used as templates to synthesize nanostructured NCA. The family of Pluronics are triblock copolymers of poly(ethylene oxide)$_m$-*b*-poly(propylene oxide)$_n$-*b*-poly(ethylene oxide)$_m$ (PEO$_m$-*b*-PPO$_n$-*b*-PEO$_m$) (for F127 m = 100, n = 65/for F108 m = 133, n = 50). F127 and F108 form micelles in dilute aqueous solutions because of the poor solubility of the PPO block in water.[38] Additionally, F127 and F108 are oxygen rich and thus should not form a reducing atmosphere upon calcination.[39] Templating with F127 and F108 alone results in structures with small pore sizes (~8 nm).[40,41] Here, a larger template is needed for the synthesis of nanostructured NCA because the high temperatures required for the crystallization of NCA (> 700 °C) result in larger grain sizes and would destroy the nanopores formed from a small template. Fortunately, the addition of pure PPO homopolymer with low molecular weights to Pluronics has been demonstrated to increase micelle/pore size in nanoporous silica materials.[42,43] The PPO homopolymer increases the size of the Pluronic polymer micelles by incorporating into the hydrophobic PPO core.[43] Similarly, when pure PEO homopolymers are added to Pluronic surfactants, the PEO homopolymers associate with the outer PEO shell of the Pluronic polymers to increase micelle/pore size.[44] Thus, the use of PPO or PEO homopolymers in combination with F127 or F108 templates for NCA should allow for the synthesis of porous nanostructured NCA without significant reduction of the surface-nickel oxidation state.

Notably, F127, F108, PPO and PEO are all low-cost and readily commercially available. This is important because low-cost and abundant materials are necessary for scaling-up syntheses for commercialization.[45] Other polymer templating materials, such as colloidal PMMA and polystyrene need to be synthesized by emulsion polymerization to obtain pure and monodisperse materials.[46,47] While this does allow for more control over the template size, it unfortunately adds processing steps and costs. The use of Pluronic surfactants plus homopolymers only allows for modest control over the template size, but can easily be incorporated into the synthesis of nanostructured NCA without additional processing steps. Therefore, the use of Pluronic polymer templates for nanostructured NCA will allow for ease of scale-up, and could help make nanostructured NCA more commercially viable.

In this paper we synthesized two different sizes of nanostructured NCA using the combination of low cost Pluronic surfactants and homopolymer templates. The templates were characterized using dynamic light scattering (DLS). X-ray diffraction (XRD) and scanning electron microscopy (SEM) were used to analyze the structure of the nanoporous NCA, and X-ray photoelectron spectroscopy (XPS) and transmission electron microscopy (TEM) were used to analyze the surface compositions of the air-sensitive nanostructured NCA materials. This characterization was complimented by a range of electrochemical analyses, such as galvanostatic rate capability, cyclic voltammetry based kinetic analyses, and electrochemical impedance spectroscopy (EIS), to determine the performance and charge storage properties of the materials. Lastly, to demonstrate the potential for practical devices, high mass loading nanostructured NCA cathode electrodes were paired with a fast-charging anode to assess the long-term performance of a practical full-cell device.

3.2 Experimental Methods

3.2.1 Materials

Lithium nitrate (98+%) and carbon nanofibers (CNF, DxL 100 nm x 20-200 μm) were purchased from Sigma. Nickel nitrate hexahydrate (99.9985%), aluminum nitrate nonahydrate (98%), PPO (MW = 400 g/mol), and tetrahydrofuran (THF, >99%) were purchased from Alfa

Aesar. Cobalt nitrate hexahydrate (99+%) and *o*-xylenes (99%, Extra Dry) were purchased from Acros Organics. Pluronic F127 ($PEO_{100}PPO_{65}PEO_{100}$ MW = 12600 g/mol) and Pluronic F108 ($PEO_{133}PPO_{50}PEO_{133}$ MW = 14600 g/mol) were purchased from BASF. PEO (MW = 8000 g/mol) was purchased from Aldrich. Multi-walled carbon nanotubes (MWCNT, >95%, OD: 5-15 nm) were purchased from US Research Nanomaterials Inc. Poly(3-hexylthioophene-2,5-diyl) (P3HT, 15000-30000 MW, 1.6-1.8 PDI, 89-94% regioregularity) was purchased from Rieke Metals. Commercial bulk NCA was purchased from Quallion Corporation.

3.2.2 Synthesis of scalable templated NCA precursor

Pluronic F127 or F108 were completely dissolved in 4 mL of water to form a 6.8 wt% solution of the Pluronic polymer. Once dissolved, 5 wt% (with respect to the Pluronic) of either PPO400 or PEO8000 was added to the solution and the solution was mixed for 1 hour. In a separate container nickel nitrate hexahydrate, cobalt nitrate hexahydrate, and aluminum nitrate nonahydrate were dissolved in 16 mL of water in stoichiometric amounts so that the total transition metal concentration (Ni+Co+Al) was 0.6 M. Additionally, 5% molar excess of lithium nitrate was dissolved in this solution. Once the salts were completely dissolved, the solution of pure homopolymers associated with Pluronic polymers was added to the salt solution. This combined solution was mixed for 3 hours before evaporation of the water at 80 °C overnight. The remaining powder was heated in a tube furnace under oxygen, first at 180 °C for 4 hours to remove any residual water, then the temperature was ramped to 450 °C at 1 °C/min, before being held at 450 °C for 2 hours to remove the polymer templates from the NCA precursor.

3.2.3 Calcination of templated NCA

The calcination of the porous NCA precursor is detailed in our previous report.[24] In short, the calcination method was used to control the NCA particle size. For small sized particles, a method analogous to rapid thermal annealing (RTA) was used where the NCA precursor was placed into an oven at 850 °C for 5 minutes, followed by a hold for 12 hours at constant temperature between 600 °C and 800 °C all under oxygen (with 700 °C being optimal for cation ordering). This synthesis is referred to here as nanoNCA-RTA. While, for medium sized particles, a conventional annealing (CA) method was used with a 1 hour ramp to 800 °C, followed by 2 hours at 800 °C all under oxygen, referred to here as nanoNCA-CA. All samples were cooled naturally to 350 °C and then transferred directly to a glovebox while hot, to minimize exposure to air.

3.2.4 Characterization

DLS experiments were performed using a Malvern Panalytical Zetasizer Nano ZSP. The Pluronic polymer or Pluronic/homopolymer solutions were diluted by a factor of 100 into deionized water. The measurements were performed at 25 °C with 3 consecutive measurements, and 13-18 runs per measurement. For THF annealing experiments, 0.2 mL of THF was added to 1 mL of the pure homopolymer associated with Pluronic polymer solutions, which was then heated, with stirring, at 30 °C for 4 hours to evaporate the THF.[48] DLS measurements were taken directly after the removal of THF using the same experimental parameters as above. SEM images were taken using a JOEL JSM-6700F field emission scanning electron microscope. Particle size distribution histograms were generated by measuring 150 particles (binned in 25 nm increments) with ImageJ from the SEM images. The histograms were fit with a log-normal distribution to find the peak in the particle size distribution. XRD was obtained using a Bruker D8 Discover Powder X-ray Diffractometer, a sample holder was used to ensure consistent sample height between samples. MAUD software was used to perform Rietveld refinement of the XRD patterns. For the NCA precursor a Micromeritics TriStar II 3020 porosimeter was used for the nitrogen porosimetry measurement. The adsorption isotherm was used to determine surface area of the precursor using the Brunauer-Emmett-Teller (BET) model and the volume weighted pore size distribution (PSD) using the Barrett-Joyner-Halenda (BJH) model with the Halsey equation and Faas correction. A Micromeritics ASAP 2020 Plus porosimeter was used for the nitrogen porosimetry measurements for the calcined NCA samples. For TEM, a FEI Technai G^2 TF20 High-Resolution EM, CryoEM, and CryoET was used at an accelerating voltage of 200 kV with a TIETZ F415MP 16 megapixel 4k x 4k CCD detector. Fast Fourier transform (FFT) of images was used to analyze lattice planes in the sample. The grids for imaging were prepared by dispersing the powdered samples in ethanol by ultra-sonication and then depositing on to carbon coated copper TEM grids. To minimize air exposure, the grids were prepared less than 30 minutes before TEM imaging. XPS was performed with a Kratos Axis Ultra DLD spectrometer with a monochromatic Al Kα source and a charge neutralizer filament was used to control charging. Samples were calibrated to advantageous carbon at 284.8 eV. For comparison of air-free and air-exposed NCA, a single sample was split in two: half of the sample was stored in an argon-atmosphere glovebox and the other half was kept in ambient air, for 1 week. An air-free sample transfer holder was used to transport samples directly from the glovebox to the XPS instrument chamber for air-free analysis. Argon ion etching was also performed in the XPS chamber using a 2x2 mm raster size, an acceleration voltage of 4 kV, and the samples were etched up to 2 minutes.

3.2.5 Electrochemical characterization

Electrodes were prepared in an argon-atmosphere glovebox with 90 wt% active material, 3 wt% MWCNT, 4 wt% CNF, 3 wt% P3HT in *o*-xylenes (15 wt% solution), and were cast as slurries on carbon-coated aluminum current collectors. The slurries were heated on a hotplate in the glovebox for 5 hours before being moved to the glovebox antechamber to dry under vacuum overnight. Still in the glovebox, 0.7 cm^2 electrodes were punched out of the slurry. Electrodes surrounding the electrode that was assembled into a coin cell were removed from the glovebox and weighed on a microbalance to calculate an average mass loading. Commercial bulk NCA slurries were cast in air, using the same compositions as above and dried in a vacuum oven at 120 °C overnight. Electrodes of NCA were assembled as half-cells against a Li anode in a CR2032 coin cell. The NCA active material mass loadings ranged from 1.3 – 2.6 mg/cm^2 for the electrodes. In the coin cell a Celgard 2400 separator was used with 1 M $LiPF_6$ in 1:1:1 EC:DMC:DEC (ethylene carbonate:dimethyl carbonate:diethyl carbonate) electrolyte. For galvanostatic cycling an Arbin Instruments BT2000 battery testing system was used, the cells were cycled from 2.7-4.2 V vs Li/Li$^+$ at various C-rates from C/5 to 64C. Cyclic voltammetry was performed with a BioLogic VSP potentiostat/galvanostat from 2.7-4.2 V vs Li/Li$^+$ at various scan rates from 0.1 – 10 mV/s. Electrochemical impedance spectroscopy (EIS) was performed with a BioLogic VSP potentiostat/galvanostat at open circuit voltage after cycling at 10C from 2.7-4.2 V vs Li/Li$^+$ with a frequency range of 100 mHz – 300 kHz and a potential amplitude of 10 mV.

Higher mass loading slurries of NCA-CA were also prepared with 90 wt% NCA-CA, 5 wt% Super P, and 5 wt% polyvinylidene fluoride (PVDF), these materials were mixed in a plastic container with zirconia beads for 24 hours to form a uniform slurry. The slurry was cast by doctor blading, followed by complete drying in a vacuum oven at 110 °C for another 24 hours. The high active mass loading NCA-CA electrodes (~10 mg/cm^2) were cycled in both half and full-cell configurations. In the full-cells the NCA cathode was paired with a high active mass loading anode (8.2 mg/cm^2) of Nb_2O_5-rGO (reduced graphene oxide) (provide by Battery Streak Inc.). The electrodes were assembled into CR2032 coin cells and were cycled galvanostatically from 2.7-4.3 V vs. Li/Li$^+$ in the half-cells and from 0.5-2.5 V in the full-cells. Half-cells were cycled at various

C-rates up to 16C. Full-cell were cycled for 2000 cycles, the cells were charged at 10C/2.5 V CCCV (constant-current/constant-voltage) with a 2C cut-off and were discharged at 5C.

3.3 Results and Discussion

3.3.1 Scalable template characterization

Pluronic F127 paired with PPO homopolymers and F108 paired with PEO homopolymers were used as templates in the synthesis of our nanostructured NCA. DLS was used to confirm the micelle size of the templates in aqueous solution. F127 and F108 alone had small micelle sizes of about 7 nm and 9 nm, respectively (Fig. 3.1a,b). Upon adding pure PPO homopolymer to F127, the micelle size stayed around 7 nm and larger (> 100 nm) aggregates formed, presumably made up of partially insoluble PPO (Fig. 3.1a). Upon addition of the PEO homopolymer to F108, the micelle size shrunk slightly to 7 nm (Fig. 3.1b). THF annealing was used force equilibration of combined polymer/Pluronic template solutions. For the DLS experiments, a small amount of THF was added to the aqueous polymer template solutions. The water/THF solution acts to molecularly solubilize both PEO and PPO blocks of F127 or F108 and disrupt the micelle structure.[48] The THF was then slowly evaporated, which allows for the micelles to reform with the PPO homopolymers more readily solubilized by the PPO core of the micelle or for the PEO homopolymers to more readily associate with the outer PEO shell of the micelle.[44,49] After THF annealing for the PPO/F127 solutions, there was a large decrease in the intensity of the pure Pluronic 7 nm micelle and a complete disappearance of the large sized pure PPO aggregate peaks (Fig. 3.1a). This was accompanied by the appearance of enlarged micelles with a size around 33 nm in diameter (Fig. 3.1a). After THF annealing of the PEO/F108 there was an increase of the micelle size to about 14 nm (Fig. 3.1b), but there was also the appearance of larger aggregates (~100-1000 nm) and unassociated PEO homopolymers (~1 nm).

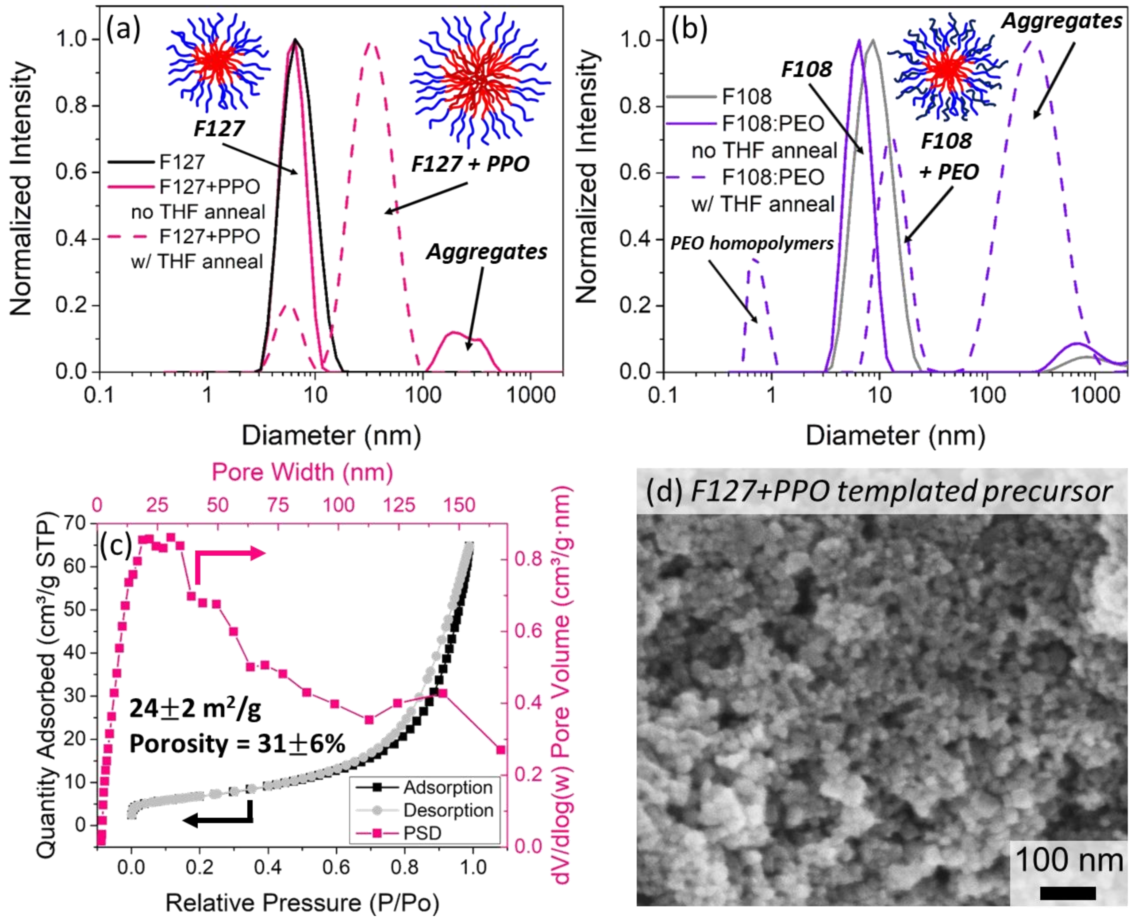

Figure 3.1. (a-b) Intensity weighted DLS data of aqueous solutions of polymer templates: (a) F127 (black), PPO/F127 without THF annealing (pink, solid line), and PPO/F127 after THF annealing (pink, dotted line). Inset (upper left): schematic of F127 micelle with the PEO blocks shown in blue and the PPO blocks shown in red. Inset (upper right): schematic of PPO homopolymers (dark red) associated with F127, which are solubilized by F127's PPO core; (b) F108 (grey), PEO/F108 without THF annealing (purple, solid line), and PEO/F108 after THF annealing (purple, dotted line). Inset (center): schematic of PEO homopolymers (dark blue) associated with F108, which associate with F108's PEO shell. (c) Nitrogen porosimetry adsorption (black) and desorption (grey) isotherms and the BJH adsorption volume-weighted PSD for F127/PPO (pink) templated NCA precursors. (d) SEM of NCA precursors templated using F127 and PPO.

We then used each Pluronic/polymer pair in the synthesis of nanoporous NCA. Aqueous template solutions were combined with metal nitrates and then dried and processed at 450 °C to volatilize both the nitrate counterions and the polymer templates, producing a nanoporous NCA precursor phase. When the F127/PPO template was used in the synthesis of nanostructured NCA, this resulted in a nanoporous NCA precursor with a surface area of 24±2 m^2/g and a porosity of 31±6%, (Fig. 3.1c,d) after heating at 450 °C. Analysis of the volume weighted pore size distribution from nitrogen porosimetry showed a peak centered around 25 nm, which agrees with the results from DLS (Fig. 3.1c). When the F108 and PEO homopolymer template was used to synthesize a nanostructured NCA precursor (Fig. 3.2a), the surface area and the porosity of the precursor were slightly lower: 14±2 m^2/g and 26±5% (Fig. S3.1), respectively. Additionally, there was not a discernable peak in the pore size distribution from nitrogen porosimetry for the F108 and PEO templated NCA precursor (Fig. S3.1), which is likely due to the polydispersity of the template size as seen from DLS. Based on these results, we conclude that F127/PPO serves as a more homogeneous template, but that both F127/PPO and F108/PEO can be used to produce similar NCA precursors. Based on this, all optimized materials produced in this study will utilize the F127/PPO combination, but some initial parameter studies will make use of the F108/PEO system.

3.3.2 Determination of the optimal NCA crystallization conditions

The nanoporous NCA precursors were then heated to obtain nanostructured NCA with the desired crystal structure. In order to determine if the desired crystal structure was obtained in the nanostructured NCA samples, XRD was used to monitor the degree of cation mixing, by calculating the integrated intensity ratio of the (003) to the (104) diffraction peaks [$I(003)/I(104)$]. When cation mixing is present, this ratio decreases because there is a decrease in the electron density contrast between the nickel and lithium layers of the (003) plane, while the electron density contrast of the (104) plane is not affected.[50] A $I(003)/I(104)$ ratio of at least 1.2 has been correlated with good electrochemical performance.[51] While the RTA method, with a short heating time (5 minutes) at 850 °C, resulted in small particle sizes compared to those crystallized using conventional annealing (CA), as shown in Fig. 3.2b,h, there was still considerable cation mixing in the RTA heated sample, as indicated by the low $I(003)/I(104)$ ratio. Fortunately, we found that by holding the NCA samples at a slightly lower temperature after the 5 minute RTA step, the cation ordering could be increased. To determine which hold temperature resulted in the best balance of particle size and cation ordering, the NCA precursor templated with PEO and F108 was heated for 5 minutes at 850 °C and then held at constant temperatures between 600 °C and 800 °C for 12

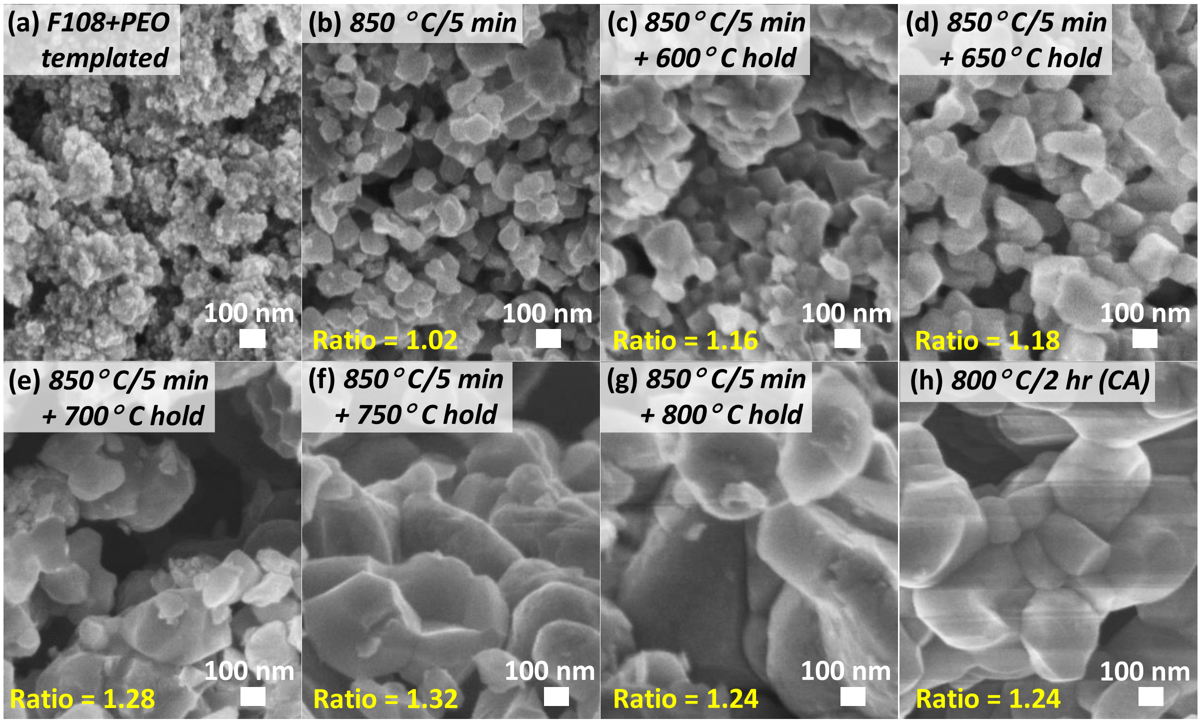

Figure 3.2. SEM images of (a) the NCA precursor templated with F108/PEO, and (b-h) nanoporous NCA templated with F108/PEO and heated under different conditions. Parts (b-g) show SEM image of nanostructured NCA after 5 minutes of heating at 850 °C, followed by immediate cooling (b), or by an addition 12 hour constant temperature hold at 600 °C (c), 650 °C (d), 700 °C (e), 750 °C (f), 800 °C (g). Part (h) shows an SEM image of nanostructured NCA after heating at 800 °C for 2 hours. The $I(003)/I(104)$ ratio for each sample is displayed on each SEM image.

hours. From hold temperatures of 600 °C to 700 °C the $I(003)/I(104)$ ratio increased without significant growth of the NCA particles (Fig. 3.2). With a constant hold at 750 °C, the $I(003)/I(104)$ ratio increased further, but there was significant grain growth (Fig. 3.2f), which is undesirable because it increases lithium-ion diffusion distances. Lastly, for the NCA sample held at 800 °C after the RTA step, the particle size was large and the $I(003)/I(104)$ ratio decreased slightly from the ratio at 750 °C (Fig. 3.2g), which could be a result of a loss of lithium at high temperatures.[52] The XRD patterns of these NCA materials are provided in supplementary figure S3.2. From these results, we determined that fast heating followed by a hold at a constant temperature of 700 °C for 12 hours, produced the optimal small particle sizes with low cation mixing, and these parameters were used for all syntheses referred to as nanoNCA-RTA. We note that while this study on the optimal hold temperate was done using F108/PEO templated NCA materials, all further templating in this study utilized F127/PPO templates, because the DLS and nitrogen porosimetry results showed smaller and more polydisperse micelles and low surface area when using F108/PEO templates.

3.3.3 Characterization of nanoporous NCA

Nanoporous NCA, templated with F127 and PPO, was heated using either the conventional annealing or our optimized rapid heating method and compared to a commercial bulk NCA. Bulk NCA has a dense microsphere structure with large secondary particle sizes of about 5 μm (Fig. 3.3d,g). Each bulk microsphere is made up of primary particles that are around 425 nm (Fig. 3.3a,g, Tbl. 3.1), but because of the dense structure, the large primary particle size likely controls diffusion kinetics. Conventional slow heating with a long heating ramp generally promotes grain growth in materials, and as a result, the nanostructured NCA synthesized by this method (nanoNCA-CA) had medium sized particles (~275 nm, Fig. 3.3b,g, Tbl. 3.1).[53] Samples crystalized using rapid

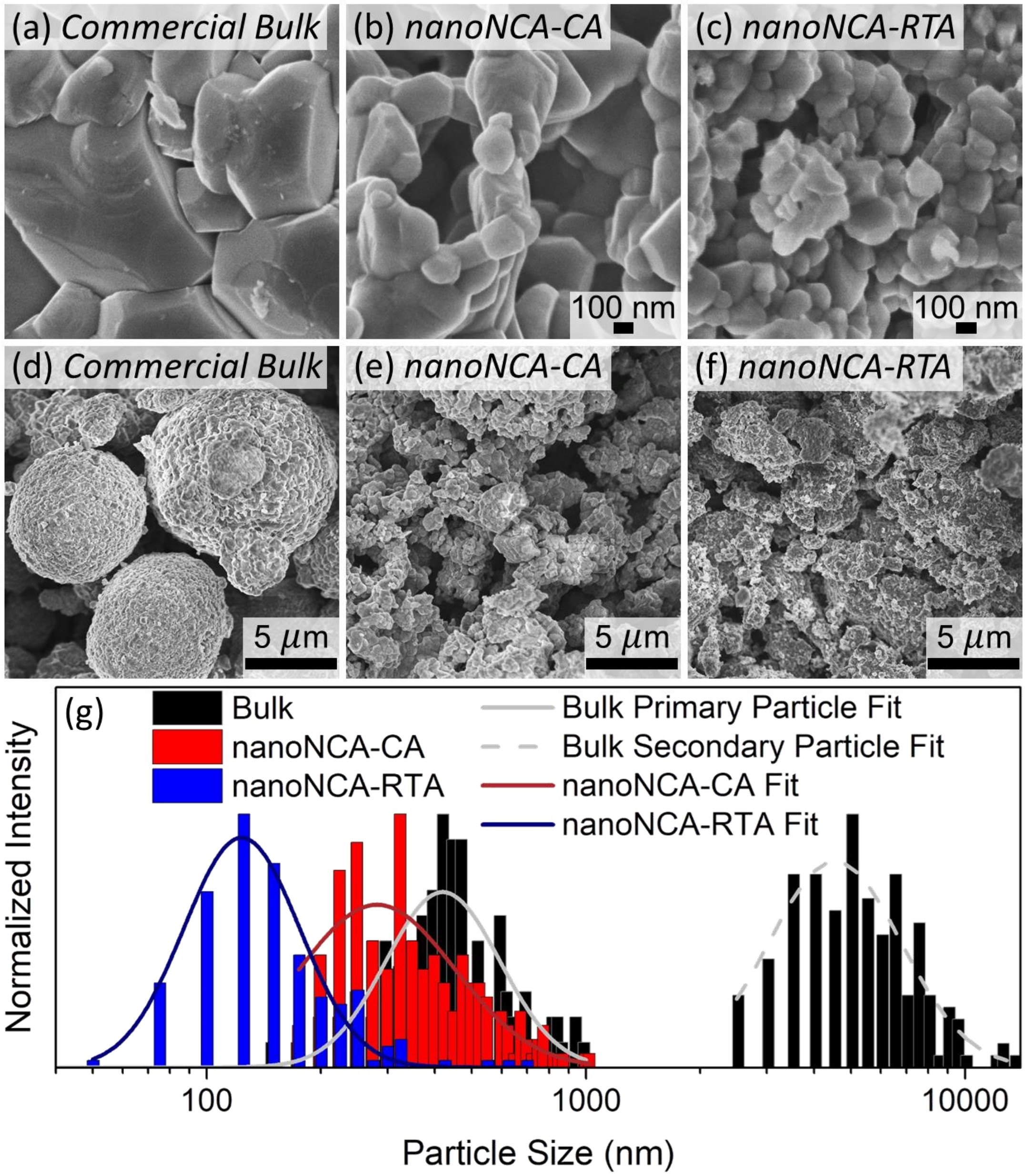

Figure 3.3. (a-c) High-magnification SEM images of commercial bulk NCA (a), nanoNCA-CA (b), and nanoNCA-RTA (c) and (d-f) low-magnification images of commercial bulk NCA (d), nanoNCA-CA (e), and nanoNCA-RTA (f) with the samples shown in parts (b), (c), (e), and (f) templated with F127/PPO. (g) Histograms and their log-normal fits representing the peak particle size distribution for the NCA samples, nanoNCA-RTA (blue, fit dark blue), nanoNCA-CA (red, fit dark red), and commercial bulk (black, fit for primary particles solid grey line, fit for secondary particles, dashed grey line) measured from 150 particles in SEM per sample. The nanoNCA-RTA, nanoNCA-CA, and bulk primary particles are binned by 25 nm; the secondary bulk particles are binned by 500 nm.

heating followed by a hold at 700 °C (nanoNCA-RTA) had smaller particles (~125 nm, Fig. 3.3c,g, Tbl. 3.1). Importantly, all of the templated NCA materials had a looser packing of their primary particles into a porous network and did not form dense microsphere structures like bulk NCA (Fig. 3.3d-f). While this allows for better electrolyte penetration in the nanostructured samples, the porosity cannot be measured by nitrogen porosimetry, because the large pores fall outside the measurable range. Additionally, the grain growth that occurred upon crystallization resulted in decreased surface area compared to the NCA precursor structure (Fig. S3.3).

The diffraction data was then used to analyze the $I(003)/I(104)$ ratios of nanoNCA-CA, nanoNCA-RTA, and bulk NCA, which all had ratios above 1.2 (Tbl. 3.1), indicating low cation mixing. To quantify the degree of cation mixing, Rietveld refinement was performed (Fig. 3.4). The XRD patterns were indexed to a hexagonal $R\bar{3}m$ space group, which resulted in reasonably low R_{wp} (< 10%). Li^+, Ni^{3+}, Co^{3+}, and Al^{3+} were placed at the 3a site (0,0,0), Li^+ and Ni^{2+} were placed at the 3b site (0,0,0.5), and O was placed at the 6c site $(0,0,z_{ox})$, where $z_{ox} \approx 0.250$ Å.[54] The amount of Ni^{2+} in the 3b sites, the amount of cation mixing, was low (< 3%) for all of the samples (Tbl. 3.1). Refinement results further indicated that the c and a lattice parameters were consistent with previously reported values for NCA and the c/a ratio for all of the samples was 4.95, which indicates a well-layered structure (Tbl. 3.1).[23,27,32] Furthermore, the c lattice parameter and z_{ox} can be used to calculate the thickness of the slab (S) and interslab (I) layers, where the slab thickness is the thickness of the transition metal slab and the interslab thickness is a measure of the lithium-ion diffusion layer.[54] The interslab thickness is slightly larger for the two nanoporous NCA materials, which can be a result of decreased cation mixing and should lead to easier lithium-ion diffusion during cycling for these samples (Tbl. 3.1).[54] Based on the Rietveld refinement results, all samples have the desired layered crystal structure and their electrochemical performance should not be limited by cation mixing.

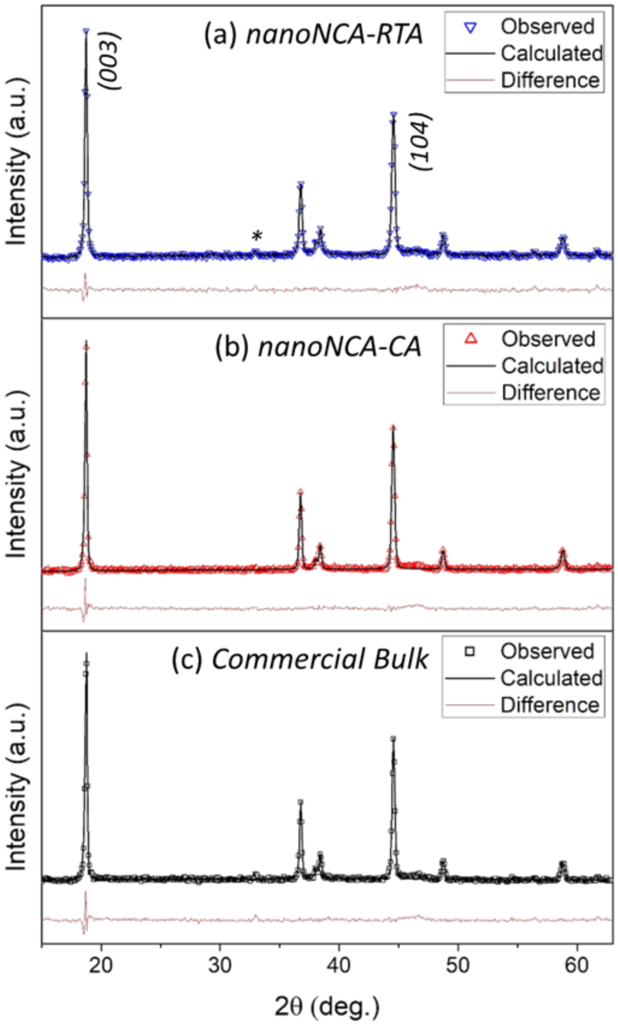

Figure 3.4. Rietveld refinement of XRD patterns for nanoNCA-RTA (a, blue) and nanoNCA-CA (b, red), templated with F127 and PPO, and commercial bulk NCA (c, black). On each graph the observed pattern is shown with open symbols, the calculated pattern with a black line, and the difference between the two patterns is shown below in dark red. * peak from silicon sample holder.

Because it is known that NCA materials are sensitive to air exposure, XPS was performed to examine the surface of the materials. An air-free capsule was used to transport samples directly from a glovebox to the XPS chamber, to avoid air exposure before measurment.[32,55] To assess the oxidation state of the nickel on the surface of the nanostructured materials, the XPS Ni 2p spectra were analyzed (Fig. S3.4). The choice of template can affect the surface oxidation state of nanostructured materials by creating more oxidizing or more reducing environments. For example, when PMMA templates were combined with RTA heat treatment, the result was a high fraction of reduced surface Ni^{2+} due to the reducing environment created by PMMA combustion.[24] Fortunately, both conventional and RTA heat treatments with F127/PPO as a template resulted in a surface that was mostly oxidized; the fraction of Ni^{2+} was 36% and 35% for nanoNCA-CA and nanoNCA-RTA, respectively (Fig. 3.5a). The relatively low amount of NiO on the surface of these materials should lead to enhanced performance. As expected, upon exposure to ambient air for 1 week, the surface of both nanoporous NCAs became highly reduced, with about 70% of the Ni appearing as Ni^{2+}, rather than Ni^{3+} (Fig. 3.5a).

Table 3.1. $I(003)/I(104)$ ratios calculated from XRD, the Rietveld refinement results, peak of the particle size distribution of primary particles observed from SEM, z_{ox}, S, and I for nanoNCA-RTA and nanoNCA-CA, templated with F127 and PPO, and commercial bulk NCA.

Sample	**I(003)/ I(104)**	**a (Å)**	**c (Å)**	**c/a**	**Ni^{2+} in Li sites**	**R_{wp} (%)**	**Peak particle size (nm)**	**z_{ox} (Å)**	**S (Å)**	**I (Å)**
nano NCA-RTA	1.22	2.8641 (3)	14.188 (3)	4.95	0.029 (9)	3.72%	125	0.260 (8)	2.08	2.65
nano NCA-CA	1.25	2.8654 (3)	14.191 (3)	4.95	0.029 (6)	4.04%	275	0.260 (7)	2.08	2.65
Comm. Bulk	1.34	2.8642 (2)	14.183 (3)	4.95	0.033 (8)	4.34%	425	0.259 (9)	2.11	2.62

S (slab thickness) = $2(\frac{1}{3} - z_{ox})c$, I (interslab thickness) = $\frac{c}{3} - S$, R_{wp} = weighted profile R-factor

Although both nanoporous samples appear to show favorable Ni oxidation states, there are a variety of other reactive components that can also impede fast charge/discharge, and XPS was also used to examine the presence of these other surface impurities on the nanostructured samples. Specifically, O 1s spectra were used to compare the fractions of NCA-lattice oxygen (~529.0 eV)

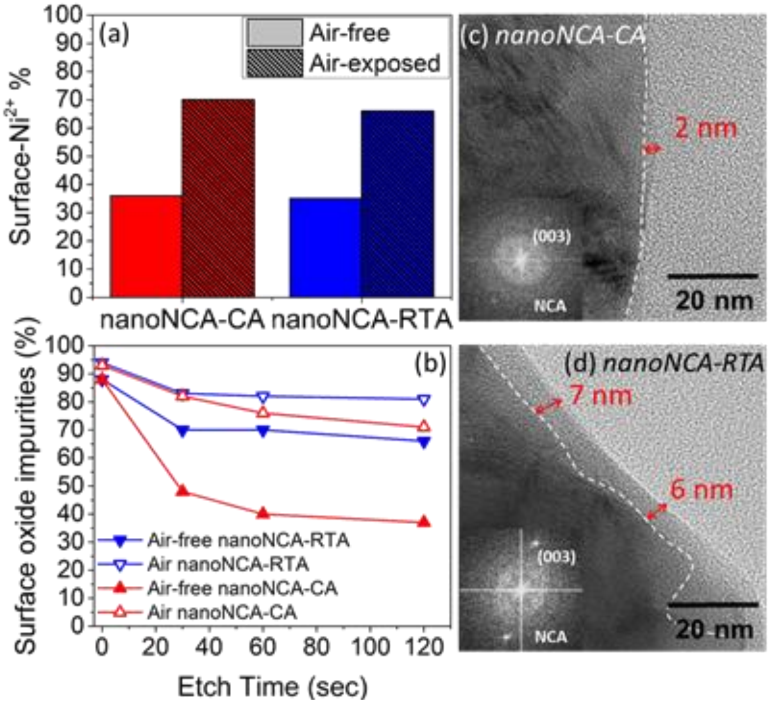

Figure 3.5. (a) Percentage of Ni^{2+} compared to Ni^{3+} from the Ni 2p XPS spectra for air-free nanoNCA-CA (red, solid) and nanoNCA-RTA (blue, solid). NCA samples were exposed to ambient air for 1 week, and the Ni^{2+} percentage was found for air-exposed nanoNCA-RTA (red, striped) and nanoNCA-RTA (blue, striped). (b) Percentage of surface oxide impurities compared to NCA from the O 1s XPS spectra for air-free nanoNCA-CA (red, solid), air-exposed nanoNCA-CA (red, open), air-free nanoNCA-RTA (blue, solid), and air-exposed nanoNCA-RTA (blue, open). TEM images of nanoNCA-CA (c) and nanoNCA-RTA (d) powders that were kept air-free before analysis. FFT patterns from the particles are shown in an inset in the bottom left corner of the TEM images.

to surface oxide impurities (~531.4 eV and ~533.9 eV) for samples kept air-free and those exposed to air for 1 week (Fig. S3.5).[32,55] Of the surface oxide impurities, the peak around 531 eV is attributed to Li_2CO_3, while the peak around 534 eV has been observed for nickel-rich materials in the literature before but it has not been well-characterized. Previously, the peak at 534 eV has been associated with surface C-O or dehydrated surface species.[32,55] Both sets of samples had high percentages of surface oxide impurities, 88% and 94%, for the air-free and air-exposed samples, respectively (Fig. 3.5b). Argon-ion etching was then used to determine the relative thickness of these surface layers. Using SiO_2 as a model system, the argon-etching rate can be roughly estimated to be 3-8 nm per minute.[56] Before etching, the air-free nanoNCA-CA sample initially had a peak at 534 eV (25%), which disappeared after the first 30 seconds of etching. After 2 minutes of etching, the air-free nanoNCA-CA had only 37% Li_2CO_3 remaining (Fig. 3.5b). Interestingly, the air-free nanoNCA-RTA still had a considerable amount of surface oxide impurities remaining (66%) after a 2 minute etch (Fig. 3.5b). We note that during the conventional anneal, there was a slow ramp to high temperatures, which allowed time for any remaining template to decompose and volatilize or burn out. In contrast, the RTA sample was heated rapidly and any remaining template could combust while in contact with the NCA surface. Additionally, because the particle sizes were smaller for nanoNCA-RTA, there was more available surface, which could cause a higher reactivity with CO_2 and water from combustion of the oxygen rich polymer template to form more surface oxide impurities. Overall, XPS suggested significantly thicker surface impurity layers in the nanoNCA-RTA material compared to the nanoNCA-CA sample. Finally, we note that although the air-free nanoNCA-RTA material had a relatively high fraction of surface impurities, the XPS results still indicated that an even thicker surface impurity layer was formed on the samples exposed to air for 1 week, which had, on average, 76% surface impurities remaining after 2 minutes of etching (Fig. 3.5b).

To further characterize the thickness of the surface impurity layers formed on the two air-free nanostructured NCA samples, TEM imaging was performed on samples that were kept air-free. TEM can be used to observe amorphous layers on the surface of the NCA particles, which are generally attributed to amorphous Li_2CO_3 and other residual lithium compounds.[31,57] As shown in figures 3.5c and S3.61-b, the nanoNCA-CA samples had thin amorphous coatings ranging from 2-3 nm in thickness. In contrast, the nanoNCA-RTA samples had thicker amorphous layers ranging from 6-9 nm (Figs. 3.5d, S3.6c-d) and up to 17 nm thick in some areas of the particle (Fig. S3.6e). The thickness of the amorphous layers observed by TEM agree well with the XPS argon-etching results of the air-free samples.

3.3.4 Electrochemical performance and electrochemical kinetic analyses

As the XPS results showed, the nanoporous NCA samples are sensitive to air exposure, therefore all samples were kept as air-free as possible during electrochemical sample preparation. Directly after annealing the materials at high temperatures, the samples were only cooled to 350 °C, while still under dry oxygen, and then immediately transferred, while hot, to an argon filled glovebox. While this quick transfer at 350 °C could still lead to some contamination from carbon dioxide, it should hinder any reaction with water. The nanostructured NCA electrodes were then prepared air-free in the glovebox for electrochemical analysis.[24,32] P3HT, a semiconducting polymer,[58] was used as a conductive binder. P3HT has previously been used as a conductive binder for NCA cathodes and resulted in high electrical and ionic conductivity, compared to the common PVDF binder, which is insultaing.[24,59] The enhanced performance of P3HT as a conductive binder is due in part to electrochemical doping of P3HT that occurs at 3.4 and 3.75 V vs. Li/Li^+.[59,60] However, P3HT does begin to undergo oxidative degradation when it is cycled above 4.2 V vs. Li/Li^+.[61] The voltage limit is not terribly problematic, as NCA also starts to undergo degradation through structural transformations at the material surface to rock-salt and spinel structures, through oxygen loss, and through transition-metal dissolution when cycled above 4.2 V.[62,63] Because of this, the voltage windows used were kept below 4.2 V vs. Li/Li$^+$ to study the optimal and reversible performance of the NCA materials.

To compare the electrochemical performance of the two nanostructured NCA materials and the commercial bulk NCA, galvanostatic cycling was performed from 2.7 to 4.2 V vs. Li/Li$^+$, at various rates up to 64C, after 3 activation cycles at C/5 (Fig. 3.6a). Both nanostructured NCA samples had greater specific capacity than the bulk NCA at slow rates. However, when the rate was increased, the capacity of nanoNCA-RTA quickly dropped to be similar to bulk at 32C and 64C, 69 mAh/g and 12 mAh/g, respectively. This resulted in a low capacity retention for the

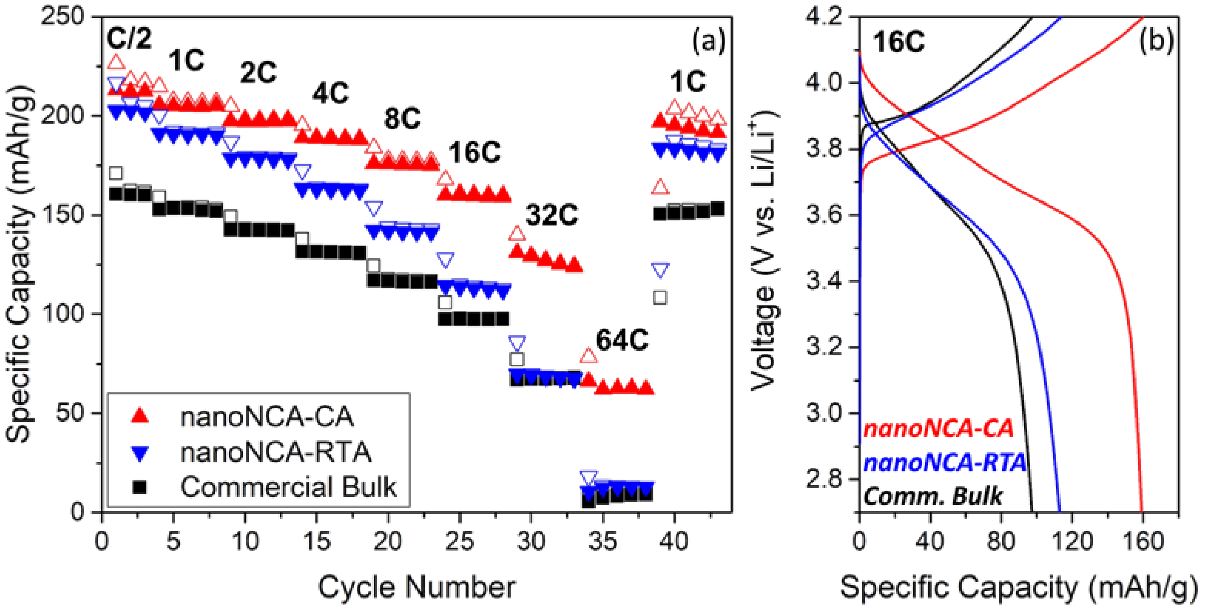

Figure 3.6. (a) Galvanostatic rate performance of nanoNCA-CA (red), nanoNCA-RTA (blue), and commercial bulk (black) NCA. The specific capacity for charge (open symbols) and discharge (filled symbols) are shown for various rates (displayed on graph) cycled from 2.7-4.2 V vs. Li/Li$^+$. (b) Individual galvanostatic charge and discharge curves at a rate of 16C for nanoNCA-CA (red), nanoNCA-RTA (blue), and commercial bulk (black) NCA.

nanoNCA-RTA sample of 34% at 32C versus a 42% capacity retention for bulk NCA (Fig. S3.7). Impressively, the nanoNCA-CA sample had specific capacities of 127 mAh/g and 63 mAh/g at 32C and 64C, respectively; with a capacity retention of 60% at 32C (Fig. S3.7). We attribute the high capacity of the two nanoporous samples at slow rates to the low amount of reduced nickel on their surface, as determined by XPS. Unfortunately, while XPS showed high amounts of Ni^{3+} when F127 was used as the template, XPS and TEM also showed that the nanoNCA-RTA sample had a higher fraction of surface oxide impurities. This thicker layer of insulating Li_2CO_3 should lead to hindered lithium-ion diffusion, especially at fast rates, which is exactly what is seen in the galvanostatic rate performance results presented here (Fig. 3.6a). Looking at the galvanostatic charge and discharge curves for all NCA samples, we observe that the voltage varied linearly with capacity (Fig. S3.8), even at fast rates (Fig. 3.6b), which is a characteristic of pseudocapacitance.[7] Additionally, the nanoporous NCA electrodes that were exposed to air, showed decreased capacity at all rates (Fig. S3.9). This decrease in performance was expected due to the increase in surface-Ni^{2+} and Li_2CO_3 formed upon exposure to air, as shown by XPS.

To understand the electrochemical kinetics and to determine the mechanism of charge storage of these nanostructured materials, they were studied using several electrochemical kinetic analyses. In the first kinetic analysis used, cyclic voltammetry (CV) was performed and the following power-law relation was used to relate the peak cathodic and anodic currents to the sweep rate.[7,64]

$$i = av^b \tag{1}$$

In equation 1, i is the peak current, v is the sweep rate, a is a constant, and b is a constant that can vary from 0.5 to 1. For typical battery materials the faradaic redox reactions are diffusion-limited and the current scales with $v^{1/2}$, following the Randles-Sevcik equation.[1,64] So a b-value of 0.5

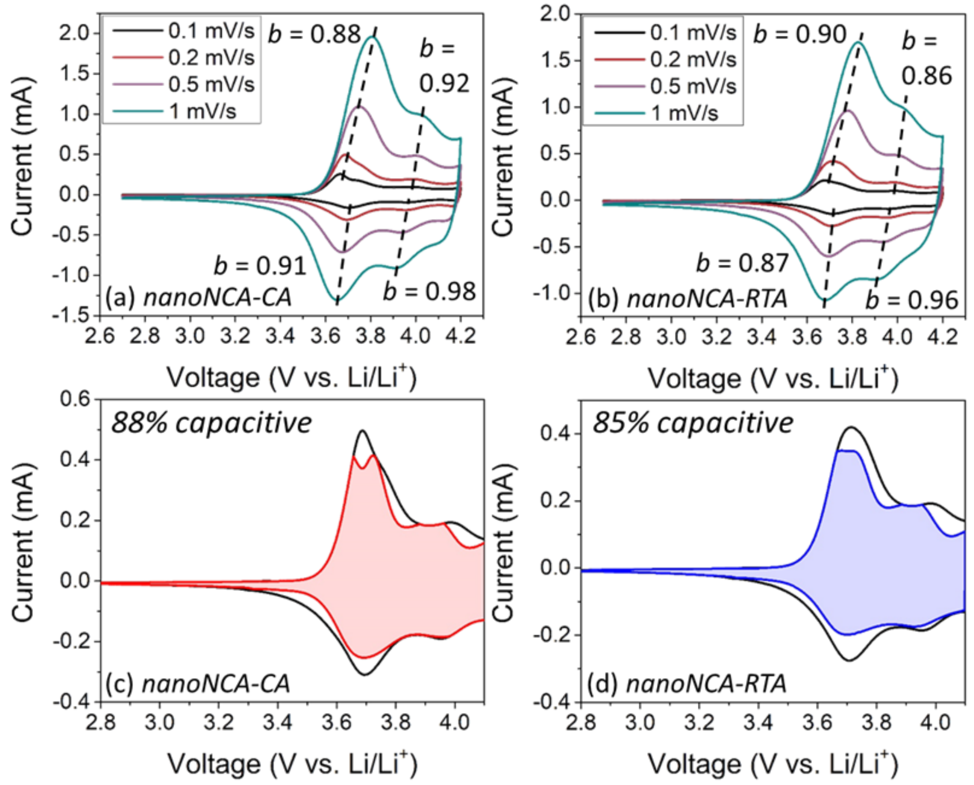

Figure 3.7. (a-b) Cyclic voltammograms at various sweep rates for nanoNCA-CA (a) and nanoNCA-RTA (b) templated with F127 and PPO, which were used to derive *b*-values, displayed on graph. (c-d) Cyclic voltammogram at a sweep rate of 0.2 mV/s for nanoNCA-CA (c, red) and nanoNCA-RTA (d, blue), where the capacitive contribution is shaded.

corresponds to charge storage though a typical battery-like diffusion-controlled process. In contrast, for a capacitor, current scales with *v*, which corresponds to a *b*-value of 1.[64] Looking at the two anodic redox peaks at 3.8 V and 4.0 V and the two cathodic peaks at 3.7 V and 3.9 V, the nanostructured NCA materials had average *b*-values of 0.92 and 0.90 for nanoNCA-CA and nanoNCA-RTA, respectively (Fig. 3.7a-b, Tbl. S3.1). Because the calculated *b*-value can vary from 0.5-1, a *b*-value close to 1 indicates a material is behaving in a largely capacitive manner. Both bulk and nanostructured NCA, with P3HT used as the binder, have previously been shown to have *b*-values near 0.9.[24,59] The same analysis was carried out on the air-exposed samples, which resulted in average *b*-values of 0.84 and 0.82, for the air-exposed nanoNCA-CA and air-exposed nanoNCA-RTA, respectively (Figs. S3.10a, S3.11a, Tbl. S3.1). While these *b*-values still correspond to significant capacitive character, the decrease does indicate increased diffusion-limitation. This decrease in capacitive character is a result of the increase in the fraction of Ni^{2+} on the surface and the growth of insulating surface layers upon exposure to air.

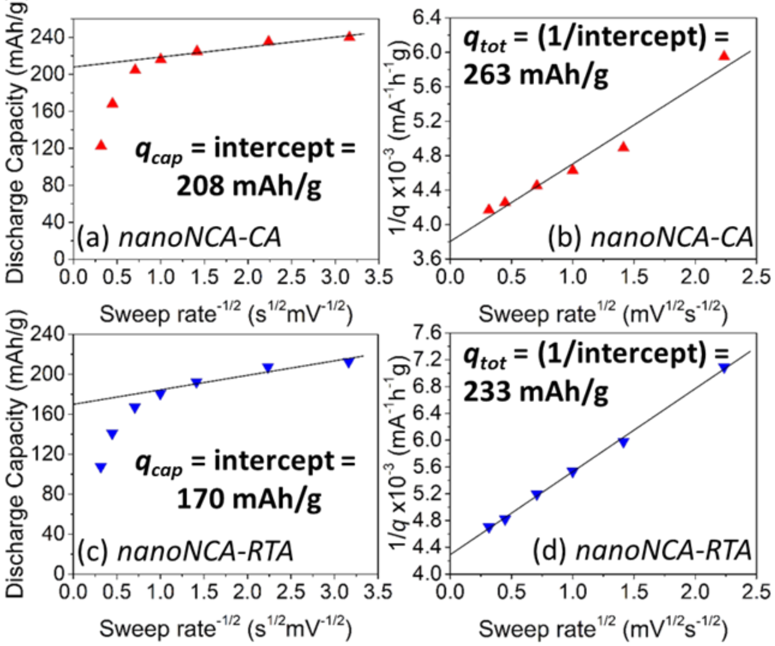

Figure 3.8. Trasatti analysis, (a and c) determination of q_{cap} from extrapolation of the y-intercept as $v \rightarrow \infty$ from the plot of capacity versus $v^{-1/2}$, (b and d) and the determination of q_{tot} from extrapolation of the y-intercept as $v \rightarrow 0$ from the plot of $1/q$ versus $v^{1/2}$.

In the next electrochemical kinetic analysis, it can be hypothesized that equation (1) can be further separated into purely capacitive (k_1) and purely diffusion-limited (k_2) contributions to current, where the sweep rate scales as either v or $v^{1/2}$, respectively, resulting in equation 2.[3,13]

$$i = k_1 v + k_2 v^{1/2} \tag{2}$$

This analysis, which will be referred to as the k_1/k_2 analysis, allows for calculation and visualization of the capacitive and diffusion-controlled contributions to current over the entire voltage range, but the hypothesis of only two possible scaling exponents remains unverified. Both nanoporous NCA materials showed predominantly capacitive behavior; the nanoNCA-CA material was 88% capacitive, while the nanoNCA-RTA material was 85% capacitive (Fig. 3.7c-d, Tbl. S3.1). When the materials were exposed to air, the capacitive contribution dropped to 86% for air-exposed nanoNCA-CA and to 84% for air-exposed nanoNCA-RTA (Tbl. S3.1). While this is not a large decrease in capacitive contribution, the biggest loss in capacitive current was at the redox peaks, which indicates added diffusion barrier for bulk intercalation after exposure to air (Figs. S3.10b, S3.11b).[17]

The previous two kinetic analyses start with similar assumptions, and therefore give similar results. For an additional and independent analysis that can help determine the capacitive contribution to the total charge, the Trasatti analysis can be used, which does not assume a functional form for the capacitive contribution.[13,65] Here, only semi-infinite diffusion ($v^{1/2}$) is assumed, to generate the following equation:[65]

$$q(v) = q_{cap} + \alpha(v^{-1/2}), \tag{3}$$

where $q(v)$ is the total measured voltammetric charge transfer and α is a constant. Equation 3 can be used to solve for the capacitive contribution (q_{cap}) by extrapolating to infinite sweep rates and assuming the high rate capacity will be dominated by capacitive processes, while slow diffusion-limited processes will be excluded.[2,65] Extrapolation to the y-intercept as $v \rightarrow \infty$ gave values of 208 and 170 mAh/g for nanoNCA-CA and nanoNCA-RTA for q_{cap}, respectively (Fig. 3.8a,c). To calculate the total capacity, equation 4 can then be extrapolated to zero sweep rate,[65]

$$\frac{1}{q(v)} = \frac{1}{q_{tot}} + \alpha(\mathrm{v}^{1/2}) \tag{4}$$

where q_{tot} is the total charge storage. Extrapolation to zero sweep rate is assumed to provide the long time-scale where all redox reactions can occur within a material.[13,65] Here, extrapolation to the y-intercept as $v \rightarrow 0$, results in q_{tot}^{-1} and the values for q_{tot} can be calculated. Calculated of values of q_{tot} were 263 and 233 mAh/g for nanoNCA-CA and nanoNCA-RTA, respectively (Fig. 3.8b,d). The extrapolated values from equation (3) and (4) can then be used to calculate the capacitive fraction of the material, which was 79% and 73% for nanoNCA-CA and nanoNCA-RTA, respectively (Tbl. S3.1). These values show the materials had largely capacitive behavior, and are in reasonable agreement with the results from the k_1/k_2 analysis and the values from the *b*-value analysis. Upon exposure to air, the capacitive fraction, as determined by the Trasatti analysis, dropped to 65% and 53% for air-exposed nanoNCA-CA and nanoNCA-RTA, respectively (Figs. S3.10c-d, S3.11c-d, Tbl. S3.1).

The results of the electrochemical kinetic analyses on the nanostructured NCA materials thus showed many signatures of pseudocapacitive behavior.[1,7] The nanoNCA-RTA NCA material had slightly lower *b*-values and capacitive values due to the thicker insulating layers on the surface, which hinder lithium-ion intercalation, despite the intrinsically smaller domain size in the nanoNCA-RTA materials. Additionally, the nanostructured NCA materials showed a small shift (< 0.20 V) in the cathodic peak up to sweep rates of 10 mV/s (Fig. S3.12). This small peak shift is another characteristic of pseudocapacitive behavior and indicates facile lithium-ion intercalation and high-power capability.[7] Finally the electrochemical kinetic analyses also showed that there was a decrease in capacitive behavior when the nanoporous NCA materials were exposed to air. This occurs because the nickel on the surface of the materials was reduced and thicker layers of insulating surface oxide impurities were formed, which are more detrimental for these nanoporous materials with higher surface.

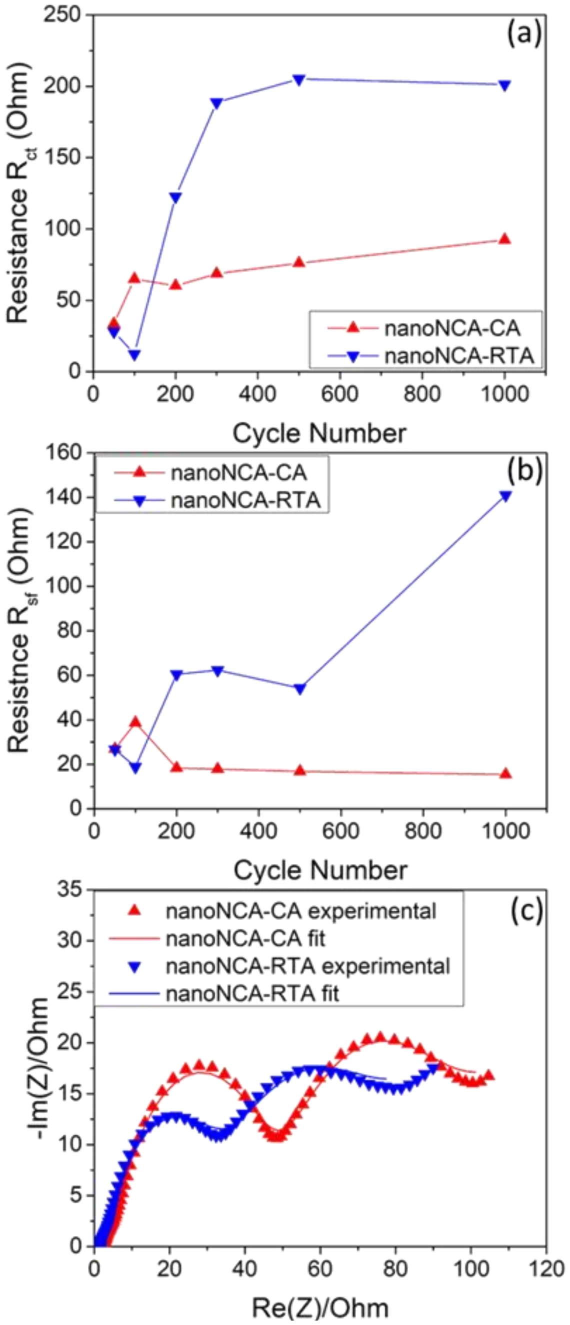

Figure 3.9. (a) Variation of R_{ct} and of (b) R_{sf} with cycle number for nanoNCA-CA (red) and nanoNCA-RTA (blue). (c) Nyquist plot for nanoNCA-CA and nanoNCA-RTA after 50 cycles, the experimental data is shown with symbols and the fit is shown with a solid line.

The nanoporous materials were also characterized by EIS up to 1000 cycles. The Nyquist plots for both samples had two semicircles (Fig. 3.9c), where the first semicircle is attributed to the resistance of lithium-ion diffusion through the solid electrolyte interphase (SEI) surface film (R_{sf}) and the second semicircle is attributed to the charge transfer resistance at the interface of the NCA particle (R_{ct}).[62] For nanoNCA-CA, the R_{ct} increased slightly and the R_{sf} stayed fairly consistent with cycling (Fig. 3.9a,b), this agrees with previous literature and suggests the presence of a stable surface layer.[66] However, for nanoNCA-RTA, there was significant increase in both the R_{ct} and the R_{sf} with cycling (Fig. 3.9a,b). According to the XPS and TEM data, the nanoNCA-RTA sample had a thick layer of Li_2CO_3 on its surface. It has previously been demonstrated that when nickel-rich materials with Li_2CO_3 surface layers are cycled in $LiPF_6$ electrolytes, HF present in the electrolyte solubilizes the Li_2CO_3 layer and replaces it with a highly resistive layer of LiF, which increases the overall impedance.[67]

3.3.5 Performance of high mass loading nanoporous NCA (nanoNCA-CA) electrodes

Lastly, the nanoporous NCA material with the best performance from the half-cell analyses, nanoNCA-CA, was assembled into higher mass loading electrodes (~10 mg/cm^2), to demonstrate the potential for scalability of the templated nanostructured NCA material, as well as its commercial potential. Although the half-cells above used P3HT as a binder, because of the high cost and limited large-scale production of P3HT, the high mass loading electrodes were made using the more scalable and commercially available PVDF binder. As previously mentioned, PVDF is more insulating than P3HT, but the use of PVDF will allow for better demonstration of integration and comparison with current works.

We first looked at high mass loading nanoNCA-CA electrodes with PVDF as the binder in a half-cell configuration, to compare to the lower-loading nanoNCA-CA results, with P3HT,

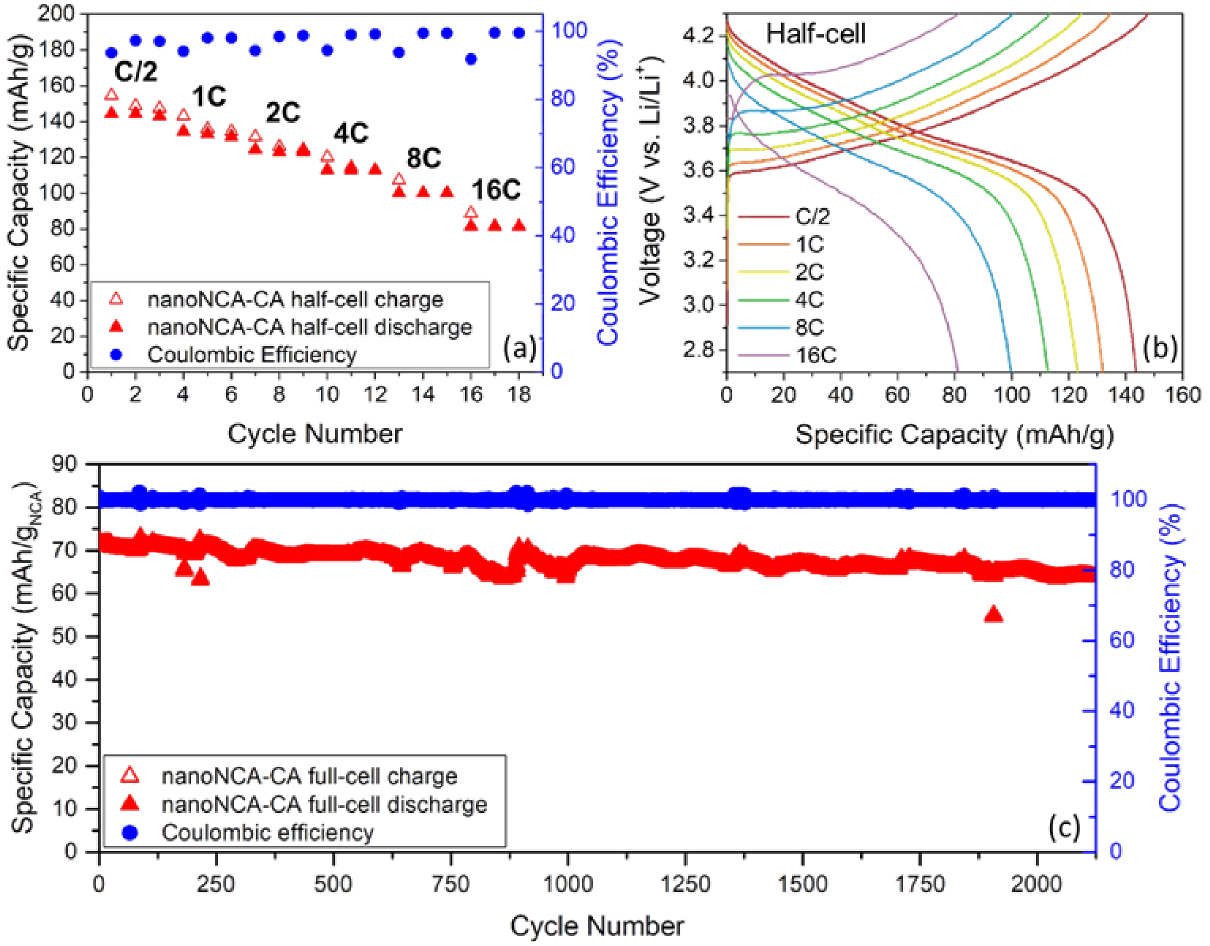

Figure 3.10. (a-b) Galvanostatic rate performance for high mass loading nanoNCA-CA half-cells cycled from 2.7-4.3 V vs. Li/Li$^+$; (a) the specific charge capacity is shown with open red triangles, specific discharge capacity with filled red triangles, and the Coulombic efficiency per cycle with blue circles. (b) Individual galvanostatic charge and discharge curves from the third cycle at each rate from (a). (c) High mass loading, full-cell device with a nanoNCA-CA cathode and an Nb_2O_5-rGO anode. The full-cell device was cycled galvanostatically using a 10C/2.5 V CCCV charge and 5C discharge, the cell was cycled from 0.5-2.5 V for 2120 cycles. Specific charge capacity (open red triangles), specific discharge capacity (filled red triangles), and Coulombic efficiency (blue circles) per cycle are plotted on the graph.

presented above. A nanoNCA-CA electrode with an active mass loading of 9.8 mg/cm^2 was cycled galvanostatically from C/2 to 16C after 3 activation cycles at C/5 (Fig. 3.10a,b). Even at a high mass loading, nanoNCA-CA can obtain a high capacity of 82 mAh/g at 16C and a capacity retention of 57% from C/2. The lower capacity and capacity retention in the thick electrodes are due to longer path-lengths and limited lithium-ion diffusion with the higher mass loadings and the insulating PVDF binder.[59,68] As expected, the high-loading, PVDF half-cells again have sloping voltage profiles at all rates (Fig. 3.10b), which agrees with the earlier nanoNCA-CA results and is a signature of pseudocapacitive behavior.

The high mass loading nanoNCA-CA cathode was then paired with a Nb_2O_5-rGO anode for a full-cell device. *T*-Nb_2O_5 is an intrinsic pseudocapacitive material that can achieve fast-rates because of the low activation energy for lithium diffusion that occurs without a phase transition.[7,9,69] Pairing the fast-charging NCA material with a fast-charging anode allows for an overall fast-charging full-cell device. Here, Nb_2O_5 was dispersed within a conductive carbon rGO network to increase electronic conductivity.[70] The high mass loading, full-cell device was cycled for 2120 cycles using a 10C/2.5 V CCCV charge and a 5C discharge, from 0.5-2.5 V (Fig. 3.10c). With respect to the nanoNCA-CA active mass, the initial specific discharge capacity was 72 mAh/g and the capacity retention after 2120 cycles was an impressive 89%. The fact that nanoNCA-CA can be assembled into a full-cell device that can be charged and discharged quickly, without significant capacity fade after many cycles, shows that this nanoporous NCA material, synthesized using low cost, scalable templates, has promise in for commercialization.

3.4 Conclusions

Nanoporous NCA was synthesized using a low cost, scalable polymer templates that resulted in a high-capacity, fast-charging cathode material. The nanostructured materials had decreased particle sizes and increased nanoscale porosity, which decreased the lithium-ion diffusion lengths and allowed for the material to be charged quickly. Additionally, because first-order phase transitions are already suppressed in bulk NCA, the nanostructured NCA did not need to be made very small to see fast-charging that was not limited by lithium-ion diffusion. In fact, we observed the best performance for the nanostructured NCA material with medium particle sizes (nanoNCA-CA). While nanoNCA-RTA had the smallest particle size, and therefore the shortest lithium-ion diffusion lengths, it had poor electrochemical performance at fast rates. This was due to the formation of insulating surface layers, caused by the incompatibility of the polymer template heated quickly in the RTA method and the reactive surface of NCA. The insulating layers hindered lithium-ion diffusion at fast rates, and so it was found that medium sized particles with nanoscale porosity, but without insulating surface layers, resulted in the optimal fast-charging performance. Both nanoporous NCA materials had signatures of pseudocapacitive behavior, as determined by electrochemical kinetic analyses, because of suppressed, first-order phase transitions and their decreased particle sizes.

Additionally, nanoNCA-CA, which had the best performance at low loadings, was assembled into high mass loading electrodes (~10 mg/cm^2) that were cycled in half and full-cell configurations, using PVDF as a binder. The full-cell device showed an impressive capacity retention of 89% after fast charging and discharging for 2120 cycles. Because a low cost polymer template was used in the synthesis of the nanoporous NCA, this synthesis can easily be scaled up for the commercial manufacturing for fast-charging applications.

3.5 Supplementary Information

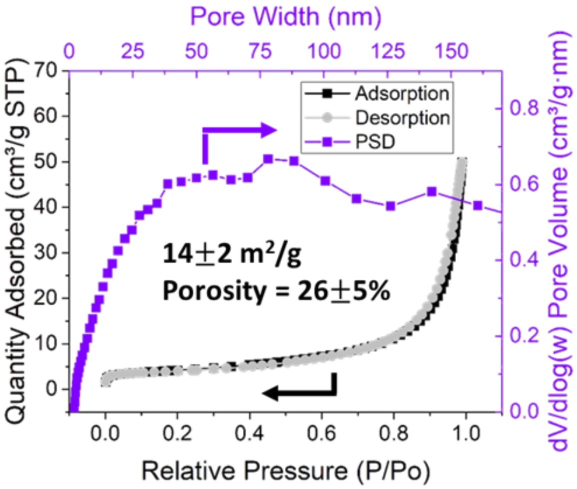

Figure S3.1. Nitrogen porosimetry adsorption (black) and desorption (grey) isotherms and the BJH adsorption volume-weighted pore size distributions (PSD) for F108/PEO (purple) templated NCA precursors.

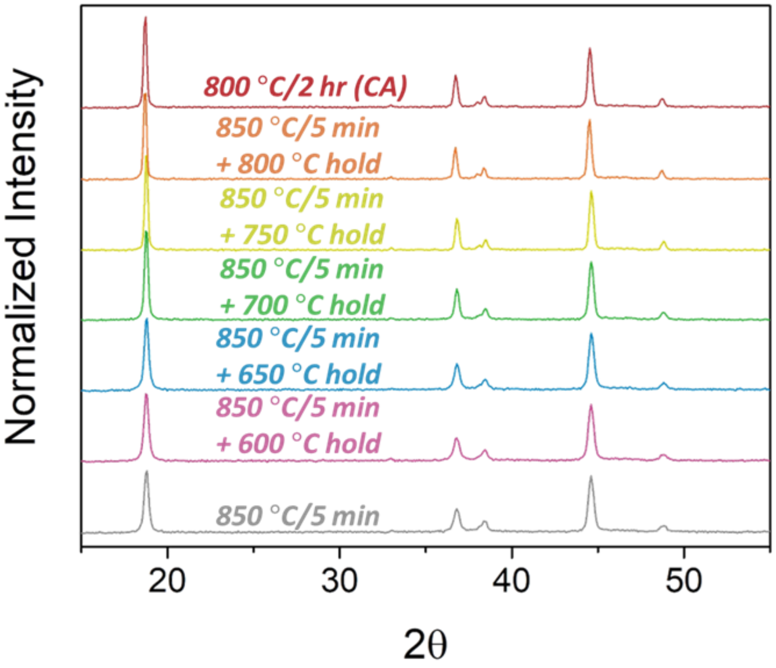

Figure S3.2. XRD patterns of nanostructured NCA templated with F108 and PEO after RTA (grey); after RTA and a constant temperature hold of 600 °C (purple), 650 °C (blue), 700 °C (green), 750 °C (yellow), and 800 °C (orange); and of nanostructured NCA templated with F108 and PEO after CA (red).

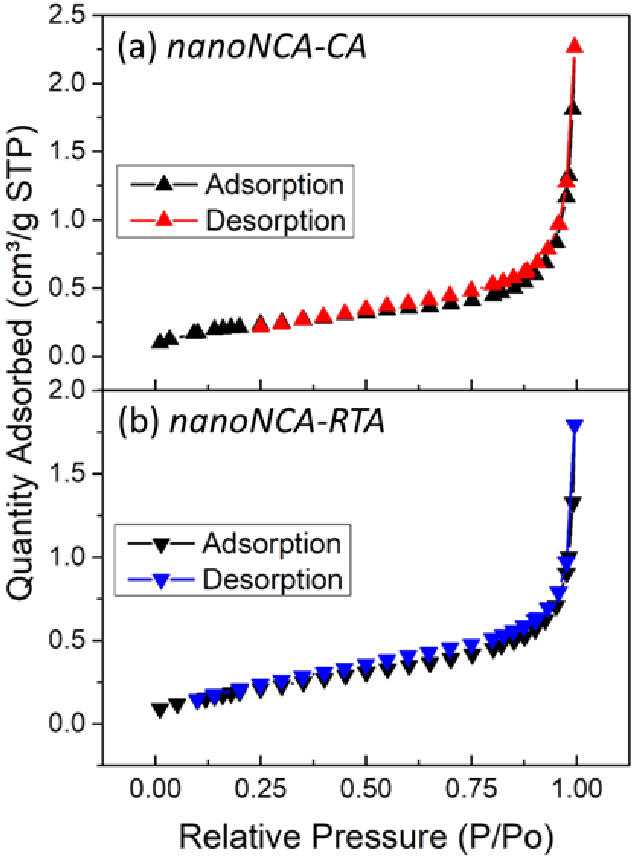

Figure S3.3. Adsorption (black) and desorption (red/blue) isotherms from nitrogen porosimetry of nanoNCA-CA (a) and nanoNCA-RTA (b).

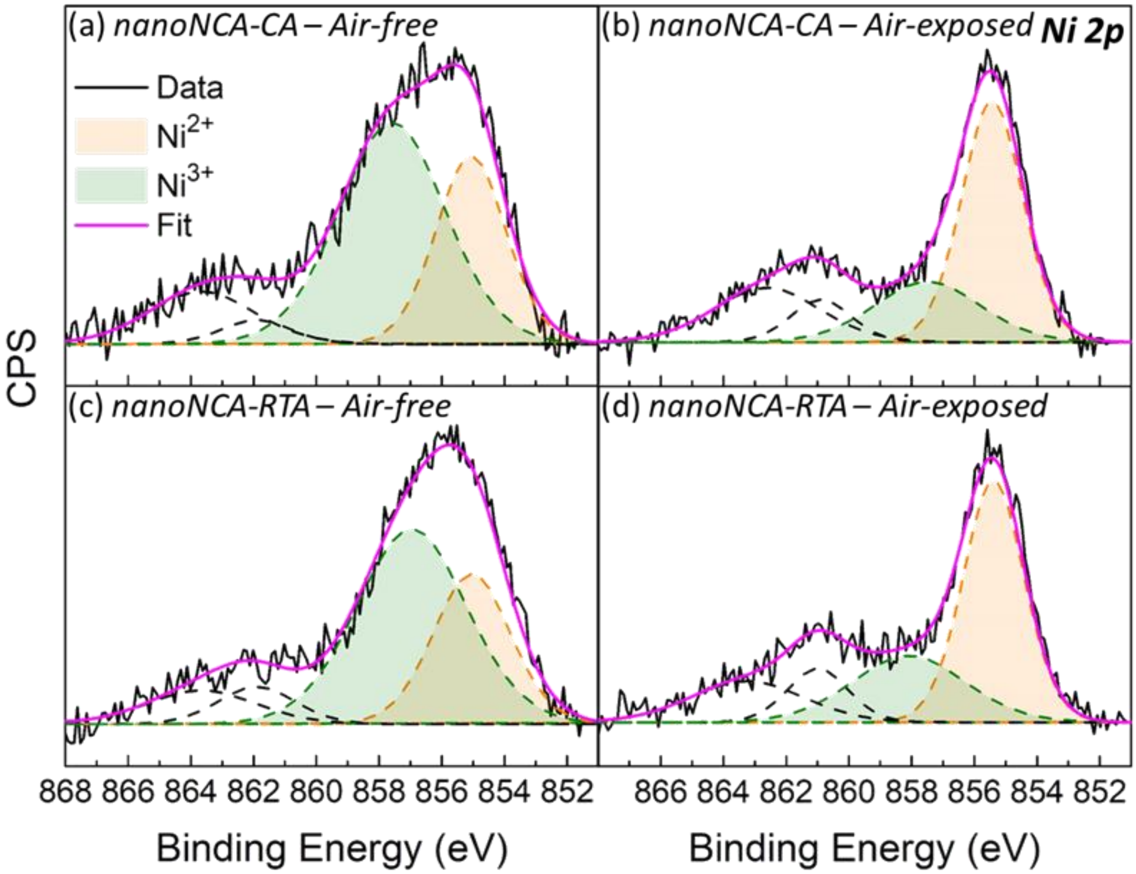

Figure S3.4. Ni $2p_{3/2}$ XPS spectra for air-free nanoNCA-CA (a), air-exposed nanoNCA-CA (b), air-free nanoNCA-RTA (c), and air-exposed nanoNCA-RTA (d). The data is shown in black, the overall fit is shown in pink, the fraction of Ni^{2+} is shaded in orange (around 857.5 eV), and the fraction of Ni^{3+} is shaded in green (around 855.2 eV). Characteristic Ni 2p satellite peaks are shown with dashed black lines.

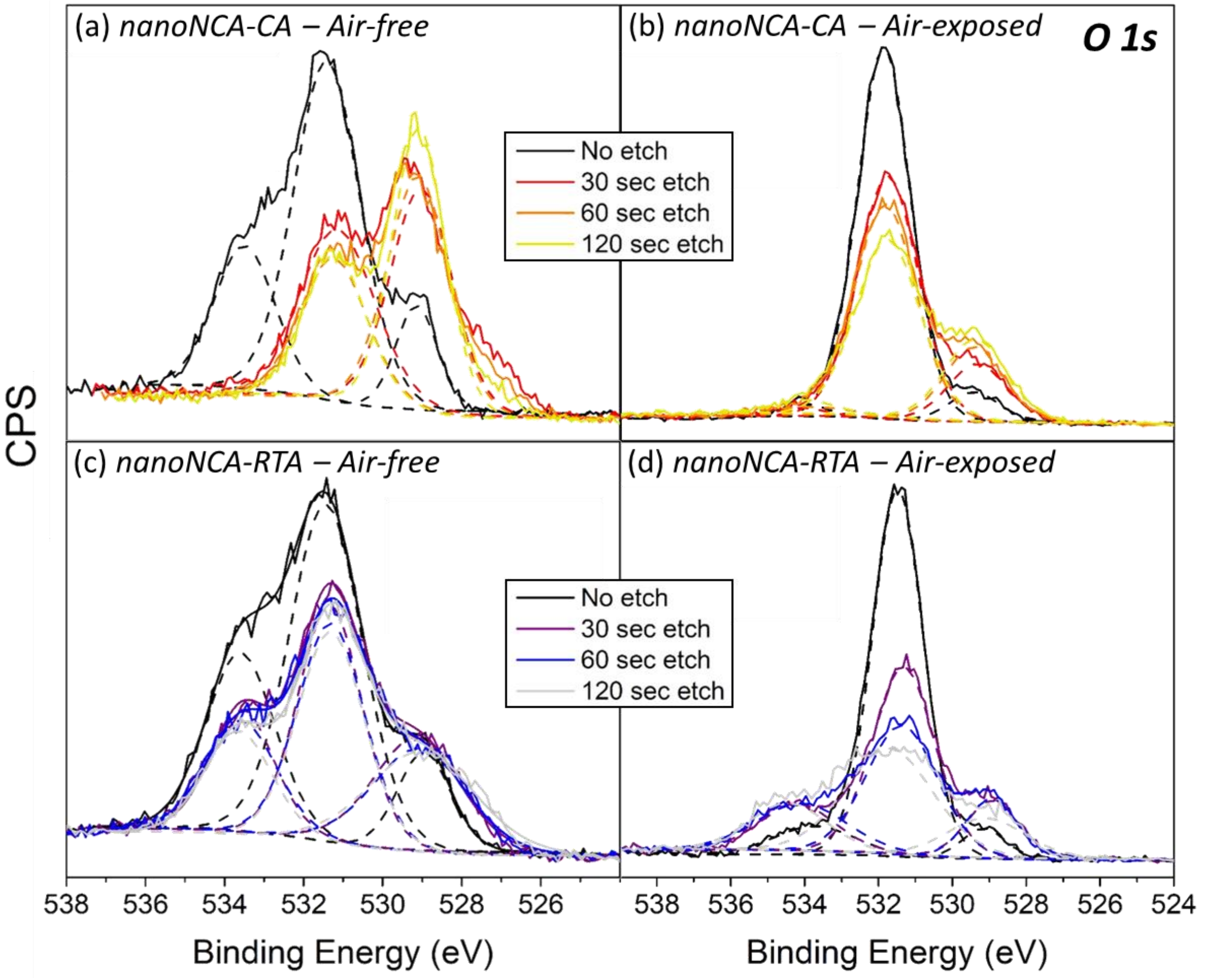

Figure S3.5. O 1s XPS spectra for air-free nanoNCA-CA (a), air-exposed nanoNCA-CA (b), air-free nanoNCA-RTA (c), and air-exposed nanoNCA-RTA (d) with argon-ion etching. For the air-free samples, the O 1s spectra without etching is shown in black, 30 seconds of etching in red, 60 seconds of etching in orange, and 120 seconds in yellow. For the air-exposed samples, no etching is shown in black, 30 seconds of etching in purple, 60 seconds of etching in blue, and 120 seconds in grey. The O 1s peak for NCA-lattice oxygen is around 529.0 eV and surface oxide impurities are around 531.4 eV and 533.9 eV.

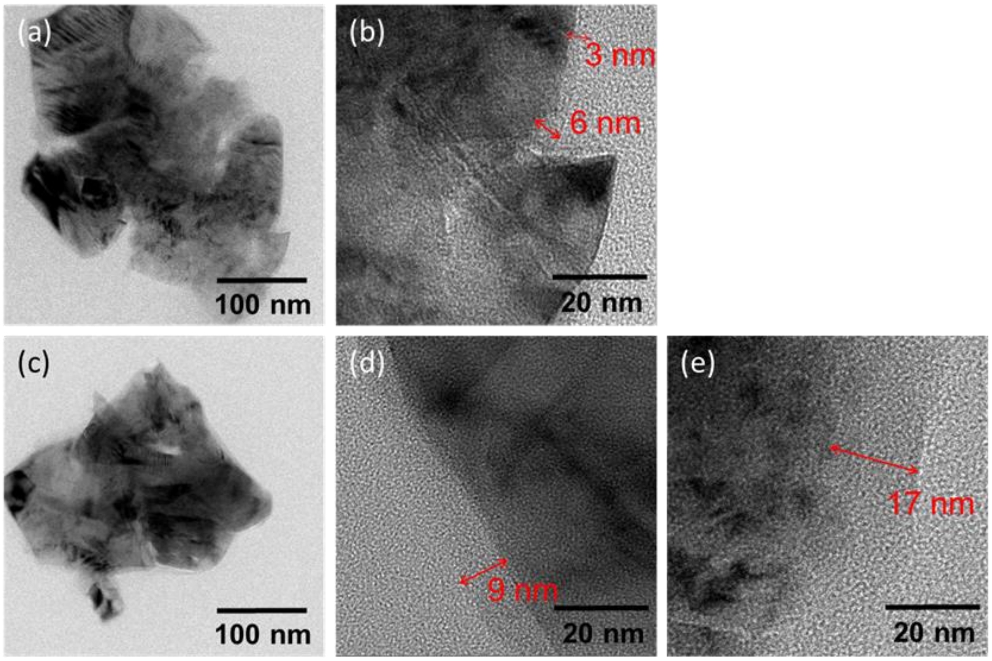

Figure S3.6. (a-b) TEM images of nanoNCA-CA; low-magnification (a) and high-magnification (b). (c-e) TEM images of nanoNCA-RTA; low-magnification (c) and high-magnification (d-e). The thickness of the amorphous surface layer is indicated by red arrows in the high-magnification images.

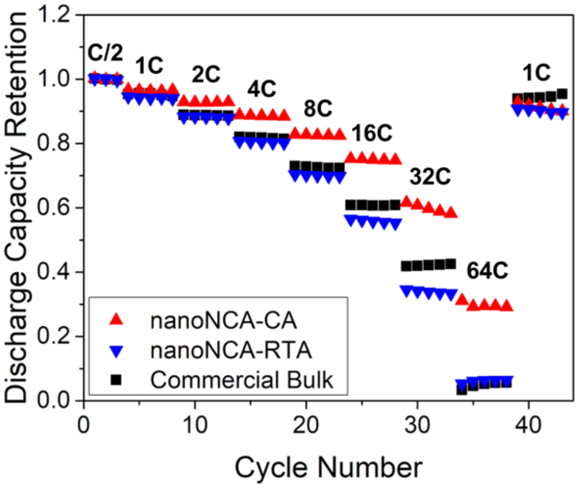

Figure S3.7. The galvanostatic discharge capacity retention of nanoNCA-CA (red), nanoNCA-RTA (blue), and commercial bulk (black) NCA from C/2 to 64C.

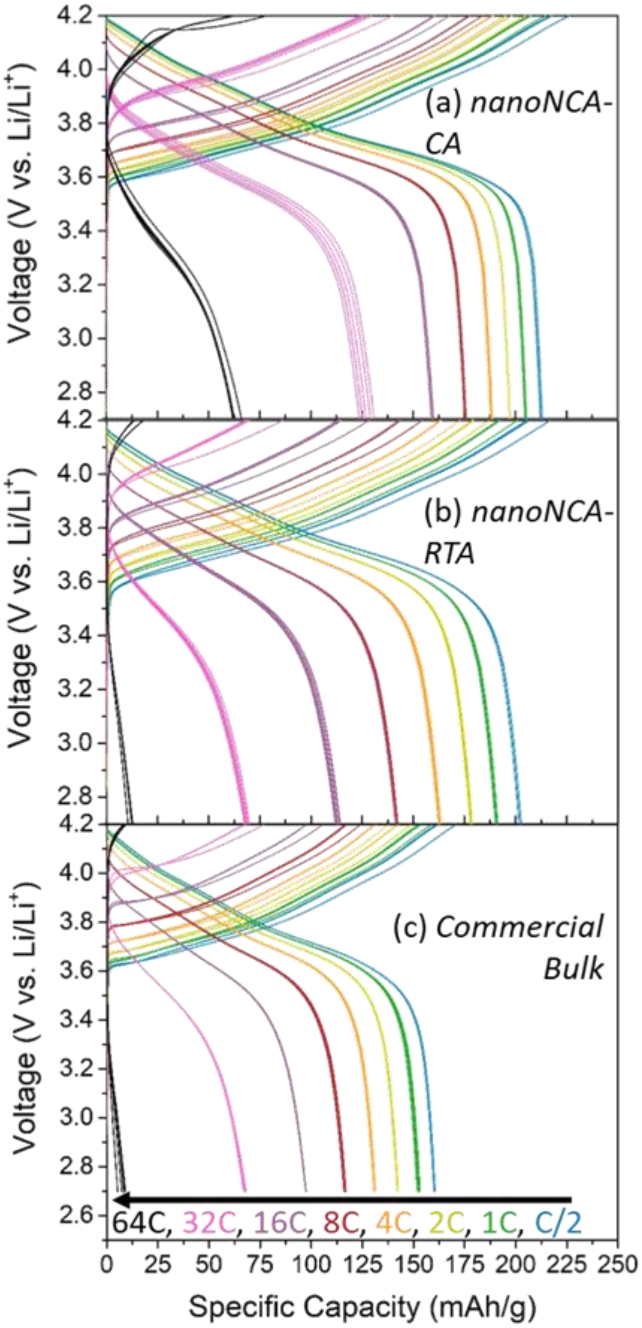

Figure S3.8. Galvanostatic charge and discharge curves for nanoNCA-CA (a), nanoNCA-RTA (b), and commercial bulk (c) NCA at various rates from C/2 to 64C.

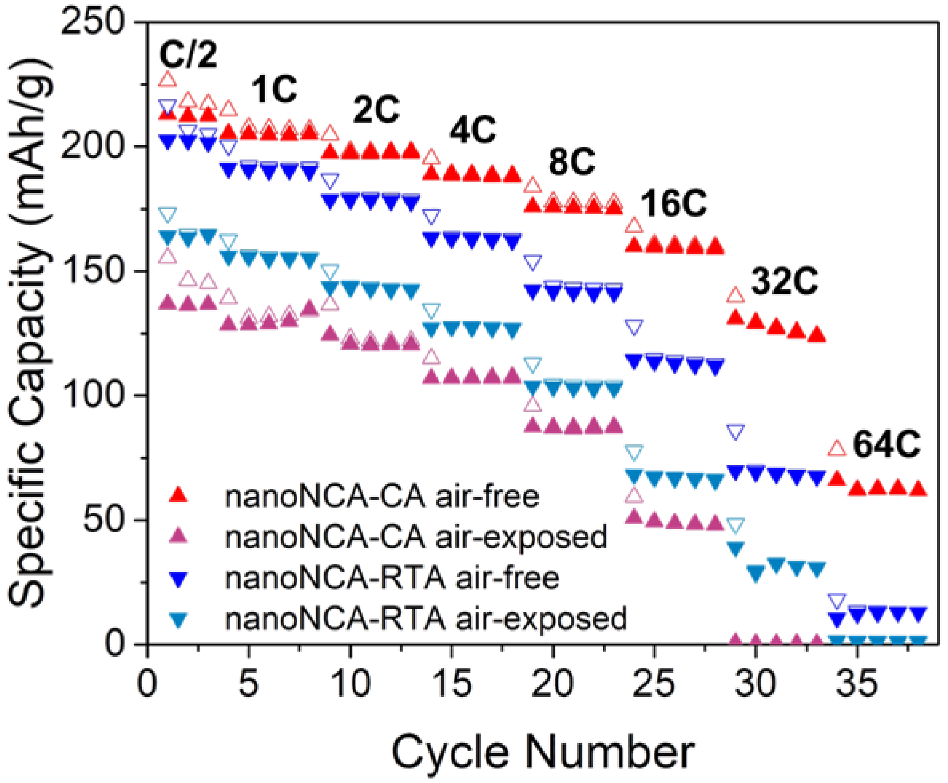

Figure S3.9. Comparison of the galvanostatic rate performance for air-free nanoNCA-CA (red), air-exposed nanoNCA-CA (dark pink), air-free nanoNCA-RTA (dark blue), and air-exposed nanoNCA-RTA (light blue) NCA samples. The specific capacity for charge is shown with an open symbol and the specific capacity for discharge is shown with a closed symbol.

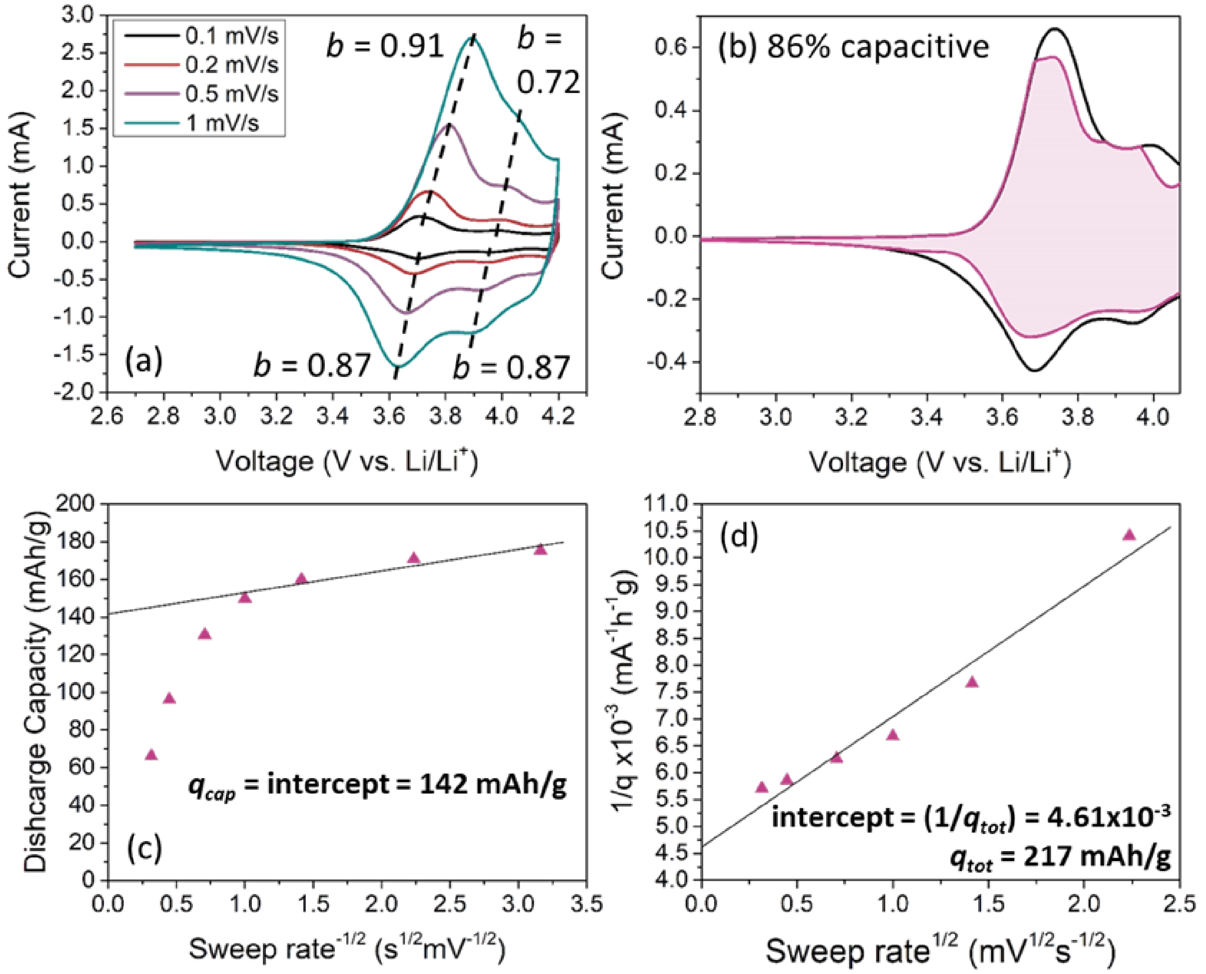

Figure S3.10. Kinetic analyses for air-exposed nanoNCA-CA. (a) CVs at various sweep rates to determine *b*-values, which are displayed on graph. (b) k_1/k_2 analysis performed at a sweep rate of 0.2 mV/s, capacitive contribution is shown as the shaded part of the graph (pink). (c) Trasatti analysis to determine q_{cap}, (d) and to determine q_{tot}.

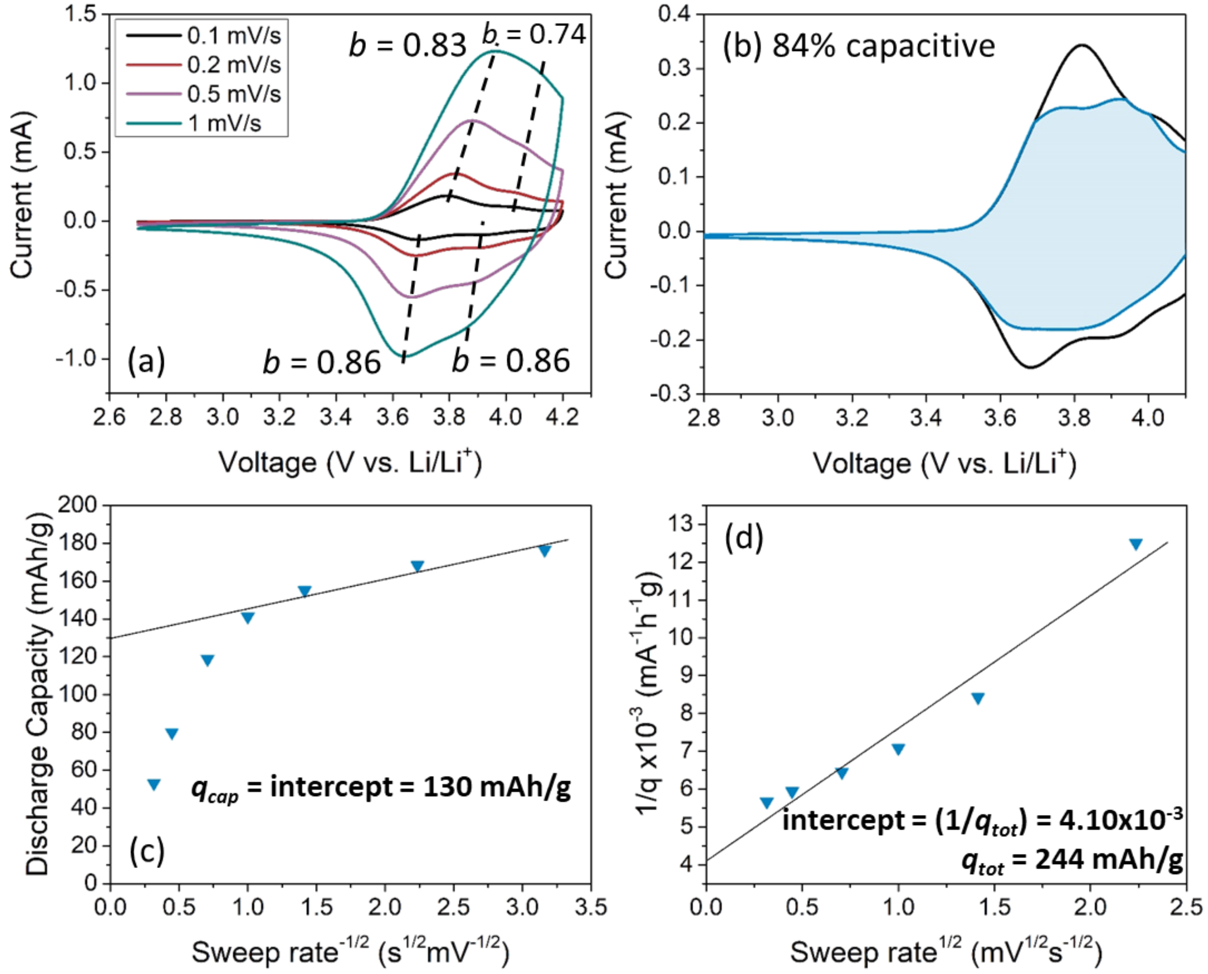

Figure S3.11. Kinetic analyses for air-exposed nanoNCA-RTA. (a) CVs at various sweep rates to determine *b*-values, which are displayed on graph. (b) k_1/k_2 analysis performed at a sweep rate of 0.2 mV/s, capacitive contribution is shown as the shaded part of the graph (light blue). (c) Trasatti analysis to determine q_{cap}, (d) and to determine q_{tot}.

Table S3.1. Summary of kinetic analyses results for nanoNCA-CA and nanoNCA-RTA NCA samples that were kept air-free or exposed to air

Sample	Capacitive % - Trasatti analysis	Average *b*-values	Capacitive % - k_1/k_2 analysis
nanoNCA-CA (air-free)	79%	0.92	88%
nanoNCA-CA (air-exposed)	65%	0.84	86%
nanoNCA-RTA (air-free)	73%	0.90	85%
nanoNCA-RTA (air-exposed)	53%	0.82	84%

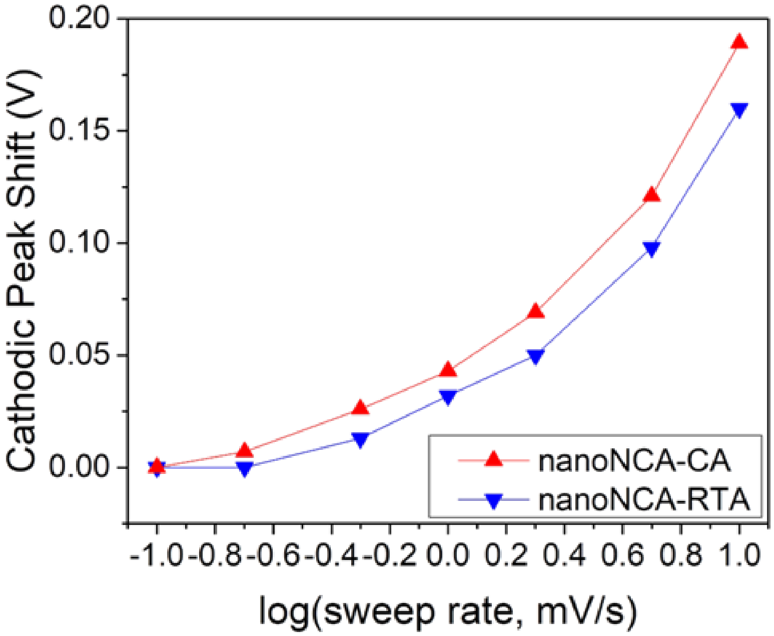

Figure S3.12. Cathodic peak shift for nanoNCA-CA (red) and nanoNCA-RTA (blue).

3.6 References

(1) Choi, C.; Ashby, D. S.; Butts, D. M.; DeBlock, R. H.; Wei, Q.; Lau, J.; Dunn, B. Achieving High Energy Density and High Power Density with Pseudocapacitive Materials. *Nat. Rev. Mater.* **2020**, *5*, 5–19. https://doi.org/10.1038/s41578-019-0142-z.

(2) Augustyn, V.; Simon, P.; Dunn, B. Pseudocapacitive Oxide Materials for High-Rate Electrochemical Energy Storage. *Energy Environ. Sci.* **2014**, *7* (5), 1597–1614. https://doi.org/10.1039/c3ee44164d.

(3) Liu, T.-C.; Pell, W. G.; Conway, B. E.; Roberson, S. L. Behavior of Molybdenum Nitrides as Materials for Electrochemical Capacitors. *J. Electrochem. Soc.* **1998**, *145* (6), 1882–188. https://doi.org/10.1149/1.1838571.

(4) Galizzioli, D.; Tantardini, F.; Trasatti, S. Ruthenium Dioxide: A New Electrode Material. I. Behaviour in Acid Solutions of Inert Electrolytes. *J. Appl. Electrochem.* **1974**, *4*, 57–67. https://doi.org/10.1007/BF00615906.

(5) Zheng, J. P.; Cygan, P. J.; Jow, T. R. Hydrous Ruthenium Oxide as an Electrode Material for Electrochemical Capacitors. *J. Electrochem.* **1995**, *142* (8), 2699–2703. https://doi.org/10.1149/1.2050077.

(6) Dmowski, W.; Egami, T.; Swider-Lyons, K. E.; Love, C. T.; Rolison, D. R. Local Atomic Structure and Conduction Mechanism of Nanocrystalline Hydrous RuO_2 from X-Ray Scattering. *J. Phys. Chem. B* **2002**, *106* (49), 12677–12683. https://doi.org/10.1021/jp026228l.

(7) Augustyn, V.; Come, J.; Lowe, M. A.; Kim, J. W.; Taberna, P.-L.; Tolbert, S. H.; Abruña, H. D.; Simon, P.; Dunn, B. High-Rate Electrochemical Energy Storage through Li^+

Intercalation Pseudocapacitance. *Nat. Mater.* **2013**, *12*, 518–522. https://doi.org/10.1038/nmat3601.

(8) Come, J.; Augustyn, V.; Kim, J. W.; Rozier, P.; Taberna, P.-L.; Gogotsi, P.; Long, J. W.; Dunn, B.; Simon, P. Electrochemical Kinetics of Nanostructured Nb_2O_5 Electrodes. *J. Electrochem. Soc.* **2014**, *161* (5), A718–A725. https://doi.org/10.1149/2.040405jes.

(9) Kodama, R.; Terada, Y.; Nakai, I.; Komaba, S.; Kumagai, N. Electrochemical and In Situ XAFS-XRD Investigation of Nb_2O_5 for Rechargeable Lithium Batteries. *J. Electrochem. Soc.* **2006**, *153* (3), A583–A588. https://doi.org/10.1149/1.2163788.

(10) Kim, H.-S.; Cook, J. B.; Tolbert, S. H.; Dunn, B. The Development of Pseudocapacitive Properties in Nanosized-MoO_2. *J. Electrochem. Soc.* **2015**, *162* (5), A5083–A5090. https://doi.org/10.1149/2.0141505jes.

(11) Zhu, Y.; Ji, X.; Cheng, S.; Chern, Z. Y.; Jia, J.; Yang, L.; Luo, H.; Yu, J.; Peng, X.; Wang, J.; Zhou, W.; Liu, M. Fast Energy Storage in Two-Dimensional MoO_2 Enabled by Uniform Oriented Tunnels. *ACS Nano* **2019**, *13* (8), 9091–9099. https://doi.org/10.1021/acsnano.9b03324.

(12) Yang, L. C.; Sun, W.; Zhong, Z. W.; Liu, J. W.; Gao, Q. S.; Hu, R. Z.; Zhu, M. Hierarchical MoO_2/N-Doped Carbon Heteronanowires with High Rate and Improved Long-Term Performance for Lithium-Ion Batteries. *J. Power Sources* **2016**, *306*, 78–84. https://doi.org/10.1016/j.jpowsour.2015.11.073.

(13) Cook, J. B.; Kim, H. S.; Yan, Y.; Ko, J. S.; Robbennolt, S.; Dunn, B.; Tolbert, S. H. Mesoporous MoS_2 as a Transition Metal Dichalcogenide Exhibiting Pseudocapacitive Li

and Na-Ion Charge Storage. *Adv. Energy Mater.* **2016**, *6* (9), 1–12. https://doi.org/10.1002/aenm.201501937.

(14) Cook, J. B.; Lin, T. C.; Kim, H. S.; Siordia, A.; Dunn, B. S.; Tolbert, S. H. Suppression of Electrochemically Driven Phase Transitions in Nanostructured MoS_2 Pseudocapacitors Probed Using Operando X-Ray Diffraction. *ACS Nano* **2019**, *13* (2), 1223–1231. https://doi.org/10.1021/acsnano.8b06381.

(15) Mahmood, Q.; Park, S. K.; Kwon, K. D.; Chang, S. J.; Hong, J. Y.; Shen, G.; Jung, Y. M.; Park, T. J.; Khang, S. W.; Kim, W. S.; Kong, J.; Park, H. S. Transition from Diffusion-Controlled Intercalation into Extrinsically Pseudocapacitive Charge Storage of MoS_2 by Nanoscale Heterostructuring. *Adv. Energy Mater.* **2016**, *6* (1), 1501115. https://doi.org/10.1002/aenm.201501115.

(16) Yoo, H. D.; Li, Y.; Liang, Y.; Lan, Y.; Wang, F.; Yao, Y. Intercalation Pseudocapacitance of Exfoliated Molybdenum Disulfide for Ultrafast Energy Storage. *ChemNanoMat* **2016**, *2* (7), 688–691. https://doi.org/10.1002/cnma.201600117.

(17) Lesel, B. K.; Cook, J. B.; Yan, Y.; Lin, T. C.; Tolbert, S. H. Using Nanoscale Domain Size to Control Charge Storage Kinetics in Pseudocapacitive Nanoporous $LiMn_2O_4$ Powders. *ACS Energy Lett.* **2017**, *2* (10), 2293–2298. https://doi.org/10.1021/acsenergylett.7b00634.

(18) Lesel, B. K.; Ko, J. S.; Dunn, B.; Tolbert, S. H. Mesoporous $Li_xMn_2O_4$ Thin Film Cathodes for Lithium-Ion Pseudocapacitors. *ACS Nano* **2016**, *10* (8), 7572–7581. https://doi.org/10.1021/acsnano.6b02608.

(19) Okubo, M.; Mizuno, Y.; Yamada, H.; Kim, J.; Hosono, E.; Zhou, H.; Kudo, T.; Honma, I.

Fast Li-Ion Insertion into Nanosized $LiMn_2O_4$ without Domain Boundaries. *ACS Nano* **2010**, *4* (2), 741–752. https://doi.org/10.1021/nn9012065.

(20) Xia, H.; Luo, Z.; Xie, J. Nanostructured $LiMn_2O_4$ and Their Composites as High-Performance Cathodes for Lithium-Ion Batteries. *Prog. Nat. Sci. Mater. Int.* **2012**, *22* (6), 572–584. https://doi.org/10.1016/j.pnsc.2012.11.014.

(21) Okubo, M.; Hosono, E.; Kim, J.; Enomoto, M.; Kojima, N.; Kudo, T.; Zhou, H.; Honma, I. Nanosize Effect on High-Rate Li-Ion Intercalation in $LiCoO_2$ Electrode. *J. Am. Chem. Soc.* **2007**, *129* (23), 7444–7452. https://doi.org/10.1021/ja0681927.

(22) Li, W.; Reimers, J. N.; Dahn, J. R. In Situ X-Ray Diffraction and Electrochemical Studies of $Li_{1-x}NiO_2$. *Solid State Ionics* **1993**, *67* (1–2), 123–130. https://doi.org/10.1016/0167-2738(93)90317-V.

(23) Zhu, X.; Zhan, H.; Liu, H.; Zhou, Y. Synthesis and Characterization of $LiNi_{0.95-x}Co_xAl_{0.05}O_2$ for Lithium-Ion Batteries. *Rare Met.* **2006**, *25* (4), 303–308. https://doi.org/10.1016/S1001-0521(06)60058-2.

(24) Basile, V. M.; Lai, C.-H.; Choi, C. S.; Butts, D. M.; King, S. C.; Dunn, B. S.; Tolbert, S. H. Nanostructured $LiNi_{0.80}Co_{0.15}Al_{0.05}O_2$ (NCA) for Fast-Charging, High-Capacity Cathodes. *In preparation.*

(25) Ruan, Z.; Zhu, Y.; Teng, X. Effect of Pre-Thermal Treatment on the Lithium Storage Performance of $LiNi_{0.8}Co_{0.15}Al_{0.05}O_2$. *J. Mater. Sci.* **2016**, *51* (3), 1400–1408. https://doi.org/10.1007/s10853-015-9459-1.

(26) Delmas, C.; Pérès, J. P.; Rougier, A.; Demourgues, A.; Weill, F.; Chadwick, A. V.;

Broussely, M.; Perton, F.; Biensan, P.; Willmann, P. On the Behavior of the Li_xNiO_2 System: An Electrochemical and Structural Overview. *J. Power Sources* **1997**, *68* (1), 120–125. https://doi.org/10.1016/S0378-7753(97)02664-5.

(27) Xiao, P.; Lv, T.; Chen, X.; Chang, C. $LiNi_{0.8}Co_{0.15}Al_{0.05}O_2$: Enhanced Electrochemical Performance from Reduced Cationic Disordering in Li Slab. *Sci. Rep.* **2017**, *7*, 1–8. https://doi.org/10.1038/s41598-017-01657-9.

(28) Rougier, A.; Saadoune, I.; Gravereau, P.; Willmann, P.; Delmas, C. Effect of Cobalt Substitution on Cationic Distribution in $LiNi_{1-y}Co_yO_2$ Electrode Materials. *Solid State Ionics* **1996**, *90* (1–4), 83–90. https://doi.org/10.1016/S0167-2738(96)00370-0.

(29) Faenza, N. V.; Pereira, N.; Halat, D. M.; Vinckeviciute, J.; Bruce, L.; Radin, M. D.; Mukherjee, P.; Badway, F.; Halajko, A.; Cosandey, F.; Grey, C. P.; Van Der Ven, A.; Amatucci, G. G. Phase Evolution and Degradation Modes of R3m $Li_xNi_{1-y-z}Co_yAl_zO_2$ Electrodes Cycled Near Complete Delithiation. *Chem. Mater.* **2018**, *30* (21), 7545–7574. https://doi.org/10.1021/acs.chemmater.8b02720.

(30) Zhuang, G. V.; Chen, G.; Shim, J.; Song, X.; Ross, P. N.; Richardson, T. J. Li_2CO_3 in $LiNi_{0.8}Co_{0.15}Al_{0.05}O_2$ Cathodes and Its Effects on Capacity and Power. *J. Power Sources* **2004**, *134* (2), 293–297. https://doi.org/10.1016/j.jpowsour.2004.02.030.

(31) Kim, J.; Lee, H.; Cha, H.; Yoon, M.; Park, M.; Cho, J. Prospect and Reality of Ni-Rich Cathode for Commercialization. *Adv. Energy Mater.* **2018**, *8* (6), 1–25. https://doi.org/10.1002/aenm.201702028.

(32) Grenier, A.; Liu, H.; Wiaderek, K. M.; Lebens-Higgins, Z. W.; Borkiewicz, O. J.; Piper, L.

F. J.; Chupas, P. J.; Chapman, K. W. Reaction Heterogeneity in $LiNi_{0.8}Co_{0.15}Al_{0.05}O_2$ Induced by Surface Layer. *Chem. Mater.* **2017**, *29* (17), 7345–7352. https://doi.org/10.1021/acs.chemmater.7b02236.

(33) Liu, H.; Yang, Y.; Zhang, J. Investigation and Improvement on the Storage Property of $LiNi_{0.8}Co_{0.2}O_2$ as a Cathode Material for Lithium-Ion Batteries. *J. Power Sources* **2006**, *162* (1), 644–650. https://doi.org/10.1016/j.jpowsour.2006.07.028.

(34) Uddin, M. J.; Alaboina, P. K.; Cho, S. J. Nanostructured Cathode Materials Synthesis for Lithium-Ion Batteries. *Mater. Today Energy* **2017**, *5*, 138–157. https://doi.org/10.1016/j.mtener.2017.06.008.

(35) Liu, Y.; Goebl, J.; Yin, Y. Templated Synthesis of Nanostructured Materials. *Chem. Soc. Rev.* **2013**, *42* (7), 2610–2653. https://doi.org/10.1039/c2cs35369e.

(36) Yan, Q.; Nukala, P.; Chiang, Y. M.; Wong, C. C. Three-Dimensional Metallic Opals Fabricated by Double Templating. *Thin Solid Films* **2009**, *517* (17), 5166–5171. https://doi.org/10.1016/j.tsf.2009.03.094.

(37) Zeng, W. R.; Li, S. F.; Chow, W. K. Review on Chemical Reactions of Burning Poly(Methyl Methacrylate) PMMA. *J. Fire Sci.* **2002**, *20* (5), 401–433. https://doi.org/10.1106/073490402031482.

(38) Alexandridis, P.; Holzwarth, J. F.; Hatton, T. A. Micellization of Poly(Ethylene Oxide)-Poly(Propylene Oxide)-Poly(Ethylene Oxide) Triblock Copolymers in Aqueous Solutions: Thermodynamics of Copolymer Association. *Macromolecules* **1994**, *27* (9), 2414–2425. https://doi.org/10.1021/ma00087a009.

(39) Sorolla-Rosario, D.; Davó-Quiñonero, A.; Bailón-García, E.; Lozano-Castelló, D.; Bueno-López, A. Key-Lock Ceria Catalysts for the Control of Diesel Engine Soot Particulate Emissions. *ChemCatChem* **2020**, *12* (6), 1772–1781. https://doi.org/10.1002/cctc.201902177.

(40) Zhao, D.; Yang, P.; Melosh, N.; Feng, J.; Chmelka, B. F.; Stucky, G. D. Continuous Mesoporous Silica Films with Highly Ordered Large Pore Structures. *Adv. Mater.* **1998**, *10* (16), 1380–1385. https://doi.org/10.1002/(SICI)1521-4095(199811)10:16<1380::AID-ADMA1380>3.0.CO;2-8.

(41) Dunphy, D. R.; Sheth, P. H.; Garcia, F. L.; Brinker, C. J. Enlarged Pore Size in Mesoporous Silica Films Templated by Pluronic F127: Use of Poloxamer Mixtures and Increased Template/SiO_2 Ratios in Materials Synthesized by Evaporation-Induced Self-Assembly. *Chem. Mater.* **2015**, *27* (1), 75–84. https://doi.org/10.1021/cm5031624.

(42) Sörensen, M. H.; Corkery, R. W.; Pedersen, J. S.; Rosenholm, J.; Alberius, P. C. Expansion of the F127-Templated Mesostructure in Aerosol-Generated Particles by Using Polypropylene Glycol as a Swelling Agent. *Microporous Mesoporous Mater.* **2008**, *113* (1–3), 1–13. https://doi.org/10.1016/j.micromeso.2007.10.045.

(43) Hwang, Y. K.; Patil, K. R.; Jhung, S. H.; Chang, J. S.; Ko, Y. J.; Park, S. E. Control of Pore Size and Condensation Rate of Cubic Mesoporous Silica Thin Films Using a Swelling Agent. *Microporous Mesoporous Mater.* **2005**, *78* (2–3), 245–253. https://doi.org/10.1016/j.micromeso.2004.10.026.

(44) Ricardo, N. M. P. S.; Ricardo, N. M. P. S.; Costa, F. de M. L. L.; Bezerra, F. W. A.; Chaibundit, C.; Hermida-Merino, D.; Greenland, B. W.; Burattini, S.; Hamley, I. W.; Keith

Nixon, S.; Yeates, S. G. Effect of Water-Soluble Polymers, Polyethylene Glycol and Poly(Vinylpyrrolidone), on the Gelation of Aqueous Micellar Solutions of Pluronic Copolymer F127. *J. Colloid Interface Sci.* **2012**, *368* (1), 336–341. https://doi.org/10.1016/j.jcis.2011.10.062.

(45) Kwade, A.; Haselrieder, W.; Leithoff, R.; Modlinger, A.; Dietrich, F.; Droeder, K. Current Status and Challenges for Automotive Battery Production Technologies. *Nat. Energy* **2018**, *3*, 290–300. https://doi.org/10.1038/s41560-018-0130-3.

(46) He, G.; Pan, Q.; Rempel, G. L. Synthesis of Poly(Methyl Methacrylate) Nanosize Particles by Differential Microemulsion Polymerization. *Macromol. Rapid Commun.* **2003**, *24* (9), 585–588. https://doi.org/10.1002/marc.200390089.

(47) Fang, J.; Xuan, Y.; Li, Q. Preparation of Polystyrene Spheres in Different Particle Sizes and Assembly of the PS Colloidal Crystals. *Sci. China Technol. Sci.* **2010**, *53* (11), 3088–3093. https://doi.org/10.1007/s11431-010-4110-5.

(48) Huber, R. C.; Ferreira, A. S.; Aguirre, J. C.; Kilbride, D.; Toso, D. B.; Mayoral, K.; Zhou, Z. H.; Kopidakis, N.; Rubin, Y.; Schwartz, B. J.; Mason, T. G.; Tolbert, S. H. Structure and Conductivity of Semiconducting Polymer Hydrogels. *J. Phys. Chem. B* **2016**, *120* (26), 6215–6224. https://doi.org/10.1021/acs.jpcb.6b02202.

(49) Malfatti, L.; Bellino, M. G.; Innocenzi, P.; Soler-Illia, G. J. A. A. One-Pot Route to Produce Hierarchically Porous Titania Thin Films by Controlled Self-Assembly, Swelling, and Phase Separation. *Chem. Mater.* **2009**, *21* (13), 2763–2769. https://doi.org/10.1021/cm900289c.

(50) Liu, W.; Oh, P.; Liu, X.; Lee, M. J.; Cho, W.; Chae, S.; Kim, Y.; Cho, J. Nickel-Rich Layered Lithium Transition-Metal Oxide for High-Energy Lithium-Ion Batteries. *Angew. Chemie - Int. Ed.* **2015**, *54* (15), 4440–4457. https://doi.org/10.1002/anie.201409262.

(51) Ohzuku, T.; Ueda, A.; Nagayama, M.; Iwakoshi, Y.; Komori, H. Comparative Study of $LiCoO_2$, $LiNi_{1/2}Co_{1/2}O_2$ and $LiNiO_2$ for 4 Volt Secondary Lithium Cells. *Electrochim. Acta* **1993**, *38* (9), 1159–1167. https://doi.org/10.1016/0013-4686(93)80046-3.

(52) Arai, H.; Okada, S.; Ohtsuka, H.; Ichimura, M.; Yamaki, J. Characterization and Cathode Performance of $Li_{1-x}Ni_{1+x}O_2$ Prepared with the Excess Lithium Method. *Solid State Ionics* **1995**, *80* (3–4), 261–269. https://doi.org/10.1016/0167-2738(95)00144-U.

(53) Yano, K.; Nandwana, V.; Poudyal, N.; Rong, C. B.; Liu, J. P. Rapid Thermal Annealing of FePt Nanoparticles. *J. Appl. Phys.* **2008**, *104* (1), 013918-1-013918–4. https://doi.org/10.1063/1.2953078.

(54) Guilmard, M.; Pouillerie, C.; Croguennec, L.; Delmas, C. Structural and Electrochemical Properties of $LiNi_{0.70}Co_{0.15}Al_{0.15}O_2$. *Solid State Ionics* **2003**, *160* (1–2), 39–50. https://doi.org/10.1016/S0167-2738(03)00106-1.

(55) You, Y.; Celio, H.; Li, J.; Dolocan, A.; Manthiram, A. Modified High-Nickel Cathodes with Stable Surface Chemistry Against Ambient Air for Lithium-Ion Batteries. *Angew. Chemie - Int. Ed.* **2018**, *57* (22), 6480–6485. https://doi.org/10.1002/anie.201801533.

(56) Lu, Y. C.; Mansour, A. N.; Yabuuchi, N.; Shao-Horn, Y. Probing the Origin of Enhanced Stability of “$AlPO_4$” Nanoparticle Coated $LiCoO_2$ during Cycling to High Voltages: Combined XRD and XPS Studies. *Chem. Mater.* **2009**, *21* (19), 4408–4424.

https://doi.org/10.1021/cm900862v.

(57) Xiong, X.; Wang, Z.; Yue, P.; Guo, H.; Wu, F.; Wang, J.; Li, X. Washing Effects on Electrochemical Performance and Storage Characteristics of $LiNi_{0.8}Co_{0.1}Mn_{0.1}O_2$ as Cathode Material for Lithium-Ion Batteries. *J. Power Sources* **2013**, *222*, 318–325. https://doi.org/10.1016/j.jpowsour.2012.08.029.

(58) Berger, P. R.; Kim, M. Polymer Solar Cells: P3HT:PCBM and Beyond. *J. Renew. Sustain. Energy* **2018**, *10* (1), 013508. https://doi.org/10.1063/1.5012992.

(59) Lai, C.-H.; Ashby, D. S.; Lin, T. C.; Lau, J.; Dawson, A.; Tolbert, S. H.; Dunn, B. S. Application of Poly(3-Hexylthiophene-2,5-Diyl) as a Protective Coating for High Rate Cathode Materials. *Chem. Mater.* **2018**, *30* (8), 2589–2599. https://doi.org/10.1021/acs.chemmater.7b05116.

(60) Enengl, C.; Enengl, S.; Pluczyk, S.; Havlicek, M.; Lapkowski, M.; Neugebauer, H.; Ehrenfreund, E. Doping-Induced Absorption Bands in P3HT: Polarons and Bipolarons. *ChemPhysChem* **2016**, *17* (23), 3836–3844. https://doi.org/10.1002/cphc.201600961.

(61) Gonçalves, R.; Pereira, E. C.; Marchesi, L. F. The Overoxidation of Poly(3-Hexylthiophene) (P3HT) Thin Film: CV and EIS Measurements. *Int. J. Electrochem. Sci.* **2017**, *12* (3), 1983–1991. https://doi.org/10.20964/2017.03.44.

(62) Yang, X.; Chen, J.; Zheng, Q.; Tu, W.; Xing, L.; Liao, Y.; Xu, M.; Huang, Q.; Cao, G.; Li, W. Mechanism of Cycling Degradation and Strategy to Stabilize a Nickel-Rich Cathode. *J. Mater. Chem. A* **2018**, *6* (33), 16149–16163. https://doi.org/10.1039/c8ta03041c.

(63) Mukherjee, P.; Faenza, N. V.; Pereira, N.; Ciston, J.; Piper, L. F. J.; Amatucci, G. G.;

Cosandey, F. Surface Structural and Chemical Evolution of Layered $LiNi_{0.8}Co_{0.15}Al_{0.05}O_2$ (NCA) under High Voltage and Elevated Temperature Conditions. *Chem. Mater.* **2018**, *30* (23), 8431–8445. https://doi.org/10.1021/acs.chemmater.7b05305.

(64) Lindström, H.; Södergren, S.; Solbrand, A.; Rensmo, H.; Hjelm, J.; Hagfeldt, A.; Lindquist, S.-E. Li^+ Ion Insertion in TiO_2 (Anatase). 2. Voltammetry on Nanoporous Films. *J. Phys. Chem. B* **1997**, *101* (39), 7717–7722. https://doi.org/10.1021/jp970490q.

(65) Ardizzone, S.; Fregonara, G.; Trasatti, S. "Inner" and "Outer" Active Surface of RuO_2 Electrodes. *Electrochim. Acta* **1990**, *35* (1), 263–267. https://doi.org/10.1016/0013-4686(90)85068-X.

(66) Chen, Y.; Li, P.; Zhao, S.; Zhuang, Y.; Zhao, S.; Zhou, Q.; Zheng, J. Influence of Integrated Microstructure on the Performance of $LiNi_{0.8}Co_{0.15}Al_{0.05}O_2$ as a Cathodic Material for Lithium Ion Batteries. *RSC Adv.* **2017**, *7* (46), 29233–29239. https://doi.org/10.1039/c7ra04206j.

(67) Aurbach, D.; Gamolsky, K.; Markovsky, B.; Salitra, G.; Gofer, Y.; Heider, U.; Oesten, R.; Schmidt, M. The Study of Surface Phenomena Related to Electrochemical Lithium Intercalation into Li_xMO_y Host Materials (M = Ni, Mn). *J. Electrochem. Soc.* **2000**, *147* (4), 1322–1331. https://doi.org/10.1149/1.1393357.

(68) Tran, H. Y.; Greco, G.; Täubert, C.; Wohlfahrt-Mehrens, M.; Haselrieder, W.; Kwade, A. Influence of Electrode Preparation on the Electrochemical Performance of $LiNi_{0.8}Co_{0.15}Al_{0.05}O_2$ Composite Electrodes for Lithium-Ion Batteries. *J. Power Sources* **2012**, *210*, 276–285. https://doi.org/10.1016/j.jpowsour.2012.03.017.

(69) Griffith, K. J.; Forse, A. C.; Griffin, J. M.; Grey, C. P. High-Rate Intercalation without Nanostructuring in Metastable Nb_2O_5 Bronze Phases. *J. Am. Chem. Soc.* **2016**, *138* (28), 8888–8899. https://doi.org/10.1021/jacs.6b04345.

(70) Lai, C. H.; Ashby, D.; Moz, M.; Gogotsi, Y.; Pilon, L.; Dunn, B. Designing Pseudocapacitance for Nb_2O_5/Carbide-Derived Carbon Electrodes and Hybrid Devices. *Langmuir* **2017**, *33* (37), 9407–9415. https://doi.org/10.1021/acs.langmuir.7b01110.

CHAPTER 4

Nanostructured $LiNi_{0.6}Mn_{0.2}Co_{0.2}O_2$ (NMC622) for Fast-Charging Lithium-Ion Batteries

4.1 Introduction

Lithium-ion batteries are used extensively in electric vehicles (EVs), but their long charging times discourage the large-scale implementation of EVs. While EVs can be charged quickly with “Supercharger” stations, which allow the battery to be charged up to 80% state of charge in about 40 minutes, this leads to large capacity fading and mechanical failure with continued use.[1] Therefore, there is a need for battery materials that can be charged quickly without causing damage to the material itself. This can be accomplished with the use of pseudocapacitive materials, which are materials that store charge through faradaic redox reactions at fast time scales, resulting in high energy density and high power density, respectively.[2–5] Pseudocapacitive materials are able to charge and discharge quickly because they are not limited by slow lithium-ion diffusion or discontinuous, first-order phase transitions.[4,6] This can be intrinsic to the material or can be induced when a traditional battery material is nanostructured such that lithium-ion diffusion is no longer rate limiting and first-order phase transitions are suppressed.[4,6–8] Materials can be examined for characteristics of pseudocapacitance, such as faradaic charge storage with highly capacitive behavior and suppressed phase transitions, using a number of electrochemical kinetic analysis methods.[3–6,9–12]

Examples of battery materials that display pseudocapacitive properties upon nanostructuring include MoO_2,[13–15] MoS_2,[8,16–18] $LiCoO_2$,[19] and $LiMn_2O_4$.[20–23] There are many ways to nanostructure materials, such as by chemical vapor deposition, chemical etching, hydrothermal, or sol-gel synthesis.[24] Here, we focused on template-directed sol-gel synthesis for its ease and tunability.[25] Specifically, the use of the Pluronic block co-polymer F127 (poly(ethylene oxide)$_{100}$-*b*-poly(propylene oxide)$_{65}$-*b*-poly(ethylene oxide)$_{100}$ (PEO_{100}-*b*-PPO_{65}-*b*-PEO_{100})) as a template, which forms micelles in dilute aqueous solutions, making it ideal for the formation of a porous structure.[26,27] Because F127 by itself forms small micelle sizes (~8 nm),[28] pure homopolymers of PPO were added to increase the size of the micelle template in solution. PPO homopolymers have been shown to associate with the PPO core of F127 micelles when they are added together in solution, which has led to increased pore sizes when F127 and PPO are used as a template for nanoporous silica materials.[29–31] Additionally, both F127 and PPO are cheap and commercially available, which is important for the scaling-up that is necessary for the commercial manufacturing of lithium-ion batteries.[32]

Layered nickel-rich cathode materials, such as $LiNi_xMn_yCo_zO_2$ (NMC) and $LiNi_{0.80}Co_{0.15}$-$Al_{0.05}O_2$ (NCA), have been the focus of intense recent study because of their higher capacity and decreased use of cobalt, compared to commonly used commercial $LiCoO_2$ cathodes.[33,34] In addition, NMC and NCA have suppressed first-order phase transitions in the bulk material.[35,36] This is of interest because it means that the kinetic limitations associated with nucleation and propagation of the phase transition should not control Li^+ intercalation kinetics. As a result, nanostructuring the materials to reduce lithium-ion diffusion distances can potentially be used to achieve fast charging in a process that is sometimes described as pseudocapacitive charge storage. Indeed, we have previously shown this to be the case in nanostructured NCA.[37,38] Here, we nanostructure NMC to study the effects of decreased particle size and increased nanoscale porosity on the electrochemical properties of NMC cathodes.

Unlike NCA, which has been found to have optimal properties at one stoichiometry,[33,39] NMC has found success in a range of stoichiometries, such as $LiNi_{1/3}Mn_{1/3}Co_{1/3}O_2$ (NMC111),

$LiNi_{0.6}Mn_{0.2}Co_{0.2}O_2$ (NMC622), and $LiNi_{0.8}Mn_{0.1}Co_{0.1}O_2$ (NMC811).[40,41] Cathode materials with high amounts of nickel benefit from high capacities, while the manganese in the NMC structure acts to improve thermal and structural stability.[40–42] However, as more Mn^{4+} is added in the structure, there is an increase in the amount of Ni^{2+} to balance the charge.[40,43,44] A high amount of Ni^{2+} is not ideal because it leads to cation mixing, where Ni^{2+} can migrate to the lithium layer due to the similar ionic radii of Ni^{2+} (0.68 Å) and Li^+ (0.74 Å).[44,45] When the material is charged, the Ni^{2+} in the lithium layer is oxidized to Ni^{3+} (ionic radius = 0.56 Å),[45] leading to the local collapse of the lithium layers, which impedes lithium-ion diffusion.[46] Fortunately, cobalt in the NMC structure acts to decrease some of the cation mixing. It has been proposed that the smaller size of Co^{3+} (ionic radius = 0.55 Å) decreases the transition metal inter-layer distances and that Co^{3+} relieves intra-plane magnetic frustrations, which make Ni^{2+} migration to the Li^+ layer more difficult.[44,47] Thus, altering the stoichiometry of NMC results in different advantages and disadvantages. NMC materials with low nickel contents, like NMC111, have high thermal stability and capacity retention, but lower capacity and rate capability.[41,48] While NMC materials with high nickel contents, like NMC811, have low thermal stability and capacity retention, but higher capacity and rate capability.[41,48] NMC materials with nickel contents in-between these two endpoints generally fall in line with this trend, thus the stoichiometric ratios can be tuned to optimize specific performance metrics.[41]

In considering the synthesis of nanoporous NMC, which by definition has increased surface area, one must also consider surface reactivity. Unfortunately, nickel-rich cathode materials are known to be sensitive to carbon dioxide and water in the ambient air. The carbon dioxide and water react with lithium species on the surface to form insulating layers of Li_2CO_3 and LiOH, which impede lithium-ion diffusion.[49] It has been observed that NMC materials with greater nickel contents form thicker insulating surface layers. For example, a thicker surface layer is formed on NMC811 than on NMC622, while little to no insulating surface layers are formed on NMC111.[50–52] Because we are interested in nanostructuring NMC, which will increase the amount of surface available to react with carbon dioxide and water in the air, this can potentially lead to the formation of greater amounts of Li_2CO_3. Thus these nanostructured materials will be kept as air-free as possible to minimize their air exposure.[52]

Taking the advantages and disadvantages of the NMC materials into consideration, we chose to study NMC622 for nanostructuring because of the balance of high capacity and rate capability that will be good for fast-charging, combined with moderate stability. Additionally, previous studies on NMC materials have shown that NMC622 has the highest lithium-ion diffusion coefficient, which is ideal for studying the fast-charging capabilities of NMC upon nanostructuring.[53] We note that NMC is an extensively studied cathode material for lithium-ion batteries and so there have been some studies on different forms of nanostructured NMC. The studies have mostly focused on NMC111,[54–58] however, with fewer examples of nanostructured NMC622. Ahn *et. al.* synthesized agglomerated nanoparticles of NMC622 by a combustion method, resulting in particle sizes around 300 nm, however the fastest (dis)charge rate used was 4C, which showed only 90 mAh/g capacity.[59] Additionally, a spray drying assisted solid-state method was used by Yue *et. al.* to produce NMC622 with particle sizes ranging from 400 nm to 1 μm; this material had a higher capacity of 125 mAh/g, but again was only (dis)charged a moderate rate of 5C.[60] In this paper, we synthesize nanostructured NMC622, with small particle sizes (~85-215 nm), and study charge/discharge characteristics at rates up to 64C. Importantly, to the best of our knowledge, none of the NMC materials have been analyzed for their pseudocapacitive properties and in this paper we will analyze the nanostructured NMC622 materials with a number of electrochemical kinetic methods to better understand the mechanism of charge storage.

4.2 Experimental Methods

4.2.1 Materials

Lithium nitrate (98+%) and carbon nanofibers (CNF, DxL 100 nm x 20-200 μm) were purchased from Sigma. Diethyl carbonate (DEC, anhydrous, ≥99%) was purchased from Aldrich. Ethylene carbonate (EC, anhydrous, 99%) and dimethyl carbonate (DMC, anhydrous, ≥99%) were purchased from Sigma-Aldrich. Nickel nitrate hexahydrate (99.9985%), manganese nitrate tetrahydrate (98%), and PPO (MW = 400 g/mol) were purchased from Alfa Aesar. Cobalt nitrate hexahydrate (99+%) and *o*-xylenes (99%, Extra Dry) were purchased from Acros Organics. Pluronic F127 ($PEO_{100}PPO_{65}PEO_{100}$ MW = 12600 g/mol) was purchased from BASF. Multi-walled carbon nanotubes (MWCNT, >95%, OD: 5-15 nm) were purchased from US Research Nanomaterials Inc. Poly(3-hexylthioophene-2,5-diyl) (P3HT, 15000-30000 MW, 1.6-1.8 PDI, 89-94% regioregularity) was purchased from Rieke Metals. Lithium hexafluorophosphate (97.0+%) was ordered from TCI America.

4.2.2 Synthesis of nanostructured NMC

In container ‘A’, a 6.8 wt% solution of Pluronic F127 was formed in 4 mL of water. The F127 was allowed to dissolve completely before the addition of pure homopolymers of PPO400 in a weight ratio of 1:20 PPO400:F127. In container ‘B’, stoichiometric amounts (for NMC622) of nickel nitrate hexahydrate, manganese nitrate tetrahydrate, and cobalt nitrate hexahydrate were dissolved in 16 mL of water, so that the total transition metal concentration (Ni+Mn+Co) was 0.6 M. Excess lithium nitrate was also dissolved in the solution so that the molar ratio of

Li/(Ni+Mn+Co) was 1.05. After containers ‘A’ and ‘B’ were stirred for 1 hour, they were combined and stirred for another 2 hours. Then the water was evaporated from the solution at 80 °C overnight, before heating at 180 °C for 4 hours to remove any remaining water, the oven was then ramped to 450 °C at 1 °C/min, and then held at 450 °C for 2 hours under oxygen flow to remove the polymer templates from the NMC precursor. The precursor was then heated in a tube furnace under oxygen flow with a 1-hour ramp to either 800 °C (NMC-800 °C), 850 °C (NMC-850 °C), or 900 °C (NMC-900 °C) for 2 hours. After heating, the samples were cooled to 350 °C and then immediately transferred to a glovebox antechamber to minimize any reactions of the NMC material with air.

4.2.3 Characterization

Scanning electron microscopy (SEM) was performed using a JOEL JSM-6700F field emission scanning electron microscope. From the SEM images, the sizes of 200 particles were measured using ImageJ to create a particle size distribution for each sample. The particle sizes were binned in increments of 10 nm and fit with a log-normal fit to find the peak in the pore size distribution. X-ray diffraction (XRD) was performed using a Bruker D8 Discover Powder X-ray Diffractometer, using a sample holder to ensure consistent sample height between samples. MAUD software was used to perform Rietveld refinement of the XRD patterns. A Micromeritics TriStar II 3020 porosimeter was used for nitrogen porosimetry measurements. The adsorption isotherm was used to determine the surface area of the materials using the Brunauer-Emmett-Teller (BET) model and the volume weighted pore size distribution using the Barrett-Joyner-Halenda (BJH) model with the Halsey equation and Faas correction.

4.2.4 Electrochemical Characterization

The NMC electrodes were prepared inside an argon-atmosphere glovebox and were composed of 80 wt% active material, 5 wt% MWCNT, 10 wt% CNF, and 5 wt% P3HT binder in *o*-xylenes (15 wt% solution). The slurries were cast onto carbon-coated aluminum current collectors, then dried on a hotplate for 4 hours before being dried in the glovebox antechamber under vacuum overnight. Electrodes of 0.7 cm^2 were punched and an average mass was calculated using surrounding electrodes. The electrodes were then assembled in CR2032 coin cells, with a glass microfiber separator (Whatman) and 1 M $LiPF_6$ in 1:1:1 EC:DMC:DEC electrolyte, against a lithium metal anode. The active material mass loading of NMC ranged from 0.9-1.0 mg/cm^2. Galvanostatic cycling was carried out using an Arbin Instruments BT2000 battery testing system and cyclic voltammetry was performed with a BioLogic VSP potentiostat/galvanostat. The cells were cycled from 3.2-4.2 V vs. Li/Li$^+$. Additionally, galvanostatic intermittent titration technique (GITT) measurements were performed using an Arbin Instruments BT2000 battery testing system from 3.2-4.2 V vs. Li/Li$^+$. A charging rate of C/10 was used to apply a current pulse for 30 minutes, which was followed by 30 minutes of relaxation; current and relaxation pulses were applied until a voltage of 4.2 V was reached.

4.3 Results and Discussion

Nanostructured NMC622 was synthesized using nitrate salts in a sol-gel-like synthesis with a polymer template consisting of F127 micelles swollen with PPO homopolymers, which we previously found to have solution phase diameters of about 30 nm.[38] This F127/PPO template was used because F127 by itself makes only very small micelles (sizes ~8 nm).[28] Because of significant grain growth that occurs for NMC at the high temperatures required for crystallization, a larger template that produces porous materials with thicker walls was desired. It has been shown that the PPO homopolymers associate with the PPO core of the F127 micelle, thereby increasing the overall template size.[29,31] The polymer template was removed by heating to 450 °C under oxygen, leaving a nanoporous NMC precursor with a surface area of 31±3 m^2/g, a porosity of 24±4%, and a pore size distribution around 10 nm (Fig. S4.1).

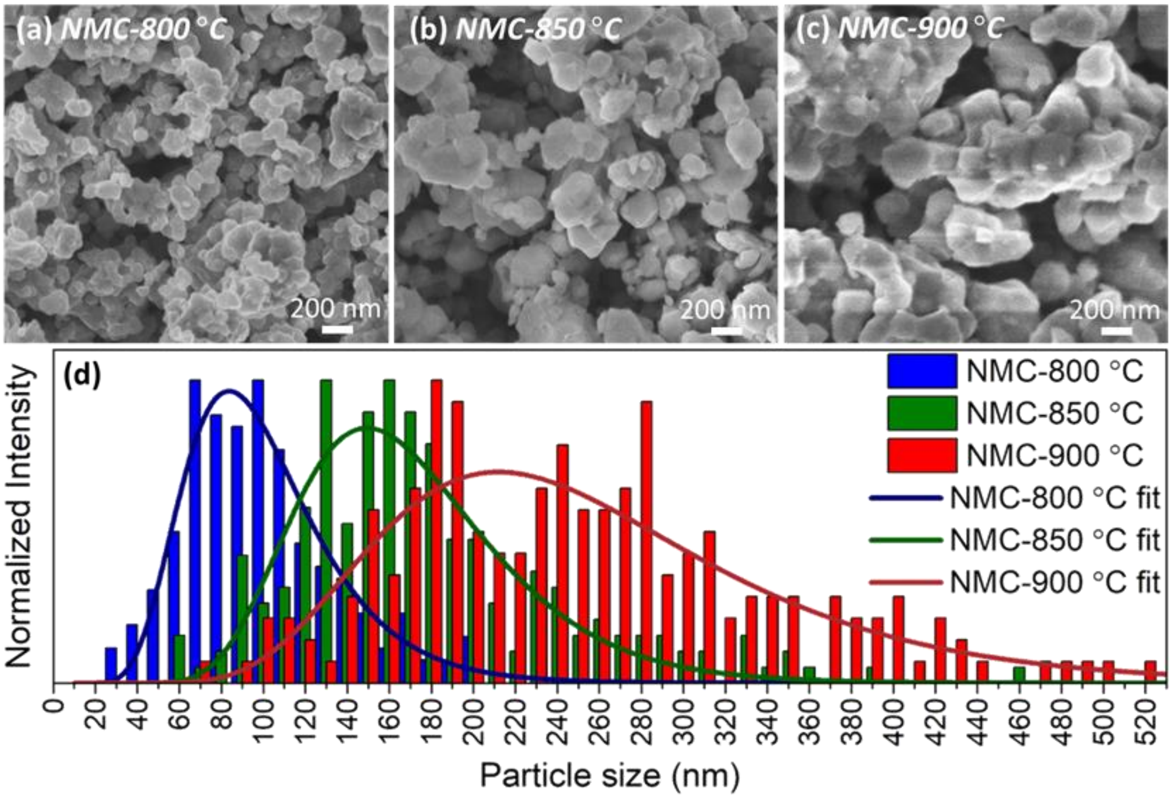

Figure 4.1. High-magnification SEM images of NMC-800 °C (a), NMC-850 °C (b), and NMC-900 °C (c). (d) Particle size distribution histograms for particles of NMC-800 °C (blue), NMC-850 °C (green), and NMC-900 °C (red) generated by measuring 200 particles from SEM, binned in 10 nm increments. The histograms were fit using a log-normal distribution to find the peak in the particle size distribution.

This NMC precursor was then heated to 800 °C (NMC-800 °C), 850 °C (NMC-850 °C), or 900 °C (NMC-900 °C) to crystallize NMC622 with a layered structure. The different calcination temperatures resulted in different particle sizes; for each NMC622 sample, 200 particles were measured by SEM to create particle size distributions (Fig. 4.1). This distribution was then fit using a log-normal function to find the peak in the particle size distribution. These values were ~85 nm, ~150 nm, and ~215 nm, for NMC-800 °C, NMC-850 °C, and NMC-900 °C, respectively (Tbl. 4.1). These data clearly indicate significant grain growth occurred during the calcination step, particularly at the higher temperatures, but unlike bulk NMC materials, which commonly have 5 - 10 micron sized, dense spherical structures,[41] all three NMC samples retained nanoscale porosity (Figs. 4.1a-c and S4.2), which should allow for greater electrolyte penetration.

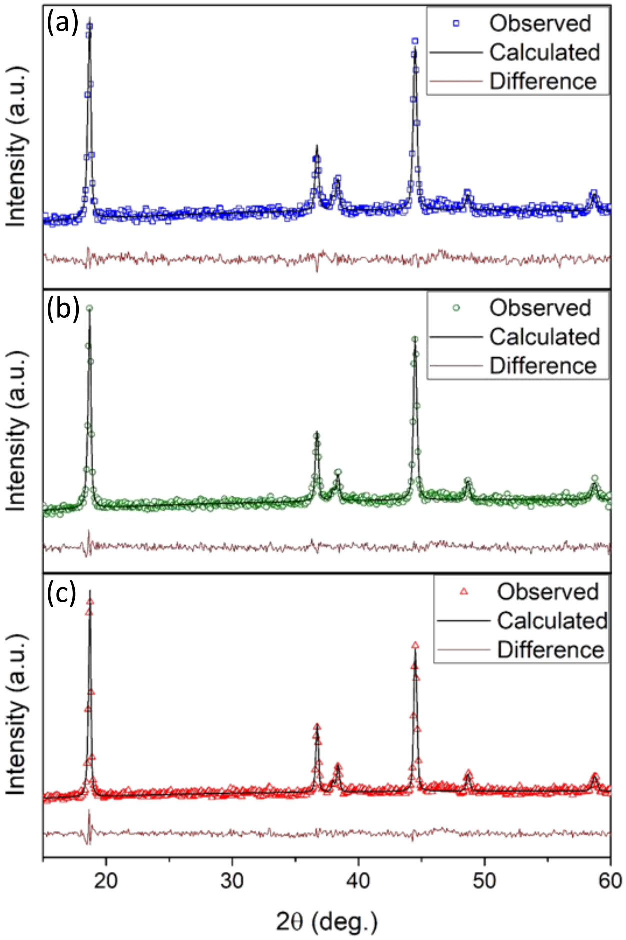

Figure 4.2. Rietveld refinement of the XRD patterns for NMC-800 °C (a), NMC-850 °C (b), and NMC-900 °C (c). The observed XRD pattern is displayed with open symbols, the calculated patterns with a black line, and the difference between the two with a dark red line below the patterns.

The crystal structures of the nanostructured NMC materials were analyzed using XRD and Rietveld refinement (Fig. 4.2). All of the nanostructured NMC622 XRD patterns could be indexed to the *R3-m* space group. For nickel-rich layered transition metal oxide materials, the integrated intensity ratio of the (003) to (104) diffraction peaks (*I*(003)/*I*(104)) can be used to assess the degree of cation mixing, where a material with a ratio above 1.2 is generally considered to have minimal cation mixing and good electrochemical properties.[61] The *I*(003)/*I*(104) ratio for the nanostructured NMC samples were all close to the desired value of 1.2; the ratios were 1.1, 1.1, and 1.2, for NMC-800 °C, NMC-850 °C, and NMC-900 °C, respectively (Tbl. 4.1). NMC-800 °C and NMC-850 °C fell slightly below the desired ratio, meaning these samples should have a slightly higher degree of cation mixing, which could hinder lithium-ion diffusion. For the Rietveld refinement, transition metals were set at the 3a site (0,0,0), Li^+ was set at the 3b site (0,0,0.5), and O was set at the 6c site (0,0,z_{ox}) where $z_{ox} \approx 0.25$ Å.[62] The refinements were evaluated using a

Table 4.1. The peak of the particle size distribution from SEM, the *I*(003)/*I*(104) ratios calculated from XRD, and the Rietveld refinement results for NMC-800 °C, NMC-850 °C, EI-NMC-850 °C, and NMC-900 °C.

Sample	**Peak particle size (nm)**	***I*(003)/ *I*(104)**	***a*** **(Å)**	***c*** **(Å)**	***c*/*a***	z_{ox} **(Å)**	***S*** **(Å)**	***I*** **(Å)**	R_{wp}
NMC-800 °C	85	1.1	2.8670(5)	14.196(7)	4.95	0.258(1)	2.14	2.59	3.22%
NMC-850 °C	150	1.1	2.8681(4)	14.212(5)	4.96	0.258(1)	2.14	2.60	3.22%
EI-NMC-850 °C	160	1.1	2.8672(3)	14.199(5)	4.95	0.260(1)	2.08	2.65	3.12%
NMC-900 °C	215	1.2	2.8671(3)	14.208(4)	4.96	0.258(1)	2.14	2.60	3.40%

weighted profile R factor (R_{wp}), which indicated a good fit for all samples ($R_{wp} < 10\%$). The c/a values were 4.95 for NMC-800 °C and 4.96 for NMC-850 °C and NMC-900 °C (Tbl. 4.1); any value above 4.899 indicates a material with a well layered structure and a high degree of cation ordering.[63,64] The c parameter along with z_{ox}, were then used to calculate the thicknesses of the slab (S) and inter-slab (I) space.[61,65]

$$S = 2\left(\frac{1}{3} - z_{ox}\right)c \tag{1}$$

$$I = \frac{c}{3} - S \tag{2}$$

Where the slab thickness is the thickness of the transition metal layer and the inter-slab thickness is the thickness of the lithium-ion diffusion layer. A larger value for I is desired for optimal lithium-ion diffusion.[65] The nanostructured NMC materials all had similar inter-slab thicknesses of 2.59 Å, 2.60 Å, and 2.60 Å, for NMC-800 °C, NMC-850 °C, and NMC-900 °C, respectively (Tbl. 4.1). These inter-slab thickness values for nanostructured NMC622 are consistent with values in the literature for bulk NMC622, indicating there was no change to the lithium-ion diffusion rate as the NMC622 particles were nanostructured.[53,66]

For electrochemical analyses, slurries of the three nanostructured NMC622 samples were prepared air-free to reduce detrimental surface reactions. Additionally, the slurries were prepared using the semiconducting polymer P3HT as a conductive binder.[67] P3HT has been used as a conductive binder in fast charging NCA electrodes due to its high electrical and ionic conductivity, as well as its ability to suppress the formation of unstable solid-electrolyte interphase (SEI) layers, both factors that become more important for nanostructured materials.[68] Unfortunately, both P3HT and NMC622 undergo degradation when cycled above 4.2 V vs. Li/Li^+, so all cycling was kept between 3.2 and 4.2 V vs. Li/Li$^+$ for optimal performance.[63,69] The nanostructured samples were evaluated using galvanostatic cycling at various rates up to 64C. All three nanostructured NMC622 samples showed fairly similar capacities and rate capability, with average specific discharge capacities of 87 mAh/g at 16C and of 48 mAh/g at 32C (Fig. 4.3). This was in stark contrast to what we observed in nanostructured NCA, which had much higher capacity at fast rates.[37,38] These results indicate that, unlike nanostructured NCA, there is very little effect of the particle size on the electrochemical properties for NMC622.

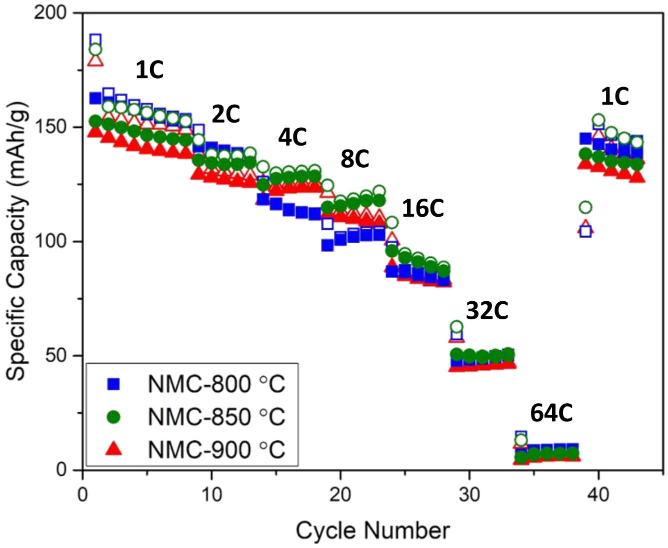

Figure 4.3. Galvanostatic cycling from 3.2-4.2 V vs Li/Li$^+$ at various rates for NMC-800 °C (blue square), NMC-850 °C (green circle), and NMC-900 °C (red triangle), the specific charge capacity is shown with an open symbol and the specific discharge capacity is shown with a filled symbol.

The nanostructured NMC samples had first cycle coulombic efficiencies of 86.4%, 82.9%, and 82.6% for NMC-800 °C, NMC-850 °C, and NMC-900 °C, respectively (Fig. 4.3). A low coulombic efficiency (~80%) for the first cycle is common and is generally attributed to irreversible structural change.[70] However, for these samples, there was continued low coulombic efficiency in further cycles at 1C (~94%) and when the rate was returned to 1C (~92%) after cycling at fast rates. This indicates the presence of some parasitic reactions.[71] The low coulombic efficiency could likely be solved with an electrolyte additive or a surface coating to suppress parasitic reactions,[71] which will be studied for this system in future studies.

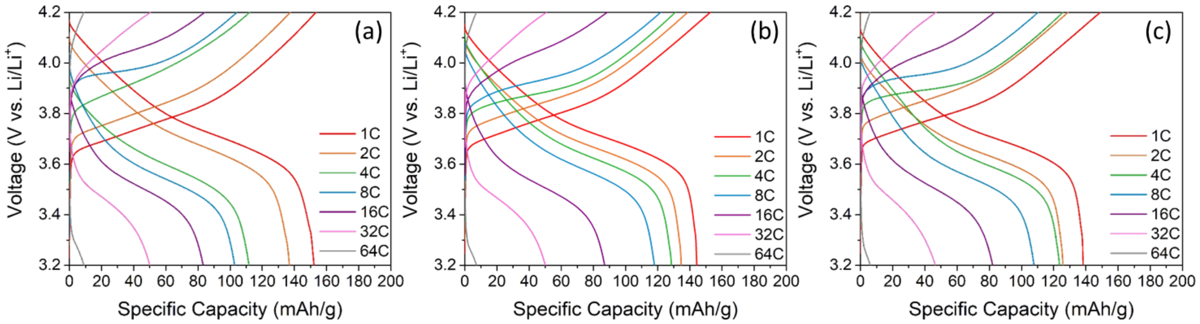

Figure 4.4. Galvanostatic dis(charge) curves of the last cycle at each rate (from Figure 4.3) for NMC-800 °C (a), NMC-850 °C (b), and NMC-900 °C (c).

In examining the galvanostatic charge and discharge curves for the nanostructured NMC samples, we found that all materials had sloping profiles (Fig. 4.4). This was expected, since the same behavior is seen for the bulk material,[35,41] and is a characteristic of a solid solution behavior or continuous phase transitions.[84] To gain greater insight into the mechanism of charge storage in the nanostructured NMC samples, each sample was analyzed using three different electrochemical kinetic analyses, all based on cyclic voltammetry (CV). In the first analysis, the peak current (*i*) is related to the sweep rate (*v*) using the following power-law relation,

$$i = av^b \tag{3}$$

where *a* is a constant and the value for *b* can vary from 0.5-1.[10] By solving for the *b*-value, the charge storage mechanism can be determined for the redox processes occurring at the peak current. If a material has a *b*-value of 0.5, equation 3 then resembles the Randles-Sevcik equation, which describes a semi-infinite diffusion-limited faradaic process, typical of battery materials.[4,10] In contrast, if a material has a *b*-value of 1, equation 3 resembles that of an electric double layer capacitor and indicates capacitor-like behavior.[5,10] Because the *b*-value can fall between 0.5 and 1, a value closer to 0.5 means lithium intercalation is mostly diffusion controlled and a value closer to 1 indicates mostly capacitive behavior. For the nanostructured NMC622 materials, the anodic/cathodic *b*-values were 0.76/0.81, 0.75/0.74, and 0.78/0.79 for NMC-800 °C, NMC-850 °C, and NMC-900 °C, respectively (Fig. 4.5a-c). These *b*-values fall almost directly in the middle of the range between 0.5 and 1, indicating mixed behavior for these nanostructured NMC622 materials.

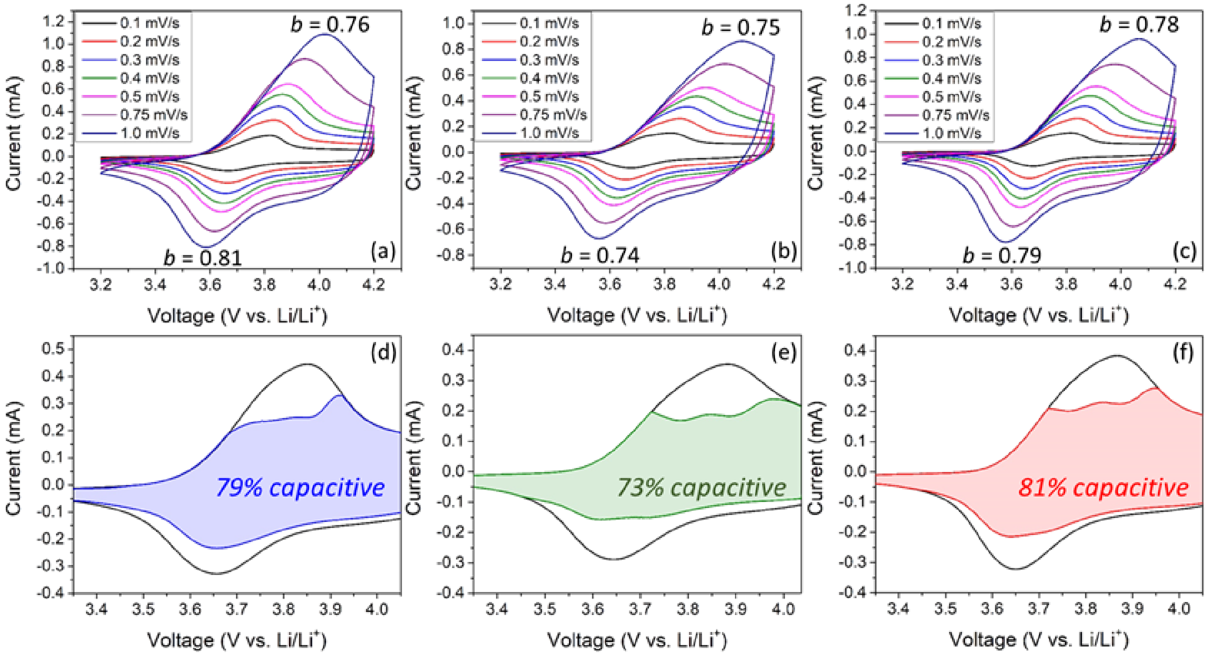

Figure 4.5. CV curves for NMC-800 °C (a), NMC-850 °C (b), and NMC-900 °C (c) at sweep rates of 0.1 mV/s to 1 mV/s. The anodic and cathodic peaks were used to derive the *b*-values, which are displayed next to their respective peak. CV curves at 0.3 mV/s for NMC-800 °C (d, blue), NMC-850 °C (e, green), and NMC-900 °C (f, red), showing the capacitive contributions to current determined by the k_1/k_2 analysis in the shaded region and the diffusion-limited contributions to current in the region that is not shaded.

In the next analysis, the same initial assumptions are made as in equation 3, but an additional assumption is also made, which is that *b* can take on only the values of 0.5 or 1. In this case, the total current can be written as the sum of capacitive current ($k_1 \cdot v$) and diffusion-limited current ($k_2 \cdot v^{1/2}$) fractions.[9]

$$i = k_1 v + k_2 v^{1/2} \tag{4}$$

This analysis, which will be referred to as the k_1/k_2 analysis, was performed over the entire potential range to determine the fraction of diffusion-limited and capacitive current at each voltage and allows for visualization of these contributions.[72] The calculated capacitive contributions were 79%, 73%, and 81% for NMC-800 °C, NMC-850 °C, and NMC-900 °C, respectively (Fig. 4.5d-f). These values indicate moderately capacitive behavior and therefore agree with the b-values presented above. Additionally, this analysis showed that there was less of a capacitive contribution to current at the redox peaks, which indicates that the intercalation reactions were largely diffusion-limited.[21,73]

Because the previous two analyses are based on the same assumptions and they should each give similar results, a third independent analysis was performed to further investigate the charge storage mechanisms of the nanostructured NMC samples. This analysis, referred to as the Trasatti analysis, analyzes the voltammetric charge with respect to sweep rate, and assuming semi-infinite linear diffusion the following two equations were used,

$$q(v) = q_{cap} + \alpha(v^{-1/2}) \tag{5}$$

$$\frac{1}{q(v)} = \frac{1}{q_{tot}} + \alpha(\mathrm{v}^{1/2}) \tag{6}$$

where $q(v)$ is the total measured voltammetric charge, q_{cap} is the capacitive contribution to charge storage, α is a constant, and q_{tot} is the total charge storage.[11] By extrapolation of equation 5 to infinite sweep rates, the value of q_{cap} can be determined (Fig. 4.6a-c). This value is generally attributed to capacitive or surface charge storage processes, because at infinitely fast sweep rates, diffusion-limited or slow processes are excluded.[11,12] Then, by extrapolation of equation 6 to a sweep rate of zero, the value of q_{tot} can be determined (Fig. 4.6d-f). At infinitely slow sweep rates, there is enough time for all charge storage processes (fast and slow) to occur, thus the total charge storage can be determined.[11,16] Finally, the capacitive contribution to charge storage can be determined by dividing q_{cap} by q_{tot}. The values for capacitive charge storage from the Trasatti analysis were 62%, 46%, and 59% for NMC-800 °C, NMC-850 °C, and NMC-900 °C, respectively (Fig. 4.6). The results of the Trasatti analysis indicate that these materials are about half capacitive, and thus agree reasonably well with the values derived from the *b*-value analysis.

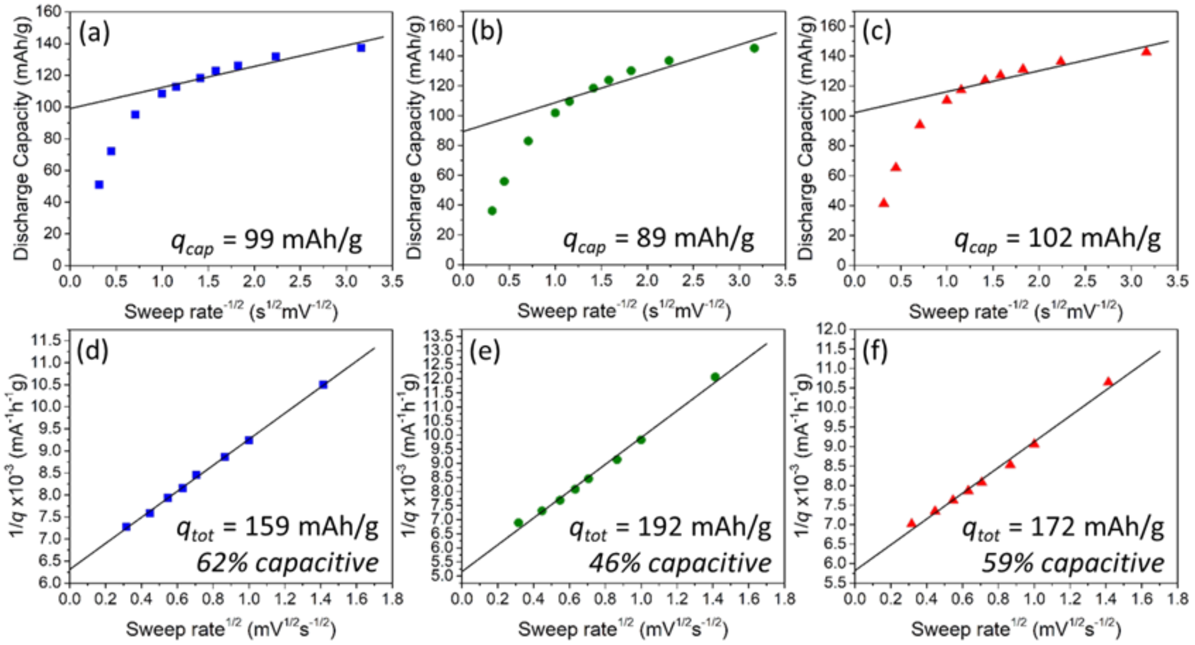

Figure 4.6. Determination of q_{cap} using the Trasatti analysis, where q_{cap} is set as the extrapolation of $v \to \infty$ at the y-intercept (for the linear portion, 0.1-1mV/s) for NMC-800 °C (a), NMC-850 °C (b), and NMC-900 °C (c). Determination of q_{tot} using the Trasatti analysis, where $1/q_{tot}$ is set as the extrapolation of $v \to 0$ at the y-intercept for NMC-800 °C (d), NMC-850 °C (e), and NMC-900 °C (f).

Each electrochemical kinetic analysis showed similar results between the three nanostructured NMC622 samples and together their combined results indicated that the electrochemical properties of the nanostructured NMC622 samples were not affected by decreasing particle sizes. While these materials do show some characteristics of pseudocapacitive charge storage, such as *b*-values indicative of mixed capacitive and diffusion-limited behavior, overall the materials were not highly pseudocapacitive. One additional characteristic of a pseudocapacitive material are small separations between the anodic and cathodic redox peaks.[6] Here the peak separations were fairly large, ~0.66 V at a sweep rate of 2 mV/s for all three nanostructured NMC622 samples (Fig. S4.3), especially when compared to the pseudocapacitive cathode material, mesoporous $LiMn_2O_4$, which had a peak separation of ~0.3 V at 100 mV/s.[20] This again indicates that the nanostructured NMC622 materials were not highly pseudocapacitive.

The results above lead to a fundamental question: if reducing grain size in nanostructured NMC622 has little effect on the electrochemical properties, even over a wide range of particle sizes, is it possible to induce pseudocapacitive behavior in the NMC622 system? Interestingly, if the inter-slab (*I*) lithium diffusion layer thickness was increased, enhanced electrochemical performance was seen. Here, a nanostructured NMC622 sample with an enlarged *I* (EI-NMC-850 °C) was synthesized. The material was annealed at 850 °C, which resulted in a peak in the particle size distribution around 160 nm, combined with nanoscale porosity (Fig. 4.7a, S4.4, Tbl. 4.1). This size was similar to that of NMC-850 °C, indicating the enlarged *I* did not affect the overall particle size. This enlarged *I* material had an inter-slab thickness of 2.65 Å as determined by Rietveld refinement (Fig. 4.7b, Tbl. 4.1), which was significantly larger than the other nanostructured NMC materials studied above (2.59-2.60 Å). To determine the electrochemical performance of the EI-NMC-850 °C material, it was cycled galvanostatically at various rates from 3.2-4.2 V vs. Li/Li^+.

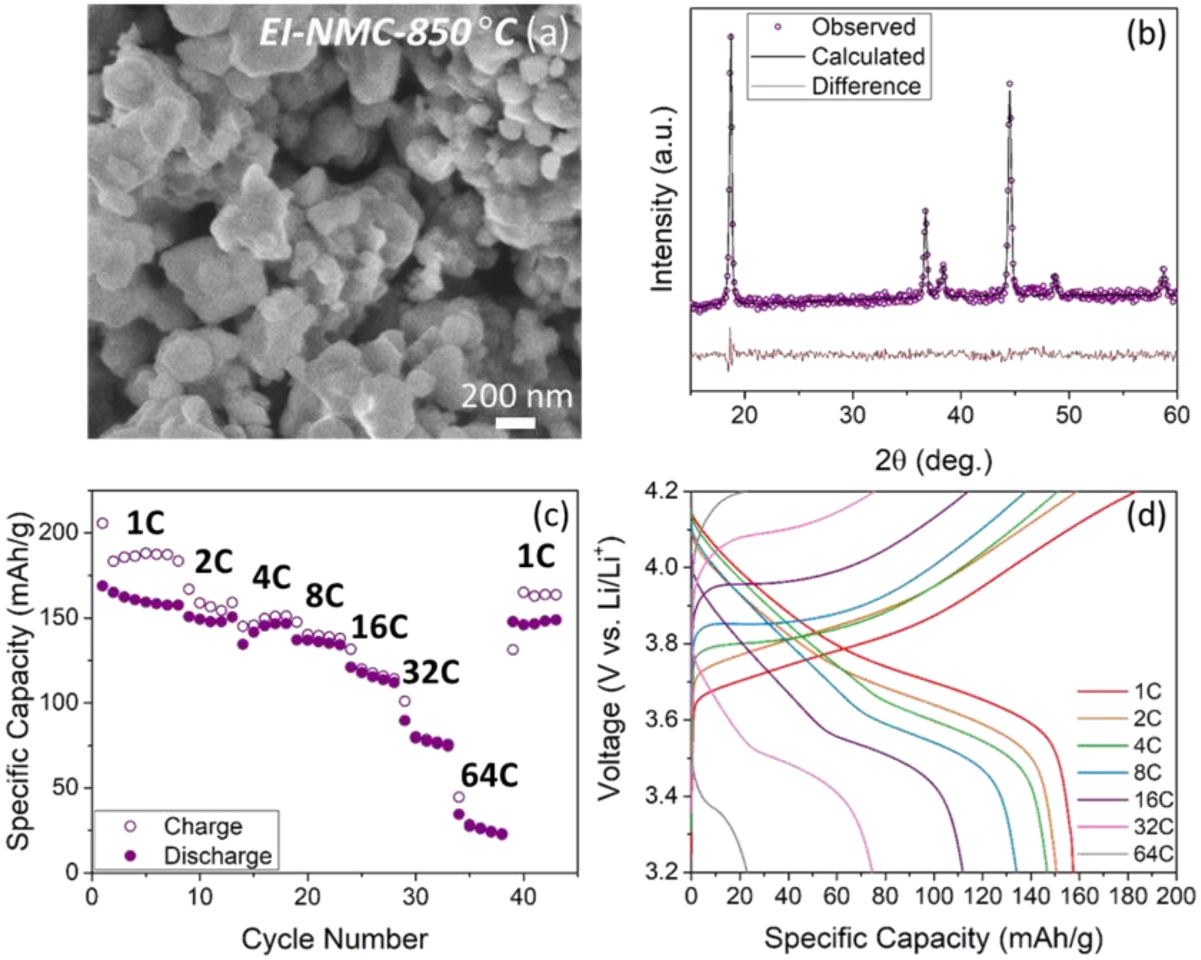

Figure 4.7. (a) High-magnification SEM image of EI-NMC-850 °C. (b) Rietveld refinement of the XRD pattern for EI-NMC-850 °C. The observed XRD pattern is displayed with open symbols, the calculated patterns with a black line, and the difference between the two with a dark red line below the pattern. (c) Galvanostatic cycling from 3.2-4.2 V vs Li/Li^+ at various rates for EI-NMC-850 °C, showing the specific charge capacity (open circle) and the specific discharge capacity (filled circle). (d) Individual galvanostatic dis(charge) curves for EI-NMC-850 °C from the last cycle at each rate.

The EI-NMC-850 °C sample showed superior rate capability compared to NMC622 materials that were nanostructured but had more conventional *I* values (Fig. 4.7c). At 16C EI-NMC-850 °C had an average discharge capacity of 116 mAh/g and at 32C the average discharge capacity was 79 mAh/g. This corresponds to a discharge capacity retention (compared to 1C) of 49% at 32C and

17% at 64C for EI-NMC-850 °C, compared to the average discharge capacity retentions of 32% at 32C and 5% at 64C for the three samples discussed previously (NMC-800 °C, NMC-850 °C, and NMC-900 °C, Fig. S4.5). The galvanostatic charge and discharge curves for EI-NMC-850 °C displayed sloping profiles (Fig. 4.7d), similar to the other nanostructured NMC622 materials. It should be noted that, EI-NMC-850 °C still had poor coulombic efficiency (Fig. 4.7c), which as mentioned before, will be studied further and could possibly be solved with an electrolyte additive or surface coating.[71]

Next, the three electrochemical kinetic analyses were performed on the nanostructured EI-NMC-850 °C material using CV. This nanostructured and enlarged *I* material had anodic and cathodic *b*-values of 0.86 and 0.90, respectively (Fig. 4.8a), these values are much close to 1, indicating much more capacitive behavior than the nanostructured NMC622 materials that had standard *I* values. The k_1/k_2 analysis showed a higher capacitive contribution to current of 85% with notably higher capacitive contributions at the redox peaks (Fig. 4.8b). Lastly, EI-NMC-850 °C had 69% of a capacitive contribution to charge storage, as determined by the Trasatti analysis (Fig. 4.8c-d). Because of the large coulombic inefficiency seen for EI-NMC-850 °C, the total capacity (charge and discharge capacity) was used for the Trasatti analysis here. The results of these three analyses again agree and indicate that this nanostructured material with an enlarged *I* was much more capacitive and now shows significant characteristics of pseudocapacitance, in contrast to the NMC622 materials that were only nanostructured, but without an enlarged *I*. Additionally, the separation between the anodic and cathodic redox peaks for EI-NMC-850 °C (0.37 V at a sweep rate of 2 mV/s) was almost half of what it was for the nanostructured NMC622 samples without an enlarged *I* value (Fig. S4.3). Further studies are currently being done on the EI-NMC-850 °C material to reproduce these results. For example, it has previously been shown that for bulk materials, the inter-slab layer can be enlarged in nickel-rich layered transition metal oxides by doping with sodium or potassium.[74,75]

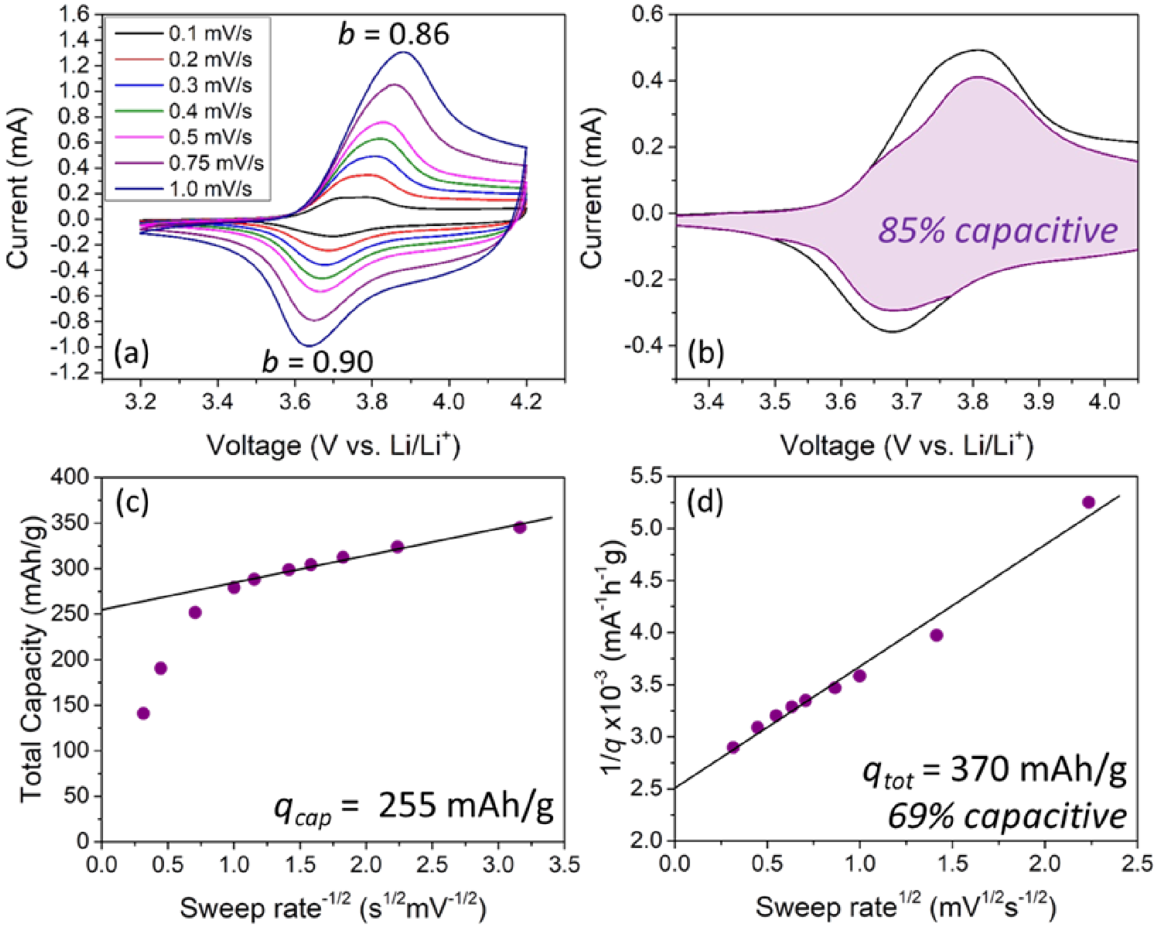

Figure 4.8. Electrochemical kinetic analyses for EI-NMC-850 °C. (a) The anodic and cathodic peaks of the CV were used to derive the *b*-values. (b) The k_1/k_2 analysis was used to determine the capacitive contribution to current for EI-NMC-850 °C, which is the purple shaded region. (c) Determination of q_{cap} for EI-NMC-850 °C using the Trasatti, where q_{cap} is set as the extrapolation of $v \rightarrow \infty$ at the y-intercept analysis (where total capacity = charge and discharge capacity). (d) Determination of q_{tot} for EI-NMC-850 °C using the Trasatti analysis, where $1/q_{tot}$ is set as the extrapolation of $v \rightarrow 0$ at the y-intercept analysis (where total capacity = charge and discharge capacity).

Lastly, GITT experiments were performed on the nanostructured NMC-900 °C and EI-NMC-850 °C materials. Specifically, we looked at the polarization of the samples during the GITT experiment on charging, which is defined here as the voltage change during the relaxation step of each GITT pulse. The polarization has contributions from ohmic polarization, charge transfer, and mass transfer, thus it can give insights into the diffusion rate of lithium within the NMC structure.[76,77] We previously saw a decrease in polarization for nanostructured NCA compared to that of bulk NCA.[37] Here, the nanostructured NMC-900 °C (Fig. 4.9a,b), which had a similar particle size to that of the nanostructured NCA materials, showed increased polarization (13 mV at 3.75 V) over that of the nanostructured NCA (4-5 mV at 3.75 V). This increase in polarization was expected because of the poorer electrochemical performance of nanostructured NMC at fast rates.[37] However, for EI-NMC-850 °C, the polarization was decreased (7 mV at 3.75V) in comparison to NMC-900 °C (Fig. 4.9), which was likely due to a combination of decreased particle size and the increased thickness of the lithium-ion diffusion layer in EI-NMC-850 °C. Thus by increasing the inter-slab layer in nanostructured NMC, we were able to increase the lithium-ion diffusion rate. Based on these results, in the large nanoscale regime explored in this work, it seems clear that lithium diffusion rate, rather than diffusion distance is the key parameter in controlling the onset of pseudocapacitive behavior.

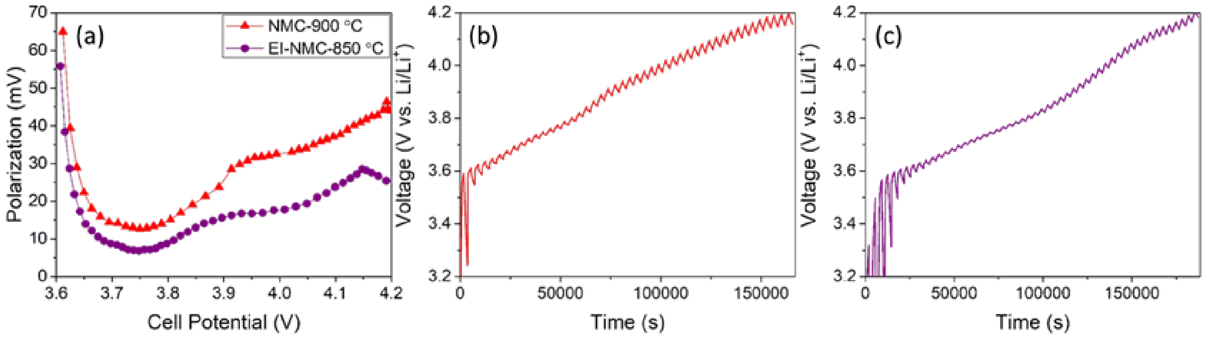

Figure 4.9. (a) The polarization versus the cell potential for NMC-900 °C (red triangle) and EI-NMC-850 °C (purple circle) obtained from a GITT experiment. The GITT curves as a function of time during charge for NMC-900 °C (b) and EI-NMC-850 °C (c).

4.4 Conclusions

Nickel-rich transition metal oxide materials, such as NCA and NMC, have suppressed discontinuous phase transitions in the bulk material, which offers the potential to observe the onset of pseudocapacitive behavior if diffusion distances are suitably decreased. Indeed, we previously synthesized nanostructured NCA with moderately decreased particle sizes and nanoscale porosity and saw highly capacitive behavior and fast rate capabilities. Thus, we synthesized nanostructured NMC622 with a polymer template to obtain a range of particle sizes with nanoscale porosity to study the effects of particle size on the electrochemical properties. Surprisingly, we discovered that the nanostructured NMC622 samples were not highly capacitive at any particle size. However, if the inter-slab lithium-ion diffusion layer thickness was increased in nanostructured NMC622, the electrochemical properties did begin to show pseudocapacitive behavior.

These results indicate that in order for a bulk battery material to transition to pseudocapacitive behavior, both decreased diffusion distances and fast diffusion rates are necessary. It has been postulated that Li^+ intercalation without a first order phase transition is one of the key requirements for high levels of pseudocapacitance in a process termed intercalation pseudocapacitance.[3,8] When suppressed phase transitions are combined with reduced diffusion distance, pseudocapacitive behavior has been observed in a broad range of materials.[8,13,15,17,19,21,22,78] The results presented above, however, indicate that it is not sufficient to just have suppressed phase transitions and decreased particle sizes, because the lithium-ion diffusion may still show something resembling semi-infinite diffusion, even at the nanoscale. It is likely that if extremely small domain sizes (10s of nanometers) could be created in standard NMC622, that pseudocapacitive behavior could be observed, but given the highly reactive nature of the surfaces of layered nickel-rich materials, it is also likely that surface reactivity would dominate performance at those very small sizes. Thus, enhancing Li^+ diffusivity appears to be the best way to develop pseudocapacitive behavior in NMC622. Overall, this work highlights the important balance between the lithium-ion diffusion rate and the lithium-ion diffusion distance, and emphasizes that diffusion rate has greater variability that needs to be optimized to create highly capacitive materials.

4.5 Supplementary Information

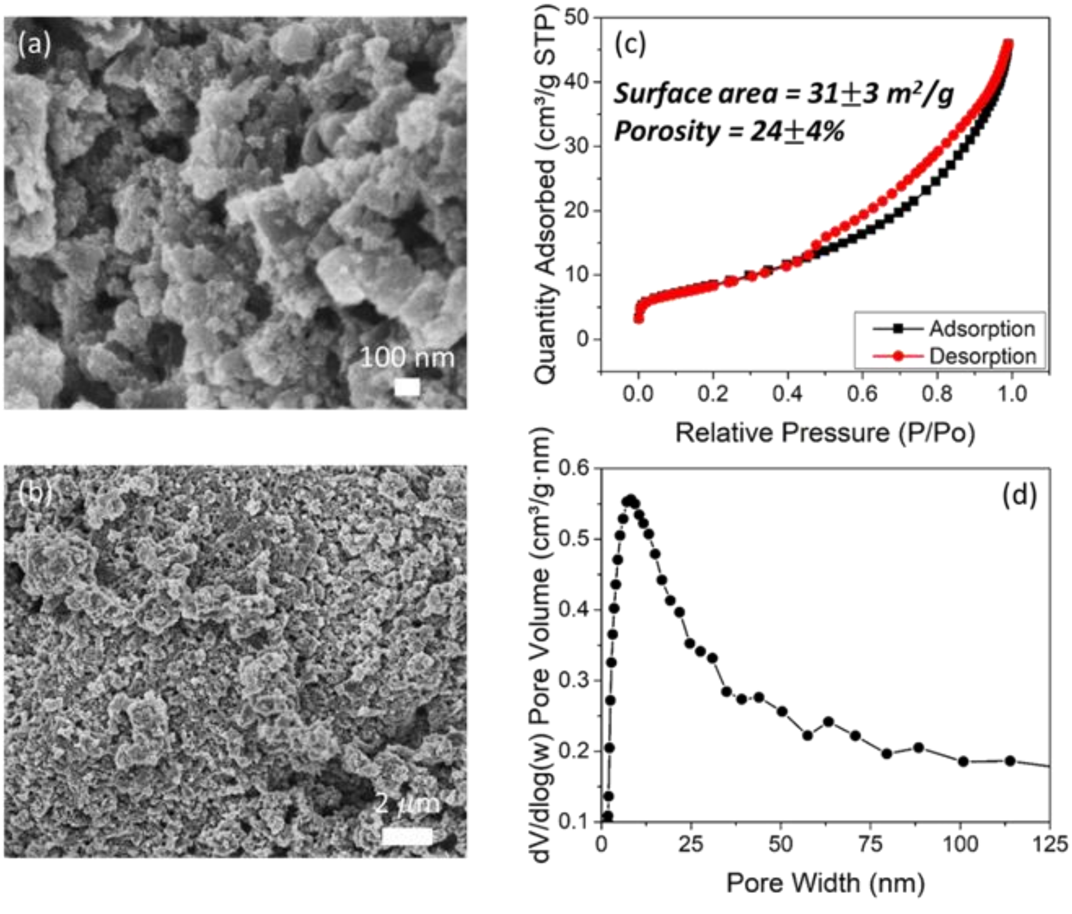

Figure S4.1. SEM images of the templated NMC622 precursor at high- (a) and low-magnifications (b). (c) Nitrogen porosimetry adsorption (black) and desorption (red) isotherms for the templated NMC622 precursor. (d) BJH adsorption volume-weighted pore size distributions for templated NMC622 precursor.

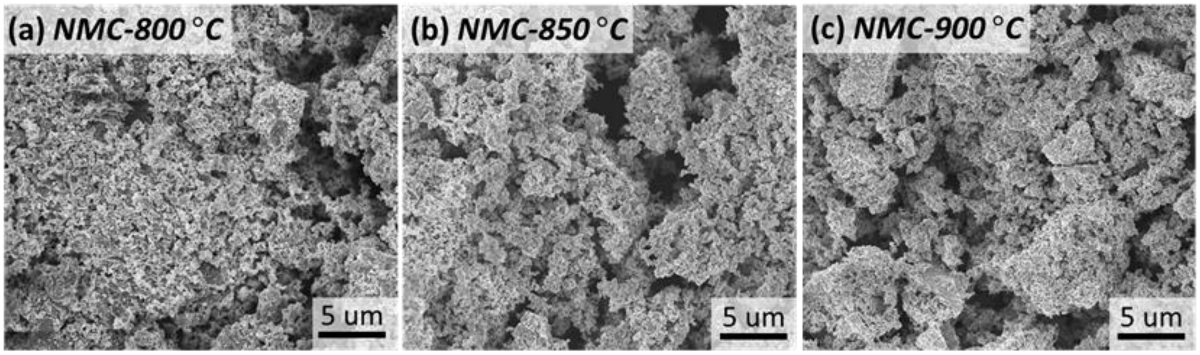

Figure S4.2. Low-magnification SEM images of NMC-800 °C (a), NMC-850 °C (b), and NMC-900 °C (c).

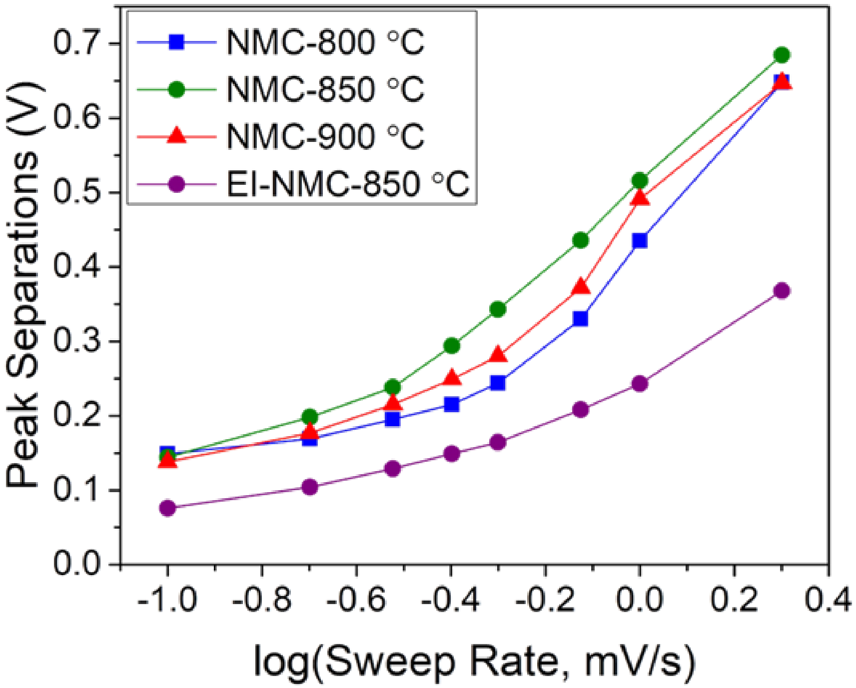

Figure S4.3. The total peak separation of the anodic and cathodic peaks from sweep rates of 0.1-2.0 mV/s for NMC-800 °C (blue square), NMC-850 °C (green circle), NMC-900 °C (red triangle), and EI-NMC-850 °C (purple circle).

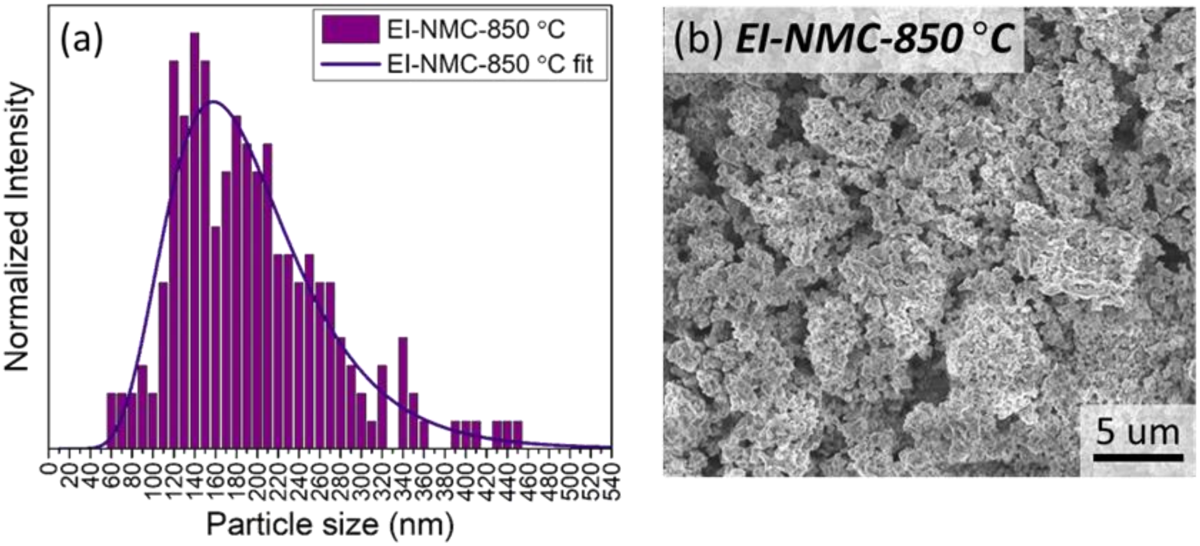

Figure S4.4. (a) Particle size distribution histogram for EI-NMC-850 °C generated by measuring 200 particles from SEM, binned in 10 nm increments, the histograms were fit using a lognormal distribution to find the peak in the particle size distribution. (b) Low-magnification SEM image of EI-NMC-850 °C.

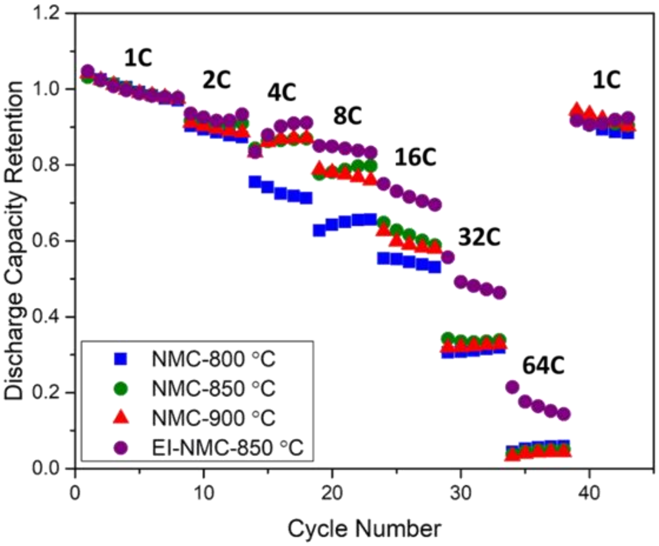

Figure S4.5. Specific discharge capacity retention (from the average discharge capacity at 1C) at various rates for NMC-800 °C (blue square), NMC-850 °C (green circle), NMC-900 °C (red triangle), and EI-NMC-850 °C (purple circle).

4.6 References

(1) Sebastian, S. S.; Dong, B.; Zerrin, T.; Pena, P. A.; Akhavi, A. S.; Li, Y.; Ozkan, C. S.; Ozkan, M. Adaptive Fast Charging Methodology for Commercial Li-ion Batteries Based on the Internal Resistance Spectrum. *Energy Storage* **2020**, *2* (4), 1–16. https://doi.org/10.1002/est2.141.

(2) Conway, B. E.; Gileadi, E. Kinetic Theory of Pseudo-Capacitance and Electrode Reactions at Appreciable Surface Coverage. *Trans. Faraday Soc.* **1962**, *58*, 2493–2509. https://doi.org/10.1039/tf9625802493.

(3) Conway, B. E. Transition from "Supercapacitor" to "Battery" Behavior in Electrochemical Energy Storage. *J. Electrochem. Soc.* **1991**, *138* (6), 1539–1548. https://doi.org/10.1149/1.2085829.

(4) Choi, C.; Ashby, D. S.; Butts, D. M.; DeBlock, R. H.; Wei, Q.; Lau, J.; Dunn, B. Achieving High Energy Density and High Power Density with Pseudocapacitive Materials. *Nat. Rev. Mater.* **2020**, *5*, 5–19. https://doi.org/10.1038/s41578-019-0142-z.

(5) Fleischmann, S.; Mitchell, J. B.; Wang, R.; Zhan, C.; Jiang, D. E.; Presser, V.; Augustyn, V. Pseudocapacitance: From Fundamental Understanding to High Power Energy Storage Materials. *Chem. Rev.* **2020**, *120* (14), 6738–6782. https://doi.org/10.1021/acs.chemrev.0c00170.

(6) Augustyn, V.; Come, J.; Lowe, M. A.; Kim, J. W.; Taberna, P.-L.; Tolbert, S. H.; Abruña, H. D.; Simon, P.; Dunn, B. High-Rate Electrochemical Energy Storage through Li^+ Intercalation Pseudocapacitance. *Nat. Mater.* **2013**, *12*, 518–522.

https://doi.org/10.1038/nmat3601.

(7) Come, J.; Augustyn, V.; Kim, J. W.; Rozier, P.; Taberna, P.-L.; Gogotsi, P.; Long, J. W.; Dunn, B.; Simon, P. Electrochemical Kinetics of Nanostructured Nb_2O_5 Electrodes. *J. Electrochem. Soc.* **2014**, *161* (5), A718–A725. https://doi.org/10.1149/2.040405jes.

(8) Cook, J. B.; Lin, T. C.; Kim, H. S.; Siordia, A.; Dunn, B. S.; Tolbert, S. H. Suppression of Electrochemically Driven Phase Transitions in Nanostructured MoS_2 Pseudocapacitors Probed Using Operando X-Ray Diffraction. *ACS Nano* **2019**, *13* (2), 1223–1231. https://doi.org/10.1021/acsnano.8b06381.

(9) Liu, T.-C.; Pell, W. G.; Conway, B. E.; Roberson, S. L. Behavior of Molybdenum Nitrides as Materials for Electrochemical Capacitors. *J. Electrochem. Soc.* **1998**, *145* (6), 1882–188. https://doi.org/10.1149/1.1838571.

(10) Lindström, H.; Södergren, S.; Solbrand, A.; Rensmo, H.; Hjelm, J.; Hagfeldt, A.; Lindquist, S.-E. Li^+ Ion Insertion in TiO_2 (Anatase). 2. Voltammetry on Nanoporous Films. *J. Phys. Chem. B* **1997**, *101* (39), 7717–7722. https://doi.org/10.1021/jp970490q.

(11) Ardizzone, S.; Fregonara, G.; Trasatti, S. “Inner” and “Outer” Active Surface of RuO_2 Electrodes. *Electrochim. Acta* **1990**, *35* (1), 263–267. https://doi.org/10.1016/0013-4686(90)85068-X.

(12) Augustyn, V.; Simon, P.; Dunn, B. Pseudocapacitive Oxide Materials for High-Rate Electrochemical Energy Storage. *Energy Environ. Sci.* **2014**, *7* (5), 1597–1614. https://doi.org/10.1039/c3ee44164d.

(13) Kim, H.-S.; Cook, J. B.; Tolbert, S. H.; Dunn, B. The Development of Pseudocapacitive

Properties in Nanosized-MoO_2. *J. Electrochem. Soc.* **2015**, *162* (5), A5083–A5090. https://doi.org/10.1149/2.0141505jes.

(14) Zhu, Y.; Ji, X.; Cheng, S.; Chern, Z. Y.; Jia, J.; Yang, L.; Luo, H.; Yu, J.; Peng, X.; Wang, J.; Zhou, W.; Liu, M. Fast Energy Storage in Two-Dimensional MoO_2 Enabled by Uniform Oriented Tunnels. *ACS Nano* **2019**, *13* (8), 9091–9099. https://doi.org/10.1021/acsnano.9b03324.

(15) Yang, L. C.; Sun, W.; Zhong, Z. W.; Liu, J. W.; Gao, Q. S.; Hu, R. Z.; Zhu, M. Hierarchical MoO_2/N-Doped Carbon Heteronanowires with High Rate and Improved Long-Term Performance for Lithium-Ion Batteries. *J. Power Sources* **2016**, *306*, 78–84. https://doi.org/10.1016/j.jpowsour.2015.11.073.

(16) Cook, J. B.; Kim, H. S.; Yan, Y.; Ko, J. S.; Robbennolt, S.; Dunn, B.; Tolbert, S. H. Mesoporous MoS_2 as a Transition Metal Dichalcogenide Exhibiting Pseudocapacitive Li and Na-Ion Charge Storage. *Adv. Energy Mater.* **2016**, *6* (9), 1–12. https://doi.org/10.1002/aenm.201501937.

(17) Mahmood, Q.; Park, S. K.; Kwon, K. D.; Chang, S. J.; Hong, J. Y.; Shen, G.; Jung, Y. M.; Park, T. J.; Khang, S. W.; Kim, W. S.; Kong, J.; Park, H. S. Transition from Diffusion-Controlled Intercalation into Extrinsically Pseudocapacitive Charge Storage of MoS_2 by Nanoscale Heterostructuring. *Adv. Energy Mater.* **2016**, *6* (1), 1501115. https://doi.org/10.1002/aenm.201501115.

(18) Luo, S.; Xu, L.; Li, J.; Yang, W.; Liu, M.; Ma, L. Facile Synthesis of MoS_2 Hierarchical Nanostructures as Electrodes for Capacitor with Enhanced Pseudocapacitive Property. *Nano* **2020**, *15* (1), 2050011. https://doi.org/10.1142/S1793292020500113.

(19) Okubo, M.; Hosono, E.; Kim, J.; Enomoto, M.; Kojima, N.; Kudo, T.; Zhou, H.; Honma, I. Nanosize Effect on High-Rate Li-Ion Intercalation in $LiCoO_2$ Electrode. *J. Am. Chem. Soc.* **2007**, *129* (23), 7444–7452. https://doi.org/10.1021/ja0681927.

(20) Lesel, B. K.; Ko, J. S.; Dunn, B.; Tolbert, S. H. Mesoporous $Li_xMn_2O_4$ Thin Film Cathodes for Lithium-Ion Pseudocapacitors. *ACS Nano* **2016**, *10* (8), 7572–7581. https://doi.org/10.1021/acsnano.6b02608.

(21) Lesel, B. K.; Cook, J. B.; Yan, Y.; Lin, T. C.; Tolbert, S. H. Using Nanoscale Domain Size to Control Charge Storage Kinetics in Pseudocapacitive Nanoporous $LiMn_2O_4$ Powders. *ACS Energy Lett.* **2017**, *2* (10), 2293–2298. https://doi.org/10.1021/acsenergylett.7b00634.

(22) Okubo, M.; Mizuno, Y.; Yamada, H.; Kim, J.; Hosono, E.; Zhou, H.; Kudo, T.; Honma, I. Fast Li-Ion Insertion into Nanosized $LiMn_2O_4$ without Domain Boundaries. *ACS Nano* **2010**, *4* (2), 741–752. https://doi.org/10.1021/nn9012065.

(23) Xia, H.; Luo, Z.; Xie, J. Nanostructured $LiMn_2O_4$ and Their Composites as High-Performance Cathodes for Lithium-Ion Batteries. *Prog. Nat. Sci. Mater. Int.* **2012**, *22* (6), 572–584. https://doi.org/10.1016/j.pnsc.2012.11.014.

(24) L, A. E.; O, U. M.; B, A. S. A Review on Synthetic Methods of Nanostructured Materials A Review on Synthetic Methods of Nanostructured Materials. *Chem. Res. J.* **2017**, *2* (5), 97–123.

(25) Liu, Y.; Goebl, J.; Yin, Y. Templated Synthesis of Nanostructured Materials. *Chem. Soc. Rev.* **2013**, *42* (7), 2610–2653. https://doi.org/10.1039/c2cs35369e.

(26) Zhao, D.; Yang, P.; Melosh, N.; Feng, J.; Chmelka, B. F.; Stucky, G. D. Continuous

Mesoporous Silica Films with Highly Ordered Large Pore Structures. *Adv. Mater.* **1998**, *10* (16), 1380–1385. https://doi.org/10.1002/(SICI)1521-4095(199811)10:16<1380::AID-ADMA1380>3.0.CO;2-8.

(27) Alexandridis, P.; Holzwarth, J. F.; Hatton, T. A. Micellization of Poly(Ethylene Oxide)-Poly(Propylene Oxide)-Poly(Ethylene Oxide) Triblock Copolymers in Aqueous Solutions: Thermodynamics of Copolymer Association. *Macromolecules* **1994**, *27* (9), 2414–2425. https://doi.org/10.1021/ma00087a009.

(28) Dunphy, D. R.; Sheth, P. H.; Garcia, F. L.; Brinker, C. J. Enlarged Pore Size in Mesoporous Silica Films Templated by Pluronic F127: Use of Poloxamer Mixtures and Increased Template/SiO_2 Ratios in Materials Synthesized by Evaporation-Induced Self-Assembly. *Chem. Mater.* **2015**, *27* (1), 75–84. https://doi.org/10.1021/cm5031624.

(29) Sörensen, M. H.; Corkery, R. W.; Pedersen, J. S.; Rosenholm, J.; Alberius, P. C. Expansion of the F127-Templated Mesostructure in Aerosol-Generated Particles by Using Polypropylene Glycol as a Swelling Agent. *Microporous Mesoporous Mater.* **2008**, *113* (1–3), 1–13. https://doi.org/10.1016/j.micromeso.2007.10.045.

(30) Fan, H.; Bentley, H. R.; Kathan, K. R.; Clem, P.; Lu, Y.; Brinker, C. J. Self-Assembled Aerogel-like Low Dielectric Constant Films. *J. Non. Cryst. Solids* **2001**, *285* (1–3), 79–83. https://doi.org/10.1016/S0022-3093(01)00435-5.

(31) Hwang, Y. K.; Patil, K. R.; Jhung, S. H.; Chang, J. S.; Ko, Y. J.; Park, S. E. Control of Pore Size and Condensation Rate of Cubic Mesoporous Silica Thin Films Using a Swelling Agent. *Microporous Mesoporous Mater.* **2005**, *78* (2–3), 245–253. https://doi.org/10.1016/j.micromeso.2004.10.026.

(32) Kwade, A.; Haselrieder, W.; Leithoff, R.; Modlinger, A.; Dietrich, F.; Droeder, K. Current Status and Challenges for Automotive Battery Production Technologies. *Nat. Energy* **2018**, *3*, 290–300. https://doi.org/10.1038/s41560-018-0130-3.

(33) Myung, S. T.; Maglia, F.; Park, K. J.; Yoon, C. S.; Lamp, P.; Kim, S. J.; Sun, Y. K. Nickel-Rich Layered Cathode Materials for Automotive Lithium-Ion Batteries: Achievements and Perspectives. *ACS Energy Lett.* **2017**, *2* (1), 196–223. https://doi.org/10.1021/acsenergylett.6b00594.

(34) Xia, Y.; Zheng, J.; Wang, C.; Gu, M. Designing Principle for Ni-Rich Cathode Materials with High Energy Density for Practical Applications. *Nano Energy* **2018**, *49*, 434–452. https://doi.org/10.1016/j.nanoen.2018.04.062.

(35) Märker, K.; Reeves, P. J.; Xu, C.; Griffith, K. J.; Grey, C. P. Evolution of Structure and Lithium Dynamics in $LiNi_{0.8}Mn_{0.1}Co_{0.1}O_2$ (NMC811) Cathodes during Electrochemical Cycling. *Chem. Mater.* **2019**, *31* (7), 2545–2554. https://doi.org/10.1021/acs.chemmater.9b00140.

(36) Zhu, X.-J.; Liu, H.-X.; Gan, X.-Y.; Cao, M.-H.; Zhou, J.; Chen, W.; Xu, Q.; Ouyang, S.-X. Preparation and Characterization of $LiNi_{0.80}Co_{0.20-x}Al_xO_2$ as Cathode Materials for Lithium Ion Batteries. *J. Electroceramics* **2006**, *17* (2–4), 645–649. https://doi.org/10.1007/s10832-006-6705-6.

(37) Basile, V. M.; Lai, C.-H.; Choi, C. S.; Butts, D. M.; King, S. C.; Dunn, B. S.; Tolbert, S. H. Nanostructured $LiNi_{0.80}Co_{0.15}Al_{0.05}O_2$ (NCA) for Fast-Charging, High-Capacity Cathodes. *In preparation.*

(38) Basile, V. M.; Lai, C.-H.; Choi, C. S.; King, S. C.; Butts, D. M.; Dunn, B. S.; Tolbert, S. H. Scalable Synthesis of Templated Nanoporous $LiNi_{0.80}Co_{0.15}Al_{0.05}O_2$ (NCA) for Fast-Charging Lithium-Ion Batteries. *In preparation.*

(39) Han, C. J.; Yoon, J. H.; Cho, W. Il; Jang, H. Electrochemical Properties of $LiNi_{0.8}Co_{0.2-x}Al_xO_2$ Prepared by a Sol–Gel Method. *J. Power Sources* **2004**, *136* (1), 132–138. https://doi.org/10.1016/j.jpowsour.2004.05.006.

(40) Kasnatscheew, J.; Evertz, M.; Kloepsch, R.; Streipert, B.; Wagner, R.; Cekic Laskovic, I.; Winter, M. Learning from Electrochemical Data: Simple Evaluation and Classification of $LiMO_2$-Type-Based Positive Electrodes for Li-Ion Batteries. *Energy Technol.* **2017**, *5* (9), 1670–1679. https://doi.org/10.1002/ente.201700068.

(41) Noh, H. J.; Youn, S.; Yoon, C. S.; Sun, Y. K. Comparison of the Structural and Electrochemical Properties of Layered $Li[Ni_xCo_yMn_z]O_2$ (x = 1/3, 0.5, 0.6, 0.7, 0.8 and 0.85) Cathode Material for Lithium-Ion Batteries. *J. Power Sources* **2013**, *233*, 121–130. https://doi.org/10.1016/j.jpowsour.2013.01.063.

(42) Kim, J. M.; Chung, H. T. Role of Transition Metals in Layered $Li[Ni,Co,Mn]O_2$ under Electrochemical Operation. *Electrochim. Acta* **2004**, *49* (21), 3573–3580. https://doi.org/10.1016/j.electacta.2004.03.025.

(43) Sun, H.; Zhao, K. Electronic Structure and Comparative Properties of $LiNi_xMn_yCo_zO_2$ Cathode Materials. *J. Phys. Chem. C* **2017**, *121* (11), 6002–6010. https://doi.org/10.1021/acs.jpcc.7b00810.

(44) Wang, D.; Xin, C.; Zhang, M.; Bai, J.; Zheng, J.; Kou, R.; Peter Ko, J. Y.; Huq, A.; Zhong,

G.; Sun, C. J.; Yang, Y.; Chen, Z.; Xiao, Y.; Amine, K.; Pan, F.; Wang, F. Intrinsic Role of Cationic Substitution in Tuning Li/Ni Mixing in High-Ni Layered Oxides. *Chem. Mater.* **2019**, *31* (8), 2731–2740. https://doi.org/10.1021/acs.chemmater.8b04673.

(45) Kalyani, P.; Kalaiselvi, N. Various Aspects of $LiNiO_2$ Chemistry: A Review. *Sci. Technol. Adv. Mater.* **2005**, *6* (6), 689–703. https://doi.org/10.1016/j.stam.2005.06.001.

(46) Delmas, C.; Pérès, J. P.; Rougier, A.; Demourgues, A.; Weill, F.; Chadwick, A. V.; Broussely, M.; Perton, F.; Biensan, P.; Willmann, P. On the Behavior of the Li_xNiO_2 System: An Electrochemical and Structural Overview. *J. Power Sources* **1997**, *68* (1), 120–125. https://doi.org/10.1016/S0378-7753(97)02664-5.

(47) Wei, Y.; Zheng, J.; Cui, S.; Song, X.; Su, Y.; Deng, W.; Wu, Z.; Wang, X.; Wang, W.; Rao, M.; Lin, Y.; Wang, C.; Amine, K.; Pan, F. Kinetics Tuning of Li-Ion Diffusion in Layered $Li(Ni_xMn_yCo_z)O_2$. *J. Am. Chem. Soc.* **2015**, *137* (26), 8364–8367. https://doi.org/10.1021/jacs.5b04040.

(48) Wang, S.; Yan, M.; Li, Y.; Vinado, C.; Yang, J. Separating Electronic and Ionic Conductivity in Mix-Conducting Layered Lithium Transition-Metal Oxides. *J. Power Sources* **2018**, *393*, 75–82. https://doi.org/10.1016/j.jpowsour.2018.05.005.

(49) Cho, D.-H.; Jo, C.-H.; Cho, W.; Kim, Y.-J.; Yashiro, H.; Sun, Y.-K.; Myung, S.-T. Effect of Residual Lithium Compounds on Layer Ni-Rich $Li[Ni_{0.7}Mn_{0.3}]O_2$. *J. Electrochem. Soc.* **2014**, *161* (6), A920–A926. https://doi.org/10.1149/2.042406jes.

(50) Zou, L.; He, Y.; Liu, Z.; Jia, H.; Zhu, J.; Zheng, J.; Wang, G.; Li, X.; Xiao, J.; Liu, J.; Zhang, J. G.; Chen, G.; Wang, C. Unlocking the Passivation Nature of the Cathode–Air Interfacial

Reactions in Lithium Ion Batteries. *Nat. Commun.* **2020**, *11*, 1–8. https://doi.org/10.1038/s41467-020-17050-6.

(51) Jung, R.; Morasch, R.; Karayaylali, P.; Phillips, K.; Maglia, F.; Stinner, C.; Shao-Horn, Y.; Gasteiger, H. A. Effect of Ambient Storage on the Degradation of Ni-Rich Positive Electrode Materials (NMC811) for Li-Ion Batteries. *J. Electrochem. Soc.* **2018**, *165* (2), A132–A141. https://doi.org/10.1149/2.0401802jes.

(52) Park, J. H.; Park, J. K.; Lee, J. W. Stability of $LiNi_{0.6}Mn_{0.2}Co_{0.2}O_2$ as a Cathode Material for Lithium-Ion Batteries against Air and Moisture. *Bull. Korean Chem. Soc.* **2016**, *37* (3), 344–348. https://doi.org/10.1002/bkcs.10679.

(53) Cui, S.; Wei, Y.; Liu, T.; Deng, W.; Hu, Z.; Su, Y.; Li, H.; Li, M.; Guo, H.; Duan, Y.; Wang, W.; Rao, M.; Zheng, J.; Wang, X.; Pan, F. Optimized Temperature Effect of Li-Ion Diffusion with Layer Distance in $Li(Ni_xMn_yCo_z)O_2$ Cathode Materials for High Performance Li-Ion Battery. *Adv. Energy Mater.* **2016**, *6* (4), 1–9. https://doi.org/10.1002/aenm.201501309.

(54) Yang, C.; Huang, J.; Huang, L.; Wang, G. Electrochemical Performance of $LiCo_{1/3}Mn_{1/3}Ni_{1/3}O_2$ Hollow Spheres as Cathode Material for Lithium Ion Batteries. *J. Power Sources* **2013**, *226*, 219–222. https://doi.org/10.1016/j.jpowsour.2012.10.089.

(55) Sinha, N. N.; Munichandraiah, N. High Rate Capability of Porous $LiNi_{1/3}Co_{1/3}Mn_{1/3}O_2$ Synthesized by Polymer Template Route. *J. Electrochem. Soc.* **2010**, *157* (6), A647–A653. https://doi.org/10.1149/1.3364944.

(56) Huang, Z.-D.; Liu, X.-M.; Oh, S.-W.; Zhang, B.; Ma, P.-C.; Kim, J.-K. Microscopically

Porous, Interconnected Single Crystal $LiNi_{1/3}Co_{1/3}Mn_{1/3}O_2$ Cathode Material for Lithium Ion Batteries. *J. Mater. Chem.* **2011**, *21* (29), 10777–10784. https://doi.org/10.1039/c1jm00059d.

(57) Wang, Y.; Roller, J.; Maric, R. Morphology-Controlled One-Step Synthesis of Nanostructured $LiNi_{1/3}Mn_{1/3}Co_{1/3}O_2$ Electrodes for Li-Ion Batteries. *ACS Omega* **2018**, *3* (4), 3966–3973. https://doi.org/10.1021/acsomega.8b00380.

(58) Zhang, Y.; Zhang, W.; Shen, S.; Yan, X.; Wu, R.; Wu, A.; Lastoskie, C.; Zhang, J. Sacrificial Template Strategy toward a Hollow $LiNi_{1/3}Co_{1/3}Mn_{1/3}O_2$ Nanosphere Cathode for Advanced Lithium-Ion Batteries. *ACS Omega* **2017**, *2* (11), 7593–7599. https://doi.org/10.1021/acsomega.7b00764.

(59) Ahn, W.; Lim, S. N.; Jung, K. N.; Yeon, S. H.; Kim, K. B.; Song, H. S.; Shin, K. H. Combustion-Synthesized $LiNi_{0.6}Mn_{0.2}Co_{0.2}O_2$ as Cathode Material for Lithium Ion Batteries. *J. Alloys Compd.* **2014**, *609*, 143–149. https://doi.org/10.1016/j.jallcom.2014.03.123.

(60) Yue, P.; Wang, Z.; Peng, W.; Li, L.; Guo, H.; Li, X.; Hu, Q.; Zhang, Y. Preparation and Electrochemical Properties of Submicron $LiNi_{0.6}Co_{0.2}Mn_{0.2}O_2$ as Cathode Material for Lithium Ion Batteries. *Scr. Mater.* **2011**, *65* (12), 1077–1080. https://doi.org/10.1016/j.scriptamat.2011.09.020.

(61) Zhang, X.; Jiang, W. J.; Mauger, A.; Qilu; Gendron, F.; Julien, C. M. Minimization of the Cation Mixing in $Li_{1+x}(NMC)_{1-x}O_2$ as Cathode Material. *J. Power Sources* **2010**, *195* (5), 1292–1301. https://doi.org/10.1016/j.jpowsour.2009.09.029.

(62) Vitoux, L.; Reichardt, M.; Sallard, S.; Novák, P.; Sheptyakov, D.; Villevieille, C. A Cylindrical Cell for Operando Neutron Diffraction of Li-Ion Battery Electrode Materials. *Front. Energy Res.* **2018**, *6*, 76. https://doi.org/10.3389/fenrg.2018.00076.

(63) Wang, Q.; Shen, C. H.; Shen, S. Y.; Xu, Y. F.; Shi, C. G.; Huang, L.; Li, J. T.; Sun, S. G. Origin of Structural Evolution in Capacity Degradation for Overcharged NMC622 via Operando Coupled Investigation. *ACS Appl. Mater. Interfaces* **2017**, *9* (29), 24731–24742. https://doi.org/10.1021/acsami.7b06326.

(64) Julien, C.; Mauger, A.; Zaghib, K.; Groult, H. Optimization of Layered Cathode Materials for Lithium-Ion Batteries. *Materials (Basel).* **2016**, *9* (7), 595. https://doi.org/10.3390/MA9070595.

(65) Sivaprakash, S.; Majumder, S. B.; Nieto, S.; Katiyar, R. S. Crystal Chemistry Modification of Lithium Nickel Cobalt Oxide Cathodes for Lithium Ion Rechargeable Batteries. *J. Power Sources* **2007**, *170* (2), 433–440. https://doi.org/10.1016/j.jpowsour.2007.04.029.

(66) Lee, W.; Muhammad, S.; Kim, T.; Kim, H.; Lee, E.; Jeong, M.; Son, S.; Ryou, J. H.; Yoon, W. S. New Insight into Ni-Rich Layered Structure for Next-Generation Li Rechargeable Batteries. *Adv. Energy Mater.* **2018**, *8* (4), 1701788. https://doi.org/10.1002/aenm.201701788.

(67) Berger, P. R.; Kim, M. Polymer Solar Cells: P3HT:PCBM and Beyond. *J. Renew. Sustain. Energy* **2018**, *10* (1), 013508. https://doi.org/10.1063/1.5012992.

(68) Lai, C.-H.; Ashby, D. S.; Lin, T. C.; Lau, J.; Dawson, A.; Tolbert, S. H.; Dunn, B. S. Application of Poly(3-Hexylthiophene-2,5-Diyl) as a Protective Coating for High Rate

Cathode Materials. *Chem. Mater.* **2018**, *30* (8), 2589–2599. https://doi.org/10.1021/acs.chemmater.7b05116.

(69) Gonçalves, R.; Pereira, E. C.; Marchesi, L. F. The Overoxidation of Poly(3-Hexylthiophene) (P3HT) Thin Film: CV and EIS Measurements. *Int. J. Electrochem. Sci.* **2017**, *12* (3), 1983–1991. https://doi.org/10.20964/2017.03.44.

(70) Kasnatscheew, J.; Evertz, M.; Streipert, B.; Wagner, R.; Klöpsch, R.; Vortmann, B.; Hahn, H.; Nowak, S.; Amereller, M.; Gentschev, A. C.; Lamp, P.; Winter, M. The Truth about the 1st Cycle Coulombic Efficiency of $LiNi_{1/3}Co_{1/3}Mn_{1/3}O_2$ (NCM) Cathodes. *Phys. Chem. Chem. Phys.* **2016**, *18* (5), 3956–3965. https://doi.org/10.1039/c5cp07718d.

(71) Li, T.; Yuan, X.-Z.; Zhang, L.; Song, D.; Shi, K.; Bock, C. Degradation Mechanisms and Mitigation Strategies of Nickel-Rich NMC-Based Lithium-Ion Batteries. *Electrochem. Energy Rev.* **2020**, *3*, 43–80. https://doi.org/10.1007/s41918-019-00053-3.

(72) Wang, J.; Polleux, J.; Lim, J.; Dunn, B. Pseudocapacitive Contributions to Electrochemical Energy Storage in TiO_2 (Anatase) Nanoparticles. *J. Phys. Chem. C* **2007**, *111* (40), 14925–14931. https://doi.org/10.1021/jp074464w.

(73) Cook, J. B.; Kim, H.-S.; Lin, T. C.; Lai, C.-H.; Dunn, B.; Tolbert, S. H. Pseudocapacitive Charge Storage in Thick Composite MoS_2 Nanocrystal-Based Electrodes. *Adv. Energy Mater.* **2017**, *7* (2), 1–12. https://doi.org/10.1002/aenm.201601283.

(74) Huang, Z.; Wang, Z.; Jing, Q.; Guo, H.; Li, X.; Yang, Z. Investigation on the Effect of Na Doping on Structure and Li-Ion Kinetics of Layered $LiNi_{0.6}Co_{0.2}Mn_{0.2}O_2$ Cathode Material. *Electrochim. Acta* **2016**, *192*, 120–126. https://doi.org/10.1016/j.electacta.2016.01.139.

(75) Yang, Z.; Guo, X.; Xiang, W.; Hua, W.; Zhang, J.; He, F.; Wang, K.; Xiao, Y.; Zhong, B. K-Doped Layered $LiNi_{0.5}Co_{0.2}Mn_{0.3}O_2$ Cathode Material: Towards the Superior Rate Capability and Cycling Performance. *J. Alloys Compd.* **2017**, *699*, 358–365. https://doi.org/10.1016/j.jallcom.2016.11.245.

(76) Ryu, J.-H. Polarization Behavior of $Li_4Ti_5O_{12}$ Negative Electrode for Lithium-Ion Batteries. *J. Electrochem. Sci. Technol.* **2011**, *2* (3), 136–142. https://doi.org/10.5229/jecst.2011.2.3.136.

(77) Makimura, Y.; Sasaki, T.; Nonaka, T.; Nishimura, Y. F.; Uyama, T.; Okuda, C.; Itou, Y.; Takeuchi, Y. Factors Affecting Cycling Life of $LiNi_{0.8}Co_{0.15}Al_{0.05}O_2$ for Lithium-Ion Batteries. *J. Mater. Chem. A* **2016**, *4* (21), 8350–8358. https://doi.org/10.1039/C6TA01251E.

(78) Rauda, I. E.; Augustyn, V.; Saldarriaga-Lopez, L. C.; Chen, X.; Schelhas, L. T.; Rubloff, G. W.; Dunn, B.; Tolbert, S. H. Nanostructured Pseudocapacitors Based on Atomic Layer Deposition of V2O5 onto Conductive Nanocrystal-Based Mesoporous ITO Scaffolds. *Adv. Funct. Mater.* **2014**, *24* (42), 6717–6728. https://doi.org/10.1002/adfm.201401284.

CHAPTER 5

Dodecaborane-Based Dopants Designed to Shield Anion Electrostatics Lead to Increased Carrier Mobility in a Doped Conjugated Polymer

5.1 Introduction

Creating electrical carriers by doping in a controlled fashion enables semiconductors to be used in a wide variety of opto-electronic applications. Indeed, doped conjugated polymers are found in commercially available organic light-emitting diode (OLED) displays,[1] used to enhance organic solar cells[2] and field-effect transistors,[3] and are receiving increased attention for thermoelectric applications.[4-9] Doping of conjugated polymers can be achieved by electrochemical[10] or electrical charge injection[11] methods, but chemical doping is the best method to produce stable carriers without the need for a continuously applied potential. Chemical doping involves the introduction of a strong electron acceptor (oxidizing agent, for p-type doping) or a strong electron donor (reducing agent, for n-type doping) that can undergo a charge transfer reaction with the polymer,[12] creating charge carriers on the polymer chain while the dopant molecules remain in the film as counterions. Most conjugated polymers are p-type semiconductors, with positive carriers (holes, often referred to as polarons) created by oxidizing dopants.

Some of the earliest molecular dopants for conjugated polymers were halogen vapors,[12] but the instability of the doped films produced this way has led to the design of more stable molecular dopants.[13] One of the most popular molecular dopants for conjugated polymers is 2,3,5,6-tetrafluoro-7,7,8,8-tetracyanoquinodimethane (F_4TCNQ);[4-9,14-22] see Figure 5.1a (red) for chemical structure. F_4TCNQ has a low-lying lowest unoccupied molecular orbital (LUMO), (≈5.2 eV vs vacuum)[23] giving it the ability to p-dope a wide variety of conjugated polymers, including poly(3-hexylthiophene-2,5-diyl) (P3HT), whose chemical structure is shown in Figure 5.1a (green). Unlike doped inorganic semiconductors, where the interactions of substitutional impurities with the generated charge carriers are screened, the majority of the doping-induced carriers in conjugated polymers remain Coulomb-bound to the dopant counterions due to the low permittivity of organic materials.[16-18] For P3HT doped with F_4TCNQ, it has been estimated that even though the majority of F_4TCNQ molecules undergo integer charge transfer with P3HT, 95% of the holes that are created remain bound to their counterions[16] and thus do not contribute to electrical conduction. Indeed, strong electrostatic interactions between polarons and their counterions are known to localize polarons. To overcome this issue of carrier localization, in this work we describe a perfunctionalized dodecaborane cluster that was designed to spatially separate the anions created when doping conjugated polymers. Dodecaborane (DDB) clusters are robust and kinetically stable due to their 3D aromaticity, which allows for electron delocalization around the boron scaffold.[24-28] Certain perfunctionalized clusters of the type $B_{12}(OR)_{12}$ (R = alkyl, aryl, H) behave as reversible, redox-active species with multiple accessible oxidation states.[27-31] Recent advances have led to the rational and rapid synthesis of such substituted dodecaboranes with tunable redox potentials.[29] We have designed a DDB cluster with a very high ground-state redox potential, which when combined with the cluster's intrinsic stabilization of electron density in its well-shielded core, makes it an outstanding candidate to molecularly dope conjugated polymers and reduce their mobilities.[15]

To overcome this issue of carrier localization, in this work we describe a perfunctionalized dodecaborane cluster that was designed to spatially separate the anions created when doping conjugated polymers. Dodecaborane (DDB) clusters are robust and kinetically stable due to their 3D aromaticity, which allows for electron delocalization around the boron scaffold.[24-28] Certain

perfunctionalized clusters of the type $B_{12}(OR)_{12}$ (R = alkyl, aryl, H) behave as reversible, redox-active species with multiple accessible oxidation states.[27-31] Recent advances have led to the rational and rapid synthesis of such substituted dodecaboranes with tunable redox potentials.[29] We have designed a DDB cluster with a very high ground-state redox potential, which when combined with the cluster's intrinsic stabilization of electron density in its well-shielded core, makes it an outstanding candidate to molecularly dope conjugated polymers.

The conventional processing method to dope polymeric semiconductors, known as blend doping, involves mixing the polymer and dopant in solution prior to casting the doped polymer onto a substrate. The solvents for most conjugated polymers, however, are nonpolar, such that at high doping levels the charges produced on the polymer and dopant render them insoluble during solution processing, yielding very poor doped film quality. This problem has been overcome by sequential doping,[5-9,14,15,19-22,32,33] which relies on exposing a precast polymer film to the dopant, either in the vapor phase[5-8,20,22,32,33] or in solution.[14] Solution sequential processing uses a semiorthogonal solvent to swell but not dissolve the polymer underlayer, allowing mass action to drive the dopant into the swollen polymer film.[5,6,8,9,14,15,19-21] Doping by solution sequential processing (SqP) maintains all of the advantages of solution-based processing methods, producing high-quality films with conductivities that are significantly better than those produced by blend doping.[14,19] We expect that SqP should be amenable for use with dodecaborane clusters given that it is routinely used to infiltrate large molecules such as fullerenes and large dopants into films of conjugated polymers.[34-38]

5.2 Results and Discussion

Here, we report the use of a newly synthesized, strongly oxidizing perfunctionalized DDB cluster as a dopant for the conjugated polymer P3HT. The chemical structure of our new cluster, shown in Figure 5.1a (blue), depicts the pseudo-icosahedral dodecaborane core with each vertex functionalized with a 3,5-bis(trifluoromethyl)benzyloxy substituent. We refer to this to this molecule as DDB-F_{72} because of the 72 electron-withdrawing F atoms placed on the periphery of the cluster. Using SqP to dope identical films of P3HT with both DDB-F_{72} and F_4TCNQ, we find that at equimolar doping concentrations, DDB-F_{72} produces doped films with conductivities that are an order of magnitude higher. We verify using NMR spectroscopy techniques that there is negligible electron transfer between DDB-F_{72} clusters, so that the conductivity improvement we see comes solely from the increased mobility of polarons on the conjugated polymer.

To understand this increased conductivity, we structurally characterize our doped polymer films by using X-ray photoelectron spectroscopy (XPS) and 2D grazing-incidence wide-angle X-ray scattering (2D-GIWAXS) to show that DDB-F_{72}-doped P3HT films are remarkably noncrystalline, likely due to the fact that the DDB cluster cannot intercalate into the crystalline polymer domains due to its large size. This is in sharp contrast to dopants such as F_4TCNQ, which reside within the polymer crystallites[9,15] in closer proximity to the polarons. In addition to residing farther from the polymer crystallites, the steric footprint associated with DDB-F_{72}'s peripheral substitutions, in combination with the delocalization of the unpaired electron within the shielded boron cluster core, allows for greatly reduced electrostatic interactions between DDB-F_{72} anions and the holes on the polymer chains.

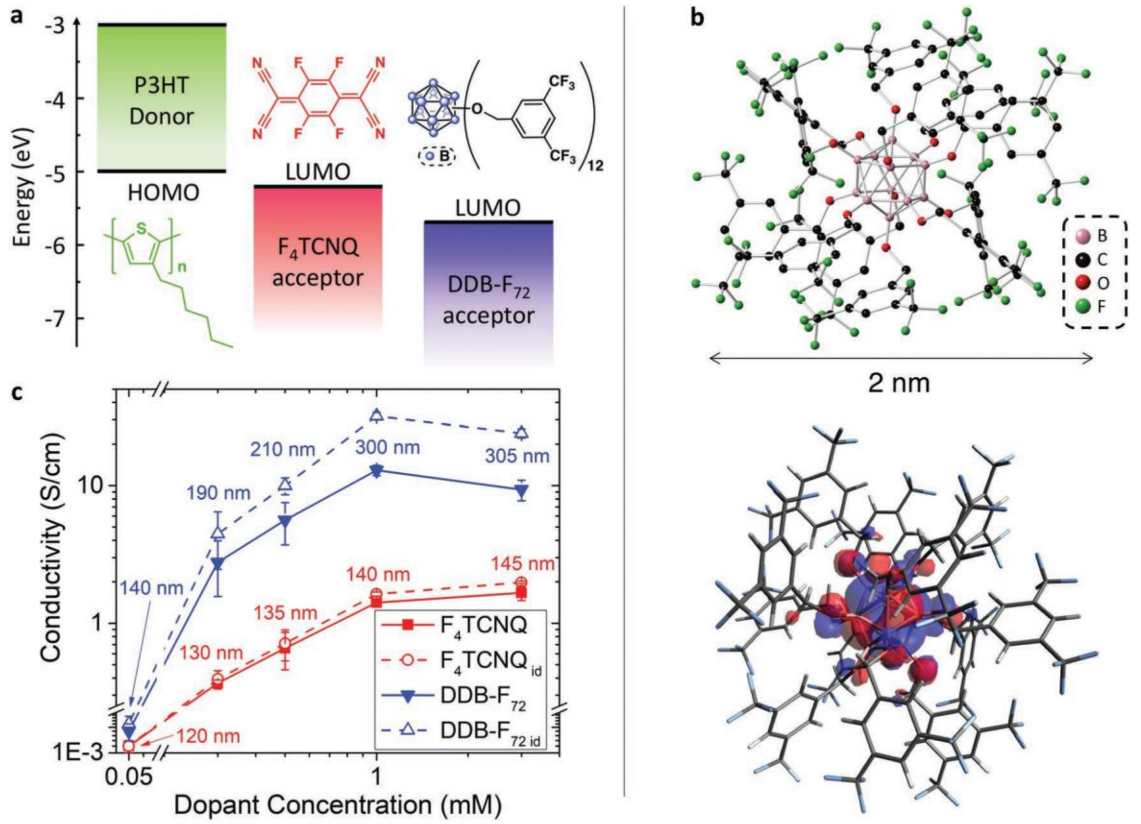

Figure 5.1 Chemical structures and schematic energy diagram of P3HT, F_4TCNQ, and DDB-F_{72} showing ≈0.5 V greater offset for DDB-F_{72} than F_4TCNQ. b) (Top) Ball-and-stick representation of the X-ray crystal structure of DDB-F_{72}; (bottom) DDB-F_{72} anion SOMO calculated by TD-DFT showing the electron localized on the DDB core. c) Conductivities (solid symbols, calculated using the measured thickness) and idealized conductivities (open symbols, calculated using the 120 nm original thickness) of P3HT films doped with F_4TCNQ (red symbols) and DDB-F_{72} (blue symbols) via solution sequential doping. The error bars are the standard deviation calculated from at least three samples. At the same dopant concentration, DDB-F_{72} produces conductivities that are an order of magnitude higher than those produced by F_4TCNQ.

With this reduced electrostatic interaction, we show using combination of AC Hall effect and IR spectroscopy measurements that the polarons on P3HT doped with DDB-F_{72} have mobilities that are an order of magnitude higher than those created by doping with F_4TCNQ; the carrier mobilities with DDB-F_{72} are comparable to those created by charge modulation with no anions present at all.[11] We calculate idealized conductivities in our DDB-F_{72}-doped P3HT films of

32 S cm^{-1}, despite the lack of crystallinity in our doped material. These findings highlight the importance of polaron delocalization effects and the corresponding need to electrostatically screen the anion from the holes. Reducing the polaron/counterion Coulomb interaction is clearly important for electrical conduction. We suspect the reason that high crystallinity is important for good conductivity with dopants such as in F_4TCNQ that it also reduces the Coulomb interaction. This is because when F_4TCNQ enters the polymer crystallites, it happens to sit in the lamellar regions among the polymer side chains so that the anion is held a fair distance away from the polymer backbone where the polaron resides, so that high crystallinity leads to a reduced Coulomb interaction. In contrast, our tailored DDB dopants are so large that they can only infiltrate amorphous regions, but electrostatic shielding is taken care of by the dopant itself so that polymer crystallinity is no longer required.

We chose P3HT for this study as it is a model conjugated polymer that has become an important reference material for the study of optoelectronic processes in organic semiconductors. The offset between the highest occupied molecular orbital (HOMO) of the polymer and LUMO of the dopant gives the energetic driving force for doping via integer charge transfer.[16] Figure 5.1a shows these energy levels for P3HT, F_4TCNQ, and DDB-F_{72} based on cyclic voltammetry (CV) measurements of the dopants (see Figure S5.6 in the Supporting Information) and literature values for P3HT.[39] Our CV measurements indicate a $0/1^-$ redox potential of 0.16 V versus Fc/Fc$^+$ for F_4TCNQ, in excellent agreement with literature values.[40] The redox potential of DDB-F_{72} is 0.67 V versus Fc/F$^+$, thus producing a 0.5 eV greater energetic driving force for doping compared to F_4TCNQ.

The X-ray crystal structure of DDB-F_{72} is shown in Figure 5.1b (top) (see the Supporting Information for CIF file). The diameter of DDB-F_{72} is ≈2 nm, nearly twice that of a C60 molecule.

The B_{12}-based core lies deep in the center of the cluster, surrounded by the corona of 12 bulky substituents, so if the additional unpaired electron on the reduced cluster is confined to the core as expected,[29,31] we should be able to achieve increased spatial separation of the electron from the polaron. Indeed, our time-dependent density functional theory (TD-DFT) calculations reveal that the singly occupied molecular orbital (SOMO) of the DDB-F_{72} anion is delocalized only on the core, as shown in Figure 5.1b (bottom).

To dope conjugated polymer films via SqP, we started by spinning 120 nm thick P3HT films out of 1,2-dichorobenzene at 1000 rpm for 60 s. We then spun the dopant (F_4TCNQ or DDB-F_{72}) out of solutions with different concentrations in dichloromethane (DCM) at 4000 rpm for 10 s on top of the pre-cast polymer film. We measured the electrical conductivity of the doped films using the Van der Pauw method,[41] a type of four-point-probe measurement, with the electrodes placed at the corners of a 1.5 cm x 1.5 cm square (see the Supporting Information for details). The results are shown in Figure 5.1c.

The filled points/solid curves in Figure 5.1c show that for the same molar concentration of dopant, the conductivities of P3HT films doped with DDB-F_{72} (blue down-pointing triangles) are about an order of magnitude higher than the F_4TCNQ-doped samples (red squares). For example, at 1×10^{-3} M dopant concentrations, we achieve P3HT conductivities of 12.9 S cm^{-1} when doped with DDB-F_{72} but only 1.4 S cm^{-1} when doped with F_4TCNQ. We were unable to explore SqP doping concentrations higher than a few millimolar because of the solubility limit of both dopants in DCM. The drop in conductivity observed for 3×10^{-3} M DDB-F_{72} solutions is due to their colloidal nature, which is above the molecular solubility limit; the colloidal solutions do not effectively deliver dopant in the P3HT film, as documented in the spectroscopy section of the Supporting Information. The DDB-F_{72}-doped films are stable under inert atmosphere for days (see the Supporting Information), suggesting the films would remain stable indefinitely if packaged appropriately.

One interesting feature of SqP is that so much of the large DDB-F_{72} dopant can be intercalated that the polymer films change thickness after doping.[34] Starting with 120 nm thick pre-cast P3HT films, we find that doping with a 1 x 10^{-3} M solution yields 140 nm thick films doped with F_4TCNQ but 300 nm thick films doped with DDB-F_{72}. Since SqP relies on swelling of the polymer followed by infiltration of the dopant into the swollen polymer matrix,[35] we worried about whether or not DDB-F_{72} was fully penetrating into the P3HT film. Given the large size of the DDB-F_{72} molecule and the fact that some large dopants have shown limited film penetration in previous work,[42] it is possible that the large increase in thickness we observe results from an overlayer of excess DDB-F_{72} on top of the P3HT film rather than uniform intercalation throughout the film.

To investigate the penetration of the dopant into the film, we used XPS, which has a penetration depth of only a few nm, to examine the oxidation state of boron near the top surface of the film. Figure 5.2 shows the B 1s XPS spectra of both the neutral DDB-F_{72} cluster (black curve) and the DDB-F_{72} anion (red curve), along with one of our DDB-F_{72}-doped P3HT films (blue curve). The data make clear that the boron on the top surface of our films is reduced, suggesting that there is no excess overlayer of neutral clusters on top of the film, and that the clusters have indeed penetrated well into the P3HT layer. Further evidence that there is no continuous cluster overlayer is that XPS is able to pick up considerable signal from the sulfur of P3HT on the top surface of this doped film (see Table S5.3 in the Supporting Information). In addition, we imaged the top surface of the films using both optical and scanning electron microscopies (SEM) (see Figures S5.9 and S5.10 of the Supporting Information). In the optical

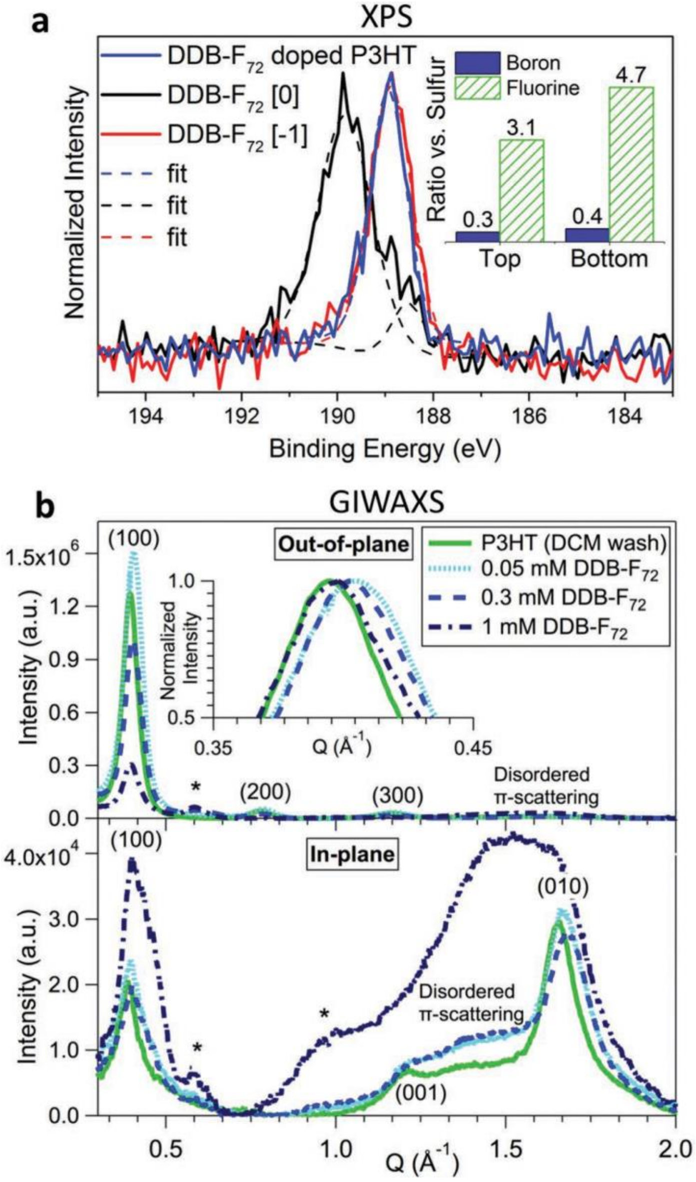

Figure 5.2 Structural characterization of DDB-cluster-doped films. a) B 1s XPS spectra of the top surface of pure DDB-F_{72} films in the neutral [0, black curve] and anionic [-1, red curve] states, overlaid with that of a DDB-F_{72}-doped P3HT film (blue curve). The overlap of the doped film and anion spectra indicates that the clusters at the top surface of the film are all reduced. (Inset) XPS-determined B:S and F:S ratios measured at the top and bottom of DDB-F_{72}-doped P3HT films indicating that the clusters penetrate the film. b) Out-of-plane (top) and in-plane (bottom) 2D-GIWAXS spectra for films of pure P3HT (green curves) and DDB-F_{72}-doped P3HT (blue curves). (Inset) Zoomed in view of the (100) peak. Dopant-induced peaks are denoted by asterisks (*). These data indicate DDB-F_{72} does not enter the crystallites given its large size and at high dopant concentration (dark blue dashed-dotted curves), there is significant loss of overall crystallinity.

images, we see sparse crystallites of DDB-F_{72} that certainly do not form a contiguous overlayer. The SEM images reveal a sharp crack pattern, which we attribute as resulting from the expansion and contraction of the film upon swelling and deswelling during the SqP process.

To further our understanding of the degree of cluster penetration, we also examined the elemental composition of both the top and bottom surfaces of our DDB-F_{72}-doped P3HT films using XPS; we accessed the bottom surfaces by floating doped films off the substrate,[34] as described in more detail in the Supporting Information. Since sulfur is unique to P3HT while boron and fluorine are unique to DDB-F_{72}, the sulfur 2p:boron 1s and sulfur 2p:fluorine 1s peak-integrated ratios, shown in the inset to Figure 5.2a, give a good measure of the film composition at each surface. The data make clear that the B:S and F:S ratios on the top and bottom of the DDB-F_{72}-doped films are similar, suggesting that the clusters are roughly evenly distributed throughout the film. Indeed, recent work has shown that other fairly large dopant molecules also are able to penetrate well into pre-cast P3HT films.[37] Moreover, the XPS peak position for boron on both the top and bottom film surfaces indicate the cluster is reduced throughout the film (see the Supporting Information for detailed XPS peak fit assignments and additional information).

It is important to note that the calculation of electrical conductivity from the measured sheet resistivity scales inversely with the thickness of a material. Given the large thickness change of our DDB-F_{72}-doped films, this makes the conductivities we measure all the more remarkable because electrical conduction takes place only on the polymer, but the polymer comprises only ~1/3 of the material in the DDB-F_{72}-doped films. To verify the conduction mechanism, we investigated the kinetics of electron self-exchange between $[\text{DDB-F72}]^{0}$ and $[\text{DDB-F72}]^{-1}$ by dynamic NMR line broadening experiments, described in more detail in the Supporting Information. Using ^{19}F NMR across a range of 40 ºC, we observed no coalescence of the peaks corresponding to the neutral and anionic forms of DDB-F_{72} in solution, indicating an electron self-exchange rate slower than that of the experimental timescale ($k_{ET} < 1.2 \times 10^3$ s^{-1} or $\tau_{ET} > 0.84$ ms), which is orders of magnitude longer than the typical collision time between clusters. This indicates that there is a high intrinsic barrier to electron transfer between DDB-F_{72} clusters, most likely the result of small electronic couplings due to poor orbital overlap between self-exchanging pairs.[43-45] Indeed, the idea of poor electron transfer between DDB clusters is in agreement with our TD-DFT calculations in Figure 5.1b, which show strong localization of the electron in the cluster interior, likely due to stabilization from the aromaticity of the B_{12} cluster. Overall, our NMR measurements strongly imply that electron hopping between DDB clusters does not occur on any reasonable timescale, and therefore the electrical conduction of our doped films takes place only through the polymer network.

Given that the doped films are 300 nm thick but that there is only an initially 120 nm thickness of polymer material in the doped film to conduct, we calculated “idealized conductivities” based on the initial polymer thickness of 120 nm rather than using the measured doped film thickness. These idealized conductivities, which represent the limit of conductivity that could be achieved with the same carrier mobility if there were no swelling of the film during doping, are shown by the dotted lines and open symbols in Figure 5.1c. The difference between the idealized conductivity and the conductivity is larger for the DDB-F_{72}-doped films due to their larger thickness increase. At the 1×10^{-3} M dopant concentration, we achieve idealized conductivities of ≈32 S cm^{-1} for the DDB-F_{72}-doped films, whereas the idealized conductivity of F_4TCNQ-doped films reaches only 2.0 S cm^{-1}.

To better understand the structure of our DDB-F_{72}-doped films, we used 2D GIWAXS. Figure 5.2b shows the out-of-plane (top) and in-plane (bottom) scattering patterns of P3HT (green solid curves) and P3HT doped with DDB-F_{72} from low-to-high concentration (light-to-dark blue curves). As expected for pure P3HT, which is well known to have a preferential edge-on orientation,[8,9,20] we see that the intensity of the π-π stacking (010) peak is largely in-plane, while strong peak intensity is observed in the out-of-plane direction for the lamellar (h00) peaks, indicating edge-on orientation with respect to the substrate.

Upon doping with DDB-F_{72} with low-to-mid concentration solutions (0.05 and 0.3 x 10^{-3} M), we see that the edge-on orientation of P3HT's crystallites is maintained as the (010) peak is still largely in-plane, consistent with the fact that SqP is known to preserve domain orientation.[14,15,36] The in-plane data reveals a shift in the (010) peak to higher Q, reminiscent of what has been previously reported for F_4TCNQ,[9,15] but with some significant differences. In F_4TCNQ-doped-P3HT, a much larger shift of the (010) π-stacking peak, out to 1.8 Q, is observed upon doping compared to what is seen here. Despite the large peak shift, the change in the π-stacking distance is actually quite small as the structural change is mainly due to reorientation of the unit cell: F_4TCNQ intercalation into the side-chain regions of the P3HT crystallites causes an adjustment of the chain angle relative to the unit cell axes.[9] DDB-F_{72} only causes a small shift of the P3HT (010) peak from 1.66 to 1.68 Q, indicating that this intercalation-induced phase transition does not take place. Additionally, for our DDB-F_{72}-doped films, we observe a small shift in the P3HT (100) lamellar peak to higher Q (see inset), which is in the opposite direction of what is typically seen with F_4TCNQ doping.[9,15] This provides a clear indication that, unlike F_4TCNQ, DDB-F_{72} does not intercalate into the P3HT lamellar regions. The lack of intercalation of large molecular structures into the polymer crystallites is not surprising as their size does not allow them to fit between P3HT side chains. Furthermore, previous work has shown that addition of bulky groups on fullerenes can inhibit their intercalation into the lamellar regions of conjugated polymers,[46] and molecules of DDB-F_{72} have approximately twice the diameter of a typical fullerene. Overall, the observed peak shifts suggest that for DDB-F_{72}, the structural changes induced by doping are solely due to the delocalization of charges within a crystallite,[9,15] likely accompanied by counterions situated around the edge of each doped crystallite.

At high (1 x 10^{-3} M) DDB-F_{72} dopant solution concentration, we see a significant loss of crystallinity and a broadening of the P3HT (100) peak rather than a shift. Since GIWAXS only reports on crystalline regions in the doped films, the broadening we observe suggests that at this high doping concentration, most of the doped regions have become amorphous and the only remaining P3HT crystallites seen via GIWAXS are those that remain undoped. The large increase in disordered P3HT π-stacking intensity seen between 1.2 and 1.5 Q further supports the idea that these high-concentration-doped films are much more disordered than those doped using solutions with lower concentrations of DDB-F_{72}.

Interestingly, we also observe the appearance of new peaks at 0.6 and 1.0 Q (marked by asterisks in Figure 5.2b) when P3HT is doped with DDB-F_{72}. These new peaks are broadened to the same extent and show a very similar texture as the P3HT peaks. The new peaks do not at all resemble those seen for DDB-F_{72} crystallites (see the Supporting Information). Therefore, we hypothesize that these new peaks either result from a new polymorph of P3HT that preferentially forms in the presence of DDB-F_{72} or a P3HT polymorph that is stable only at very high doping levels.

To characterize the extent of charge carrier delocalization in DDB-F_{72}-doped films, we turn to spectroscopic measurements. Spano and co-workers have argued theoretically that the degree of delocalization of holes on P3HT is directly reflected in the shape and position of the polaron's IR

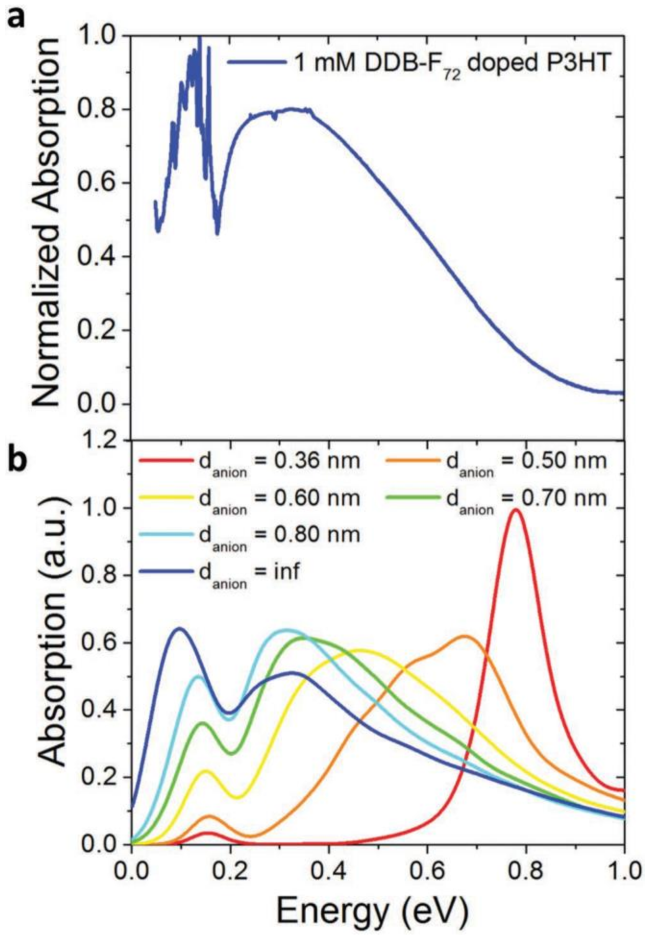

Figure 5.3 Delocalized polaron IR-spectrum. a) Experimental IR absorption spectrum of the polaron in a 1 x 10^{-3} M DDB-F_{72}-doped P3HT film. b) Simulated P3HT polaron absorption spectrum for different anion– polaron distances, taken from ref. 15. The measured spectrum is in excellent agreement with the theoretical spectrum for an anion at infinite distance, indicating that the polarons in the chemically doped DDB-F_{72} sample are as delocalized as possible. Note: A distance-dependent permittivity for the pure polymer was used for the calculation. Although the use of a different permittivity would change the shape of the spectrum of the more Coulomb-localized polarons, the spectrum calculated for infinite anion distance is invariant with respect to the choice of permittivity.[15]

absorption spectrum.[15,21,47-49] Their predictions for how the spectral shape changes when the polarons are localized by proximity to an anion, reproduced from ref. 15, are shown in Figure 5.3b, where the blue curve shows the spectrum of a fully delocalized P3HT polaron with no confinement by an anion. We have shown previously using F_4TCNQ-doped P3HT films with different crystallinities that the spectrum of polarons with different degrees of delocalization matches well with Spano and coworkers' theory, and indeed correlates strongly with the experimentally measured polaron mobility.[15]

Figure 5.3a shows the measured IR spectrum of our DDB-F_{72}-doped P3HT films. The shape and position of the spectrum we measure is essentially identical to that predicted for a fully delocalized polaron that has no Coulombic interaction with an anion. Indeed, similar IR spectra have been measured in P3HT films doped by charge modulation with no anion present (i.e., doped by the presence of a large applied voltage).[11] A similar polaron spectrum also has been observed in recent work doping P3HT with large molybdenum dithiolene complexes, although the conductivities were much lower than we see here, likely due to low carrier densities, and carrier mobilities were not reported.[38] This indicates that the electron on the DDB-F_{72} anion is sufficiently isolated to have no effect on the polaron, despite the relatively low dielectric constant of P3HT. This is because the electron is localized entirely in the cluster interior, which by Gauss' law means that it effectively behaves as a point charge at the center of the cluster. The steric bulk associated with the substituted DDB cluster means that at no point can the polaron–anion distance be less than the radius of the cluster, which is ~1 nm. We believe that it is the combination of electron localization to the dopant interior, shielded by the bulky substituents, with the fact that the dopants sit outside the P3HT crystallites that leads to this unusual but highly favorable situation where the polaron is entirely unaffected by the dopant counterion.

To further characterize the extent of delocalization of the polarons in our DDB-F_{72}-doped P3HT films, we performed AC Hall effect measurements,[50-53] the results of which for identically prepared F_4TCNQ- and DDB-F_{72}-doped P3HT films[14] are summarized in Table 5.1. The concentrations chosen for both dopants were their solubility limits in DCM. We note that for low-mobility materials such as doped conjugated polymers, screening effects can cause Hall effect measurements to slightly overestimate the mobile carrier concentration and thus slightly underestimate the free carrier mobility,[53] as discussed in more detail in the Supporting Information.

Table 5.1 Comparison of carrier density (n), mobility (μ), and conductivity(σ) measured by the AC Hall effect for P3HT films doped with DDB-F_{72} and F_4TCNQ at their respective solubility limits in DCM. Also shown is the number density of dopant molecules in the film estimated via mass measurements (Nest); see the Supporting Information for details. The F4TCNQ data is taken from ref. 14.

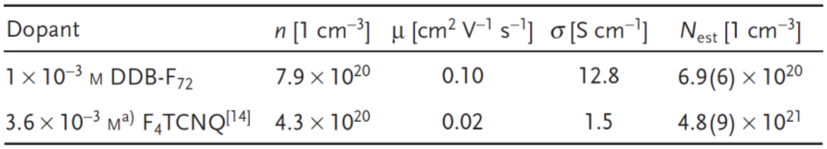

Dopant	n [1 cm^{-3}]	μ [cm^2 V^{-1} s^{-1}]	σ [S cm^{-1}]	N_{est} [1 cm^{-3}]
1×10^{-3} M DDB-F_{72}	7.9×10^{20}	0.10	12.8	$6.9(6) \times 10^{20}$
3.6×10^{-3} M$^{a)}$ F_4TCNQ[14]	4.3×10^{20}	0.02	1.5	$4.8(9) \times 10^{21}$

In our P3HT sample doped with 1 x 10^{-3} m DDB-F_{72}, we measure a mobile carrier concentration that is roughly twice that of the F_4TCNQ-doped sample. We believe that this results from a higher ratio of integer charge transfer due to the greater energetic driving force for doping with DDB-F_{72}, summarized in Figure 5.1a, and an increase in free carrier (as opposed to trapped carrier) generation due to less Coulomb interaction with DDB-F_{72}. In fact, we have estimated the overall concentration of dopant clusters in the film by directly measuring the change in mass upon doping the films (see the Supporting Information for details). For F_4TCNQ, the dopant density is 4.8(9) x 10^{21} cm^{-3} yielding a doping efficiency of ~10% (slightly higher than the 5% value determined by Pingel and Neher[16,17] likely due to the fact that we are in a much higher doping regime and/or to the potential overestimation of the free carrier concentration via AC Hall measurements[53]). For DDB-F_{72}, the dopant concentration is 6.9(6) ± 1.2 x 10^{20} cm^{-3}, which agrees within error with the carrier concentration we measure via the AC Hall effect (which we also expect to be slightly overestimated[53]). This strongly suggests that essentially every DDB-F_{72}

dopant molecule gives rise to a free polaron on P3HT, a full order of magnitude improvement over the ~5–10% free carrier yield estimated for F_4TCNQ.

Perhaps more importantly, the carrier mobility of 0.1 $cm^2\ V^{-1}\ s^{-1}$ is five times higher for DDB-F_{72} than F_4TCNQ, a direct reflection of the higher degree of polaron delocalization with DDB-F_{72}. Moreover, the polaron mobility in the DDB-F_{72}-doped P3HT films is comparable to mobilities seen only in charge-modulation-doped films with no anions present[11] or in highly crystalline doped 100% regioregular P3HT.[15] Finally, the large degree of polaron delocalization is also supported by the results of temperature-dependent conductivity experiments, which are discussed in the Supporting Information.

5.3 Conclusions

Overall, we have demonstrated that by using a functionalized dodecaborane dopant, we can achieve spatial separation of the conjugated polymer polaron and counterion leading to highly delocalized and mobile charge carriers even in poorly crystalline polymer material. The dodecaborate cluster anions cannot infiltrate into P3HT crystallites, resulting in a substantial loss in crystallinity upon doping. Thus, the counterions reside outside any remaining P3HT crystallites, and the unpaired electron on the DDB-F_{72} anion is further separated from the polarons on the polymer by being confined to the cluster core. The shielding provided by the cluster's physical and electronic structure relaxes the crystallinity constraints typically needed to achieve high conductivities and mobilities in doped conjugated polymer materials. Thus, with other dopants such as F_4TCNQ, crystallinity is important both for improving the delocalization of the polarons and for keeping the anion as far from the polymer backbone as possible. With our dodecaborane cluster dopant, on the other hand, we see that reducing the polaron localization by the anion is at least as important as delocalization due to crystallinity in determining polaron mobility and thus overall conductivity. We achieve conductivities of 12.8 S cm^{-1} and mobilities of 0.1 cm^{2} V^{-1} s^{-1} with our DDB-F$_{72}$-doped P3HT, values that are an order of magnitude higher than those obtained with comparable doping by F$_4$TCNQ. Since the DDB-F¬$_{72}$-doped P3HT films significantly increase in thickness upon doping and the DDB clusters themselves do not conduct, this means that the idealized P3HT hole conductivities reach 32 S cm^{-1}. Thus, by carefully designing new molecular dopants, we can produce stable molecularly doped conjugated polymer films with polaron mobilities limited only by intrinsic materials properties, rather than being limited by electrostatic attraction to the proximal dopant anion.

5.4 Supplementary Information

Materials, Synthesis and Characterization

P3HT (Rieke metals inc., 4002-EE, Mn = 50-70 kg/mol, regioregularity 91-94%) and F$_4$TCNQ (TCI Chemicals) were purchased and used as received. NBu$_4$[DDB-F$_{72}$] and [NBu$_4$]$_2$[B$_{12}$(OH)$_{12}$] were synthesized following similar methods to previously reported procedures.[54]

Microwave reactions were performed using a CEM Discover SP microwave synthesis reactor. The reactions were conducted in glass 10 mL microwave reactor vials purchased from CEM with silicone/PTFE caps equipped with a stirbar. 3,5-bis(trifluoromethyl)benzyl bromide (97 %) was purchased from Oakwood Chemicals and used as received. N,N-diisopropylethylamine (>99 %) was purchased from Sigma Aldrich and used as received. Reagent grade hexanes, acetone, and ethyl acetate used for column chromatography were purchased from Sigma Aldrich and used as received. The CH3CN (anhydrous, 99.8 %) used for the synthesis of DDB-F$_{72}$ was purified using a solvent purification system and was stored in a nitrogen-filled glovebox over activated 3

Å molecular sieves. NMR spectra were recorded using Bruker AV500 or Bruker AV300 spectrometers at 300 or 500 MHz (1H), 161 MHz (11B), and 282 MHz (19F) reported in δ (parts per million) relative to tetramethylsilane (1H), $BF_3{\cdot}Et_2O$ (^{11}B) or C_6H_5F (^{19}F), respectively, and referenced to residual 1H signals of the deuterated solvent (^1H (δ) $CDCl_3$ 7.26; 11B (δ) BF_3Et_2O 0.00 ppm; ^{19}F (δ) C_6H_5F -113.15 ppm). Deuterated solvents (Cambridge Isotope Laboratories) for NMR spectroscopic analyses were stored over 3 Å molecular sieves.

$B_{12}(OCH_2((3,5\text{-}CF_3)2C_6H_3))_{12}$ (DDB-F_{72}) : $[NBu_4]2B_{12}(OH)_{12}$ (200mg, 0.244 mmol) was charged to a 10 mL glass CEM microwave vial equipped with a stirbar. 3 mL of CH_3CN was added, followed by N,N-diisopropyl-N-ethylamine (0.81 mL, 4.64 mmol) and 3,5-bis(trifluoromethyl)benzyl bromide (2.69 mL, 14.7 mmol). The mixture was heated to 140 ºC in a microwave for 45 min. Upon cooling, the purple mixture was concentrated under reduced pressure and was subjected to column chromatography. The purple mixture was loaded with 65/35 hexanes/ethyl acetate (some of the material did not fully dissolve) and the excess benzyl bromide was eluted. The column was flushed with acetone and the eluent was collected. The acetone fraction was dried in vacuo. The resulting residue was charged to a vial equipped with a stirbar and brought into the glovebox, where it was dissolved in ~ 5 mL CH_3CN and was charged with $NOBF_4$ (71 mg, 0.607 mmol). The resulting mixture, which gradually developed an orange precipitate, was stirred for 12 h. The orange mixture was placed in the freezer (~ −30 °C) overnight and was then isolated by filtration on a glass frit and washed three times with cold (~ −30 °C) CH_3CN. The resulting orange powder was dried in vacuo and was used without further purification. (448 mg, 60%) ^1H NMR (500 MHz, $CDCl_3$) 7.77 (s, 12H, Ar), 7.52 (s, 24H, Ar), 5.47 (s, 24H, CH_2); ^{11}B NMR (161 MHz): 41.28 (s); ^{19}F NMR (282 MHz): 63.73 (s).

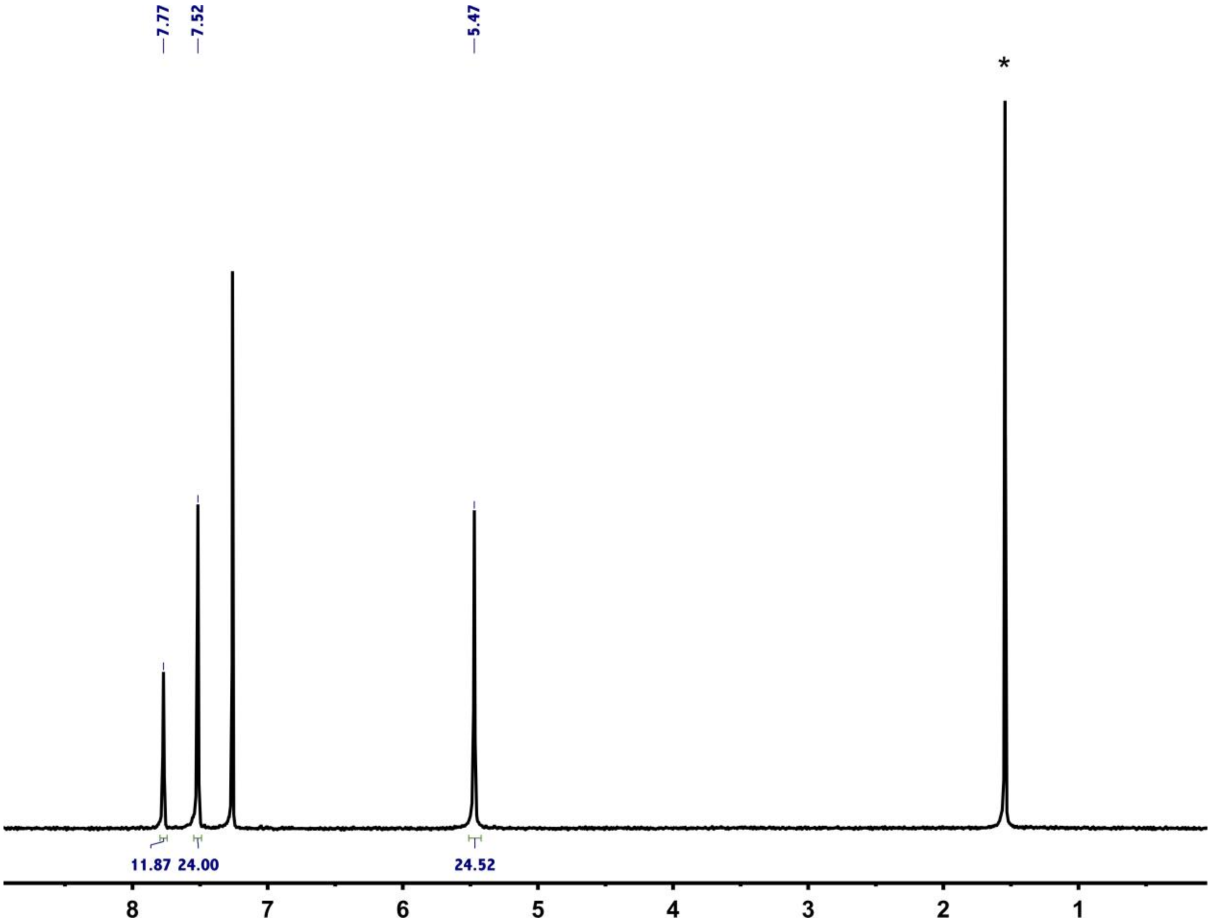

Figure S5.1. ^{1}H NMR of DDB-F_{72}, * residual H_2O.

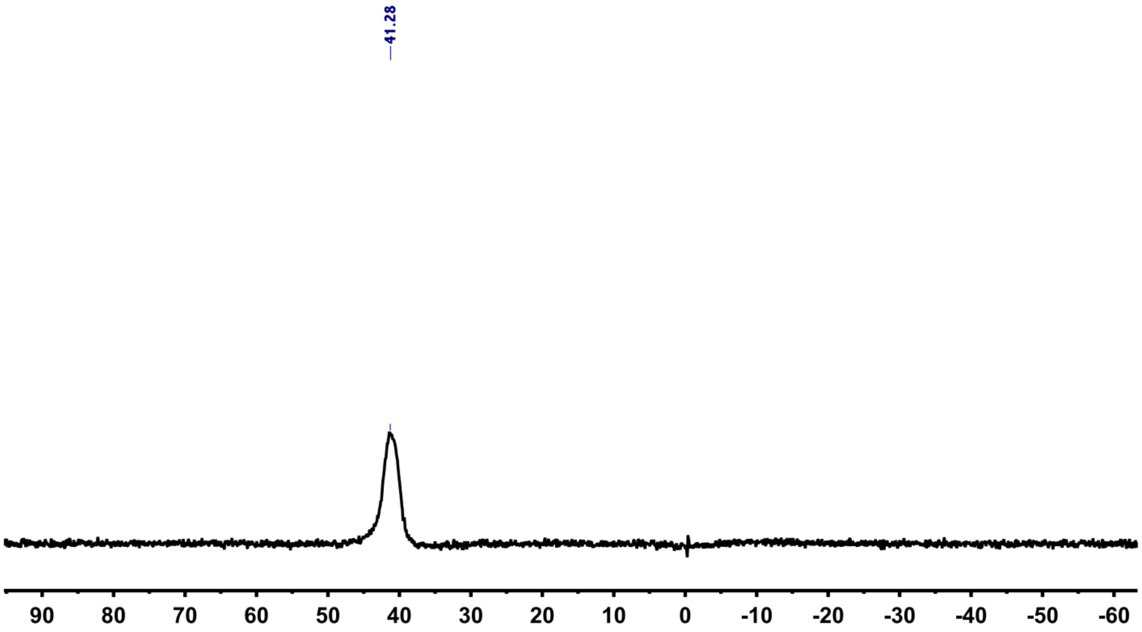

Figure S5.2. ^{11}B NMR of DDB-F_{72}.

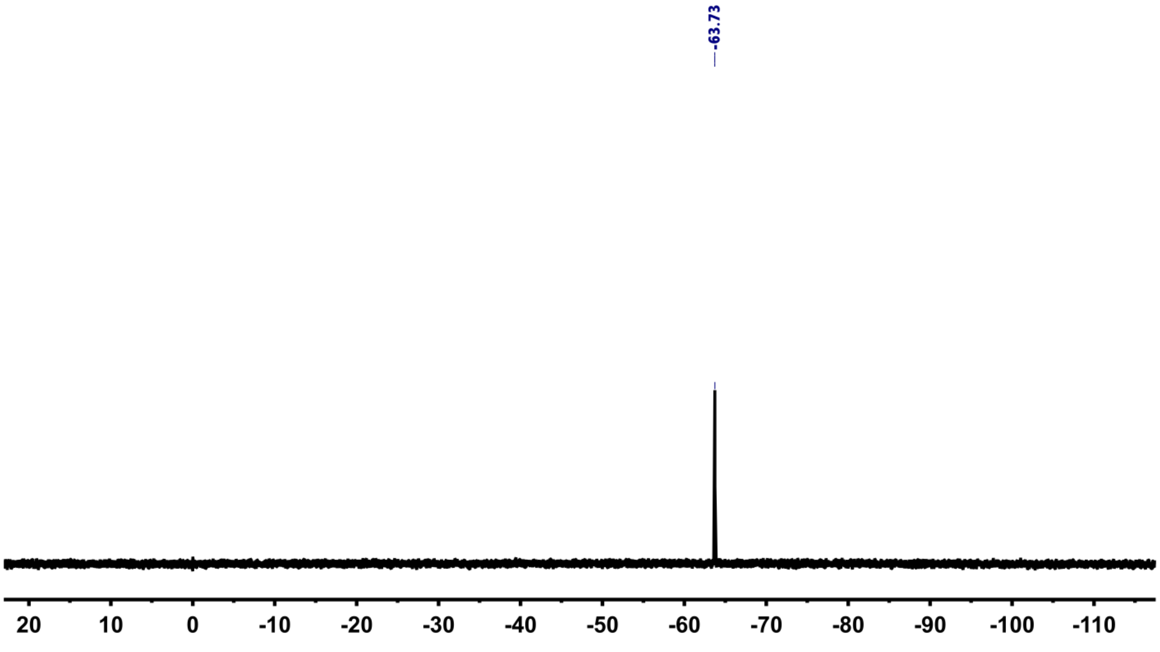

Figure S5.3. ^{19}F NMR of DDB-F_{72}.

Experimental Methods

Cyclic Voltammetry The redox potentials of F_4TCNQ and DDB-F_{72} were measured in-house by cyclic voltammetry using a CH Instruments CHI630D potentiostat with a glassy carbon disc working electrode, Pt wire counter electrode, and Ag/Ag^+ wire pseudoreference. All experiments were conducted at a 0.5 mM analyte concentration in 0.1M $[NnBu_4]PF_6/CH_2Cl_2$ at a scan rate of 0.1 mV/s and referenced to an internal ferrocene standard. The solution was degassed by bubbling Ar, and the CV measurements were performed under Ar gas.

TD-DFT Ground state geometry optimization of the neutral DDB-F_{72} molecule was performed using Turbomole[55] for which the initial coordinates were adopted from the single crystal X-ray structure. The τ-dependent gradient-corrected functional of Tao, Perdew, Staroverov, and Scuseria (TPSS)[56] with the def2-TZVP[57,58] basis set was used. In order to access the energies of the anion SOMO, the TD-DFT formalism was used with the hybrid functional of TPSS(TPSSh)[56,59] with cc-pvdz[60,61] basis set. Gaussian 09[62] was used for the excited state calculation and Avogadro was used for visualization.

Electron transfer self-exchange rate by NMR Under an inert atmosphere, 0.1 mM stock solutions of [DDB-F_{72}]0 and [DDB-F_{72}]$^-$ were prepared using 4:1 o-difluorobenzene:benzene as the solvent. Five aliquots of the oxidized species were then added to separate J-Young NMR tubes giving volumes of 0 L, 200 L, 400 L, 600 L, and 800 L respectively. To these samples, aliquots of the reduced species were added such that the final sampled volume totaled 800 L. This afforded five samples whose mole fraction of reduced species was near 1, 0.75, 0.5, 0.25, and 0 respectively. All samples were analyzed immediately on a Bruker 300 MHz NMR spectrometer and analyzed using iNMR software. A total of 64 scans of 65536 data points (2.04 Hz resolution) were collected from +20.0 to −216.0 ppm.

Film fabrication Substrates were cleaned by sequential sonication in alconox detergent solution, deionized water, acetone, and isopropanol. Subsequent film preparation steps were carried out in nitrogen glove box atmosphere. P3HT films were spin-coated at a rate of 1000 rpm for 60 seconds from a 20 mg/mL polymer solution in orthodichlorobenzene, producing ~120-nm thick films. The films were doped in a second step in which the dopant solution was deposited on the pre-cast polymer film and spin-coated at 4000 rpm for 10 seconds. All DDB-F_{72} and F_4TCNQ dopant solutions were prepared in dichloromethane at the concentrations stated in text. Film thicknesses were measured using a Dektak 150 stylus profilometer. Mass measurements were taken with a Mettler AT20 analytical microbalance. Dodecaborane clusters are stored in air and show no signs of degradation. The cluster is also structurally stable in solution, however, it can undergo a redox reaction with the solvent if left for too long. Solutions were used within a few days of making them. Doped films are stable under inert atmosphere for days.

Conductivity Devices for conductivity measurements were fabricated on 1.5 cm × 1.5 cm glass substrates. Following film fabrication, electrodes were placed on the corners of the sample using PELCO conductive silver paint. The Van der Pauw method was used to measure conductivities in-house as well as the values reported in Table 5.1 of the main text, which were measured independently at Lake Shore Cryotronics on samples prepared for AC-Hall measurements (described below). Our Van der Pauw measurements were performed using a custom-made apparatus in ambient atmosphere using a Kiethley 2400 Sourcemeter controlled by Labview software where the maximum current sourced was held to 1 mW total power. All reported values were averaged over multiple measurements taken on at least 3 samples.

Sample Imaging Optical images were taken using a Carl Zeiss Axiotech 100HD microscope. Scanning Electron Microscopy (SEM) images of the 1 mM DDB-F_{72} doped films have been studied using a JEOL 7500F HRSEM with a 5 kV accelerating voltage.

XPS

XPS was performed using a Kratos Axis Ultra DLD spectrometer with a monochromatic Al Kα radiation source and a charge neutralizer filament was used to control charging of the sample. A pass energy of 20 eV was used for all spectra with a 0.1 eV step size and 300 ms dwell time. All spectra were calibrated to the advantageous carbon 1s peak at 284.8 eV. Films for standard XPS were fabricated on sapphire substrates to minimize interference from the silicon 2s plasmon peaks with the boron 1s signal. In order to analyze dopant infiltration, spectra of the top (front) and bottom (back) of the films were obtained by floating films off glass substrates and placing them on copper tape. Floating was accomplished by cutting a grid pattern into the film using the free edge of a razor, and applying deionized water. No sacrificial layers such as poly(3,4-ethylenedioxythiophene) polystyrene sulfonate or polyacrylic acid were used as they were difficult to remove completely, which affected the obtained surface sensitive ratios. Analysis was performed using CasaXPS software and the relative sensitivity factors used were from the CASAXPS library.

GIWAXS Films for 2-D GIWAXS measurements were prepared on silicon substrates. Measurements were performed at the Stanford Synchrotron Radiation Lightsource on beamline 11-3 using a wavelength of 0.9742 Å with an incidence angle of 0.12°. Diffraction patterns were collected in a helium chamber to increase signal-to-noise with a sample to detector distance of 250 mm and a spot size of ~150 μm on the image plate. The 2-D diffractograms were radially integrated from to 0-10° and 80-90° to obtain the in-plane and out-of-plane diffraction patterns.

The software package WxDiff was used to reduce the GIWAXS data and subsequent analysis was performed in IgorPro. The intensities on the opposite sides of the diffractogram (90-180°) were also checked to ensure they matched the chosen limits. Each integration was background corrected for substrate scattering. The subtractions were performed on the raw scattering data to ensure that no errors occurred due to background subtraction. To ensure reproducibility in diffraction intensity and shape, all samples were made and measured in triplicate.

Spectroscopy UV-VIS-NIR absorption spectra were acquired from 300-2500 nm using a Shimadzu UV3101PC UV-VIS-NIR Scanning Spectrophotometer for films prepared on both glass substrates and KBr pellets (cleaned in chlorobenzene and acetone). FTIR data was acquired from 220-7000 cm^{-1} for films on KBr plates using a Jasco FT/IR-420 spectrometer.

AC-Hall Devices for AC-Hall effect measurements were prepared on 1 cm × 1 cm glass substrates. Following film fabrication, silver electrodes were deposited on the corners of the samples with an Angstrom Engineering, Inc. evaporator at a pressure of < (1×10^{-6} Torr). The silver layer was deposited at a rate of 0.5 Å/s up to 10 nm, followed by 1 Å/s to a final total thickness of 60 nm. Samples were packaged in scintillation vials under argon atmosphere before being sent to Lakeshore Cryotronics for testing. AC magnetic field Hall measurements were performed with a Lake Shore model 8400 series AC Hall probe system at a field strength of 0.6484 T and a current of 1.00×10^{-5}. Nitrogen was flowed continuously over the samples to reduce error from sample degradation. The technique is similar to DC Hall Effect, but with an oscillating magnetic field at a certain frequency such that the hall voltage (resulting from the Lorentz force) becomes time dependent. This allows the hall voltage to be distinguished from the static misalignment offset voltage, which is large in low mobility materials.

Electron transfer self-exchange rate by NMR

According to Marcus-Hush theory of electron transfer (ET), the rates of electron self-exchange (k_{et}) can be directly related to rates of intermolecular ET with other redox species and the total reorganization energy (λ_{tot}) for ET.[63] The kinetics of electron self-exchange in DDB-F_{72} were investigated by dynamic NMR through the application of line broadening experiments. The NMR spectrum was recorded for samples in which the mole fraction of the reduced species ([DDB-$F_{72}]^{-}$) was varied relative to the oxidized species ([DDB-$F_{72}]^{0}$). The NMR line shape is highly sensitive to the rate of exchange and when exchange is in the fast regime $k(C_{\mathrm{tot}}) >> 2\pi(\Delta\nu)$, the chemical shifts of the exchanging species are fund to be the averages of the diamagnetic and paramagnetic chemical shifts weighted by their respective mole fractions.[64] Rate constants can then be determined by equation 1 after spectral deconvolution:[64]

$$k_{et} = \frac{4\pi\chi_{red}\chi_{ox}(\Delta v)^2}{(\omega_{ro} - \chi_{red}\omega_{red} - \chi_{ox}\omega_{ox})C_{tot}}$$

Here, χ_{red} and χ_{ox} are the mole fractions of reduced and oxidized species, $\Delta\nu$ is the difference in chemical shift between reduced and oxidized species in Hertz, ω_{ro} is the peak width at half maximum of the mixture in question, ω_{red} and ω_{ox} are the peak widths at half maximum of the pure reduced and oxidized species, and C_{tot} is the total concentration in moles per liter. Although any NMR active nucleus may be used to determine the rates of self-exchange, in this present study, ^{19}F NMR was used to determine the rates of self-exchange as the large number of fluorine atoms present offered an excellent spectroscopic handle.

The NMR scans taken for five mole fractions of [DDB-F72]$^{0/-}$ at 20 °C (bottom), 40 °C (middle), and 60 °C (top) in a solution of 4:1 o-difluorobenzene:benzene are shown in Fig. S5.4. The lack of coalesced spectra across a 40 °C temperature range suggest that intermolecular self-exchange for the [DDB-$F_{72}]^{0/-}$ redox couple occurs much slower than the NMR time-scale[65] (k_{et} <

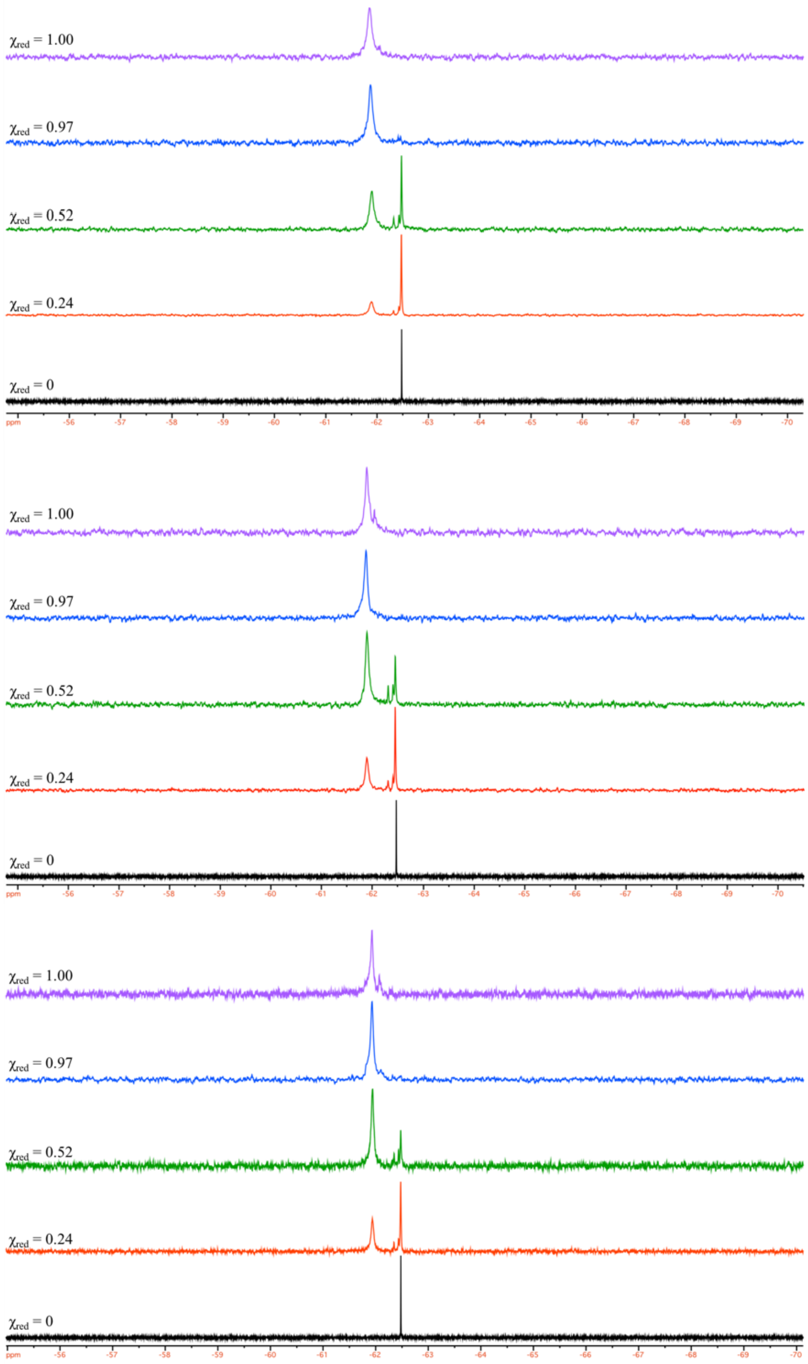

Figure S5.4. ^{19}F NMR of the one-electron self-exchange interaction of the [DDB-F72]$^{0/–}$ redox couple with increasing mole fraction of [DDB-F$_{72}$]$^{–}$ from bottom to top in any given series. Spectra were recorded at 20 °C (bottom), 40 °C (middle), and 60 °C (top) in a 4:1 o-difluorobenzene:benzene mixture and referenced to an internal standard of trifluoroethanol sealed in a capillary tube.

$1.2 \times 10^3\ s^{-1}$ or $t_{et} < 0.84$ ms). This timescale is orders of magnitude slower than the expected collision time for two clusters. The concentration of DDB-F_{72} used was 0.1 mM, which means there are ∼10 particles in a 550 nm^3 volume, or an average distance between clusters of ∼8 nm. According to the Stokes-Einstein equation, the diffusion constant of 2-nm spherical particles in a typical organic liquid at room temperature is $\sim1.8\times10^{-10}\ m^2/s$. This means one of our DDB-F72 clusters should diffuse far enough to encounter each other on a 60 ns time scale, which is much faster than the 840 μs timescale of the NMR experiment. Thus, even after over 1000 collisions between particles, there is no sign of motional narrowing and thus ET between the clusters. These results support high intrinsic barriers to ET most likely attributed to small electronic couplings (Hab) and poor orbital overlap between self-exchanging pairs.[43-45]

The minimal distortion observed between the solid state structures of $[DDB\text{-}F72]^0$ and $[DDB\text{-}F72]^-$ shown in Fig. S5.5 suggests that reorganization energies do not contribute significantly to the electron self-exchange barrier in these systems. The largest observed distortion is found in the capping benzyl ligands, which most likely arises from packing in the solid state as they are believed to be freely rotating in solution. Instead, the lack of a large chemical shift between the ^{19}F signals in these two oxidation states suggests that the benzyl capping ligands experience minimal electron-density and that the odd electron in $[DDB\text{-}F_{72}]^-$ is primarily localized on the core of the borane clusters (See DFT results). The capping ligands effectively screen the core and prevent donor- acceptor overlap from occurring. This ultimately leads to negligible electronic coupling and slow rates of electron self-exchange.

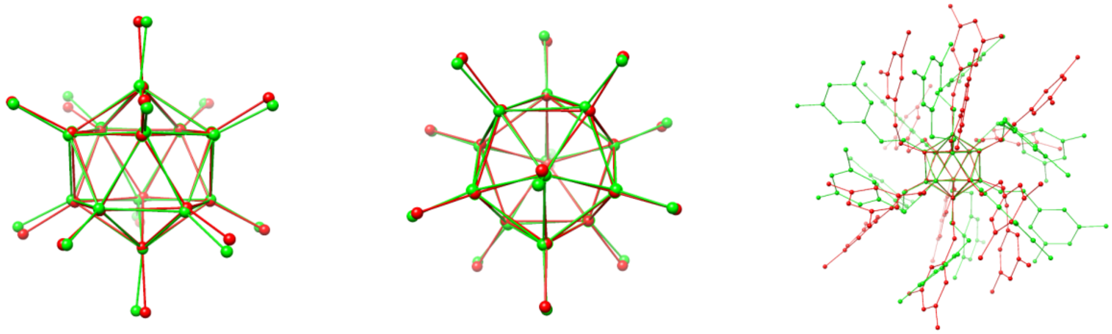

Figure S5.5. Overlapped solid state structures of [DDB-F_{72}]^0 (green) and [DDB-F_{72}]$^-$ (red) obtained from single crystal X-ray diffraction studies. Left and middle figures highlight the minor structural rearrangement in the core upon a one electron reduction while the right side highlights the capping ligands. Capping benzyl ligands have been omitted for clarity in the left and middle figures while hydrogen and fluorine atoms have been omitted for the right figure.

Cyclic Voltammetry

In order to characterize the offset between the HOMO of the polymer and the LUMO the dopants, we performed side-by-side cyclic voltammetry on F_4TCNQ and DDB-F_{72}. The 2-/1- transition occurs at −0.48 V for F_4TCNQ and −0.07 V for DDB-F_{72}, while the 1-/0 transition occurs at +0.16 V for F_4TCNQ and +0.67 V for DDB-F_{72}. All potentials are referenced to an internal ferrocene standard. The redox potential of DDB-F_{72} is therefore ~0.5 V higher than F_4TCNQ giving it a much higher energetic driving force for doping.

Conductivity Data

Devices were fabricated as described in the main text on 1.5 cm × 1.5 cm glass substrates with silver paste applied as electrical contacts. The Van der Pauw technique[41] was used to measure conductivity, a type of four-point probe method in which current is flowed from negative to positive along one edge of the sample and the voltage is measured across the opposite edge. The sample is then rotated 90°, and the measurement is repeated. The resistance values obtained from

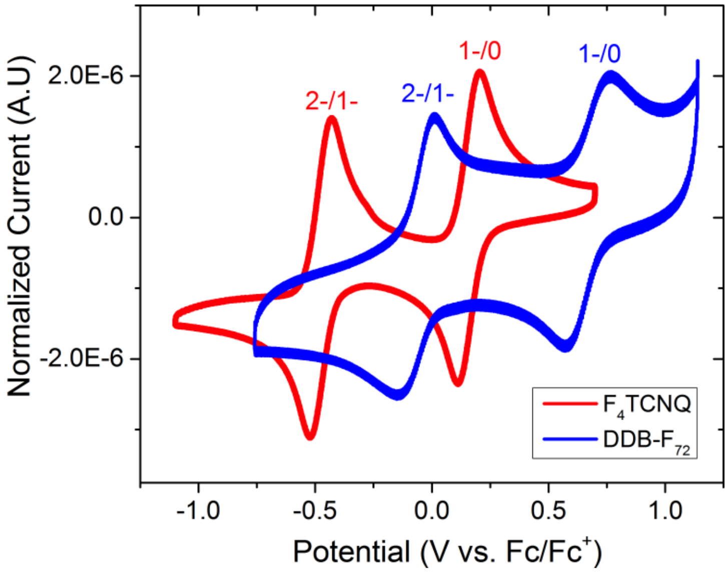

Figure S5.6. Cyclic voltammogram of F_4TCNQ (red) and DDB-F_{72} (blue) demonstrating two reversible single-electron oxidation/reductions.

the slope of the I − V curves are fit to the Van der Pauw equation to obtain the sheet resistance (RD). The thickness (t) of the samples was obtained in three locations using a Dektak 150 stylus profilometer. The reported values for RD and t in Table S5.1 and Table S5.2 are averaged over all measured values for all samples while the reported conductivities (σ) are averaged over the values obtained for each sample (i.e., the average RD and t for each sample were used to calculate the conductivity of that sample, and the obtained conductivities were averaged over the samples to yield the values reported.) The ideal conductivities (σ_{id}) were calculated using the initial polymer thickness of 120 nm. In each case, the reported error is the standard deviation of the measurements. The calculation of idealized conductivity makes a bigger difference for the DDB-F_{72} samples due to the large thickness increase due to incorporation of the dopant, which does not conduct as shown by the self-exchange experiments and the p-type conductivity found using AC hall measurements.

Table S5.1. F_4TCNQ Conductivity Measurements

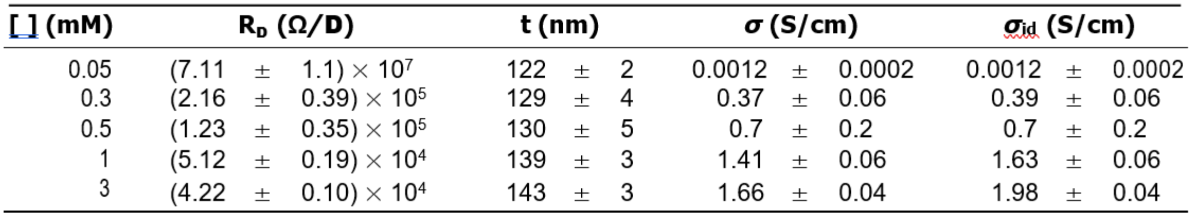

[ ] (mM)	R_D (Ω/D)	t (nm)	σ (S/cm)	σ_{id} (S/cm)
0.05	$(7.11 \pm 1.1) \times 10^{7}$	122 ± 2	0.0012 ± 0.0002	0.0012 ± 0.0002
0.3	$(2.16 \pm 0.39) \times 10^{5}$	129 ± 4	0.37 ± 0.06	0.39 ± 0.06
0.5	$(1.23 \pm 0.35) \times 10^{5}$	130 ± 5	0.7 ± 0.2	0.7 ± 0.2
1	$(5.12 \pm 0.19) \times 10^{4}$	139 ± 3	1.41 ± 0.06	1.63 ± 0.06
3	$(4.22 \pm 0.10) \times 10^{4}$	143 ± 3	1.66 ± 0.04	1.98 ± 0.04

Table S5.2. DDB-F_{72} Conductivity Measurements

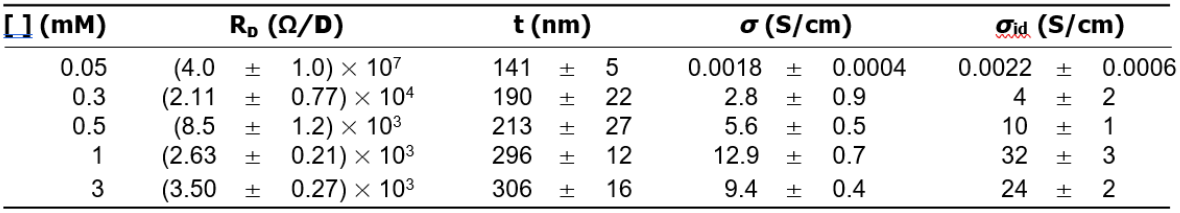

[ ] (mM)	R_D (Ω/D)	t (nm)	σ (S/cm)	σ_{id} (S/cm)
0.05	$(4.0 \pm 1.0) \times 10^{7}$	141 ± 5	0.0018 ± 0.0004	0.0022 ± 0.0006
0.3	$(2.11 \pm 0.77) \times 10^{4}$	190 ± 22	2.8 ± 0.9	4 ± 2
0.5	$(8.5 \pm 1.2) \times 10^{3}$	213 ± 27	5.6 ± 0.5	10 ± 1
1	$(2.63 \pm 0.21) \times 10^{3}$	296 ± 12	12.9 ± 0.7	32 ± 3
3	$(3.50 \pm 0.27) \times 10^{3}$	306 ± 16	9.4 ± 0.4	24 ± 2

Although the conductivity values we report do not represent an all-time record, to the best of our knowledge, the 12.7 S/cm we report is the highest achieved for solution doping of a film of commercially-available P3HT. It is important to note that all of the highest conductivities reported for F_4TCNQ-doped P3HT in the literature were achieved for films where the order was carefully preserved (e.g., by vapor doping, by using 100% regioregular P3HT, keeping the films very thin (≤25 nm) to enhance their crystallinity/crystalline domain orientation, or by casting the polymer onto a rub-aligned substrate). Table S5.3 below shows some of these leading conductivity values for F_4TCNQ-doped P3HT from the literature. Given that our DDB-F_{72}-doped films are ~300-nm thick and have almost no crystallinity, the conductivities and mobilities we achieve are completely unprecedented, demonstrating the importance of anion interactions on the conductivity.

Table S5.3. Conductivity values for F4TCNQ-doped P3HT from literature.

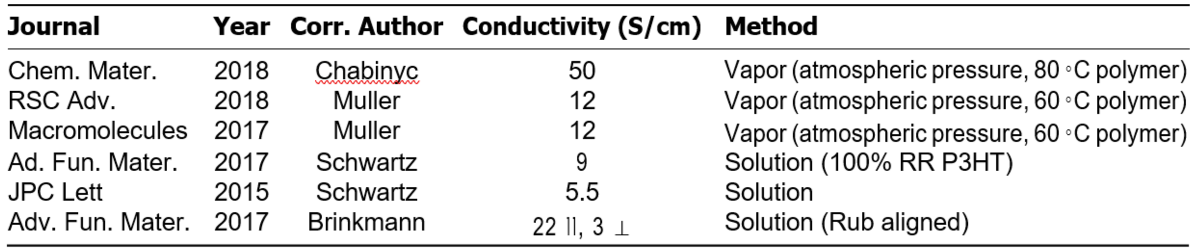

Journal	Year	Corr. Author	Conductivity (S/cm)	Method
Chem. Mater.	2018	Chabinyc	50	Vapor (atmospheric pressure, 80 ◦C polymer)
RSC Adv.	2018	Muller	12	Vapor (atmospheric pressure, 60 ◦C polymer)
Macromolecules	2017	Muller	12	Vapor (atmospheric pressure, 60 ◦C polymer)
Ad. Fun. Mater.	2017	Schwartz	9	Solution (100% RR P3HT)
JPC Lett	2015	Schwartz	5.5	Solution
Adv. Fun. Mater.	2017	Brinkmann	22 ∥, 3 ⊥	Solution (Rub aligned)

Stability measurements on doped films

In order to assess the stability of our doped films we measured the conductivity of P3HT films doped with both DDB-F_{72} and F_4TCNQ as a function of time in both an inert environment (argon glovebox) and in air. Figure S5.7 shows that the doped films are quite stable under inert atmosphere for 24 hours (panel a), but show signs of degradation over the same time period in air (panel b), with a reduction in conductivity of about 25% for the DDB-F_{72} doped film and about 50% for the F_4TCNQ doped film. Interestingly, the DDB-F_{72}-doped film only decreases from its initial conductivity after 6 hours of air exposure, whereas the conductivity of the F_4TCNQ-doped sample decreases from the beginning of the measurement. Thus, the stability of DDB-F_{72}-doped P3HT films is comparable to but slightly better than that of F_4TCNQ-doped P3HT films.

To see how robust the stability of the DDB-F_{72} films are under inert atmosphere, the conductivity of three samples were also measured on a daily basis. Over a period of 5 days, the conductivity stayed constant within an error of 2 standard deviations. These results suggest that the DDB-F_{72}-doped films would be stable essentially indefinitely if packaged appropriately (Fig. S5.8).

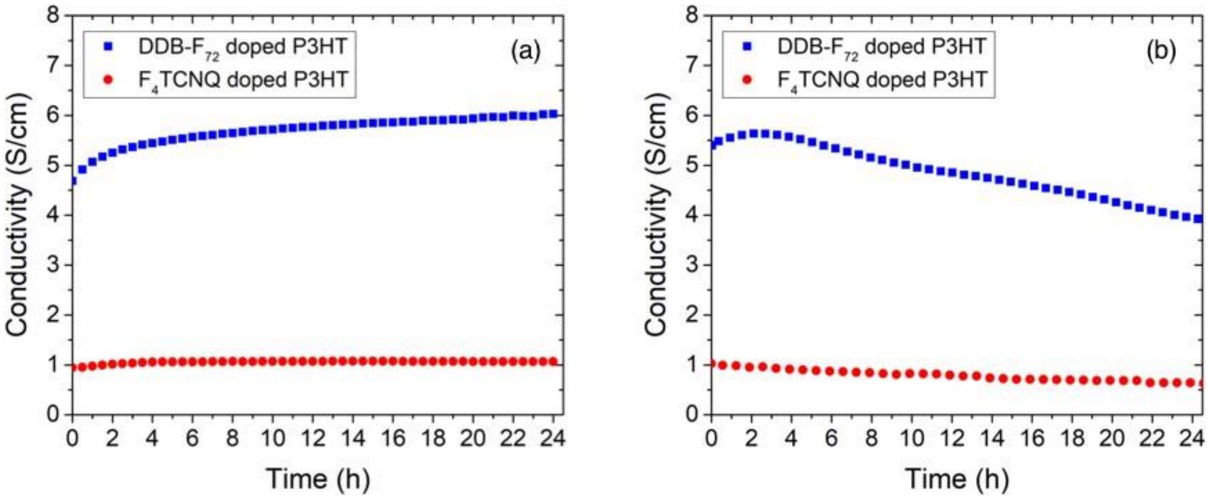

Figure S5.7. Conductivity over time of DDB-F_{72} (blue) and F_4TCNQ (red) doped P3HT films in the glovebox under inert argon atmosphere (a) and under ambient atmosphere in air (b) as a function of time after film fabrication as measured by 4-point probe.

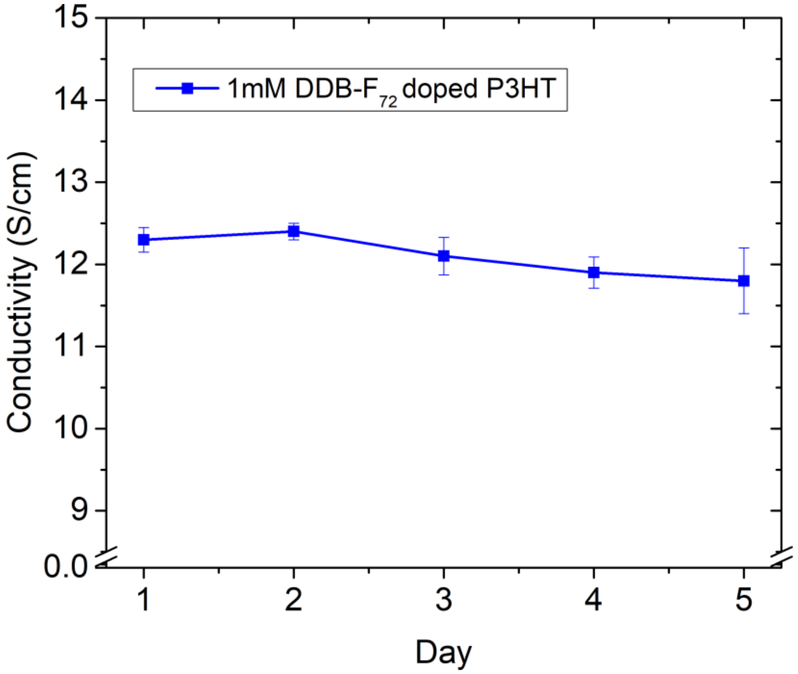

Figure S5.8. Conductivity of DDB-F_{72}-doped P3HT film samples measured over 5 days via the Van der Pauw method. The samples were briefly exposed to air for each measurement and then returned for storage under inert atmosphere. The error bars are the standard deviation of measurements on three separate samples.

Optical and SEM images of the Doped Film's Surface

Given the large film thickness increase observed following doping P3HT with DDB-F_{72}, we took optical and SEM images of the surface of the films to examine the possibility of formation of an overlayer of boron clusters. Figure S5.9 shows images of the clusters at 5× (a) and 50× (b,c) showing the appearance of a few particles on the surface of the film. The particles light up under polarized light in (c) indicating that they are likely crystalline in nature; we conclude that these must be small crystallites of boron clusters on top of the film. The particles are sparsely distributed, which indicates that there is not an overlayer of boron cluster crystallites on top of the film.

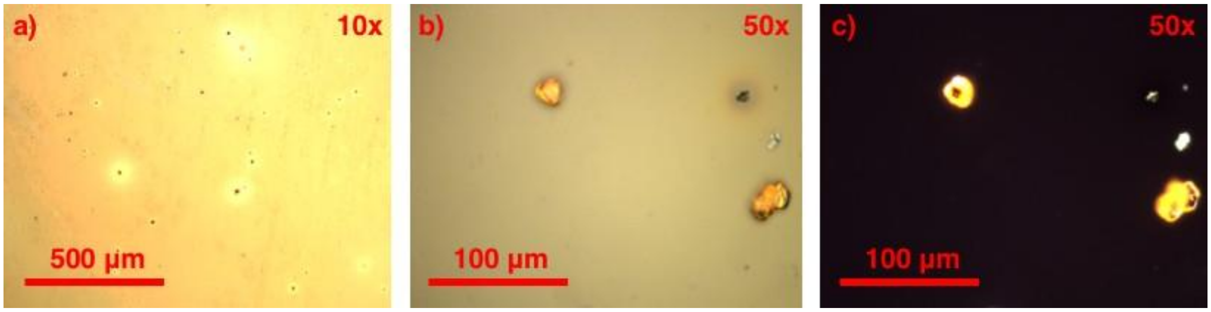

Figure S5.9. Optical images of 1mM DDB-F_{72} doped P3HT at 5x (a) and 50x (b) magnification as well as at 50x magnification under polarizers (c).

Figure S5.10 shows SEM images of a 1 mM DDB-F_{72} doped film of P3HT. The images show a clear pattern of sharp cracks, which are likely due to the expansion and contraction of the film upon swelling and deswelling during the solution sequential doping process. We believe that during SqP doping, the peak thickness of the film is greater than the final 300-nm thickness, so that as the solvent evaporates and the film shrinks to its final (albeit still highly swollen size), the strain from drying opens these sharp crack-like features. The sharp features are not what one would expect if the DDB-F_{72} clusters were immiscible with the P3HT and formed a dewetting layer on top, as a dewetting layer would have smooth interfaces to minimize the surface tension between the immiscible phases. Thus, the optical and SEM images both confirm the conclusion from the XPS data in the main text that SqP mixes the DDB-F_{72} clusters throughout the P3HT underlayer.

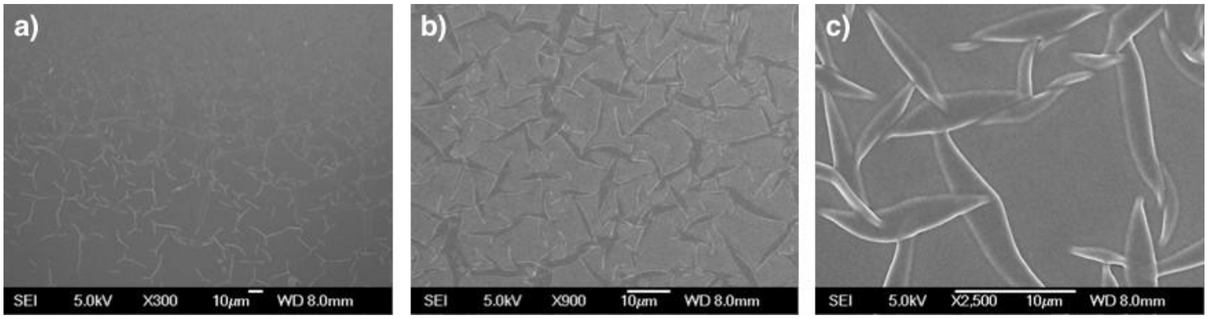

Figure S5.10. SEM images of a P3HT film that has been doped with 1 mM DDB-F_{72} at low to high magnification (a-c).

XPS

Table S5.4. XPS fits

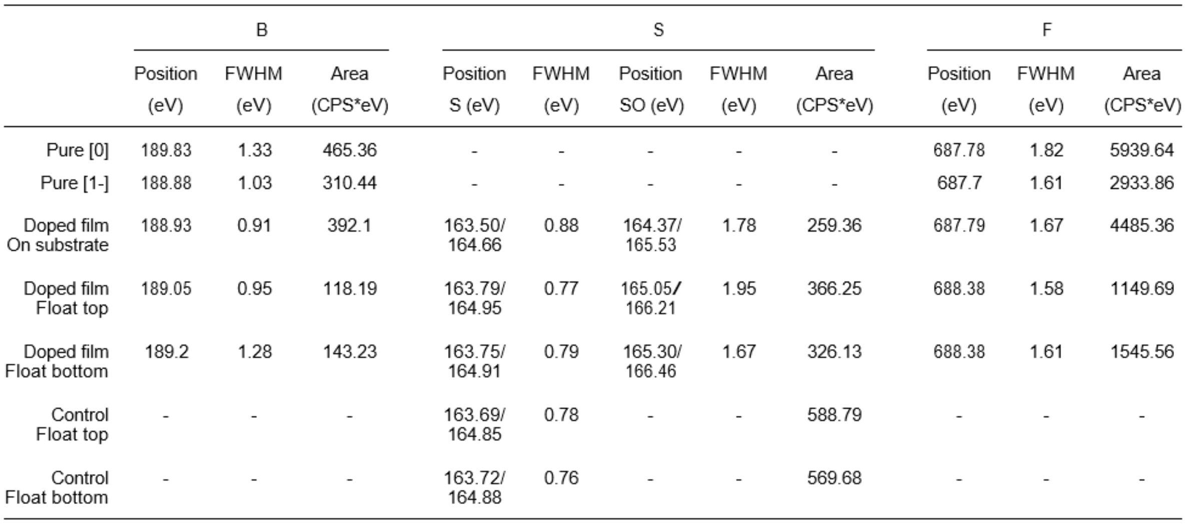

	B			S					F		
	Position (eV)	FWHM (eV)	Area (CPS*eV)	Position S (eV)	FWHM (eV)	Position SO (eV)	FWHM (eV)	Area (CPS*eV)	Position (eV)	FWHM (eV)	Area (CPS*eV)
Pure [0]	189.83	1.33	465.36	-	-	-	-	-	687.78	1.82	5939.64
Pure [1-]	188.88	1.03	310.44	-	-	-	-	-	687.7	1.61	2933.86
Doped film On substrate	188.93	0.91	392.1	163.50/ 164.66	0.88	164.37/ 165.53	1.78	259.36	687.79	1.67	4485.36
Doped film Float top	189.05	0.95	118.19	163.79/ 164.95	0.77	165.05/ 166.21	1.95	366.25	688.38	1.58	1149.69
Doped film Float bottom	189.2	1.28	143.23	163.75/ 164.91	0.79	165.30/ 166.46	1.67	326.13	688.38	1.61	1545.56
Control Float top	-	-	-	163.69/ 164.85	0.78	-	-	588.79	-	-	-
Control Float bottom	-	-	-	163.72/ 164.88	0.76	-	-	569.68	-	-	-

Table S5.4 shows all of the peak fit information for pure DDB-F_{72}, DDB-F_{72} [1-], a 1 mM DDB-F_{72} doped P3HT film on sapphire substrate and the front and back of a 1 mM DDB-F72 doped P3HT as well as an undoped P3HT films obtained via the floating procedure described in the methods section. Figure S5.11 shows the data and peak fits for each of the doped films. Floating the films off the substrate allowed us to obtain information about the cluster content at both the top (front) and bottom (back) surfaces of the films. The sulfur signal comes only from P3HT

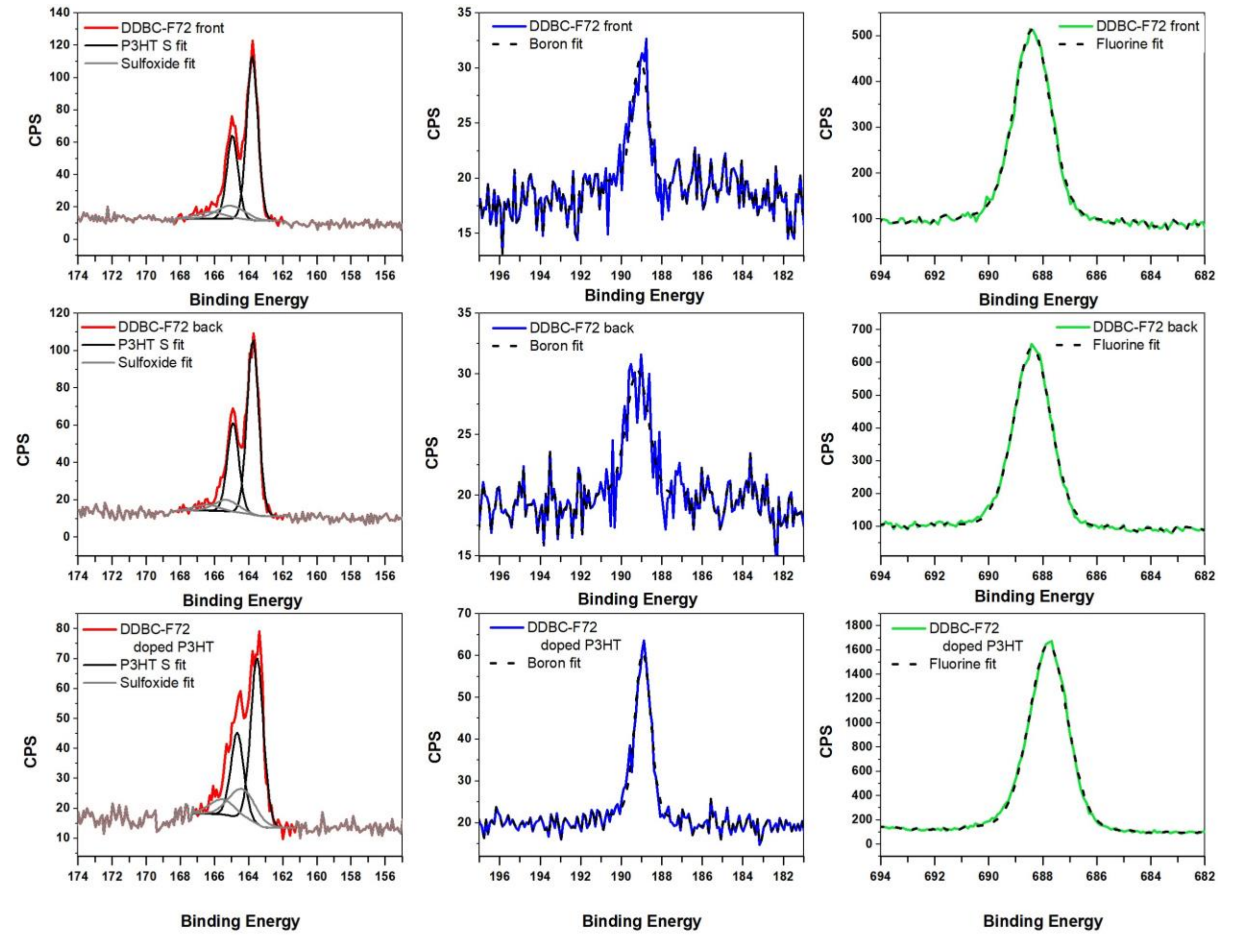

Figure S5.11. XPS data and S, SO, B, and F peak fits for DDB-F_{72} doped P3HT (bottom), floated back of DDB-F_{72} doped P3HT film (middle), and floated front of DDB-F_{72} doped P3HT (top).

whereas the B and F signals come only from DDB-F_{72}. Integrated peak areas were used to calculate the B:S and F:S ratios reported in the main text. The drop in relative B:S and F:S peak intensity ratios for the doped film on sapphire compared to the floated films indicates that some clusters gets washed off during the floating process, but this does not prohibit us from obtaining relative information about the cluster content at the top and bottom surfaces. As discussed in the main text, the B:S and F:S ratios are roughly similar at the top and bottom of the film (and if anything, slightly higher at the bottom of the film), indicating that the clusters do indeed penetrate throughout the polymer film. To ensure that cluster was not somehow being added to the films during the floating process, we floated a pure P3HT film in the same wash used for the doped film. As shown by the peak fit information in Table S5.4, no boron, fluorine or sulfur peaks were found, indicating that the floating process indeed cannot add clusters to the films. Finally, based on the boron peak positions, the doped films contain only the DDB-F_{72} anion, indicating that the cluster effectively dopes the film and no neutral clusters are in the film or form an excess overlayer on top of the film.

GIWAXS

The full integration of the diffractogram for a drop-cast film of pure DDB-F_{72} out of DCM is shown in Figure S5.12. The diffractogram displays sharp peaks with no broadening, as is typically seen for small crystallites. The dopant induced peaks indicated by (*) in Figure 5.2 of the main text therefore must involve the polymer as they have the same broadening and texture as the polymer peaks.

Figure S5.13 shows the full 2D-GIWAXS diffractograms for pure P3HT and P3HT doped with different concentrations of DDB-F_{72}. The out-of-plane and in-plane integrations are shown in the main text and the peak fit information for the out-of-plane (100) and in-plane (010) are shown in Table S5.5 and Table S5.6, respectively. No peak fit information is reported for the in-plane (010) 1 mM DDB-F_{72} doped sample due to high amounts of amorphous π-scattering making definition of this peak difficult.

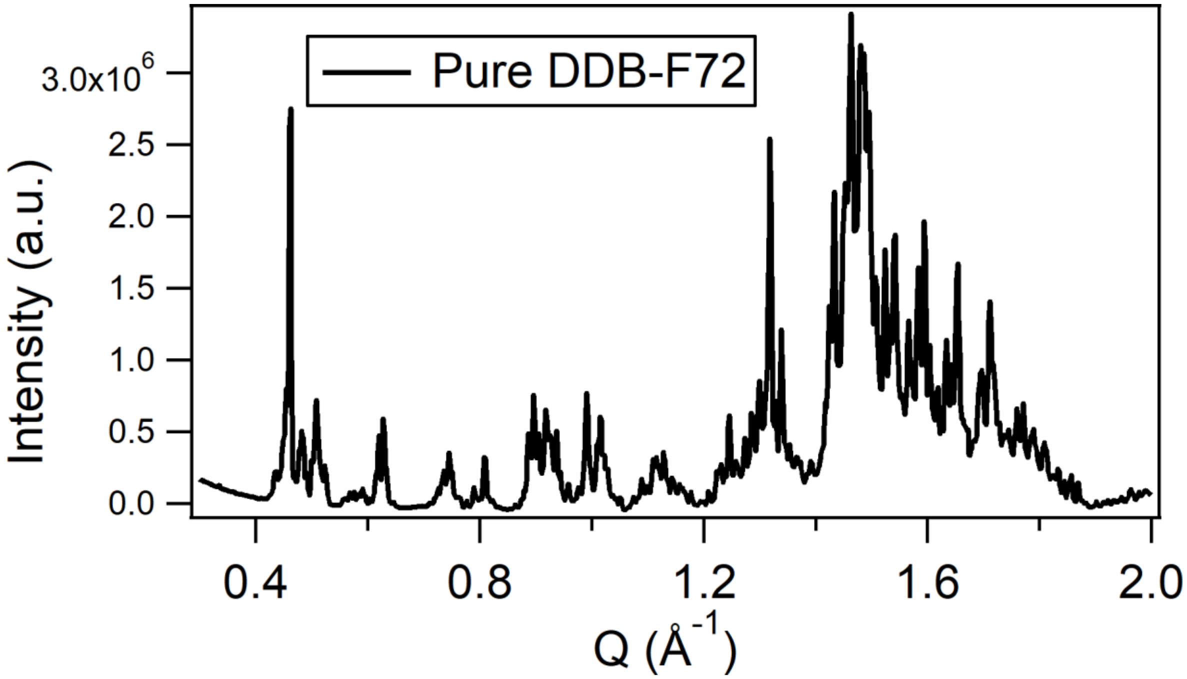

Figure S5.12. Full integration of GIWAXS diffractogram for pure DDB-F_{72} showing sharp crystallite peaks.

Table S5.5. Out-of-Plane (100) Peak Fit Information

Sample	Location (Q)	d-spacing (Å)	Height	Area	FWHM
Undoped P3HT	0.396	15.9	3.75×10^6	2.04×10^5	0.051
0.05 mM DDB-F_{72}	0.403	15.6	3.48×10^6	1.99×10^5	0.054
0.3 mM DDB-F_{72}	0.398	15.8	1.36×10^6	1.72×10^5	0.119
1 mM DDB-F_{72}	0.396	15.9	9.98×10^5	5.20×10^5	0.049

Table S5.6. In-Plane (010) Peak Fit Information

Sample	Location (Q)	d-spacing (Å)	Height	Area	FWHM
Undoped P3HT	1.66	3.79	1.84×10^4	1.82×10^3	0.093
0.05 mM DDB-F_{72}	1.67	3.76	1.72×10^4	1.93×10^3	0.106
0.3 mM DDB-F_{72}	1.68	3.73	1.56×10^4	1.83×10^3	0.110
1 mM DDB-F_{72}	-	-	-	-	-

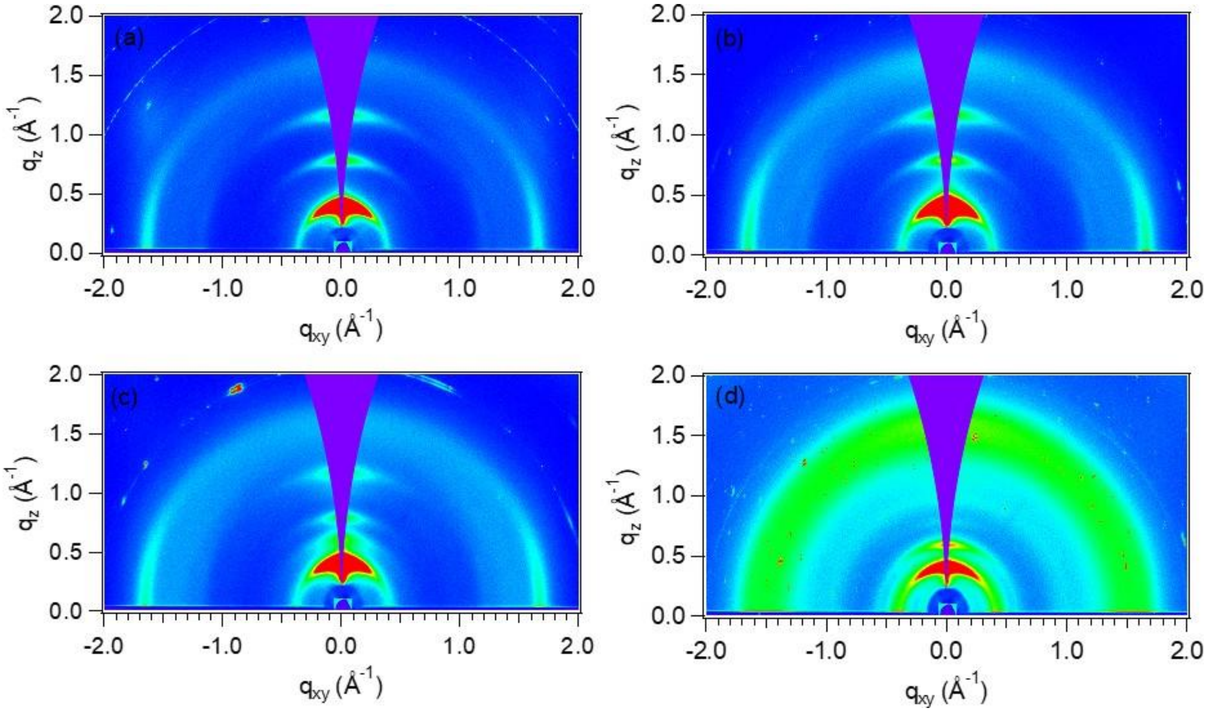

Figure S5.13. Full 2D-GIWAXS diffractograms for pure undoped P3HT (a), P3HT doped with 0.05 mM (b), 0.3 mM (c), and 1 mM DDB-F_{72} (d).

Spectroscopic Characterization

Figure S5.14 shows the absorption spectra for films of pure and doped P3HT with different concentrations of DDB-F_{72} in DCM. The inset shows the standard energy band diagram for the formation of polarons. In the doped films, we see spectroscopic signatures of the P1, P2, and P3 transitions and a bleach of the neutral polymer absorption. The absorption in the 2.3-eV region contains contributions from the neutral (dashed yellow curve) and anionic (dashed pink curve) forms of DDB-F_{72} as well as any residual undoped P3HT (black curve), making it difficult to deconvolute the individual contributions of each component in the doped films. The intensity of the polaron bands increase monotonically up to 1 mM, but at the 3 mM concentration, there is a slight decrease in optical density for these transitions. This indicates that less cluster is infiltrating into the film despite the higher dopant concentration. We suspect, given the colloidal nature of the 3-mM DDB-F_{72} solution, that there may actually be fewer free solubilized clusters in solution due to an equilibrium with clusters of DDB-F_{72} clusters. Additionally, the morphology of the 3-mM doped film is likely worse due to the colloidal nature of the solution, resulting in the observed slight drop in conductivity.

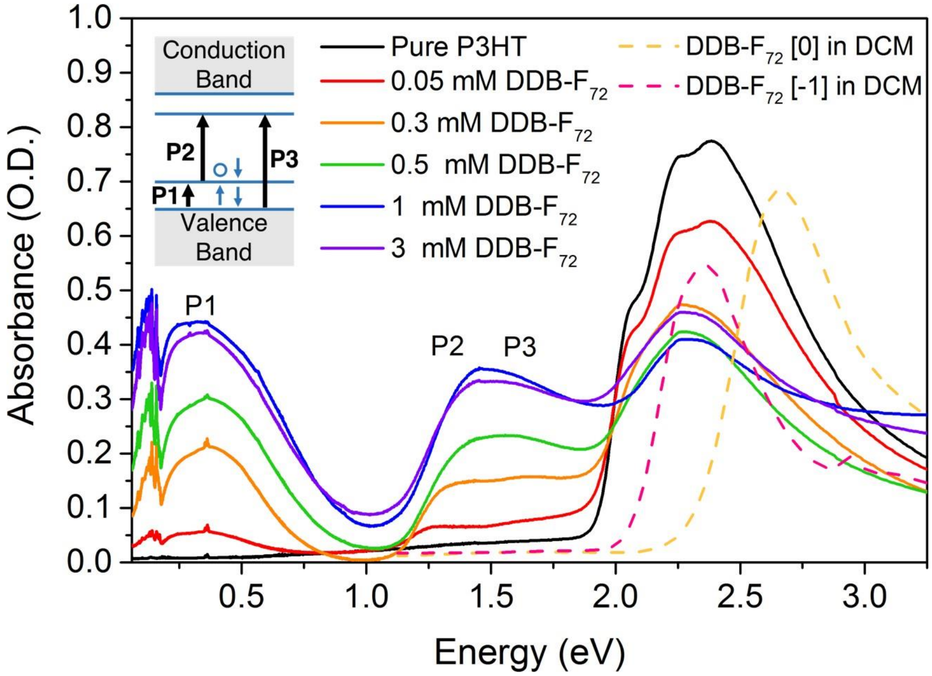

Figure S5.14. Combined FTIR and UV-vis-NIR absorption data for pure P3HT (black curve), P3HT doped with different molar concentrations of DDB-F_{72} (colored solid curves), and neutral (yellow dashed curve) and reduced (pink dashed curve) DDB-F_{72} cluster in DCM.

Transport Mechanisms from temperature-dependent behavior of the conductivity

The dominant charge transport mechanisms can be determined from the temperature dependence of the conductivity.[66-69] We looked at the conductivity of our 1 mM DDB-F_{72}-doped P3HT films over a 50 K to 300 K temperature range. Figure S5.15 shows the conductivity plotted against the temperature raised to various fractional powers, allowing us to visualize agreement with the power laws as straight lines. At low temperatures, the $T^{1/2}$ plot yields a straight line,

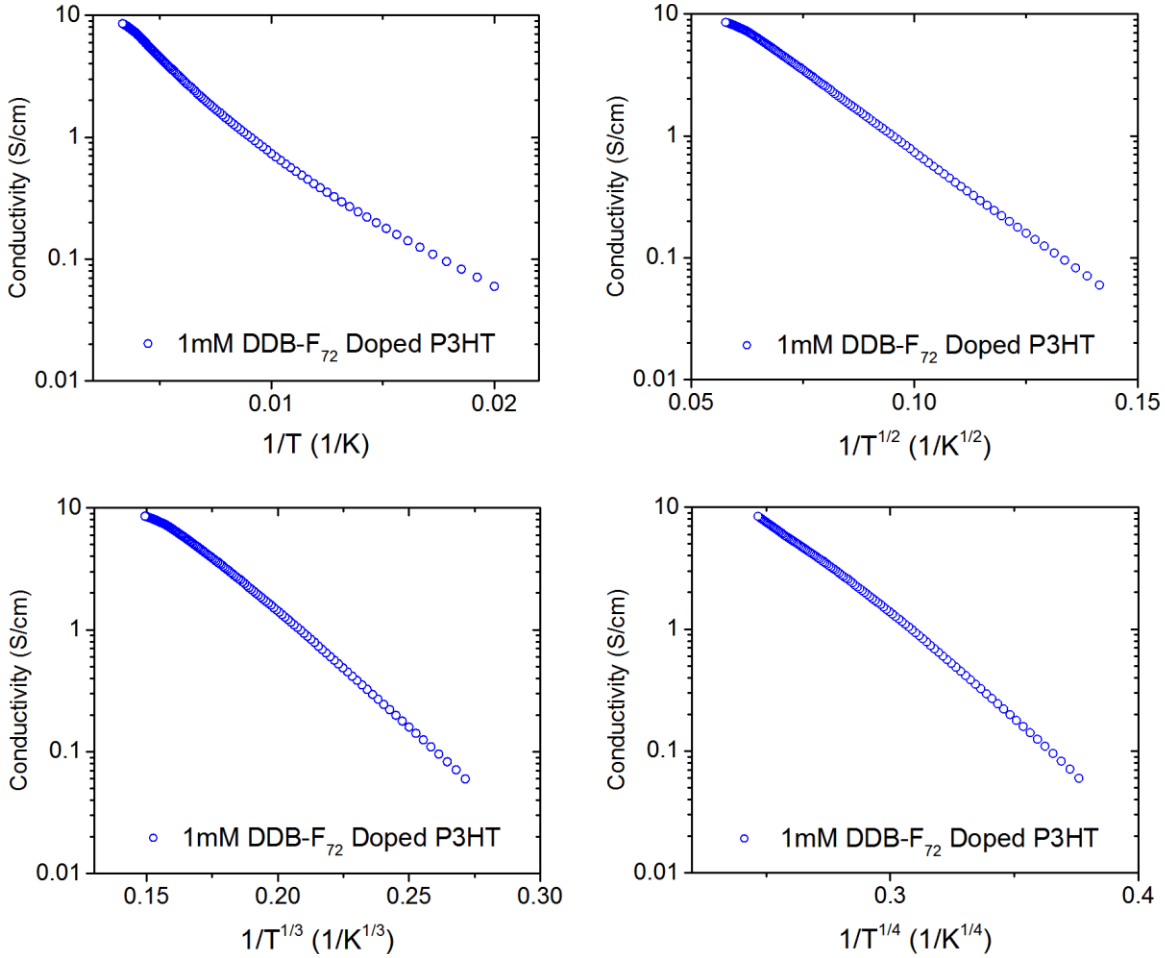

Figure S5.15. Conductivity of 1 mM DDB-F_{72} doped P3HT as a function of temperature, plotted as a function of inverse temperature raised to various powers that correspond to different transport models.

indicating the temperature dependence of the low temperature region can be described by the Efros Shklovskii Variable Range Hopping (VRH) model,[66] which means that Coulomb interactions still dominate. At higher temperature, the charge transport mechanism transitions over to a traditional Mott VRH model[67] with a $T^{1/4}$ temperature dependence, which disregards Coulomb interactions and suggests more diffusive transport. A more analytical approach to extract transport mechanisms is to perform logarithmic differentiation to linearize the temperature-dependent conductivity,[67,68] as shown in Figure S5.16. By fitting the different slopes, we again find Efros Shklovskii VRH at low temperatures and Mott VRH at high temperatures. As we approach room temperature there is a drastic decrease in the T-dependence of the conductivity, indicating a regime that deviates from hopping-dominated transport and is approaching a diffusive mechanism of charge transport. This is very similar to behavior we observed in a previous study that compared P3HT of different

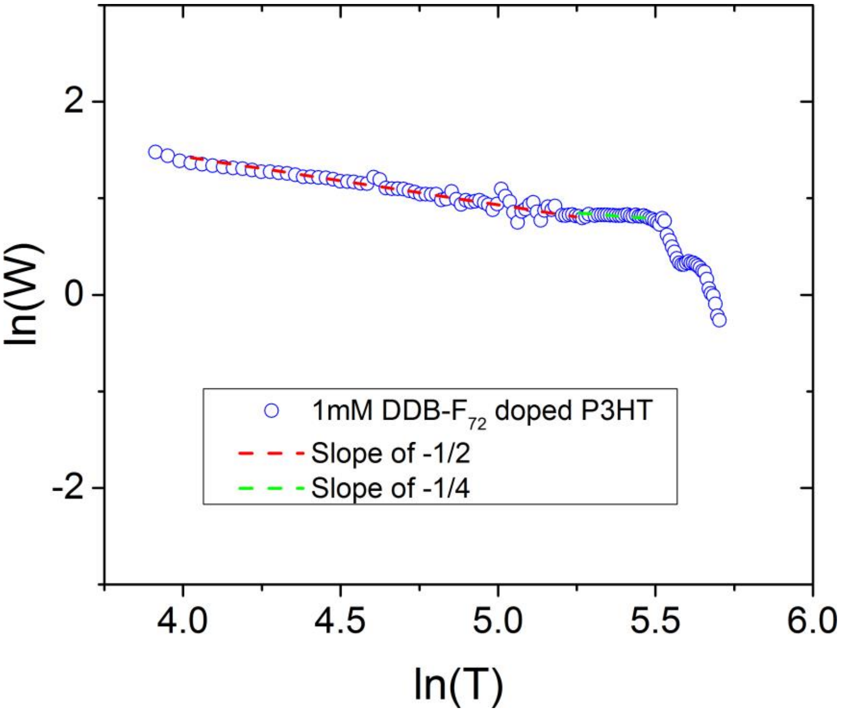

Figure S5.16. Logarithmic derivative of the resistivity ($W = d\ln(\rho)/d\ln(T)$) vs. $\ln(T)$. The dashed lines are linear fits with the corresponding slopes given in the legend.

crystallinity doped with F_4TCNQ.[15] Only in the most crystalline 100% regioregular samples was the $T^{1/4}$ temperature dependence observed over the same temperature range. By contrast, we know from our GIWAXS measurements that the crystallinity of the DDB-F_{72} doped P3HT is very low, exposing the importance of counterion shielding for better charge transport. In the F_4TCNQ samples, due to the proximity of the counterion, the only way to achieve diffusive transport is through the P3HT crystallites.

AC-Hall Measurements

The carrier concentrations we report were obtained through AC Hall measurements using the traditional Hall coefficient equations, which assume band-like transport. However, as we have just shown in the previous section, band-like transport is only beginning to occur at room temperature and carrier transport in our films still likely consists of both band-like and hopping-type mechanisms. As Podzorov and coworkers have shown[53] and noted in the main text, Hall effect measurements in organic semiconductors likely result in an overestimate of the carrier density due to different behavior of these carriers. Although any band-like carriers will experience both the Lorentz and electric forces, the hopping carriers only respond to the electric forces, resulting in carriers being moved to opposite sides of the channel and thus a reduced hall voltage, which is inversely proportional to the reported carrier density. The reported mobilities are calculated from both an independent measurement of the sample conductivity as well as the Hall voltage, this time in a direct proportionality, thus resulting in an underestimate of the mobility. We therefore note that the mobilities we report are likely underestimated, with correspondingly overestimated carrier densities, but this is true for both the F_4TCNQ- and DDB-F_{72}-doped P3HT samples that we use comparison.

Calculation of Dopant Density Based on Mass Measurements

One simple method to obtain an estimate of the doping efficiency (the number of free carriers produced over the dopant molecules) is to combine our AC-Hall measurements with an estimate of the dopant density by measuring the change in mass after doping. Using the measured mass increase and film volume (1.5 cm × 1.5 cm × 300 nm for DDB-F_{72} and 1.5 cm × 1.5 cm x 145 nm for F_4TCNQ), the density of dopant molecules in the film can be approximated. For these measurements, precisely cut ITO was used as the substrate for its uniformity in size and the samples were weighed on an analytical microbalance. The samples were placed under rough-pump vacuum before the measurements were taken to remove any residual solvent. A set of 6 repeats were measured for each dopant and the results are shown in Tables S5.7 and S5.8.

For DDB-F_{72}, the average dopant density is 6.9×10^{20} cm^{-3} with a standard deviation (σ) of 0.6×10^{20} cm^{-3}. Therefore, the carrier density we obtain via our AC Hall measurements (7.9×10^{20} cm^{-3}) lies well within the 95% confidence limits (2σ) of this data (5.7 to 8.1×10^{20} cm^{-3}), as discussed in the main text. This means that we have about as many carriers as we do dopants and a doping efficiency of ∼100%, supporting the notion that the majority of carriers in DDB-F_{72} doped films are free due to the reduced Coulomb interaction between the shielded anion and the polaron. Finally, the fact that the carriers measured via the AC Hall effect fall at the upper limit of this range is likely due to the tendency of Hall measurements to overestimate the number of free carriers due to screening effects, as discussed above.

For F_4TCNQ, the average dopant density is $4.8(9)\times10^{21}$ cm^{-3} while the carrier density found via AC-Hall is 4.3×10^{20} cm^{-3}, yielding a doping efficiency of ∼10%, an order of magnitude lower than for DDB-F_{72}. It should be noted that the 10% value we measure is slightly higher than the 5% value determined in careful previous work by Pingel and Neher.[17] The reasons for this could be two-fold. One is that we are in a much higher doping regime than the previous work and therefore have started to saturate traps and thus have increased the proportion of free carriers. The other is that, as mentioned in the main text, the AC Hall effect has the potential to overestimate the free carrier density due to screening of the applied magnetic field by the low-mobility carriers, so that the ratio of free carriers to dopants could be slightly lower than what we report.

Table S5.7. Mass measurements of 6 films before and after doping and carrier density of DDB-F_{72}-doped P3HT films based on the measured mass and a film volume of 1.5 cm × 1.5 cm × 300 nm

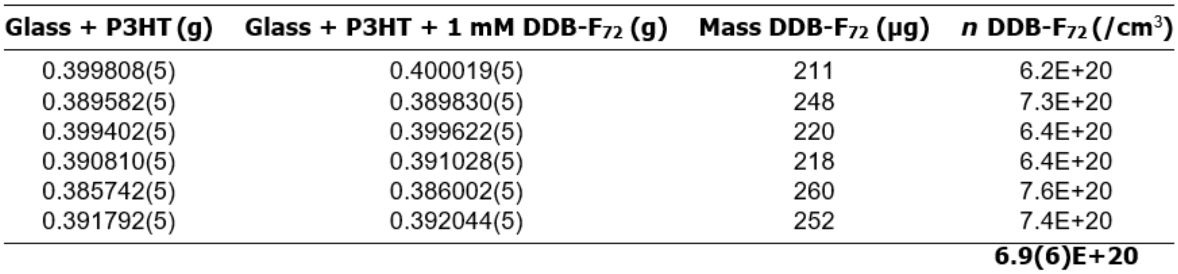

Glass + P3HT (g)	Glass + P3HT + 1 mM DDB-F_{72} (g)	Mass DDB-F_{72} (μg)	*n* DDB-F_{72} (/cm^3)
0.399808(5)	0.400019(5)	211	6.2E+20
0.389582(5)	0.389830(5)	248	7.3E+20
0.399402(5)	0.399622(5)	220	6.4E+20
0.390810(5)	0.391028(5)	218	6.4E+20
0.385742(5)	0.386002(5)	260	7.6E+20
0.391792(5)	0.392044(5)	252	7.4E+20
			6.9(6)E+20

Table S5.8. Mass measurements of 6 films before and after doping and carrier density of F_4TCNQ-doped P3HT films based on the measured mass and a film volume of 1.5 cm × 1.5 cm × 300 nm

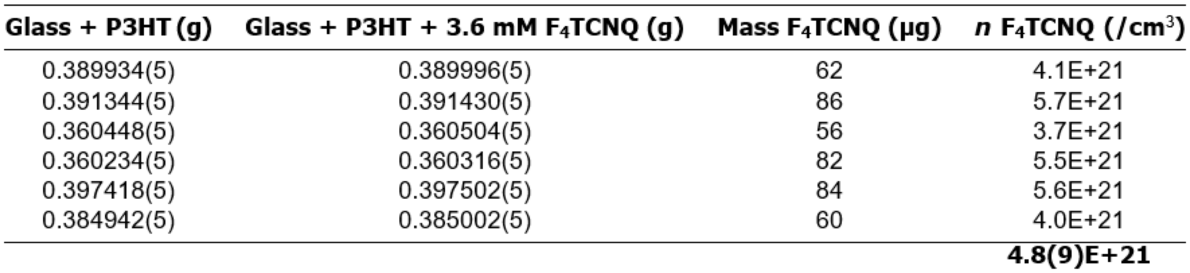

Glass + P3HT (g)	Glass + P3HT + 3.6 mM F_4TCNQ (g)	Mass F_4TCNQ (μg)	*n* F_4TCNQ (/cm^3)
0.389934(5)	0.389996(5)	62	4.1E+21
0.391344(5)	0.391430(5)	86	5.7E+21
0.360448(5)	0.360504(5)	56	3.7E+21
0.360234(5)	0.360316(5)	82	5.5E+21
0.397418(5)	0.397502(5)	84	5.6E+21
0.384942(5)	0.385002(5)	60	4.0E+21
			4.8(9)E+21

5.5 References

(1) Lüssem, B.; Riede, M.; Leo, K. *Doping of Organic Semiconductors*; 2013; Vol. 210. https://doi.org/10.1002/pssa.201228310.

(2) Zhou, H.; Zhang, Y.; Mai, C. K.; Collins, S. D.; Nguyen, T. Q.; Bazan, G. C.; Heeger, A. J. Conductive Conjugated Polyelectrolyte as Hole-Transporting Layer for Organic Bulk Heterojunction Solar Cells. *Adv. Mater.* **2014**, *26* (5), 780–785. https://doi.org/10.1002/adma.201302845

(3) Nikolka, M.; Nasrallah, I.; Rose, B.; Ravva, M. K.; Broch, K.; Sadhanala, A.; Harkin, D.; Charmet, J.; Hurhangee, M.; Brown, A.; et al. High Operational and Environmental Stability of High-Mobility Conjugated Polymer Field-Effect Transistors through the Use of Molecular Additives. *Nat. Mater.* **2017**, *16* (3), 356–362. https://doi.org/10.1038/nmat4785

(4) Glaudell, A. M.; Cochran, J. E.; Patel, S. N.; Chabinyc, M. L. Impact of the Doping Method on Conductivity and Thermopower in Semiconducting Polythiophenes. *Adv. Energy Mater.* **2015**, *5* (4). https://doi.org/10.1002/aenm.201401072.

(5) Patel, S. N.; Glaudell, A. M.; Peterson, K. A.; Thomas, E. M.; O'Hara, K. A.; Lim, E.; Chabinyc, M. L. Morphology Controls the Thermoelectric Power Factor of a Doped Semiconducting Polymer. *Sci. Adv.* **2017**, *3* (6), 24–26. https://doi.org/10.1126/sciadv.170043

(6) Zuo, G.; Andersson, O.; Abdalla, H.; Kemerink, M. High Thermoelectric Power Factor from Multilayer Solution-Processed Organic Films. *Appl. Phys. Lett.* **2018**, *112* (8), 1–5. https://doi.org/10.1063/1.5016908.

(7) Hynynen, J.; Kiefer, D.; Müller, C. Influence of Crystallinity on the Thermoelectric Power Factor of P3HT Vapour-Doped with F4TCNQ. *RSC Adv.* **2018**, *8* (3), 1593–1599. https://doi.org/10.1039/c7ra11912gH.

(8) Lim, E.; Peterson, K. A.; Su, G. M.; Chabinyc, M. L. Thermoelectric Properties of Poly(3-Hexylthiophene) (P3HT) Doped with 2,3,5,6-Tetrafluoro-7,7,8,8-Tetracyanoquinodimethane (F4TCNQ) by Vapor-Phase Infiltration. *Chem. Mater.* **2018**, *30* (3), 998–1010. https://doi.org/10.1021/acs.chemmater.7b04849.

(9) Hamidi-Sakr, A.; Biniek, L.; Bantignies, J. L.; Maurin, D.; Herrmann, L.; Leclerc, N.; Lévêque, P.; Vijayakumar, V.; Zimmermann, N.; Brinkmann, M. A Versatile Method to Fabricate Highly In-Plane Aligned Conducting Polymer Films with Anisotropic Charge Transport and Thermoelectric Properties: The Key Role of Alkyl Side Chain Layers on the Doping Mechanism. *Adv. Funct. Mater.* **2017**, *27* (25), 1–13. https://doi.org/10.1002/adfm.201700173.

(10) Yuen, J. D.; Dhoot, A. S.; Namdas, E. B.; Coates, N. E.; Heeney, M.; McCulloch, I.; Moses, D.; Heeger, A. J. Electrochemical Doping in Electrolyte-Gated Polymer Transistors. *J. Am. Chem. Soc.* **2007**, *129* (46), 14367–14371. https://doi.org/10.1021/ja0749845.

(11) Chang, J. F.; Clark, J.; Zhao, N.; Sirringhaus, H.; Breiby, D. W.; Andreasen, J. W.; Nielsen, M. M.; Giles, M.; Heeney, M.; McCulloch, I. Molecular-Weight Dependence of Interchain Polaron Delocalization and Exciton Bandwidth in High-Mobility Conjugated Polymers. *Phys. Rev. B - Condens. Matter Mater. Phys.* **2006**, *74* (11), 1–12. https://doi.org/10.1103/PhysRevB.74.115318.

(12) Chiang, C. K.; Gau, S. C.; Fincher, C. R.; Park, Y. W.; MacDiarmid, A. G.; Heeger, A. J. Polyacetylene, $(CH)_x$: N-Type and p-Type Doping and Compensation. *Appl. Phys. Lett.* **1978**, *33* (1), 18–20. https://doi.org/10.1063/1.90166.

(13) Kislyuk, V. V.; Dimitriev, O. P.; Pud, A. A.; Lautru, J.; Ledoux-Rak, I. In-Situ Conductivity and UV-VIS Absorption Monitoring of Iodine Doping-Dedoping Processes in Poly(3-

Hexylthiophene) (P3HT). *J. Phys. Conf. Ser.* **2011**, *286* (1). https://doi.org/10.1088/1742-6596/286/1/012009.

(14) Scholes, D. T.; Hawks, S. A.; Yee, P. Y.; Wu, H.; Lindemuth, J. R.; Tolbert, S. H.; Schwartz, B. J. Overcoming Film Quality Issues for Conjugated Polymers Doped with F4TCNQ by Solution Sequential Processing: Hall Effect, Structural, and Optical Measurements. *J. Phys. Chem. Lett.* **2015**, *6* (23), 4786–4793. https://doi.org/10.1021/acs.jpclett.5b02332.

(15) Scholes, D. T.; Yee, P. Y.; Lindemuth, J. R.; Kang, H.; Onorato, J.; Ghosh, R.; Luscombe, C. K.; Spano, F. C.; Tolbert, S. H.; Schwartz, B. J. The Effects of Crystallinity on Charge Transport and the Structure of Sequentially Processed F4TCNQ-Doped Conjugated Polymer Films. *Adv. Funct. Mater.* **2017**, *27* (44), 1–13. https://doi.org/10.1002/adfm.201702654.

(16) Pingel, P.; Neher, D. Comprehensive Picture of P-Type Doping of P3HT with the Molecular Acceptor F4TCNQ. *Phys. Rev. B* **2013**, *87* (11), 1–9. https://doi.org/10.1103/PhysRevB.87.115209.

(17) Pingel, P.; Arvind, M.; Kölln, L.; Steyrleuthner, R.; Kraffert, F.; Behrends, J.; Janietz, S.; Neher, D. P-Type Doping of Poly(3-Hexylthiophene) with the Strong Lewis Acid Tris(Pentafluorophenyl)Borane. *Adv. Electron. Mater.* **2016**, *2* (10), 1600204. https://doi.org/10.1002/aelm.201600204.

(18) Mityashin, A.; Olivier, Y.; Van Regemorter, T.; Rolin, C.; Verlaak, S.; Martinelli, N. G.; Beljonne, D.; Cornil, J.; Genoe, J.; Heremans, P. Unraveling the Mechanism of Molecular Doping in Organic Semiconductors. *Adv. Mater.* **2012**, *24* (12), 1535–1539. https://doi.org/10.1002/adma.201104269.

(19) Jacobs, I. E.; Aasen, E. W.; Oliveira, J. L.; Fonseca, T. N.; Roehling, J. D.; Li, J.; Zhang, G.; Augustine, M. P.; Mascal, M.; Moulé, A. J. Comparison of Solution-Mixed and Sequentially Processed P3HT:F4TCNQ Films: Effect of Doping-Induced Aggregation on Film Morphology. *J. Mater. Chem. C* **2016**, *4* (16), 3454–3466. https://doi.org/10.1039/C5TC04207K.

(20) Hynynen, J.; Kiefer, D.; Yu, L.; Kroon, R.; Munir, R.; Amassian, A.; Kemerink, M.; Müller, C. Enhanced Electrical Conductivity of Molecularly P-Doped Poly(3-Hexylthiophene) through Understanding the Correlation with Solid-State Order. *Macromolecules* **2017**, *50* (20), 8140–8148. https://doi.org/10.1021/acs.macromol.7b00968.

(21) Chew, A. R.; Ghosh, R.; Shang, Z.; Spano, F. C.; Salleo, A. Sequential Doping Reveals the Importance of Amorphous Chain Rigidity in Charge Transport of Semi-Crystalline Polymers. *J. Phys. Chem. Lett.* **2017**, 4974–4980. https://doi.org/10.1021/acs.jpclett.7b01989.

(22) Kang, K.; Watanabe, S.; Broch, K.; Sepe, A.; Brown, A.; Nasrallah, I.; Nikolka, M.; Fei, Z.; Heeney, M.; Matsumoto, D.; et al. 2D Coherent Charge Transport in Highly Ordered Conducting Polymers Doped by Solid State Diffusion. *Nat. Mater.* **2016**, *15* (8), 896–902. https://doi.org/10.1038/nmat4634

(23) Gao, W.; Kahn, A. Controlled P-Doping of Zinc Phthalocyanine by Coevaporation with Tetrafluorotetracyanoquinodimethane: A Direct and Inverse Photoemission Study. *Appl. Phys. Lett.* **2001**, *79* (24), 4040–4042. https://doi.org/10.1063/1.1424067.

(24) King, R. B. Three-Dimensional Aromaticity in Polyhedral Boranes and Related Molecules. *Chem. Rev.* **2001**, *101* (5), 1119–1152. https://doi.org/10.1021/cr000442t.

(25) Peymann, T.; Knobler, C. B.; Khan, S. I.; Hawthorne, M. F. Dodeca(Benzyloxy)Dodecaborane, B12(OCH2Ph)12: A Stable Derivative of Hypercloso-$B_{12}H_{12}$. *Angew. Chemie - Int. Ed.* **2001**, *40* (9), 1664–1667. https://doi.org/10.1002/1521-3773(20010504)40:9<1664::AID-ANIE16640>3.0.CO;2-O.

(26) Peymann, T.; Knobler, C. B.; Hawthorne, M. F. An Unpaired Electron Incarcerated within an Icosahedral Borane Cage: Synthesis and Crystal Structure of the Blue, Air-Stable {[Closo-$B_{12}(CH_3)_{12}$]·}-Radical. *Chem. Commun.* **1999**, *12* (20), 2039–2040. https://doi.org/10.1039/a905406e.

(27) Van, N.; Tiritiris, I.; Winter, R. F.; Sarkar, B.; Singh, P.; Duboc, C.; Muñoz-Castro, A.; Arratia-Pérez, R.; Kaim, W.; Schleid, T. Oxidative Perhydroxylation of [Closo-$B_{12}H_{12}]^{2-}$ to the Stable Inorganic Cluster Redox System $[B_{12}(OH)_{12}]^{2-/\cdot-}$: Experiment and Theory. *Chem. - A Eur. J.* **2010**, *16* (37), 11242–11245. https://doi.org/10.1002/chem.201001374.

(28) Farha, O. K.; Julius, R. L.; Lee, M. W.; Huertas, R. E.; Knobler, C. B.; Hawthorne, M. F. Synthesis of Stable Dodecaalkoxy Derivatives of Hypercloso-$B_{12}H_{12}$. *J. Am. Chem. Soc.* **2005**, *127* (51), 18243–18251. https://doi.org/10.1021/ja0556373

(29) Axtell, J. C.; Saleh, L. M. A. A.; Qian, E. A.; Wixtrom, A. I.; Spokoyny, A. M. Synthesis and Applications of Perfunctionalized Boron Clusters. *Inorg. Chem.* **2018**, *57* (5), 2333–2350. https://doi.org/10.1021/acs.inorgchem.7b02912.

(30) Jung, D.; Saleh, L. M. A.; Berkson, Z. J.; El-Kady, M. F.; Hwang, J. Y.; Mohamed, N.; Wixtrom, A. I.; Titarenko, E.; Shao, Y.; McCarthy, K.; et al. A Molecular Cross-Linking Approach

for Hybrid Metal Oxides. *Nat. Mater.* **2018**, *17* (4), 341–348. https://doi.org/10.1038/s41563-018-0021-9.

(31) Messina, M. S.; Axtell, J. C.; Wang, Y.; Chong, P.; Wixtrom, A. I.; Kirlikovali, K. O.; Upton, B. M.; Hunter, B. M.; Shafaat, O. S.; Khan, S. I.; et al. Visible-Light-Induced Olefin Activation Using 3D Aromatic Boron-Rich Cluster Photooxidants. *J. Am. Chem. Soc.* **2016**, *138* (22), 6952–6955. https://doi.org/10.1021/jacs.6b03568.

(32) Khatib, O.; Lee, B.; Yuen, J.; Li, Z. Q.; Di Ventra, M.; Heeger, A. J.; Podzorov, V.; Basov, D. N. Infrared Signatures of High Carrier Densities Induced in Semiconducting Poly(3-Hexylthiophene) by Fluorinated Organosilane Molecules. *J. Appl. Phys.* **2010**, *107* (12). https://doi.org/10.1063/1.3436567.

(33) Kao, C. Y.; Lee, B.; Wielunski, L. S.; Heeney, M.; McCulloch, I.; Garfunkel, E.; Feldman, L. C.; Podzorov, V. Doping of Conjugated Polythiophenes with Alkyl Silanes. *Adv. Funct. Mater.* **2009**, *19* (12), 1906–1911. https://doi.org/10.1002/adfm.200900120.

(34) Hawks, S. A.; Aguirre, J. C.; Schelhas, L. T.; Thompson, R. J.; Huber, R. C.; Ferreira, A. S.; Zhang, G.; Herzing, A. A.; Tolbert, S. H.; Schwartz, B. J. Comparing Matched Polymer:Fullerene Solar Cells Made by Solution-Sequential Processing and Traditional Blend Casting: Nanoscale Structure and Device Performance. *J. Phys. Chem. C* **2014**, *118* (31), 17413–17425. https://doi.org/10.1021/jp504560r.

(35) Aguirre, J. C.; Hawks, S. A.; Ferreira, A. S.; Yee, P.; Subramaniyan, S.; Jenekhe, S. A.; Tolbert, S. H.; Schwartz, B. J. Sequential Processing for Organic Photovoltaics: Design Rules for

Morphology Control by Tailored Semi-Orthogonal Solvent Blends. *Adv. Energy Mater.* **2015**, *5* (11), 1402020. https://doi.org/10.1002/aenm.20140202.

(36) Aubry, T. J.; Ferreira, A. S.; Yee, P. Y.; Aguirre, J. C.; Hawks, S. A.; Fontana, M. T.; Schwartz, B. J.; Tolbert, S. H. Processing Methods for Obtaining a Face-On Crystalline Domain Orientation in Conjugated Polymer-Based Photovoltaics. *J. Phys. Chem. C* **2018**, *122* (27), 15078–15089. https://doi.org/10.1021/acs.jpcc.8b02859.

(37) Reiser, P.; Müller, L.; Sivanesan, V.; Lovrincic, R.; Barlow, S.; Marder, S. R.; Pucci, A.; Jaegermann, W.; Mankel, E.; Beck, S. Dopant Diffusion in Sequentially Doped Poly(3-Hexylthiophene) Studied by Infrared and Photoelectron Spectroscopy. *J. Phys. Chem. C* **2018**, *122* (26), 14518–14527. https://doi.org/10.1021/acs.jpcc.8b02657.

(38) Liang, Z.; Zhang, Y.; Souri, M.; Luo, X.; Boehm, A. M.; Li, R.; Zhang, Y.; Wang, T.; Kim, D. Y.; Mei, J.; et al. Influence of Dopant Size and Electron Affinity on the Electrical Conductivity and Thermoelectric Properties of a Series of Conjugated Polymers. *J. Mater. Chem. A* **2018**, *6* (34), 16495–16505. https://doi.org/10.1039/c8ta05922e

(39) Müller, L.; Nanova, D.; Glaser, T.; Beck, S.; Pucci, A.; Kast, A. K.; Schröder, R. R.; Mankel, E.; Pingel, P.; Neher, D.; et al. Charge-Transfer-Solvent Interaction Predefines Doping Efficiency in p-Doped P3HT Films. *Chem. Mater.* **2016**, *28* (12), 4432–4439. https://doi.org/10.1021/acs.chemmater.6b01629.

(40) Kivala, M.; Boudon, C.; Gisselbreeht, J. P.; Enko, B.; Seiler, P.; Imke, B. M.; Langer, N.; Jarowski, P. D.; Geseheidt, G.; Diederich, F. Organic Super-Acceptors with Efficient Intramolecular Charge-Transfer Interactions by [2+2] Cycloadditions of TCNE, TCNQ, and F4-

TCNQ to Donor-Substituted Cyanoalkynes. *Chem. - A Eur. J.* **2009**, *15* (16), 4111–4123. https://doi.org/10.1002/chem.200802563.

(41) Van der Pauw, L. J. A Method of Measuring the Resistivity and Hall Coefficient on Lamellae of Arbitraty Shape. *Phys. Tech. Rev.* **1958**, *1958* (I), 220–224.

(42) Kolesov, V. A.; Fuentes-Hernandez, C.; Chou, W. F.; Aizawa, N.; Larrain, F. A.; Wang, M.; Perrotta, A.; Choi, S.; Graham, S.; Bazan, G. C.; et al. Solution-Based Electrical Doping of Semiconducting Polymer Films over a Limited Depth. *Nat. Mater.* **2017**, *16* (4), 474–481. https://doi.org/10.1038/NMAT4818.

(43) Goeltz, J. C.; Hanson, C. J.; Kubiak, C. P. Rates of Electron Self-Exchange Reactions between Oxo-Centered Ruthenium Clusters Are Determined by Orbital Overlap. *Inorg. Chem.* **2009**, *48* (11), 4763–4767. https://doi.org/10.1021/ic8022024.

(44) Goeltz, J. C.; Benson, E. E.; Kubiak, C. P. Electronic Structural Effects in Self-Exchange Reactions. *J. Phys. Chem. B* **2010**, *114* (45), 14729–14734. https://doi.org/10.1021/jp103009b.

(45) Porter, T. M.; Canzi, G. C.; Chabolla, S. A.; Kubiak, C. P. Tuning Electron Delocalization and Transfer Rates in Mixed-Valent Ru_3O Complexes through "Push-Pull" Effects. *J. Phys. Chem. A* **2016**, *120* (32), 6309–6316. https://doi.org/10.1021/acs.jpca.6b05485.

(46) Miller, N. C.; Cho, E.; Gysel, R.; Risko, C.; Coropceanu, V.; Miller, C. E.; Sweetnam, S.; Sellinger, A.; Heeney, M.; McCulloch, I.; et al. Factors Governing Intercalation of Fullerenes and Other Small Molecules Between the Side Chains of Semiconducting Polymers Used in Solar Cells. *Adv. Energy Mater.* **2012**, *2* (10), 1208–1217. https://doi.org/10.1002/aenm.201200392.

(47) Pochas, C. M.; Spano, F. C. New Insights on the Nature of Two-Dimensional Polarons in Semiconducting Polymers: Infrared Absorption in Poly(3-Hexylthiophene). *J. Chem. Phys.* **2014**, *140* (24). https://doi.org/10.1063/1.4882696.

(48) Ghosh, R.; Pochas, C. M.; Spano, F. C. Polaron Delocalization in Conjugated Polymer Films. *J. Phys. Chem. C* **2016**, *120* (21), 11394–11406. https://doi.org/10.1021/acs.jpcc.6b02917.

(49) Ghosh, R.; Chew, A. R.; Onorato, J.; Pakhnyuk, V.; Luscombe, C. K.; Salleo, A.; Spano, F. C. Spectral Signatures and Spatial Coherence of Bound and Unbound Polarons in P3HT Films: Theory Versus Experiment. *J. Phys. Chem. C* **2018**, acs.jpcc.8b03873. https://doi.org/10.1021/acs.jpcc.8b03873

(50) Lindemuth, J. Variable Temperature Hall Measurements on Low-Mobility Materials. *Spie* **2012**, *8470* (October 2012), 84700G. https://doi.org/10.1117/12.929655

(51) Chen, Y.; Yi, H. T.; Podzorov, V. High-Resolution Ac Measurements of the Hall Effect in Organic Field-Effect Transistors. *Phys. Rev. Appl.* **2016**, *5* (3), 1–9. https://doi.org/10.1103/PhysRevApplied.5.034008.

(52) Werner, F. Hall Measurements on Low-Mobility Thin Films. *J. Appl. Phys.* **2017**, *122* (13). https://doi.org/10.1063/1.4990470.

(53) Yi, H. T.; Gartstein, Y. N.; Podzorov, V. Charge Carrier Coherence and Hall Effect in Organic Semiconductors. *Sci. Rep.* **2016**, *6* (March), 1–11. https://doi.org/10.1038/srep23650.

(54) Wixtrom, A. I.; Shao, Y.; Jung, D.; Machan, C. W.; Kevork, S. N.; Qian, E. A.; Axtell, J. C.; Khan, S. I.; Kubiak, C. P.; Spokoyny, A. M. Rapid Synthesis of Redox-Active Dodecaborane

$B_{12}(OR)_{12}$ Clusters under Ambient Conditions. *Inorg. Chem. Front.* **2016**, *3* (5), 711–717. https://doi.org/10.1039/C5QI00263J

(55) TURBOMOLE V6.6 2014, a development of University of Karlsruhe and Forschungszentrum Karlsruhe GmbH, 1989-2007, TURBOMOLE GmbH, since 2007; available from http://www.turbomole.com

(56) Tao, J.; Perdew, J. P.; Staroverov, V. N.; Scuseria, G. E. Climbing the Density Functional Ladder: Nonempirical Meta–Generalized Gradient Approximation Designed for Molecules and Solids. *Phys. Rev. Lett.* **2003**, *91* (14), 3–6. https://doi.org/10.1103/PhysRevLett.91.146401

(57) Weigend, F.; Ahlrichs, R. Balanced Basis Sets of Split Valence, Triple Zeta Valence and Quadruple Zeta Valence Quality for H to Rn: Design and Assessment of Accuracy. *Phys. Chem. Chem. Phys.* **2005**, *7* (18), 3297–3305. https://doi.org/10.1039/b508541a

(58) Weigend, F. Accurate Coulomb-Fitting Basis Sets for H to Rn. *Phys. Chem. Chem. Phys.* **2006**, *8* (9), 1057–1065. https://doi.org/10.1039/b515623h

(59) Staroverov, V. N.; Scuseria, G. E.; Tao, J.; Perdew, J. P. Comparative Assessment of a New Nonempirical Density Functional: Molecules and Hydrogen-Bonded Complexes. *J. Chem. Phys.* **2003**, *119* (23), 12129–12137. https://doi.org/10.1063/1.1626543.

(60) Dunning, T. H. Gaussian Basis Sets for Use in Correlated Molecular Calculations. I. The Atoms Boron through Neon and Hydrogen. *J. Chem. Phys.* **1989**, *90* (2), 1007–1023. https://doi.org/10.1063/1.4561.

(61) Davidson, E. R.; McMurchie, L. E.; Day, S. J. The B K Method: Application to Methylene. *J. Chem. Phys.* **1981**, *74* (10), 5491–5496. https://doi.org/10.1063/1.440954.

(62) Gaussian 09, Revision A.02, M. J. Frisch, G. W. Trucks, H. B. Schlegel, G. E. Scuseria, M. A. Robb, J. R. Cheeseman, G. Scalmani, V. Barone, G. A. Petersson, H. Nakatsuji, X. Li, M. Caricato, A. Marenich, J. Bloino, B. G. Janesko, R. Gomperts, B. Mennucci, H. P. Hratchian, J. V. Ortiz, A. F. Izmaylov, J. L. Sonnenberg, D. Williams-Young, F. Ding, F. Lipparini, F. Egidi, J. Goings, B. Peng, A. Petrone, T. Henderson, D. Ranasinghe, V. G. Zakrzewski, J. Gao, N. Rega, G. Zheng, W. Liang, M. Hada, M. Ehara, K. Toyota, R. Fukuda, J. Hasegawa, M. Ishida, T. Nakajima, Y. Honda, O. Kitao, H. Nakai, T. Vreven, K. Throssell, J. A. Montgomery, Jr., J. E. Peralta, F. Ogliaro, M. Bearpark, J. J. Heyd, E. Brothers, K. N. Kudin, V. N. Staroverov, T. Keith, R. Kobayashi, J. Normand, K. Raghavachari, A. Rendell, J. C. Burant, S. S. Iyengar, J. Tomasi, M. Cossi, J. M. Millam, M. Klene, C. Adamo, R. Cammi, J. W. Ochterski, R. L. Martin, K. Morokuma, O. Farkas, J. B. Foresman, and D. J. Fox, Gaussian, Inc., Wallingford CT, 2016

(63) Nelsen, S. F.; Ramm, M. T.; Ismagilov, R. F.; Nagy, M. A.; Trieber, D. A.; Powell, D. R.; Chen, X.; Gengler, J. J.; Qu, Q.; Brandt, J. L.; et al. Estimation of Self-Exchange Electron Transfer Rate Constants for Organic Compounds from Stopped-Flow Studies. *J. Am. Chem. Soc.* **1997**, *119* (25), 5900–5907. https://doi.org/10.1021/ja970321j.

(64) Chan, M. S.; DeRoos, J. B.; Wahl, A. C. Rate of Electron Transfer between Tris(3,4,7,8-Tetramethyl-1,10-Phenanthroline)Iron(II) and -(III) Ions from Nuclear Magnetic Resonance Studies. *J. Phys. Chem.* **1973**, *77* (18), 2163–2165. https://doi.org/10.1021/j100637a001.

(65) Hart, D. W.; Blackburn, T. F.; Schwartz, J. Hydrozirconation. III. Stereospecific and Regioselective Functionalization of Alkylacetylenes via Vinylzirconium(IV) Intermediates. *J. Am. Chem. Soc.* **1975**, *97* (3), 679–680. https://doi.org/10.1021/ja00836a056.

(66) Efros, A. L.; Shklovskii, B. I. Coulomb Gap and Low Temperature Conductivity of Disordered Systems. *J. Phys. C Solid State Phys.* **1975**, *8* (4). https://doi.org/10.1088/0022-3719/8/4/003.

(67) Mott, N. F. Conduction in Glasses Containing Transition Metal Ions. *J. Non. Cryst. Solids* **1968**, *1* (1), 1–17. https://doi.org/10.1016/0022-3093(68)90002-1.

(68) Nishino, H.; Yu, G.; Heeger, A. J.; Chen, T. A.; Rieke, R. D. Electroluminescence from Blend Films of Poly(3-Hexylthiophene) and Poly(N-Vinylcarbazole). *Synth. Met.* **1995**, *68* (3), 243–247. https://doi.org/10.1016/0379-6779(94)02295-A

(69) Wang, S.; Ha, M.; Manno, M.; Daniel Frisbie, C.; Leighton, C. Hopping Transport and the Hall Effect near the Insulator-Metal Transition in Electrochemically Gated Poly(3-Hexylthiophene) Transistors. *Nat. Commun.* **2012**, *3*, 0–6. https://doi.org/10.1038/ncomms2213.

CHAPTER 6

Conclusions

The implementation of pseudocapacitive or fast-charging materials in lithium-ion batteries shows promise for lessening our societal dependence on fossil fuels. Fast-charging lithium-ion batteries should provide electric vehicles with comparable charging times to the re-fueling speeds of traditional internal combustion engine vehicles, which would allow for widespread adoption of electric vehicles. Renewable energy sources, such as solar cells, will allow for the clean charging of these fast-charging lithium-ion batteries. Semiconducting polymers can be used in organic solar cells to offer a tunable and low-cost source of clean energy.

The first part of this thesis has shown that nanostructured nickel-rich cathode materials can behave as high-capacity and fast-charging materials for lithium-ion batteries. Because the nickel-rich cathode materials already lacked discontinuous phase transitions in the bulk, we found that only moderate reductions in particle size were necessary to decrease lithium-ion diffusion distances to obtain fast-charging capabilities and the appearance of pseudocapacitive properties in nanostructured NCA. However, we ultimately found superior capacity and fast-charging performance with nanostructured NCA over nanostructured NMC. This was likely due to the higher overall nickel content in NCA and the fact that the presence of Mn^{4+} leads to increased amounts of Ni^{2+}, and thus greater cation mixing in NMC. Interestingly, we found that nanostructured NMC possessed electrochemical kinetics that did not depend on particle size, although fast charging capabilities could be induced by expanding the lithium-ion diffusion layer thickness. These results indicate that for these nickel-rich cathode materials control over both the lithium-ion diffusion distance and the lithium-ion diffusion rate are important for obtaining fast-charging capabilities.

Additionally, we showed the practicality for commercialization of the nanostructured NCA materials, which were synthesized with readily available F127 templates for a scalable synthesis. Thick NCA electrodes were prepared and paired with pseudocapacitive Nb_2O_5 anodes to form fast-charging full-cell devices with commercially relevant loadings. The full-cell devices showed long-term cycling at fast rates, without significant losses in capacity. The next step for these nickel-rich materials would be to study a surface coating or electrolyte additive that will protect the surface without forming thick insulating layers or removing redox active components, so that they can be handled easily in air.

Finally, the second part of this thesis has shown that molecular doping can be used to increase the conductivity of a semiconducting P3HT polymer film. The molecular dopant used was a large dodecaborane-based dopant, which allowed for spatial separation of the electron and polaron to create highly mobile charge carriers. Additionally, the large dopant was able to fully penetrate the polymer film because of its high redox potential that acted as an energetic driving force for doping. This is important because it indicates that this molecular doping process with dodecaborane-based dopants could be scaled-up to thicker films for commercial organic electronic applications. Thus the next steps would be to tune the redox potential of the dodecaborane-based dopant to tune the level of doping in the polymer films and to study the molecular doping in thicker films for electronic applications.

APPENDIX A

Detailed Procedure for X-Ray Diffraction of Nickel-Rich Layered Transition Metal Oxides

This section describes the detailed procedure for running X-ray diffraction (XRD) on nickel-rich layered transition metal oxides to determine the degree of cation mixing.

A.1 Preparation and use of sample holder for X-ray diffraction

As mentioned previously, nickel-rich layered transition metal oxides can undergo cation mixing, where Ni^{2+} can migrate from the transition metal layer to the Li^+ layer due to their similar ionic size. The degree of cation mixing can be assessed using XRD, by determining the integrated intensity ratio of the (003) peak to the (104) peak. However, the integrated intensity of these peaks is also sensitive to the height of the sample in the diffractometer. If the sample height is not kept consistent between samples, this can lead to errors in interpretation of the ratio. Therefore, it is very important to try to keep the sample height the same for every measurement.

Here a Bruker D8 Powder X-ray Diffractometer was used with a sample stage that holds a circular plastic sample holder, which can be spun during measurement to allow for the elimination of texturing effects. In order to ensure a consistent sample height between measurements a special sample holder was designed (Fig. A.1). A Dremel was used to grind a small square indentation into a silicon wafer so that the powder sample can be packed into the indentation to sit flush with the silicon (this gives the exact same sample height each time). The plastic sample holder for the instrument has a rectangular indentation to hold the sample and it was determined that this indentation was the thickness of exactly two silicon wafers. A larger piece of silicon was cut with the exact dimensions of the indentation in the plastic holder, so that the silicon wafer can be placed into the plastic holder in the same position each time. Then the smaller silicon wafer with the indentation for the powder sample was super-glued on top of the larger silicon piece so that the sample will sit in the exact middle of the plastic holder and the sample will be flush with the top for measurement. Silicon also has a large diffraction peak at 76° (2θ), which can be used to calibrate the peak positions.

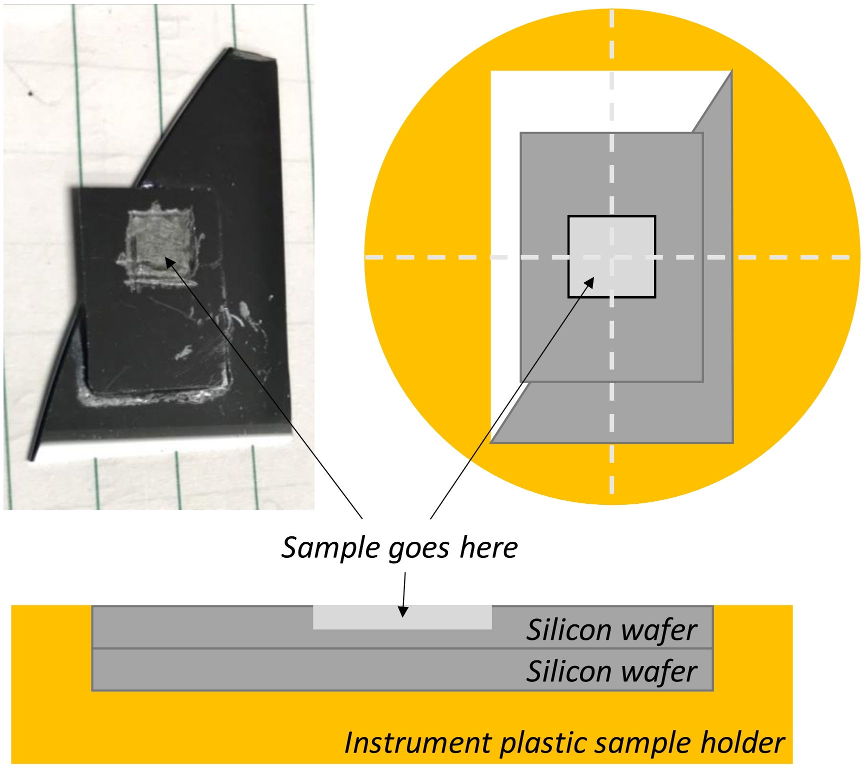

Figure A.1. (top left) Image of the designed sample holder. (top right) Top-down schematic of the silicon sample holder in the circular plastic holder, showing that the bottom silicon wafer has the same dimensions as the rectangular indentation and that the sample is placed in the exact middle of the overall holder. (bottom) Side-view schematic of the sample holder, showing that when the sample is packed into the indentation of the silicon wafer, it sits flush with the top of the sample holder.